DYNAMICS AND FREE-SURFACE GEOMETRY OF TURBULENT LIQUID SHEETS

A Dissertation
Presented to
The Academic Faculty

By

Samuel Glen Durbin II

In Partial Fulfillment
Of the Requirements for the Degree
Doctor of Philosophy in Mechanical Engineering

Georgia Institute of Technology

January 2005

DYNAMICS AND FREE-SURFACE GEOMETRY OF TURBULENT LIQUID SHEETS

Approved by:

Dr. Minami Yoda, Co-Advisor
Woodruff School of Mechanical Engineering
Georgia Institute of Technology

Dr. Said I. Abdel Khalik, Co-Advisor
Woodruff School of Mechanical Engineering
Georgia Institute of Technology

Dr. Cyrus K. Aidun
Woodruff School of Mechanical Engineering
Georgia Institute of Technology

Dr. Donald R. Webster
School of Civil & Environmental Engineering
Georgia Institute of Technology

Dr. S. Mostafa Ghiaasiaan
Woodruff School of Mechanical Engineering
Georgia Institute of Technology

Dr. Ralph W. Moir
Lawrence Livermore National Laboratory

Date Approved: January 31, 2005

ACKNOWLEDGEMENTS

I would like to express my sincere gratitude to those who have made this work possible. I would like to thank my advisors Dr. Said Abdel-Khalik and Dr. Minami Yoda for their unfailing guidance and support. I would also like to thank Dr. Ralph Moir for his unceasing inspiration and friendship over the years. The advice and recommendations of the remaining members of my committee including Dr. Cyrus Aidun, Dr. Mostafa Ghiaasiaan, and Dr. Don Webster are also greatly appreciated

I would also like to thank my laboratory colleagues whose support and friendship have been invaluable: Jon Anderson, Ulf Andresen, Justin Collins, Lance Elwell, Tim Koehler, Charlotte Kotas, Haifeng Li, Jeff Reperant, Brian Shellabarger, Reza Sadr, Jörg Stromberger, and Claudia Zettner. Special thanks go to Mr. Dennis Sadowski for his tireless efforts in the successful design and construction of the experimental apparatus. In addition, I gratefully thank my colleagues at Lawrence Livermore National Laboratory for their hospitality and collaboration during my student internship: Ryan Abbott, Dr. Jeff Latkowski, Dr. Susanna Reyes, and Dr. Wayne Meier.

Most of all I wish to express my deepest appreciation to my family, without whom all my achievements would be meaningless. I would especially like to thank my wife Tracie for her undying love, support, and understanding.

Finally, I would like to acknowledge the support and opportunities afforded me by the Fusion Energy Sciences Fellowship program and the Oak Ridge Institute for Science and Education.

TABLE OF CONTENTS

ACKNOWLEDGEMENTS iii

LIST OF TABLES vii

LIST OF FIGURES ix

NOMENCLATURE xvi

ABSTRACT xix

CHAPTER 1
INTRODUCTION 1

1.1 Background 2
1.1.1 Inertial Fusion Energy 2
1.1.2 High-Yield Lithium-Injection Fusion Energy Power Plant 5
1.2 Objectives 9

CHAPTER 2
LITERATURE REVIEW 11

2.1 Liquid Protection in Fusion Power Plants 11
2.2 Submerged Plane Jets 13
2.3 Low Reynolds Number Jets 14
2.4 Initial Condition Studies on Liquid Sheets 17
2.5 Surface Ripple Studies 18
2.6 Turbulent Jet Stability and Breakup 20
2.7 Nozzle and Flow Conditioning Design Studies 21
2.8 Previous Studies at the Georgia Tech Large-Scale Test Facility 23

CHAPTER 3
EXPERIMENTAL APPARATUS AND PROCEDURES 26

3.1 Flow Components 26
3.1.1 Flow Loop 26
3.1.2 Flow Conditioning Design 31
3.1.3 Nozzle Design 34
3.1.4 Boundary-Layer Cutter Design 36
3.2 Laser-Doppler Velocimetry 39
3.2.1 Principles of LDV 39
3.2.2 LDV Experimental Setup 43
3.2.3 LDV Procedures 48

3.3 Planar Laser-Induced Fluorescence 52
3.3.1 Experimental Setup for PLIF 52
3.3.2 PLIF Procedures 55
3.4 Primary Turbulent Breakup 57
3.4.1 Mass Collection Experimental Setup 57
3.4.2 Mass Collection Procedures 59
3.4.3 Droplet Visualizations 61

CHAPTER 4
RESULTS AND DISCUSSION 62

4.1 LDV Measurements 62
4.1.1 Effect of *Re* 62
4.1.2 Effect of Flow Conditioning 69
4.2 PLIF Measurements 76
4.2.1 Effect of *Re* 76
4.2.2 Effect of Flow Conditioning 81
4.2.3 Effect of Boundary-Layer Cutting 88
4.3 Mass Collection Measurements 94
4.3.1 Effect of Initial Conditions 94
4.3.2 Droplet Visualizations 96
4.3.3 Comparison to Correlations 98

CHAPTER 5
CONCLUSIONS AND RECOMMENDATIONS 100

5.1 Conclusions 100
5.1.1 Initial Conditions 101
5.1.1.1 Effect of Re 101
5.1.1.2 Effect of Flow Conditioning 102
5.1.2 Free-Surface Behavior 103
5.1.2.1 Effect of Re 103
5.1.2.2 Effect of Flow Conditioning 103
5.1.2.3 Effect of Boundary-Layer Cutting 105
5.1.3 Turbulent Breakup 106
5.1.3.1 Effect of Initial Conditions 106
5.1.3.2 Comparison to Breakup Correlations 107
5.2 Implications for Thick Liquid Protection 108
5.3 Contributions 109
5.4 Recommendations 110

APPENDIX A
PRIMARY TURBULENT BREAKUP CORRELATIONS **112**

APPENDIX B
ERROR ANALYSIS **117**

B.1 Error Propagation Analysis 117
B.1.1 Uncertainty in Mean Nozzle Exit Velocity 118
B.1.2 Uncertainty in LDV Results 120
B.1.3 Uncertainty in PLIF Results 126
B.1.4 Uncertainty in Normalized Mass Collection Results 128
B.1.5 Uncertainty in Normalized Mass Cut Rate 130
B.1 Experimental Reproducibility 131
B.2.1 Reproducibility of LDV Results 131
B.2.2 LDV System Noise in Transverse Measurements 133
B.2.3 Reproducibility of PLIF Results 135

APPENDIX C
ADDITIONAL EXPERIMENTAL DATA **138**

C.1 LDV Measurements 138
C.2 PLIF Measurements 143

APPENDIX D
JOURNAL PUBLICATIONS **149**

REFERENCES **201**

LIST OF TABLES

Table 1.1.	Comparison of flow parameters between HYLIFE-II and scaled experiments.	8
Table 3.1.	Detailed list of the experimental apparatus hardware components.	29
Table 3.2.	Flow conditioner sections.	32
Table 3.3.	Flow conditioning elements.	32
Table 3.4.	Detailed list of the LDV system components.	44
Table 4.1.	Streamwise and transverse rms fluctuations averaged over $\lvert z / b \rvert \leq 0.375$ for Type I.A flow conditioning and Re = 53,000.	68
Table 4.2.	Streamwise and transverse rms fluctuations averaged over $\lvert z / b \rvert \leq 0.375$ for Type I.A flow conditioning and Re = 120,000.	68
Table 4.3.	Pressure loss coefficients across three different flow conditioning schemes for Re = 120,000.	70
Table B.1.	Measurement uncertainties and intermediate calculations for U_o.	119
Table B.2.	Measurement uncertainties and intermediate calculations for u / U_o.	121
Table B.3.	Measurement uncertainties and intermediate calculations for u' / U_o.	123
Table B.4.	Measurement uncertainties and intermediate calculations for w / U_o.	124
Table B.5.	Measurement uncertainties and intermediate calculations for w' / U_o.	124
Table B.6.	Measurement uncertainties and intermediate calculations for y / W_o.	125

Table B.7. Measurement uncertainties and intermediate calculations for z/b. 125

Table B.8. Measurement uncertainties and intermediate calculations for x/δ. 126

Table B.9. Measurement uncertainties and intermediate calculations for σ_z/δ. 128

Table B.10. Measurement uncertainties and intermediate calculations for $\dot{m}_{coll}/\dot{m}_{fl}$. 129

Table B.11. Measurement uncertainties and intermediate calculations for $\dot{m}_{cut}/\dot{m}_{fl}$. 130

Table B.12. Statistical results obtained from reproducibility tests of mean velocity. 132

Table B.13. Statistical results obtained from reproducibility tests of σ_z/δ. 137

LIST OF FIGURES

Figure 1.1.	Illustration of the indirect-drive ignition process in IFE. (Shown for laser drive.)	3
Figure 1.2.	Sketches of liquid sheets forming the stationary sheet lattice (left) for protecting the front and back walls and the array of obliquely oscillated sheets (right) for protecting the sidewalls.	4
Figure 1.3.	Orthogonal views of the HYLIFE-II reaction chamber (Moir *et al.*, 1994).	6
Figure 1.4.	Illustration of driver interface issues in thick liquid protection. For efficient shielding the beam/jet standoff should be minimized without causing interference from free-surface fluctuations and droplets due to primary breakup.	7
Figure 3.1.	Definition of the coordinate system at the nozzle exit.	27
Figure 3.2.	Schematic of the experimental facility.	28
Figure 3.3.	Flow conditioner assemblies with nozzle attached for (*a*) Type I.A and (*b*) Type II.A,B configuration.	33
Figure 3.4.	Plot of the 5^{th} order polynomial contraction of the nozzle.	34
Figure 3.5.	Photo of the sheet nozzle designs: (*a*) Original nozzle, (*b*) Modified for LDV, and (*c*) Redesigned for external clamping.	36
Figure 3.6.	Schematic of BL cutter (enclosure around cutter blade not shown).	37
Figure 3.7.	BL cutter assembly shown in (*a*) isometric and (*b*) cross-section.	38
Figure 3.8.	Photo of the BL cutter apparatus in operation. (Shown without spacer plate.)	38
Figure 3.9.	Dual-beam backscatter LDV system components.	40

Figure 3.10. Sketch of the wave fronts of two intersecting light beams creating the interference fringes which comprise the probe volume. A tracer particle is shown passing through the probe volume perpendicular to the fringes. 41

Figure 3.11. Typical LDV signal decomposed into the pedestal and Doppler signals. 42

Figure 3.12. Power spectrum of the signal generated by an LDV system. 43

Figure 3.13. Schematic of the MiniLDV system. 44

Figure 3.14. Sample of an ideal Doppler burst after signal filtering. 46

Figure 3.15. Photograph of the LDV sensor head aligned to measure streamwise (*x*-component) velocity. 48

Figure 3.16. Schematic demonstrating procedure for determining LDV probe volume center with respect to the *y*-axis. Stage positions are recorded when (*a*) the shift signal is first detected, and (*b*) the signal is lost. 49

Figure 3.17. Geometry of the probe volume location (only one beam shown at exaggerated angles for emphasis). 50

Figure 3.18. Schematic showing orientation of typical profile locations. Profiles are indicated by dashed lines. 52

Figure 3.19. Free-surface visualization setup. An argon-ion laser light sheet illuminates the uranine-doped jet, with the resulting fluorescence obliquely imaged from below by a CCD camera. 53

Figure 3.20. Spectra for absorption and emission by disodium fluorescein dye. Adapted from Figure B-1 in Dahm (1985). 54

Figure 3.21. Image processing steps for identifying the liquid sheet free surface: (*a*) Raw PLIF image; (*b*) Thresholded image; and (*c*) Free surface obtained with edge detection. 56

Figure 3.22. Schematic of mass collection technique. The cuvettes are brought to a distance Δz_s from the nominal free surface (dashed lines) at angle $\theta = 6.5°$ from the vertical. 58

Figure 3.23. Detail view of the cuvette holder. 59

Figure 4.1. Schematic showing *i*) local nozzle thickness, b, at x = -6 mm and *ii*) three representative profile locations at y / W_o = 0.1188, 0.3688, and 0.4838. 63

Figure 4.2. Mean velocity profiles for Type I.A flow conditioning and Re = 53,000 and y / W_o = 0.1188 (+), 0.3688 (●), 0.4163 (▲), 0.4438 (◆), and 0.4838 (■). The open and closed symbols represent u / U_o and w / U_o, respectively, while the dashed lines indicate the expected velocity values. 64

Figure 4.3. Mean velocity profiles, similar to Figure 4.2, for Type I.A flow conditioning and Re =120,000. 64

Figure 4.4. Rms velocity fluctuation profiles for Type I.A flow conditioning and Re = 53,000 and y / W_o = 0.1188 (+), 0.3688 (●), 0.4163 (▲), 0.4438 (◆), and 0.4838 (■). The open and closed symbols represent u' / U_o and w' / U_o, respectively. 66

Figure 4.5. Rms velocity fluctuation profiles, similar to Figure 4.4, for Type I.A flow conditioning and Re =120,000. 66

Figure 4.6. Definition of the nozzle control volume. 67

Figure 4.7. Mean velocity profiles at y / W_o = 0.3688 for Re = 120,000 and Type I.A (▲), Type I.N (◆), and Type II.A,B (■). The open and closed symbols represent u / U_o and w / U_o, respectively. Dashed lines indicate the expected velocity values. 71

Figure 4.8. Mean velocity profiles, similar to Figure 4.6, at y / W_o = 0.4438. 71

Figure 4.9. Mean velocity profiles, similar to Figure 4.6, at y / W_o = 0.4838. 72

Figure 4.10. Rms velocity fluctuation profiles at y / W_o = 0.3688 for Re = 120,000 and Type I.A (▲), Type I.N (◆), and Type II.A,B (■). The open and closed symbols represent u' / U_o and w' / U_o, respectively. 73

Figure 4.11. Rms velocity fluctuation profiles, similar to Figure 4.9, at y / W_o = 0.4438. 74

Figure 4.12. Rms velocity fluctuation profiles, similar to Figure 4.9, at $y / W_o = 0.4838$. 74

Figure 4.13. Rms velocity fluctuation profiles as a function of y / W_o for Re = 120,000 and Type I.A (▲), Type I.N (◆), and Type II.A,B (■). The open and closed symbols represent u'_{avg} / U_o and w'_{avg} / U_o, respectively. 76

Figure 4.14. Free surface of the liquid sheet for Re = 53,000 at different downstream distances. Note: Flow is out of page and vertical axis is magnified 5×. 78

Figure 4.15. Free surface of the liquid sheet for Re = 120,000 at different downstream distances. Note: Flow is out of page and vertical axis is magnified 5×. 79

Figure 4.16. Normalized free-surface rms fluctuations as a function of y / W_o for x / δ = 25 and Re = 120,000. The jet exhibits nearly 2-D behavior in the region marked in the graph. 80

Figure 4.17. Graph of σ_z / δ *vs.* x / δ for Re = 53,000 (gray) and 120,000 (black). 81

Figure 4.18. Free surface profiles at x / δ = 25 for Re = 120,000 and flow conditioning (*a*) Type I.A, (*b*) Type I.N, and (*c*) Type II.A,B. Dashed lines indicate the nozzle exit. Note: Flow is out of page and vertical axis is magnified 5×. 83

Figure 4.19. Normalized free-surface rms fluctuations for flow conditioning Type I.N (gray) and Type I.A (black) *vs.* y / W_o at x / δ = 25 and Re = 120,000. Note the central peak in fluctuations for Type I.N flow conditioning. 84

Figure 4.20. Graph of σ_z / δ *vs.* x / δ for Re = 53,000 (gray) and 120,000 (black) and flow conditioning Type I.A (▲), Type I.N (◆), and Type II.A,B (■). 85

Figure 4.21. Plot showing the average (black) and ± 1·σ_z fluctuations (gray) of the sheet free surface for (*a*) Type I.A and (*b*) Type I.N flow conditioning at x / δ = 25. The recommended 0.07δ beam-to-jet standoff of Latkowski and Meier (2001) is superimposed for each case. 86

Figure 4.22. Surface ripple of the free surface at $x / \delta = 25$ for different flow conditioning configurations with Re = 53,000 (gray) and 120,000 (black). 87

Figure 4.23. Surface ripple vs. the wire diameter of fine screen for Type I flow conditioning at $x / \delta = 25$ and Re = 53,000 (gray) and 120,000 (black). 88

Figure 4.24. Normalized cut flow rate as a function of cut depth, Δz_{cut}. Two calibration data sets obtained 8 weeks apart are shown, Trial 1 (open) and Trial 2 (closed). 89

Figure 4.25. Free-surface profiles at $x / \delta = 25$ for Re =120,000 and BL cutting ranging from 0.0–1.9 %. Dashed lines indicate the nozzle exit. Note: Flow is out of page and vertical axis is magnified 5×. 91

Figure 4.26. Graph of σ_z / δ *vs.* $\dot{m}_{cut} / \dot{m}_{fl}$ at $x / \delta = 15$ (▲), 20 (◆), and 25 (■). 92

Figure 4.27. Graph of σ_z / δ *vs.* x / δ for flow conditioning Type I.N (gray) and Type I.A (black). Symbols indicate no cutting (closed) and $\dot{m}_{cut} / \dot{m}_{fl}$ = 1.9% (open). 93

Figure 4.28. Normalized collected mass rate and the resulting equivalent number density *vs.* $\Delta z_s / \delta$ for Type I.A (black) and Type I.N (gray) configurations $\dot{m}_{cut} / \dot{m}_{fl}$ = 0.0% (■), 1.0% (◆), and 1.9% (▲). 95

Figure 4.29. Droplets collected from jet with (*a*) Type I.A and (*b*) Type I.N flow conditioning at $x / \delta = 25$. Scale in lower left corner represents 100 μm. 97

Figure 4.30. G_{exp} / G_{corr} *vs.* $\Delta z_s / \delta$ for Type I.A (black) and Type I.N (gray) flow conditioner configurations at $\dot{m}_{cut} / \dot{m}_{fl}$ = 0.0% (■), 1.0% (◆), and 1.9% (▲). 99

Figure A.1. Schematic of droplet trajectories based on correlations. The standoff from the nominal free surface and downstream cuvette location are denoted by Δz and x_o, respectively. 114

Figure A.2. Schematic of cuvettes inside (Case 1) and partially inside droplet halo (Case 2). Droplets following dashed lines are predicted to enter cuvettes. The bold trajectories indicate the boundary of the halo. 115

Figure A.3. Schematic of cuvette centerline position, z_o. 116

Figure B.1. Two independent normalized mean velocity and rms fluctuation profiles Test 1 (■) and Test 2 (■) at y / W_o = 0.4438 and Re = 120,000 with Type I.A flow conditioning. The open and closed symbols represent u / U_o and u' / U_o, respectively. Note: Error bars indicate 95% experimental uncertainty. 131

Figure B.2. Ratio of turbulent rms to measured rms as a function of the signal strength-to-noise. 134

Figure B.3. Histogram of f_{shift} calibration data. 135

Figure B.4. Two independent free-surface profiles, Test 1 (▬) and Test 2 (▬) for Re = 120,000 and Type I.A flow conditioning. 136

Figure B.5. Two independent normalized free-surface fluctuation measurements, Test 1 (■) and Test 2 (■) for Re = 120,000 and Type I.A flow conditioning. Note: Error bars indicate 95% experimental uncertainty. 137

Figure C.1. Mean velocity profiles for Type I.N flow conditioning and Re = 53,000 and y / W_o = 0.1188 (+), 0.3688 (●), 0.4163 (▲), 0.4438 (◆), and 0.4838 (■). The open and closed symbols represent u / U_o and w / U_o, respectively, while the dashed lines indicate the expected velocity values. 139

Figure C.2. Mean velocity profiles, similar to Figure C.1, for Type I.N flow conditioning and Re = 120,000. 139

Figure C.3. Rms velocity profiles for Type I.N flow conditioning and Re = 53,000 and y / W_o = 0.1188 (+), 0.3688 (●), 0.4163 (▲), 0.4438 (◆), and 0.4838 (■). The open and closed symbols represent u' / U_o and w' / U_o, respectively. 140

Figure C.4. Rms velocity profiles, similar to Figure C.3, for Type I.N flow conditioning and Re = 120,000. 140

Figure C.5. Mean velocity profiles for Type II.A,B flow conditioning and Re = 53,000 and y / W_o = 0.1188 (+), 0.3688 (●), 0.4163 (▲), 0.4438 (◆), and 0.4838 (■). The open and closed symbols represent u / U_o and w / U_o, respectively, while the dashed lines indicate the expected velocity values. 141

Figure C.6. Mean velocity profiles, similar to Figure C.5, for Type II.A,B flow conditioning and Re = 120,000. 141

Figure C.7. Rms velocity profiles for Type II.A,B flow conditioning and Re = 53,000 and y / W_o = 0.1188 (+), 0.3688 (●), 0.4163 (▲), 0.4438 (◆), and 0.4838 (■). The open and closed symbols represent u'/ U_o and w'/ U_o, respectively. 142

Figure C.8. Rms velocity profiles, similar to Figure C.7, for Type II.A,B flow conditioning and Re = 120,000. 142

Figure C.9. Free surface profiles at x / δ = 15 for Re = 120,000 and flow conditioning (*a*) Type I.A, (*b*) Type I.N, and (*c*) Type II.A,B. Dashed lines indicate the nozzle exit. Note: Flow is out of page and vertical axis is magnified 5×. 143

Figure C.10. Free surface profiles at x / δ = 20 for Re = 120,000 and flow conditioning (a) Type I.A, (b) Type I.N, and (c) Type II.A,B. Dashed lines indicate the nozzle exit. Note: Flow is out of page and vertical axis is magnified 5×. 144

Figure C.11. Free surface of the liquid sheet for Type II.A,B flow conditioning and Re = 53,000 at different downstream distances. Note: Flow is out of page and vertical axis is magnified 5×. 145

Figure C.12. Free surface of the liquid sheet for Type II.A,B and Re = 120,000 at different downstream distances. Note: Flow is out of page and vertical axis is magnified 5×. 146

Figure C.13. Free surface of the liquid sheet for different flow conditioning types and Re = 53,000 at x / δ = 25. Note: Flow is out of page and vertical axis is magnified 5×. 147

Figure C.14. Free surface of the liquid sheet for different flow conditioning types and Re = 120,000 at x / δ = 25. Note: Flow is out of page and vertical axis is magnified 5×. 148

NOMENCLATURE

Symbols

A	area (cm^2)
b	local nozzle thickness for LDV traverses (mm)
d_{fr}	fringe spacing (μm)
f_D	Doppler frequency (Hz)
f_{shift}	shift frequency (Hz)
Fr	Froude number $Fr = U_o^2/g\delta$
G	mass flux ($kg/m^2 \cdot s$)
g	gravitational acceleration (m/s^2)
M	molecular weight (g/mol)
$\dot{m}$	mass flow rate (kg/s)
N	equivalent number density (m^{-3})
N_A	Avogadro's number (#/mol)
n	index of refraction
Oh	Ohnesorge number $Oh = \mu/(\rho\delta\sigma)^{0.5}$
Re	Reynolds number $Re = U_o\delta/\nu$
We	Weber number $We = \rho U_o^2\delta/\sigma$
u	x-velocity component (m/s)
U_o	volumetric averaged speed at nozzle exit (m/s)
W_o	nozzle exit width, y-dimension (cm)
w	y-velocity component (m/s)

x x-coordinate, streamwise flow direction (cm)

y y-coordinate (cm)

z z-coordinate, transverse flow direction (cm)

$( )'$ root-mean-square

Greek Letters

Δz z-position relative to the nominal free surface (mm)

δ nozzle exit thickness, z-dimension (mm)

δ_{BL} boundary-layer thickness (mm)

κ converging beam half-angle (degrees)

λ wavelength (nm)

μ dynamic viscosity ($N \cdot s/m^2$)

ν kinematic viscosity (m^2/sec)

ρ density (kg/m^3)

ρ_{eff} effective line density (kg/m^3)

σ surface tension (N/m)

σ_z rms of free-surface fluctuations in z-direction (mm)

τ convective time scale $\tau = \delta/U_o$ (sec)

Subscripts

a	air
avg	average
coll	collected
corr	correlation
cut	cut rate
cuv	cuvette
D	hydraulic diameter
exp	experiment
fl	sheet flow rate
L	Lexan
o	initial
s	standoff
tot	total
w	water

ABSTRACT

Turbulent liquid sheets have been proposed to protect solid structures in fusion power plants by attenuating damaging radiation. For the High-Yield Lithium-Injection Fusion Energy (HYLIFE-II) inertial fusion energy (IFE) power plant concept, arrays of molten-salt sheets form a sacrificial barrier between the fusion event and the chamber first wall while permitting target injection and ignition. Thick liquid protection can help make fusion energy commercially attractive by reducing chamber size and prolonging chamber lifetime. Establishing an experimental design database for this basic "building block" flow will provide valuable information about various thick liquid protection schemes and allow reactor designers to establish acceptable tolerances between chamber components.

Turbulent water sheets issuing downwards into ambient air were studied experimentally at Reynolds numbers of 53,000 – 120,000 and Weber numbers of 2,900 – 19,000 based on average velocity and the short dimension of the nozzle exit (δ). Initial conditions were quantified by the streamwise (x) and transverse (z) velocity components using laser-Doppler velocimetry just upstream of the nozzle exit. Characterization of the mean free-surface position and free-surface fluctuations, or surface ripple, and estimation of the amount of mass ejected as droplets from the free surface were quantified in the near-field (within 25δ of the nozzle exit). Surface ripple and mean sheet geometry were determined directly from planar laser-induced fluorescence visualizations of the free surface. The droplets due to the turbulent breakup of the jet, termed here the hydrodynamic source term, were measured using a simple collection technique to within

1δ of the nominal free surface of the jet. The influence of various passive flow control techniques such as removing low-momentum fluid at the free surface ("boundary-layer cutting") on sheet geometry, surface ripple, and turbulent breakup were also quantified. The data obtained in this research will allow designers of inertial fusion energy systems to identify the parameter ranges necessary for successful implementation of the thick liquid wall protection system.

CHAPTER 1

INTRODUCTION

A liquid sheet is a two-dimensional jet of liquid issuing into a lower density (usually gaseous) medium. Phenomena such as gravity, surface tension, and turbulence levels affect the stability of liquid sheets. Aerodynamic shear at the free surface may also be relevant for jets of density ratios less than about 500 (Wu, *et al.* 1995). Inertial fusion energy (IFE) has stimulated interest in these flows as "liquid curtains" for protecting the reactor chamber first walls by absorbing the brunt of the damaging X-rays, ions, and neutrons produced by the fusion microexplosion.

Despite the fundamental nature of these flows, the dynamics of turbulent liquid sheets are not well-characterized. Previous studies have been motivated in part by the paper industry, where turbulent liquid sheets of dilute fiber suspensions are used in paper manufacture. The breakup and atomization of high-speed liquid sheets have also been studied in connection with fuel injectors and the bow sheets of naval vessels. Given the extremely high energy fluxes associated with the fusion microexplosion, flows used in liquid protection schemes in IFE applications are typically turbulent and high Reynolds number but must minimize breakup and surface fluctuations to minimize interference with ignition beam propagation and target injection.

1.1 Background

1.1.1 Inertial Fusion Energy

Fusion is the power source of the stars, including the Sun. In a fusion reaction, lightweight elements are combined at high temperatures and densities resulting in a release of energy defined by Einstein's famous equation, $E = mc^2$. The enormous gravitational forces of a star confine the plasma long enough for the fusion reaction to occur. On Earth, other approaches are required to contain the atoms until fusion may occur. In inertial confinement fusion, a tiny pellet of hydrogen isotopes is compressed and heated by intense energy beams so quickly that fusion occurs before the atoms can blow apart. The combination of deuterium (D) and tritium (T) is of particular importance given the relatively low input energy and the abundance of deuterium in the world's water supply. The IFE concept seeks to harness the energy released by igniting DT fuel capsules in a reactor chamber on a cyclical basis several times per second.

Beginning in 1994, the US Department of Energy declassified large portions of its inertial confinement research program, including the physics of indirect-drive targets. Figure 1.1 shows the basic steps to achieve fusion in an indirectly-driven IFE microexplosion. The DT fuel capsule is enclosed inside a container made of a high atomic weight material known as a hohlraum. First, the inner surface of the hohlraum is rapidly heated with heavy-ion or laser driver beams and then emits X-rays which heat the surface of the fuel. A rocket-like blowoff of high-pressure plasma is ejected from the fuel surface, forcing an inwardly focused compression wave propagating towards the center of the fuel. Ignition is achieved as the temperature and pressure near the center reach values of up to O(100 million K) and O(100 Gbar), respectively. After fusion is

initiated at this central "hot spot," the thermonuclear reaction propagates radially outward into the remaining fuel.

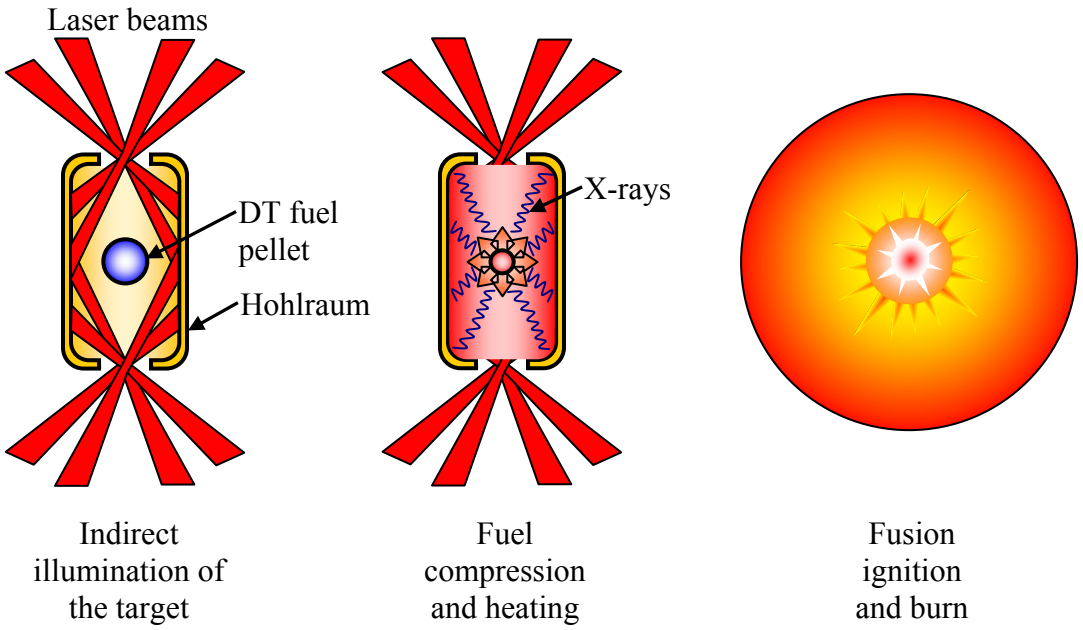

Figure 1.1. Illustration of the indirect-drive ignition process in IFE. (Shown for laser drive.)

The issue of chamber life is of central importance for the successful commercial operation of an IFE power plant. Current target designs yield energy releases of 10^2 – 10^3 MJ, a large portion of which is composed of energetic X-rays and neutrons. If exposed directly to the target threat spectrum, the chamber first walls would quickly deteriorate due to spallation, high thermal stresses, evaporation, and other mechanisms. One innovative solution to this problem is thick liquid protection. Here, "thick" denotes that the characteristic length of the protective flows is greater than the mean attenuation length of the fusion neutrons.

Thick liquid protection designs, such as that proposed for the HYLIFE-II conceptual reactor (Moir *et al.* 1994), rely on arrays of stationary and/or oscillating jets to shield the chamber (Figure 1.2). The stationary lattice forms a protective grid through which driver beams and targets may propagate while shielding the front and back walls of the chamber. The oscillating pocket provides shielding for the chamber sidewalls and dynamically clears the center of the chamber of debris prior to the injection of the next fuel target. Annular and cylindrical jets have been proposed as alternatives to liquid sheets (Maniscalco and Meier 1977, Abbot *et al.* 2001). However, geometric simplicity and high packing densities make rectangular jets an attractive option for IFE chamber protection.

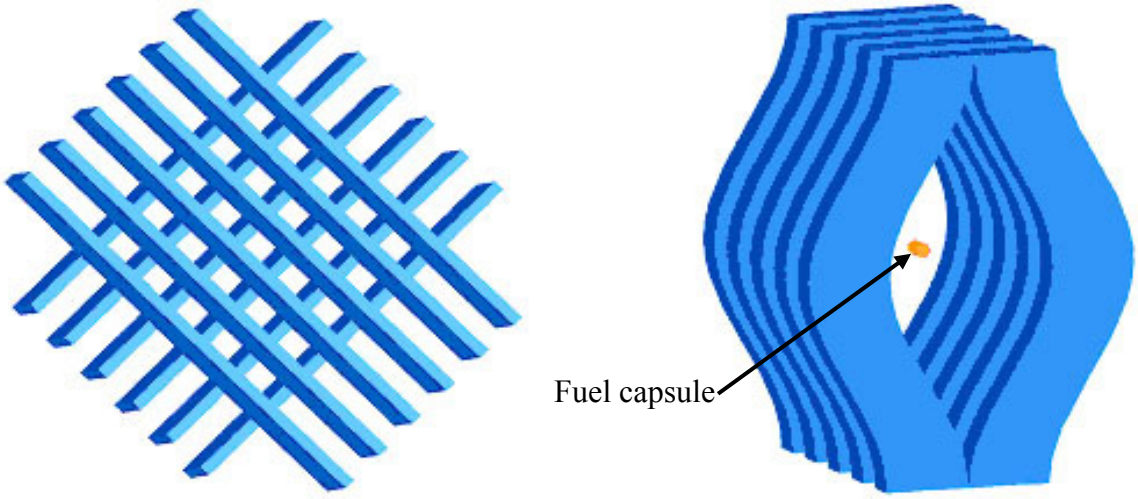

Figure 1.2. Sketches of liquid sheets forming the stationary sheet lattice (left) for protecting the front and back walls and the array of obliquely oscillated sheets (right) for protecting the sidewalls.

While a working fusion power plant has yet to be built, the appeal of a nearly limitless fuel supply and absence of greenhouse gas emissions make fusion energy a

promising solution to future global energy needs. The cost of electricity for fusion is projected to be economically competitive with fission and fossil fuels in the next 25 years based on comparative extrapolations of existing and future technologies (Delene, 1994). Magnetic fusion energy (MFE), which has been under development for over 50 years, has yet to demonstrate a commercially feasible power plant. Development of IFE as an alternative "pathway" to commercial fusion energy has therefore been an increasingly important part of the U.S. fusion energy program since the mid-1990s, as demonstrated by the National Ignition Facility (NIF) at Lawrence Livermore National Laboratory (LLNL). Although built primarily as a fundamental part of the stockpile stewardship program, experiments in the NIF will also be capable accessing fusion regimes of interest in energy applications. The NIF uses 192 high-power lasers to deliver 1.8 MJ onto a target within a time span of ~3 nsec. Proposed experiments for NIF will develop an understanding of laser ignition, target physics, and chamber response. Currently the NIF chamber is scheduled for a working life of about 12 years with an estimated total number of shots less than 1×10^4. In comparison, a commercial IFE power plant will need to sustain upwards of 5×10^9 shots over a 30 year lifetime. Therefore, protective schemes such as thick liquid protection, which extend first wall lifetimes, are critical to the successful commercialization of IFE energy.

1.1.2 High-Yield Lithium-Injection Fusion Energy Power Plant

The High-Yield Lithium-Injection Fusion Energy (HYLIFE-II) power plant design proposed in Moir, *et al.* (1994) uses liquid sheets of molten Flibe (Li_2BeF_4) to form a protective pocket that allows target injection and driver propagation (Figure 1.3). The liquid sheets not only attenuate radiation and neutrons but also breed tritium and

provide a means of removing heat from the chamber. The tritium that is consumed in the fusion microexplosions is replaced by tritium bred by neutron reactions with the lithium contained in the molten salt. The tritium is extracted from the salt to provide fuel for continuous operation of the power plant. The thermal energy contained in the exiting molten salt is converted to electricity by a conventional power cycle.

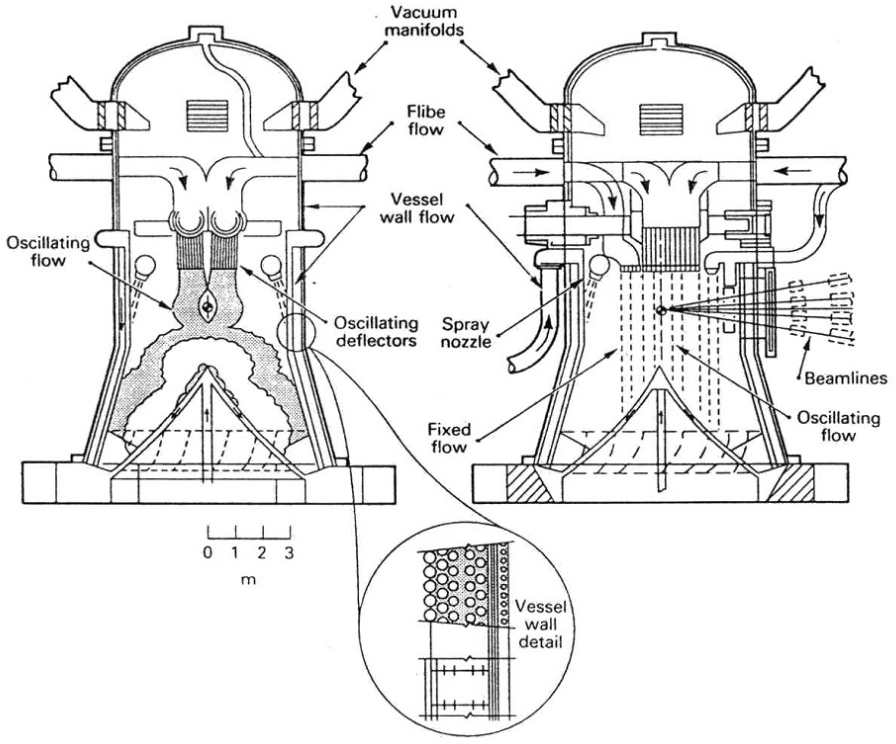

Figure 1.3. Orthogonal views of the HYLIFE-II reaction chamber (Moir *et al*., 1994).

Thick liquid protection has the potential of greatly reducing capital and operating costs by decreasing reactor chamber size and increasing chamber lifetime. For maximum protection, the distance between jets must be minimized while still allowing driver beam propagation and target injection. This requirement means surface fluctuations of the liquid sheets must be minimized. Neutronics calculations for the HYLIFE-II lattice of

slab jets show that a standoff distance between the jet free surface and the edge of the driver beam of 5 mm, or 7% of the initial sheet thickness, will give final focus magnet lifetimes in excess of 30 years (Latkowski and Meier, 2001). Reducing surface fluctuation below these levels is therefore of primary importance.

The turbulent breakup of the protective flows might also pose a threat to driver beam and target propagation inside the chamber. Here, the "hydrodynamic source term" refers to any liquid emanating from the protective jets via breakup. Droplets or jet fragments could prove catastrophic for heavy ion beam propagation given the proximity of the jets to the beam pathlines and the resulting beam attenuation. Figure 1.4 summarizes the clearance issues affecting beam-to-jet interfaces. Target trajectory and survival would also be affected should the target encounter droplets of coolant in the chamber prior to ignition. Therefore the primary turbulent breakup must be minimized or even eliminated if possible.

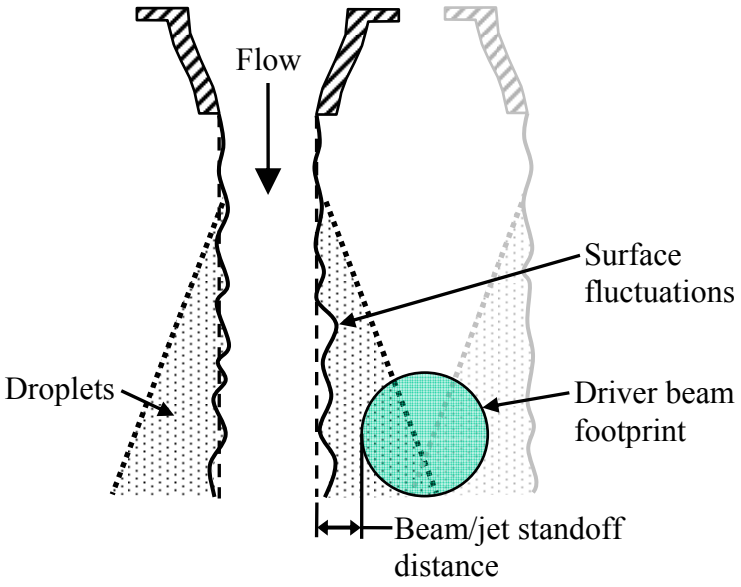

Figure 1.4. Illustration of driver interface issues in thick liquid protection. For efficient shielding the beam/jet standoff should be minimized without causing interference from free-surface fluctuations and droplets due to primary breakup.

Jets are often created by passing the fluid through a flow conditioning section followed by a converging nozzle. The flow conditioner, or flow straightener, typically uses components such as perforated plate, honeycomb, and fine mesh screens to remove swirl and break up any moderate-scale flow structures. The flow is then accelerated through the converging nozzle to produce a nearly uniform velocity profile across the nozzle exit. A basic physical understanding of how initial conditions impact the free-surface geometry and breakup of turbulent liquid sheets is vital in improving IFE thick liquid protection. In addition, the pressure loss across the flow conditioner must be considered in the final analysis of any design as this head loss will dictate the pumping power required to drive the protective flows in the reactor.

Table 1.1 shows a comparison between the flow parameters of this investigation and those proposed in the HYLIFE-II concept. Reynolds and Weber numbers of the scaled experiments are approximately 50% and 20% of the prototypical values, respectively. Nevertheless, the liquid sheets in these experiments will exhibit dynamic behavior and stability characteristics similar to the HYLIFE-II jets.

Table 1.1. Comparison of flow parameters between HYLIFE-II and scaled experiments.

Flow Parameters	HYLIFE-II (Flibe)	Experiments (Water)
Reynolds number $Re = (U_o\delta)/\nu$	2.4×10^5	5.3×10^4, 1.2×10^5
Weber number $We = (\rho_L U_o^2\delta)/\sigma$	1.0×10^5	2.9×10^3, 1.9×10^4
Nozzle aspect ratio W_o/δ	14.3	10
Normalized fall distance x/δ	29	0–25
Jet nozzle thickness δ	0.07 m	0.01 m
Jet speed at nozzle U_o Fluid density ρ_L	12 m/s 1963 kg/m^3	5.21, 10.85 m/s 997 kg/m^3
Fluid kinematic viscosity ν	3.5×10^{-6} m^2/s	9.1×10^{-7} m^2/s
Surface tension σ	0.193 N/m	0.072 N/m

1.2 Objectives

The aim of this doctoral thesis is to study the impact of initial conditions on the downstream characteristics of turbulent liquid sheets, specifically the geometry and breakup of the free surface. The three main objectives are to:

1. Understand the influence of different conditioning schemes and elements. Flow conditioning has a significant impact on the initial conditions of the jet, and a slight modification to the conditioning can cause drastic changes in overall jet behavior.
2. Study the impact of boundary-layer cutting. Removing the lower momentum fluid just downstream of the nozzle exit will create a sheet with a nearly uniform velocity profile. According to theoretical predictions, this is the most stable configuration possible for this flow.
3. Quantify the mass flux due to droplets ejected from the surface of the jet as a function of standoff distance from the jet surface. The turbulent breakup of a jet occurs when the local kinetic forces are higher than surface tension forces, and a parcel of fluid is ejected from the jet surface. These droplets can represent a substantial amount of the initial flow rate for unconditioned jets and are desirable for some applications such as fuel injectors. However, for IFE applications the droplets represent a threat to target and driver beam propagation.

This work will expand the general database on turbulent liquid sheets and set design parameters for future IFE chamber concepts.

The remainder of this thesis is organized as follows. Chapter 2 gives a brief overview of the literature available on thick liquid protection schemes in IFE, relevant flows, and previous investigations at the Georgia Tech Large-Scale Test Facility.

Chapter 3 details the equipment and procedures used in the current investigation. Experimental results characterizing initial conditions and the resulting downstream behavior of turbulent liquid sheets are reported in Chapter 4. Chapter 5 summarizes the conclusions of this investigation and offers recommendations for future turbulent liquid sheet research. Appendix A gives details of the turbulent breakup correlations of Sallam *et al.* (2002) as applied in this research. Error analysis and experimental repeatability are examined in Appendix B. Additional experimental results are included in Appendix C. Finally, Appendix D contains copies of the refereed journal articles authored during the course of this doctoral research project.

CHAPTER 2

LITERATURE REVIEW

A wealth of information exists that is relevant to the study of turbulent liquid sheets for use in inertial fusion reactors. Studies of the reactor concepts themselves are an obvious starting point for learning the requirements and intentions of the reactor designers. Next a comprehensive survey of the fluid mechanics literature will provide details and comparisons of previous work. These sources should give insight into the behavior and role of turbulent liquid sheets in fusion.

2.1 Liquid Protection in Fusion Power Plants

Burke and Cutting (1974) and Seifritz and Naegele (1975) were among the first to introduce the concept of using liquid jets as a "protective blanket". The High-Yield Lithium-Injection Fusion Energy (HYLIFE) reactor concept was described three years later in a formal design by Monsler *et al.* (1978). Extensive analyses of the fluid mechanics issues associated with this design were performed by Glenn (1981). Blink *et al.* (1985) summarized the final HYLIFE design and thoroughly describes the fluid mechanics issues and requirements of the reactor.

Due to fire hazards associated with the liquid lithium coolant chosen for HYLIFE-I, a new design was made (HYLIFE-II) in which the liquid lithium was replaced by a molten salt called Flibe, Li_2BeF_4. Other advantages of Flibe over lithium include lower

vapor pressure, less corrosion, and higher thermal capacity. Further information on the properties of Flibe can be found in Rosenthal *et al.* (1972). Details of the first publications on HYLIFE-II were published by Moir *et al.* (1991) and Moir (1992). While the original HYLIFE design was based on a target gain of 400 with a laser energy input of 4.5 MJ, the HYLIFE-II design is based on a moderate gain of 70 and a driver energy input of 5 MJ, assuming a heavy ion driver. This lower gain results in a target yield reduction from 1800 MJ to 350 MJ and an increased pulse rate from 1.5 Hz to 6 Hz. Further information on the status of the HYLIFE-II development can be found in Moir *et al.* (1994), Moir (1995), and House (1999). It has also been suggested that liquid first walls could be used in magnetic fusion reaction chamber designs (Moir, 1997). In a recent study, the advanced power extraction (APEX) study by Abdou *et al.* (2001) confirmed the potential benefits of using liquid protection in a MFE reactor design.

A number of alternatives to the HYLIFE/HYLIFE-II reactor designs have been proposed, but to our knowledge are not currently under development. An updated HYLIFE-II concept that uses shielding grids of cylindrical jets instead of liquid sheets was proposed in Abbott *et al.* (2001). A "wetted wall" liquid protection scheme was proposed in the OSIRIS reactor design, which consisted of a chamber first wall of porous carbon fabric with a layer of Flibe seeping along the inner surface (Bourque *et al.*, 1992). PROMETHEUS-H was a heavy-ion-driven design that used a similar protection scheme consisting of a thin film of liquid lead to protect a porous SiC first wall (Waganer, 1994). In contrast to these two designs, the HYLIFE-II design uses ordinary stainless steel (304 SS) as a first wall, which represents a substantial advantage in terms of maintenance and simplicity.

An emerging concept in the IFE community is the Z-Pinch Power Plant (ZP-3). Rochau *et al.* 2003 summarizes the conceptual operation of the plant. First, a sacrificial cartridge containing the DT fuel is inserted into the chamber. Next, electrical contact between the cartridge and the recyclable transmission lines is secured. Energy is then delivered to the target hohlraum in the form of X-rays using Z-pinch technology. This concept avoids any interfaces with the protective flows altogether. The current chamber design does however make use of thick liquid protection to mitigate the shock and radiation from the proposed 1 to 20 GJ target.

2.2 Submerged Plane Jets

Submerged plane jets are of interest because they have the same basic geometry as that of the liquid sheet but are distinct in that there are no surface tension effects since the jet and ambient fluids are identical. While liquid jets issue into a vacuum or low-density gas such as air, submerged jets issue into an ambient fluid that is the same as the jet fluid. As a result of this difference, the interaction between the two fluids is of much greater importance in the case of the submerged jet. Entrainment and mixing of the jet and ambient fluids is a first order effect. A large number of studies have dealt with both the laminar and turbulent submerged plane jet with emphasis on the issues of spread rate, virtual origin analysis, and velocity decay (Kotsovinos, 1976). These investigations include Sforza *et al*. (1966), Sfeir (1976, 1978), Krothapalli (1981), Grinstein (2001). The role of vortex dynamics in the near field including entrainment properties and axis switching can be found in Hertzberg and Ho (1995) and Grinstein (2001). A thorough review of literature on the topic can be found in Gutmark and Grinstein (1999). These investigations indicate that the spreading rate is highly dependent on initial conditions.

2.3 Low Reynolds Number Jets

The stability of free-surface laminar round jets has been studied extensively in the literature. The main focus of these studies has been the growth of axisymmetric (or dilatational) surface waves and the subsequent breakup of the jet into drops of size comparable to that of the jet diameter at the time of breakup. Reviews of these studies have been given by Miesse (1955), Chandrasekhar (1961), Chen and Davis (1964), Grant and Middleman (1966), McCarthy and Malloy (1974), Anno (1977), and Bogy (1979) among others; recent reviews include Faeth *et al.* (1995), Lin and Reitz (1998), Sallam *et al.* (1999), Aslanov (1999) and Mazallon *et al.* (1999).

The use of annular jets represents one of the earliest concepts for liquid protection of IFE target chamber first walls (Maniscalco and Meier, 1977). The annular jet is similar to the 2-D liquid sheet in that both have two free surfaces vs. the cylindrical jet, which has only one. A liquid annular jet will converge and form a liquid "curtain" due to the combined effects of surface tension, gravity and a pressure difference on the two sides of the jet. The significant non-dimensional parameters considered in studies of laminar annular jets are the Froude number *Fr*, Weber number *We*, and a non-dimensional pressure coefficient based on the pressure difference between the inside and outside of the liquid curtain. Annular jets have been studied extensively in the literature. Important investigations include those by York *et al.* (1953), Taylor (1959a), Baird and Davidson (1962), Hovingh (1977), Paul (1978), Hoffman *et al*. (1980), Esser and Abdel-Khalik (1980), Kihm and Chigier (1990), and Ramos (1998). The study done by Hasan *et al*. (1998) focused on the use of annular jets in the IFE reactor and concluded that the

concept was feasible for use as a protection scheme, although venting of the protective pocket and chamber pressurization may be concerns.

More akin to the flows of interest in this research are those with rectangular cross-sections. There have been several studies on laminar liquid sheets with applications in coating processes and IFE research. Generally, these flows encompass a Reynolds number range that is one to two orders of magnitude lower than the flow considered in this thesis. The relevant results from these studies are summarized here. Specifically, it was found that the surface tension force on the jet surface always acts as a restoring or damping force, and aerodynamic forces of an inviscid ambient gas are the main reasons for observed instabilities. Important factors involved in these flows include surface tension, flow velocity, and ambient gas properties including density and viscosity. Therefore, the non-dimensional parameters that are of concern with these flows are: the Reynolds number *Re* (which relates inertial force to viscous force), Weber number *We* (relates inertial force to surface tension force), the Froude number *Fr* (inertial force to gravitational force), and the Ohnesorge number *Oh* (viscous force to inertial and surface tension forces). These parameters are generally defined by the following equations: $Re = \frac{U_o \delta}{\nu}$, $We = \frac{\rho_L U_o^2 \delta}{\sigma}$, $Fr = \frac{U_o^2}{g\delta}$, and $Oh = \frac{\mu}{(\rho\delta\sigma)^{0.5}}$, where ρ_L is the fluid density, δ is a characteristic length, ν is the kinematic viscosity of the fluid, μ is the dynamic viscosity, U_o is a characteristic velocity, g is the acceleration due to gravity, and σ is the surface tension of the fluid.

A linear analysis of the Kelvin-Helmholtz instability in laminar liquid sheets including surface tension was conducted by Rayleigh (1894), Squire (1953), Hagerty and

Shea (1955), and Taylor (1959a, b). Rayleigh neglected the effects of an ambient gas and identified two distinct modes of instability: one involving symmetric (dilatational) disturbances about the longitudinal jet axis and one involving anti-symmetric (sinuous) disturbances. Hagerty and Shea (1955) and Squire (1953) included the effect of a motionless inviscid gas (air) surrounding the sheet and found the same two modes of instability. In a theoretical and experimental investigation, Hagerty and Shea (1955) found that the sheet was unstable for a limited range of disturbance frequencies. Externally excited growth modes are studied in Asare *et al.* (1981) and are found to agree with linear theory for small excitation amplitudes. A recent analysis performed by Rangel and Sirignano (1991) used non-linear vortex discretization theory to verify the presence of the two distinct surface wave modes found by Squire (1953). Lin *et al*. (1990) studied the effects of gas-liquid density ratio and found that for Weber numbers smaller than 0.5, the symmetric surface wave mode is stable if the gas-liquid density ratio is zero, otherwise it is convectively unstable. The anti-symmetric surface wave mode was found to be always unstable unless the gas-liquid density ratio is zero, in which case it is asymptotically stable. It was further shown by Lin *et al*. (1990) that when $We > 0.5$, the mechanism of rupture is capillary instability, and that when $We \leq 0.5$, the convective instability is due to the interfacial pressure fluctuation. Mansour and Chigier (1991) experimentally studied the influence of aerodynamic shear on the instability of liquid sheets. For low liquid flow rates, the sinuous mode dominates the free-surface instability while the dilatational mode becomes dominant at higher flow rates.

Chubb and Calfo (1993) studied the geometry of a stationary laminar liquid sheet at Re = 200-300 issuing into vacuum and found the sheet shape to be approximately

triangular. They developed a simple 1-D model that includes the effects of gravity and surface tension, but neglects aerodynamic drag, for predicting jet width as a function of distance downstream of the nozzle exit. Two distinct regions of the flow were identified; a flat sheet-like central region and rounded edge protrusions where surface tension forces have smoothed the sharp corners of the sheet.

2.4 Initial Condition Studies on Liquid Sheets

Several investigations into the impact of initial conditions on liquid sheets have been motivated by the paper industry. Paper starts out in a mill as a turbulent sheet of a dilute fiber suspension issuing from the headbox nozzle at a small angle with respect to the horizontal; this sheet then impacts a wire mesh, which traps the cellulose fibers that eventually form the finished paper product. Non-uniformities in the liquid sheet are known to contribute to variations in the physical properties and anisotropy of the finished paper product. Söderberg and Alfredsson (1998) studied plane water jets issuing from a channel and slit nozzles for $Re \leq 2.5 \times 10^4$. Velocity profile relaxation was shown to introduce wave instabilities with the sinuous modes dominating. Breakup of the surface capillary waves was observed at higher velocities and appeared as strong streamwise streaks. Surface instabilities were not detected for flows produced with the slit nozzle, indicating a uniform velocity profile is the most stable configuration.

Aidun (1997) noted that streaks in the free surface of a forming jet may be produced not by turbulent fluctuations, but by small-scale secondary flows introduced upstream of the nozzle. These secondary flows are introduced inside the headbox by the interaction of jets from feed tubes. Secondary flows, turbulence, and exiting velocity profile all contribute to the downstream stability of liquid sheets.

Parsheh *et al.* (2005) detailed the turbulent energy production mechanisms inside a linear contraction. The flow geometry of interest was rectangular with an overall contraction ratio of ~ 11. The findings of this study indicate that the streamwise velocity fluctuations initially decrease inside the contraction with turbulent energy directed into transverse fluctuations. However, streamwise fluctuations did increase near the nozzle exit, possibly due to a net transfer of turbulent kinetic energy from the transverse component.

Motivated by the study of atomization mechanisms as opposed to paper forming, Heukelbach (2003) used different nozzle geometries to determine the relative impact of nozzle boundary layers and turbulence on the stability of liquid sheets at Reynolds numbers of $Re \leq 1.7 \times 10^4$. This work did not directly characterize the breakup of the jet but instead sought to illustrate the growth of capillary surface waves as a mechanism of atomization. These studies concluded that increased streamwise turbulence inside the nozzle may in fact stabilize the sheet through increasing turbulent (eddy) viscosity, whereas transverse perturbations act to enhance breakup. The experimentally observed capillary waves on the free surface of the sheet were found to be much smaller than those predicted by linear stability theory, due to the assumption of uniform velocity in the linear stability analysis.

2.5 Surface Ripple Studies

As discussed previously, effective operation of liquid wall protection schemes in commercial IFE reactors places stringent requirements upon the surface smoothness of the liquid sheets. The importance of minimizing free-surface ripple in IFE applications is reviewed in (among others) Cavanaugh and Peterson (1994) and Ying and Abdou (1998).

Studies of wave phenomena on free-surface jets using either water or lithium as the jet fluid were performed by Hoyt and Taylor (1977a, b), Howard (1979), Hassberger (1983). More recent investigations have been conducted by Nakamura *et al.* (1997), Itoh *et al.* (1999), and Söderberg (2003). Hassberger investigated the wavelengths of the free-surface waves by acquiring measurements from high speed photographs of the surface taken using a short duration strobe light. Experiments performed by Nakamura *et al.* (1997) and Itoh *et al.* (1999) investigated the stability of the free surface of a liquid jet for the purposes of developing a neutron source using liquid metal free-surface jets as a target for deuteron beams. Their experiments included attempts to measure the free-surface wave amplitudes on the surface of a planar jet. These studies examined a horizontal liquid "wall jet" with one free surface, a back wall and two sidewalls. Free-surface amplitudes were measured indirectly by measuring the local slope angles of the liquid surface by recording laser beam refraction at the liquid free surface. Söderberg (2003) imaged the free surface of both acoustically forced and unforced liquid sheets using shadowgraphy. Surface wave amplitudes, both naturally occurring and forced, were found to increase with downstream distance.

Morley *et al.* (1998) performed experiments to simulate the liquid slab jets of HYLIFE-II and measure surface ripple. Experimental investigations of vertical free liquid metal jets in a vacuum by Morley *et al.* (1998) have reported wave structures of approximately 15% of the jet thickness at the exit of their nozzle. These measurements were obtained by photographing the jet with a digital camera and using image analysis to measure the size of the disturbances. Konkachbaev *et al*. (2000) studied the stability and contraction of the rectangular liquid sheet in a vacuum environment using an

experimental procedure similar to that of Morley *et al*. (1998). This experimental procedure consisted of a high-speed digital camera with motion analysis software to analyze the dimension and velocity of the liquid sheet produced by various nozzle designs at various turbulence levels.

2.6 Turbulent Jet Stability and Breakup

A liquid jet issuing from a nozzle into an ambient gas is inherently unstable. The four characteristic breakup regimes are 1) Rayleigh, 2) first wind-induced, 3) second wind-induced, and 4) atomization (Lin and Reitz, 1998). The first two regimes are reasonably understood and are well predicted by linear stability theories such as those put forward in Sterling and Sleicher (1975). The last two regimes, which are relevant to this work, are less understood and can only be modeled with experiments, given the turbulent nature of these flows. Atomization and the second-wind induced regime result in droplets much smaller than the jet length scale. Breakup in these regimes is highly dependent on nozzle design and initial conditions, specifically the exiting nozzle velocity profile (McCarthy and Malloy, 1974).

The mechanism for atomization is generally thought to be caused by the formation of instabilities followed by ligaments and then droplets at the free surface. The source of the surface instabilities is thought to be due to turbulence generated inside the nozzle. Instability in the boundary layer and sudden velocity profile relaxation are both sources for surface disturbances (Chigier 1991). Hoyt and Taylor (1977b) point to aerodynamic forces as promoting the destabilization of the jet surface. Lasheras and Hopfinger (2000) discuss the role of interfacial aerodynamic stresses on the turbulent breakup of a round jet in the presence of a high-speed annular gas jet. However, reviews

of atomization literature point to no specific explanation for the dominant cause of breakup.

Experimental atomization studies of high-speed round and annular jets are summarized in Sallam *et al.* (2002). This work represents the cumulative efforts of Dai *et al.* (1998), Sallam *et al.* (1999), Wu and Faeth (1993, 1995), and Wu *et al.* (1992, 1995). These studies used pulsed photography and holography to observe the free surface. Primary breakup properties were dominated by effects of vorticity and turbulence at the jet exit for liquid/gas ratios greater than 500. Correlations for mean droplet mass flux from the jet surface as a function of downstream distance are provided. Streamwise droplet velocities are shown to be comparable to mean streamwise jet velocities with cross-stream droplet velocities comparable to cross-stream rms velocity fluctuations in the jet.

Closer examination of Wu *et al.* (1995) indicates that primary breakup at the surface of the jet can be controlled. By removing the boundary layer fluid at the nozzle exit with a knife edge, turbulent primary breakup along the free surface was "entirely suppressed." A similar result was observed in Karasawa (1992) for the study of a supercavitating injector. Vorticity was prevented from developing in this flow due to the flow separating at the passage inlet and not reattaching. The resulting jet showed no signs of turbulent breakup. These results indicate that a jet of uniform velocity profile will not undergo atomization-type breakup.

2.7 Nozzle and Flow Conditioning Design Studies

Nozzle design studies have a particular importance in the work presented here, thus a discussion of the literature concerning nozzle design studies and their relation with

smoothness of the liquid sheet is useful. The earliest investigations done by Bidone (1829) studied the geometrical form of jets formed by nozzles of regular but noncircular cross section. Subsequent studies in this area include Boussinesq (1877), Wada (1950), Erikson (1952), and the review of McCarthy and Molloy (1974). These studies have drawn the following conclusions: first, the best nozzle design for achieving the smoothest liquid sheet is a sudden, smooth contraction of the flow area from the supply line to the desired nozzle geometry area. It is unclear if there is a single "optimum" nozzle angle of convergence, but the angle should be between 15° and 100°. Smoothing the internal surface of the nozzle, both in terms of surface roughness and rounding corners, appears to improve the free-surface smoothness.

Flow conditioners, usually consisting of a combination of screens or perforated plates and honeycomb, can be used to straighten (*i.e.*, remove swirl from) and remove larger-scale coherent structures from the flow to improve the flow uniformity. The control and management of turbulence in flow test sections by means of screens and honeycombs is presented in Loehrke and Nagib (1976) and Tan-atichat *et al.* (1982). The flow conditioners to be used in this study are based on the results of Farell and Youssef (1996). These consist of a combination of perforated plate and honeycomb followed immediately downstream by a fine mesh screen, as detailed in Durbin *et al.* (2003) and Elwell (2000). The pressure drop across the flow conditioner must also be considered, as this loss will be directly linked to the required pumping power to drive the flow.

2.8 Previous Studies at the Georgia Tech Large-Scale Test Facility

The work detailed in this thesis follows the experimental studies of Elwell (2000), Collins (2000), Reperant (2002), and Koehler (2004). These studies provide a significant contribution to the physical understanding of turbulent liquid sheets.

Elwell measured the trajectory and spread rate of an oscillating liquid sheet for a range of experimental parameters Re = 8,500 – 37,000 and St = 0.006 – 0.06. These studies were conducted for water sheets with cross sections of 1 × 10 cm and 0.5 × 5 cm issuing into air at ambient conditions. The facility was a gravity-driven recirculating flow loop capable of mean velocities of up to 3.7 m/s at the nozzle exit. The sheet was visualized by illuminating the flow with a flash lamp and filming it at 30 Hz with a CCD camera. The trajectory and width of the sheet were determined as a function of downstream distance for oscillation amplitudes ranging from 1 mm to 5 mm and oscillation angles (measured from the centerline of the long dimension of the nozzle) from 0° to 90°. Mean jet width (*i.e.*, y-dimension) was found to decrease linearly with downstream distance after an initial expansion, with mean jet width decreasing more slowly at higher Reynolds numbers. The trajectory of the sheet was well predicted by a model based on the initial flow velocities imparted at the nozzle exit and gravitational acceleration.

Collins developed non-intrusive optical techniques to characterize liquid sheets at Reynolds up to 34,000. The experiments were conducted on the same apparatus as in Elwell (2000) but were performed for stationary sheets only. Planar-laser induced fluorescence (PLIF) was used to visualize the free surface of the flow at downstream locations of $x / \delta \leq 25$. The initial PLIF results focused on the wake regions of the flow,

which emanated from the corners of the nozzle. The free-surface fluctuations in these regions were found to be normally distributed about the mean free-surface position and grew logarithmically with downstream distance. Laser-Doppler velocimetry (LDV) was used to measure mean streamwise (x-component) velocity profiles and rms fluctuations inside the sheet at normalized downstream distances of $x / \delta = 0$, 10, 20, and 30. Velocity inside the sheet was essentially uniform for all configurations with the maximum velocity obtained consistently in the center. Fluctuations of velocity increased with downstream distance but remained constant for any given x-location.

The GTLTF was modified to a direct pump-driven recirculating loop in the summer of 2000 capable of producing flows up to Re = 130,000. Reperant used this facility to continue the flow visualizations begun by Collins. Statistical characterization of the free surface was again performed in the near field of the flow $x / \delta \leq 25$. In particular, the influence of nozzle design and blockages in the flow conditioner were closely studied. The optimal nozzle contour design was found to be a sudden, smooth contraction with sharp corners. Nozzles with rounded corners actually increased surface fluctuations at the edge of the sheet contrary to the suggestions of McCarthy and Molloy (1974). Fluctuations were approximately 3× higher at the edges of the sheet compared to those in the center. Area blockages of 2.5% placed in the flow conditioner were found to increase surface fluctuations by 8.5× compared to unrestricted flows. Preventing even minor blockages in the flow conditioner is therefore a major concern in producing sheets compatible with thick liquid protection schemes.

Koehler used a single component LDV system to record the mean and rms fluctuations of velocity in the streamwise direction of the flow at Re = 53,000, 97,000,

and 120,000. Unlike the work of Collins, these profiles were taken inside the nozzle since the free surface at the higher flow rates proved too rough for optical accessibility. The effect of the nozzle contraction and the presence (or absence) of a fine screen in the flow conditioner were quantified. The average streamwise velocity was accelerated through the nozzle, suppressing boundary layer growth and forcing energy into the streamwise velocity fluctuations. Mean and rms fluctuations of streamwise velocity were found to be independent of the flow conditioner design, despite evidence of the impact of the fine screen in free-surface behavior (Durbin *et al.*, 2005).

CHAPTER 3

EXPERIMENTAL APPARATUS AND PROCEDURES

This chapter describes the experimental equipment and procedures used in these investigations in the following order:

1) the Georgia Tech Large-Scale Test Facility (GTLTF);
2) the laser-Doppler velocimetry (LDV) system used to quantify the *x*- and *z*-velocity components;
3) the setup used for planar laser-induced fluorescence (PLIF) visualizations; and
4) the mass collection setup.

All sections first give details of the experimental equipment and then discuss the experimental procedures.

3.1 Flow Components

3.1.1 Flow Loop

The coordinate system used in these experiments is defined in Figure 3.1. The origin is located at the center of the nozzle exit with the *x*-axis along the flow direction. The *y*- and *z*-axes are along the long (width) and short (thickness) dimensions of the nozzle exit, respectively. The nozzle exit dimensions are W_o = 10 cm and δ = 1 cm.

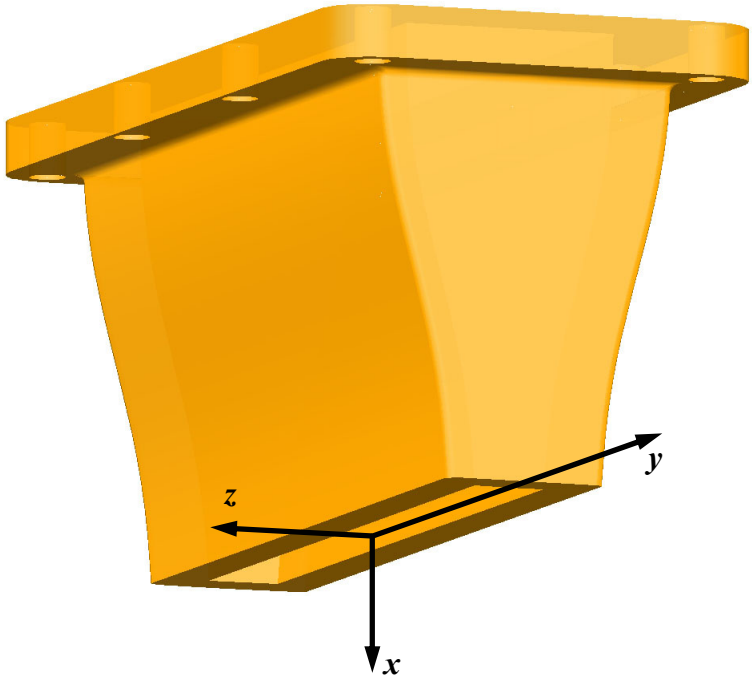

Figure 3.1. Definition of the coordinate system at the nozzle exit.

The recirculating flow loop is shown schematically in Figure 3.2. The main components of the flow loop are identified by letters; a detailed list of these components is given in Table 3.1. The flow loop occupies two floors and spans a total height of approximately 5.5 m. The upper part of the flow loop contains the open test section, while the lower part contains the main circulation pump and storage tanks.

The recirculating flow loop is driven by a 7.5 hp, (5.62 kW) three-phase centrifugal pump (A). Water is pumped up through 7.62 cm ID Schedule 40 PVC pipe over the entire apparatus height of approximately 5.5 m above the pump (A). A flow meter (C) just above the pump measures the flow rate to the test section. Just upstream of the flow conditioner, a pressure gage (D) measures the static pressure of the flow. A flexible rubber coupling (E) connects the 7.62 cm PVC pipe to the 12.7 cm diameter

flange of the flow conditioner (F). The water passes through the 10 cm × 3 cm flow conditioner inlet, then exits the flow conditioner into the nozzle where the flow cross section is contracted to the nozzle exit dimensions of 10 cm × 1 cm. Spectral analysis of the signal from an accelerometer attached to the nozzle determined the natural frequency of the flow loop to be 8.6 kHz which is well above the 60 Hz pump frequency. Therefore, it is expected that excitation of the flow by the pump is minimal.

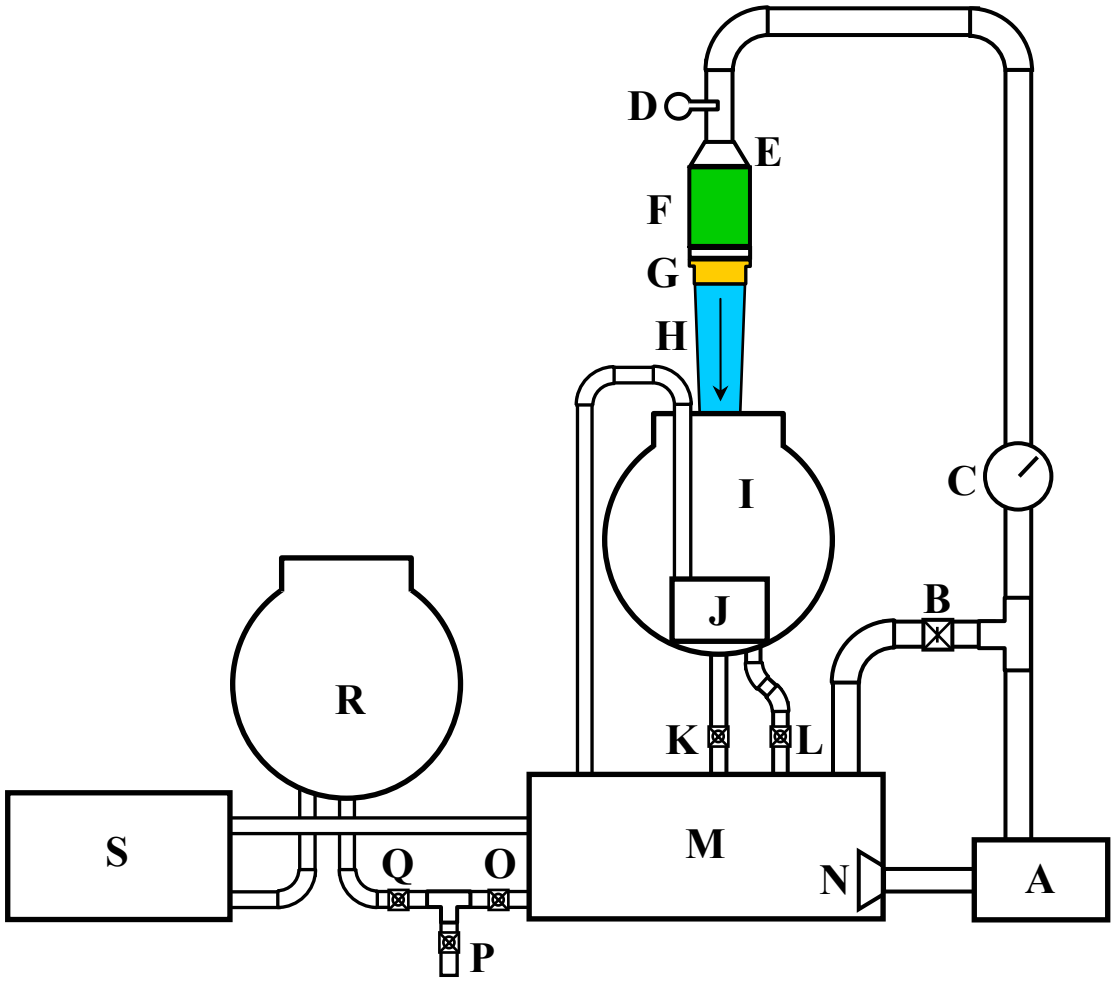

Figure 3.2. Schematic of the experimental facility.

Table 3.1. Detailed list of the experimental apparatus hardware components.

Label	Description	Manufacturer	Model	Serial number
A	Recirculating pump 5.62 kW 3465 RPM PH 3 19.2-9.5 Amps 60 Hz 230-360 Volts	TEEL	6406291A	C04-640829A-H
B	Bypass Valve PVC 7.62 cm valve 10.3 bar	SPEARS	-	-
C	Flow meter 0.04-0.4 $m^3.min^{-1}$ 13.8 bar	SEE-FLO	3223-12T2	003212
D	Pressure gage 0-2 bar	MARSH	-	-
E	Flexible rubber coupling 7.62 cm to 12.7 cm connection	Mc Master	-	-
F	Flow conditioner	In house construction	-	-
G	Nozzle	In house construction	-	-
H	Liquid sheet	-	-	-
I	Upper receiving tank 1.5 m^3 capacity	-	-	-
J	Sump pump 0.3 kW 1700 RPM PH 1 9 Amps 60 Hz 115 Volts	TEEL	4RK65	21F01
K	Ball valve Bronze 5.08 cm valve 12.1 bar	MILWAUKEE	-	-
L	Butterfly valve Bronze 5.08 cm valve 10.3 bar	GRINNELL	-	-
M	Bottom supply tank 1.23 m^3 capacity	-	-	-
N	Filter Monofilament polyester mesh 45.7 × 45.7 mesh 0.037 cm opening	Mc MASTER	9218T65	-
O,P	Ball valve PVC 5.08 cm valve 10.3 bar	WATERWHIZ	-	-
Q	Ball valve PVC 5.08 cm valve	HAYNARD	-	-
R	Bottom overflow tank 1.5 m^3 capacity	-	-	-
S	20 kW Chiller	AFFINITY	FAA-050D	005421

Water issues into ambient air from the nozzle exit, forming the liquid sheet in the open test section (H), and falls about 1.9 m before collecting in the upper 1.5 m^3 receiving tank (I). Two 5.08 cm ID PVC pipes drain the water to the lower 1.23 m^3 supply tank (M); the flow through these pipes is controlled by a ball and a butterfly valve (K and L, respectively). These experiments had a maximum Reynolds number of 120,000, corresponding to a 0.65 m^3/min flow rate. Since the maximum capacity of valves K and L together is only 0.49 m^3/min, a sump pump (J) is used to keep the water level in the bottom tank steady for experiments at the highest Reynolds number of 120,000. The sump pump is connected to a 5.08 cm ID PVC pipe leading to the bottom supply tank. A float switch activates the sump pump when the water level in the upper tank reaches two-thirds of the tank volume to provide additional drainage to the bottom tank required at the highest Reynolds number. The water level in the bottom supply tank therefore rises or drops when the sump pump is activated or deactivated, respectively.

The flow to the test section is controlled by a bypass butterfly valve (B). When valve B is fully open, all the flow is recirculated at a flow rate of 0.79 m^3/min from the tank M through a monofilament polyester mesh filter (N) placed across the inlet to pump A. This filter traps debris, thereby minimizing blockage of the flow conditioner. A nozzle with an open area 1.25 times that of the pump inlet is located downstream of the mesh filter to prevent cavitation and pressure loss due to the filter. By partially closing valve B, a portion of the flow is redirected to the open test section, with the remainder passing through the recirculation loop.

The overflow tank (R) is connected to the bottom supply tank by a length of 5.08 cm ID PVC pipe. Ball valves O, P, and Q allow drainage of the entire flow loop through

a drain in the laboratory floor, with O and Q allowing the bottom supply tank to be drained separately from the overflow tank. A 20 kW chiller (S) maintains the temperature of the water at a constant value of approximately 24°C. The chiller pulls water from the overflow tank through an ordinary garden hose and discharges the chilled water to the bottom supply tank. A water level alarm sounds when the bottom supply tank is approximately 10 cm from overflowing.

Prior to each experimental run, the flow conditioning sections were examined for any debris collected from prior experiments, usually scale formed inside the cast iron pump housing. Any debris was removed using jets of water and compressed air with the flow conditioner removed from the test section. After reinstalling the flow conditioner, the flow loop was set to a volumetric flow rate corresponding to the desired Reynolds number by adjusting the bypass valve. The valves controlling the gravity drainage to the bottom tank were left completely open, with the sump pump providing additional drainage as needed at higher flow rates.

3.1.2 Flow Conditioner Design

The flow conditioner reduces cross-stream flow and turbulence levels by breaking up the large-scale eddies, thereby increasing the rate of dissipation of turbulent kinetic energy. The flow conditioner used in these experiments was designed by Durbin *et al.* (2003) based on the recommendations of Farrell and Youssef (1996). It was produced in multiple sections by stereolithography rapid prototyping at the Georgia Tech Rapid Prototyping and Manufacturing Institute. Three-dimensional CAD drawings made using I-DEAS 8.0 software were used to produce the flow conditioner sections. A list of all flow conditioning sections is provided in Table 3.2.

Table 3.2. Flow conditioner sections.

Designation	Description	Resin	*x*-dim. (cm)
1	PP – HC section: Round to rectangle adapter	DSM Somos 7100	6.9
2A	Primary screen flange	DSM Somos 7100	0.9
2B	Secondary screen flange	DSM Somos 8100	3.3
3	Calming chamber	Vantico 7510	13.8

The effect of several different flow conditioning elements were studied. The combination of one or more fine screens (FS) was of particular interest, since these are the elements encountered by the flow just upstream of the nozzle. Table 3.3 gives a list of the various flow conditioning elements used in these investigations. All flow conditioning designs studied here included both the perforated plate and honeycomb. Five fine screens with different dimensions, designated by various letters, were chosen to study the impact of initial conditions on free surface behavior in the near-field of the turbulent liquid sheet.

Table 3.3. Flow conditioning elements.

Designation	Element Type	Description
PP	Perforated plate	50% open area with 4.8 mm staggered holes
HC	Honeycomb	3.2 mm dia. × 25.4 mm circular cells
FS-A	Fine screen (30 × 30)	37.1% open area, 0.33 mm wire dia. w/ cell width 0.51 mm
FS-B	Fine screen (40 × 40)	36.0% open area, 0.25 mm wire dia. w/ cell width 0.38 mm
FS-C	Fine screen (20 × 20)	67.2% open area, 0.23 mm wire dia. w/ cell width 1.04 mm
FS-D	Fine screen (30 × 30)	51.1% open area, 0.24 mm wire dia. w/ cell width 0.61 mm
FS-E	Fine screen (30 × 30)	64.8% open area, 0.17 mm wire dia. w/ cell width 0.68 mm

Figure 3.3 shows the two types of flow conditioning configurations used in these studies. Only the primary screen flange was utilized for "Type I" flow conditioning. A letter designation after the flow conditioning type was used to denote the screen contained in the screen flange. Therefore, Type I.A flow conditioning contained the fine screen designated as FS-A. Note that the Type I.A configuration was the "baseline" design and was used in all previous studies conducted at GTLTF. Experiments were also conducted using a "Type II" flow conditioning with an additional screen flange. The letter designation for these cases denotes the screens contained in the flanges in the order of appearance. Type II.A,B flow conditioning therefore indicates that the flow conditioner contained FS-A followed downstream by FS-B. The designation "N" is used to indicate designs with no screens.

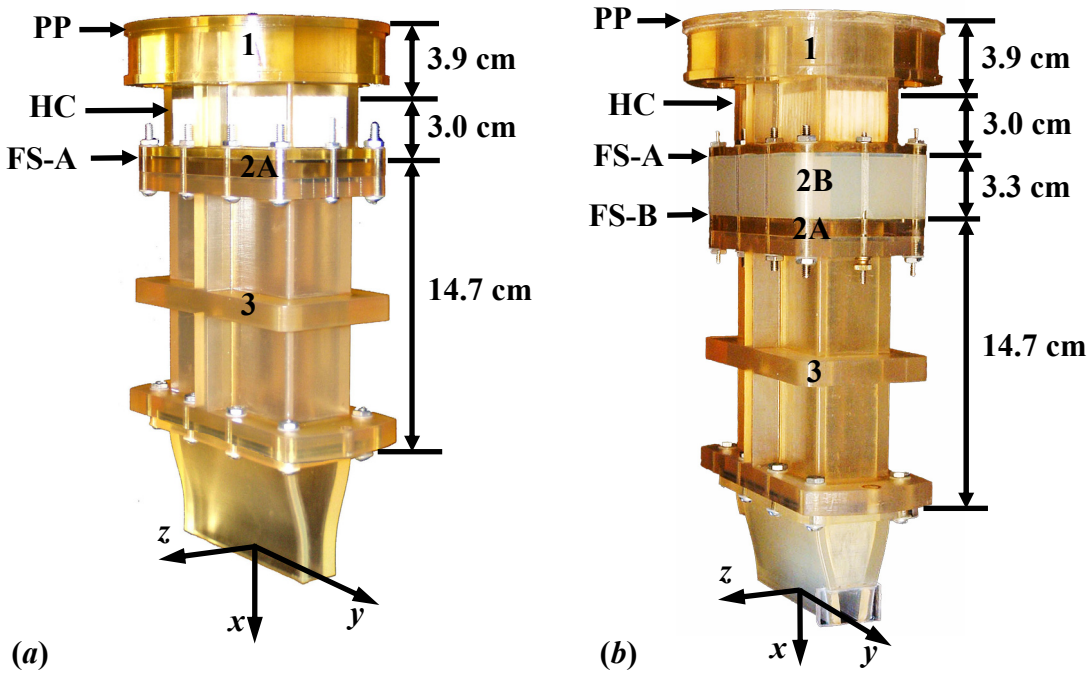

Figure 3.3. Flow conditioner assemblies with nozzle attached for (*a*) Type I.A and (*b*) Type II.A,B configuration.

3.1.3 Nozzle Design

A single nozzle geometry was used in all the experiments based on prior studies (Durbin *et al.*, 2003 and Reperant, 2002). The nozzle had a 5th order polynomial contraction along its *z*-dimension, contracting from a rectangular cross section of 3 cm × 10 cm ($z \times y$) to an exit cross-section of 1 cm × 10 cm ($\delta \times W_o$). The exit of the nozzle has a slight contraction with a taper of 4°. The 5th order polynomial $f(x)$ describing the contraction contour was determined from the following boundary conditions:

Inlet ($x = -63$ mm):	$f = 15$ mm;	$\frac{df}{dx} = 0$;	$\frac{d^2 f}{dx^2} = 0$
Exit ($x = 0$ mm):	$f = 5$ mm;	$\frac{df}{dx} = -\tan(4°)$;	$\frac{d^2 f}{dx^2} = 0$

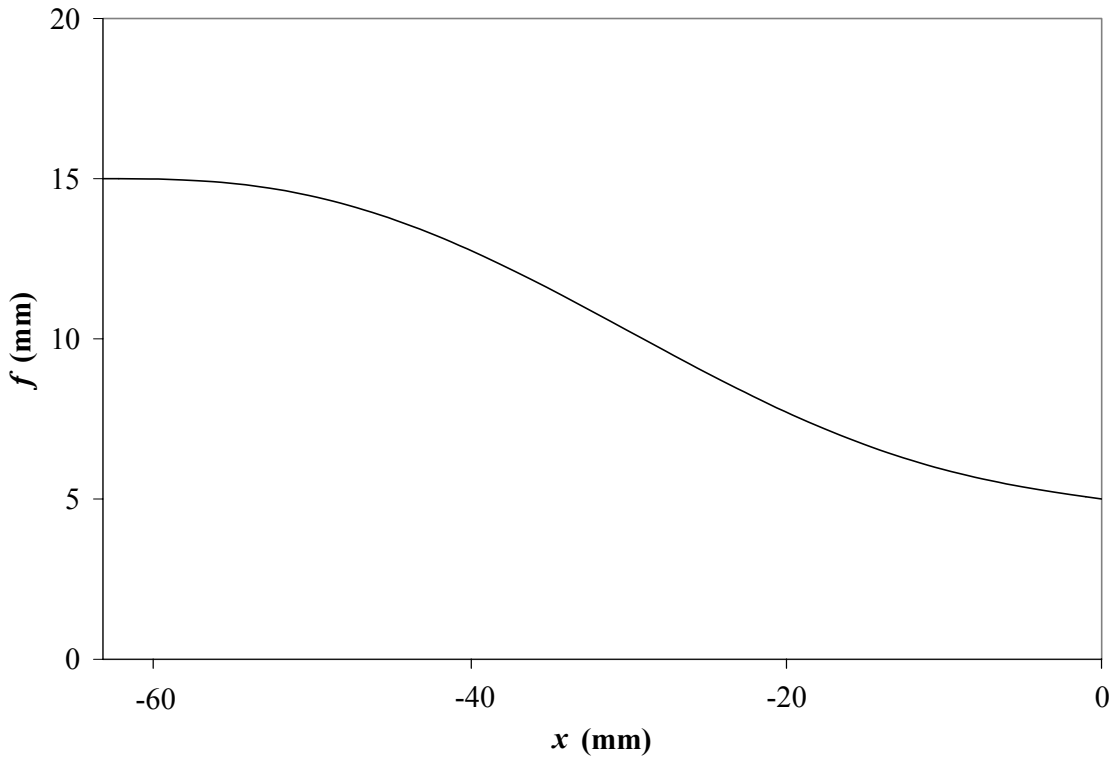

Figure 3.4. Plot of the 5th order polynomial contraction of the nozzle.

The nozzles were rapid prototyped at the Georgia Tech Rapid Prototyping and Manufacturing Institute using Vantico SL 7510, a resin with mechanical properties similar to ABS plastics. Ultimately, three versions of the nozzle were made for the experiments (Figure 3.5). The original nozzle had contoured outer nozzle walls of constant thickness 6.4 mm. Although this design was functional, the curvature of the nozzle walls precluded effective external clamping to prevent distortion from the pressure of the flow during long experimental runs. The outer walls of the nozzle were therefore redesigned to incorporate a straight section near the nozzle exit that provided a good surface for external bracing.

Modifications were made to a copy of the original nozzle design to allow optical access within the nozzle for LDV measurements. Optical access was provided by replacing a portion of one sidewall with a polycarbonate (Lexan) window after manufacture. Once the resin had cured, one of the two flat sides of the nozzle was milled away for $-3.6 \text{ cm} \leq x \leq 0$ and replaced with a 0.56 cm thick flat plate of polycarbonate. The window was affixed to the nozzle using Super Glue®, achieving a very strong bond that neither failed nor distorted, even at the highest flow rates studied here.

The surface roughness of the rapid prototyped nozzles was measured using a two dimensional Taylor Hobson Ltd. Form Talysurf optical profilometer. The surface roughness, characterized by average peak-to-valley height, was about 5 μm for the nozzles made of the Vantico 7510 resin. It is expected that the surface roughness has negligible effects on the free-surface fluctuations since previous experiments have determined that these fluctuations are much greater than the measured nozzle surface

roughness (Durbin *et al.*, 2004). The Lexan window had a surface roughness significantly less than that of the nozzles.

Figure 3.5. Photo of the sheet nozzle designs: (*a*) Original nozzle, (*b*) Modified for LDV, and (*c*) Redesigned for external clamping.

3.1.4 Boundary-Layer Cutter Design

Figure 3.6 shows the boundary-layer (BL) cutter and its placement with respect to the nozzle. The BL cutter used in this study, which was mounted independently from the nozzle, removed fluid from only one face along the *y*-axis of the jet just downstream of the nozzle exit at $x = 0.076$ cm. The cutter assembly was supported on a linear stage that enabled fine adjustments along the *z*-direction. The cutter blade, machined from aluminum, had a reattachment length of 7.5 mm and a width (*y*-extent) of 12 cm that extended 1 cm beyond the jet on both sides. The reattachment length was much smaller than the *x*-extent of the nozzle 63 mm so as to prevent significant BL re-growth. All experiments with boundary-layer cutting were conducted at the highest flow rate corresponding to $Re = 120{,}000$. Different levels of BL cutting ranging from $\dot{m}_{cut} / \dot{m}_{fl} = 0$

to 1.9% (where $\dot{m}_{cut}$ is the diverted mass flow rate) were evaluated at the highest jet mass flow rate $\dot{m}_{fl}$ = 10.82 kg/s.

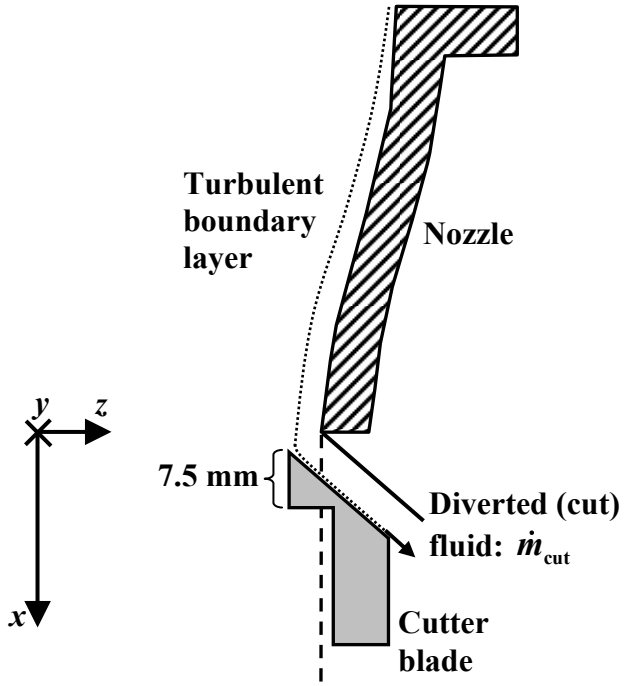

Figure 3.6. Schematic of BL cutter (enclosure around cutter blade not shown).

The BL cutter assembly consisted of six pieces (Figure 3.7). The cutter blade was mounted to the aluminum cutter mounting arm with four screws. The lower sections of the assembly were machined from acrylic and formed a channel for the cut fluid to drain under the influence of gravity. The top plate of acrylic confined the diverted fluid within the channel. The swirl rib, glued to the top plate, prevented the water from swirling back towards the cutter blade. The top plate, cutter arm, and lower sections of the assembly were all joined together with four through bolts. Figure 3.8 shows the BL cutter assembly in operation.

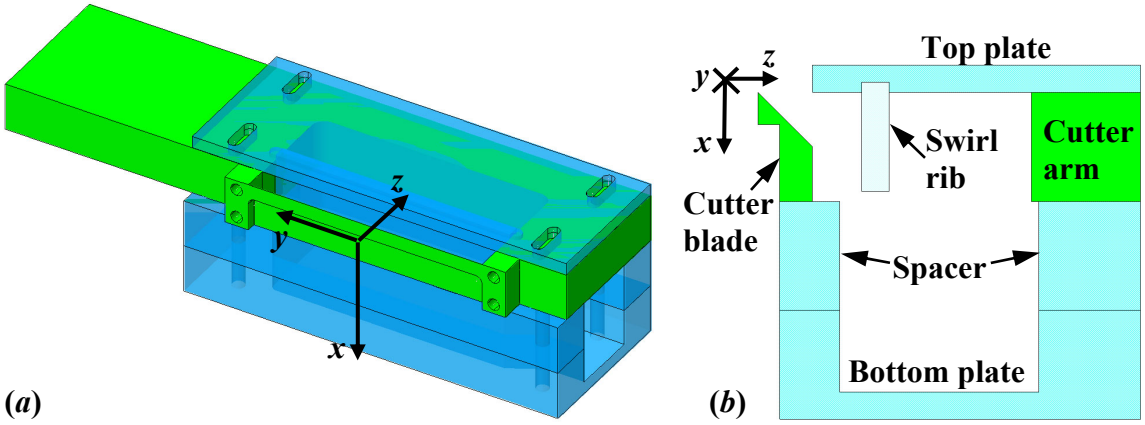

Figure 3.7. BL cutter assembly shown in (*a*) isometric and (*b*) cross-section.

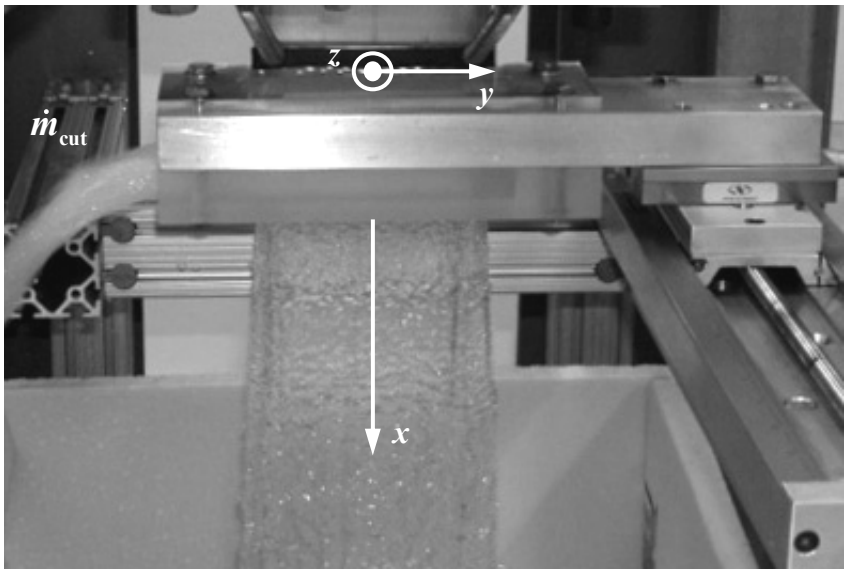

Figure 3.8. Photo of the BL cutter apparatus in operation. (Shown without spacer plate.)

The mass flow rate of the cut fluid was measured directly by measuring the time required to fill a 3.8 L receptacle. This fill time, typically 14 to 70 s, was measured with a stopwatch to within 0.01 s. The receptacle was weighed before and after collecting the fluid to obtain a measured mass difference, which when divided by the fill time then gave

the mass flow rate removed from the jet by the BL cutter, $\dot{m}_{cut}$. The position of the *z*-stage corresponding to this measured value of $\dot{m}_{cut}$ was also recorded, but it was discovered that this *z*-position was not reproducible (at least in terms $\dot{m}_{cut}$) due to inaccuracies and backlash in the lead screw.

3.2 Laser-Doppler Velocimetry

Laser-Doppler velocimetry (LDV) is a common, non-intrusive, optical technique used to measure instantaneous velocity at a single point. LDV is often used instead of mechanical flow measurement devices such as hot-wire and hot-film anemometers, which can obstruct the flow, especially in recirculating flows. The principal advantage of LDV is that instantaneous velocities can be measured without disturbing the flow. However, the flow must be optically accessible. LDV is a commonly used technique, and further information on LDV theory can be found in Durst *et al.* (1981) and Goldstein (1996).

3.2.1 Principles of LDV

The most common method of LDV used at present is the dual-beam anemometer system. Typically, a single laser beam is split into two mutually coherent polarized light waves which intersect to form a spheroid-shaped region called the probe volume. Particles passing through the probe volume with a given velocity scatter light from the light beams to produce the LDV signal. For the investigations detailed herein, a dual-beam system operating in backscatter mode as shown in Figure 3.9 was used. The photo detector was an avalanche photodiode (APD), and a rotating diffraction grating was used to introduce a frequency shift, which is discussed in detail later in this section.

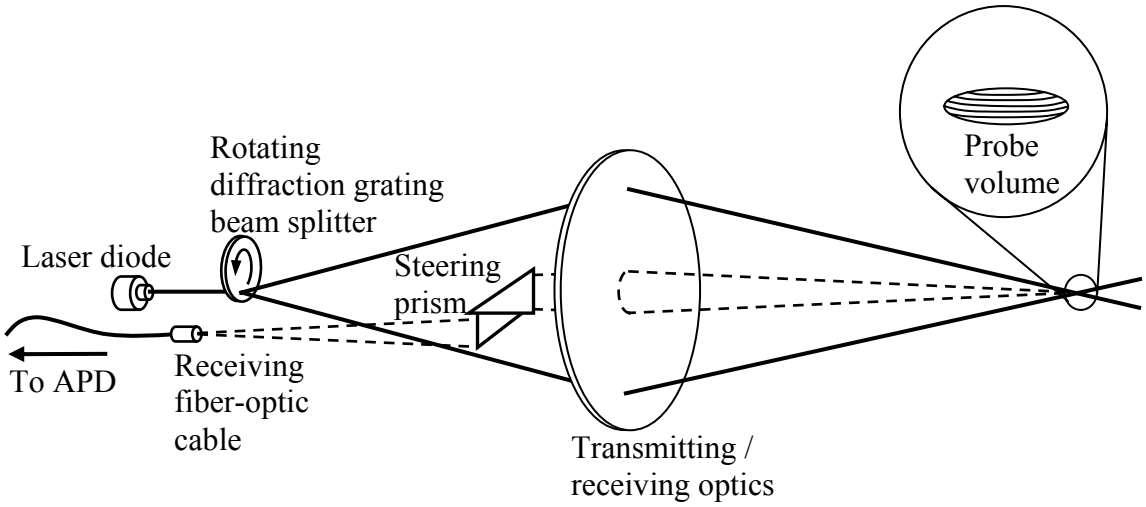

Figure 3.9. Dual-beam backscatter LDV system components.

The LDV technique is based on the Doppler shift of light scattered by small particles present in the flow. The LDV signal is generated by the optical heterodyne mixing of the scattered light from the two illuminating beams. The scattered light from both beams is received simultaneously by the photo detector, yielding a mix of the two Doppler shifted signals. This composite signal can be separated into two components; the first having a frequency equal to the average frequency of the incident beams and a second with a frequency equal to the difference of the input frequencies. The second frequency is referred to as the beat frequency and is proportional to the velocity of the particle.

A visual interpretation of the operation of the dual-beam LDV is given by the fringe model. This model avoids reference to the Doppler shift effect and instead makes use of the interference fringes created in the probe volume by the crossing of two incident coherent light beams. In Figure 3.10, the wave fronts of the two beams are shown to form interference fringes with spacing d_{fr}. The bright fringes are created from the

constructive interference of the incident light beams and the dark fringes are a result of destructive interference. The fringe spacing d_{fr} is determined from equation 3.1, where κ is the half angle of the beam intersection and λ is the wavelength of the incident light beams.

$$d_{fr} = \frac{\lambda}{2 \sin \kappa} \qquad 3.1$$

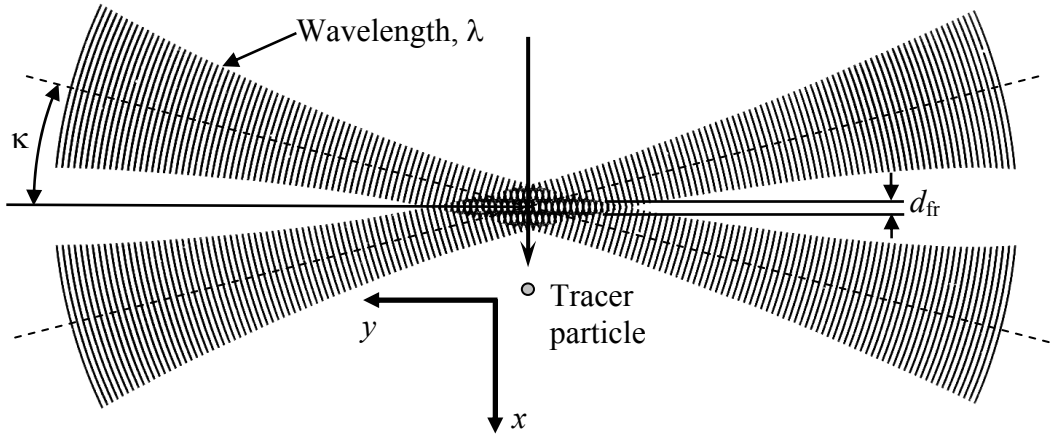

Figure 3.10. Sketch of the wave fronts of two intersecting light beams creating the interference fringes which comprise the probe volume. A tracer particle is shown passing through the probe volume perpendicular to the fringes.

A particle passing through the probe volume perpendicular to the fringes with a velocity u will scatter light with varying intensities as the fringes are passed. The resulting signal will have a fringe-passing frequency, f_D, equal to the frequency of the beat signal from the heterodyne model. Thus both models result in the measurement of the particle velocity that is proportional to the Doppler frequency of a beat signal

generated in the probe volume. The relationship of the particle velocity to the Doppler frequency is given in equation 3.2.

$$u = \frac{f_D \lambda}{2 \sin \kappa} \tag{3.2}$$

A practical LDV signal contains the Doppler signal and a pedestal signal (Figure 3.11). The pedestal component is typically removed with high-pass filtering. However, high-pass filtering is only effective when the Doppler signal is significantly greater than the pedestal $f_D > f_{ped}$, which is not the case for near-zero mean velocities. In addition, filtering does not resolve the 180° directional ambiguity of the Doppler signal (*i.e.* the system is unable to distinguish between $-f_D$ and f_D). The introduction of a frequency shift to the LDV signal resolves both of these situations.

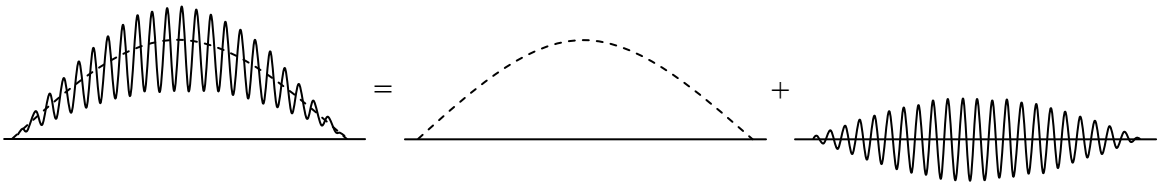

Figure 3.11. Typical LDV signal decomposed into the pedestal and Doppler signals.

The frequency shift is obtained when the two intersecting light beams have different frequencies. The presence of the frequency difference results in the apparent movement of the fringe pattern within the probe volume at the prescribed frequency shift, f_{shift}. One of the simplest ways to obtain the frequency difference is to pass the beams through a rotating diffraction grating (*cf.* Figure 3.9). The shift frequency is then linearly proportional to the rotational speed of the grating. The addition of the frequency shift to

the Doppler signal avoids interference with the pedestal signal as shown in Figure 3.12. The 180° directional ambiguity is also resolved, since $f_D + f_{shift} \neq -f_D + f_{shift}$.

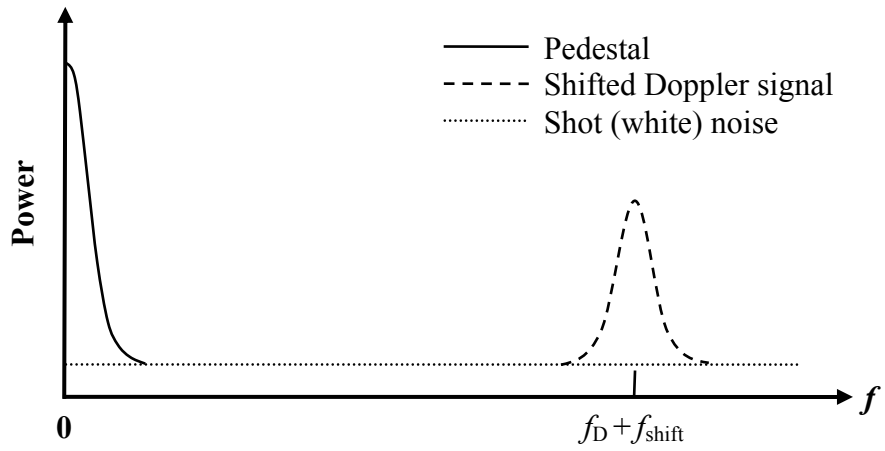

Figure 3.12. Power spectrum of the signal generated by an LDV system.

3.2.2 LDV Experimental Setup

The instantaneous velocity and rms velocity fluctuations were measured in these experiments by a single-component laser-Doppler velocimeter (VioSense MiniLDV-80). This LDV system, shown schematically in Figure 3.13, is composed of the MiniLDV sensor head, an avalanche photodiode (APD) and controller unit, a tunable filter-amplifier, a high-speed digitizer card, and data processing software. A detailed list of the LDV system components is given in Table 3.4.

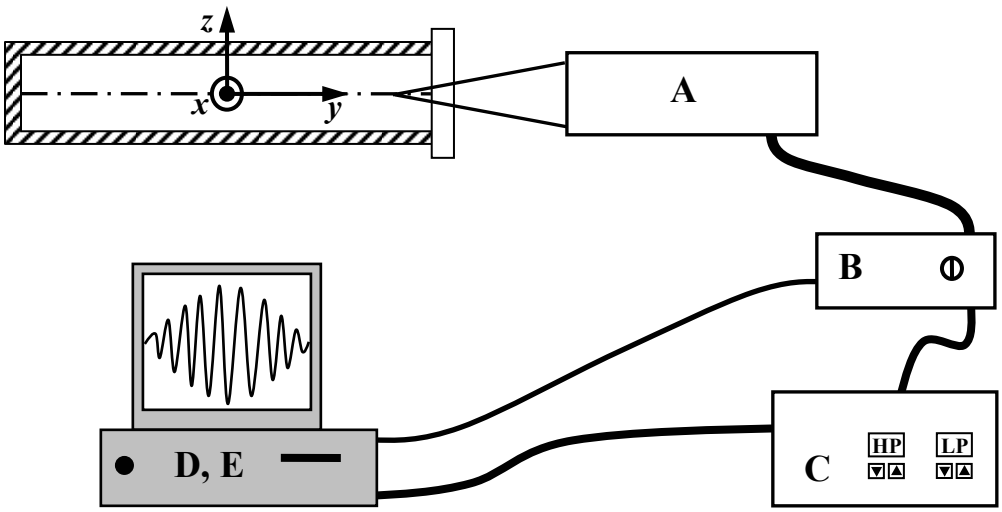

Figure 3.13. Schematic of the MiniLDV system.

Table 3.4. Detailed list of the LDV system components.

Label	Description	Manufacturer	Model
A	Sensor head	VioSense	MiniLDV-80
B	APD / Controller	VioSense	MiniLDV-80
C	Filter-amplifier	Krohn-Hite	3940
D	High-speed digitizer	National Instruments	5112
E	Processing software	VioSense	VioBP-1.19

The sensor head consists of a laser diode, a rotating diffraction grating beam splitter, a brushless shift motor, and transmitting / receiving optics. The single laser beam emitted from the diode was split into two coherently polarized beams using a diffraction grating beam splitter. Each beam leaving the diffraction grating has a wavelength of approximately 660 nm and a separation distance of 20.88 mm at the transmitting optics. The diffraction grating is then rotated to produce the desired frequency shift. The beams converge at a half-angle of $\kappa = 7.44°$ with a working distance of 80 mm in air to form a probe volume of 230 μm (x) × 1250 μm (y) × 50 μm (z) with

the beams oriented in the *xy* plane. This small probe volume allows for a high spatial resolution in the velocity profile. The probe volume has a power intensity of 13.3 mW and a fringe spacing d_{fr} = 2.55 μm. The MiniLDV system works in backscatter mode, which uses the same optics for both transmitting and receiving.

The shift motor is capable of frequency shifts between 0.4 to 1.35 MHz. All measurements of the transverse velocity (*z*-component) were conducted with f_{shift} = 1.3 MHz. This high shift frequency was required in order to ensure a minimum of 6 fringes would sweep across a particle before passing through the probe volume; a minimum of 6 – 8 fringes was necessary to accurately portray the Doppler signal within the VioSense software. The frequency shift was also necessary to avoid the pedestal signal, since the un-shifted Doppler signal for this component coincided with that of the pedestal.

The Doppler signal for streamwise (*x*-component) measurements was measured without frequency shifting. This velocity component was of sufficient magnitude ($f_D > f_{ped}$) to avoid confusion of the Doppler and pedestal signals. Directional ambiguity was also not an issue for the streamwise velocity component.

The water in the flow loop was seeded with 0.3 μm typical diameter (1 μm maximum diameter) TiO_2 particles at a volume fraction of about 3.4 ppm. These particles passing through the probe volume scatter light, creating Doppler bursts which are detected by the avalanche photodiode (APD) in the sensor head. The APD converts the photons from the scattered light into a voltage signal. The signal created by the APD contains the aforementioned pedestal signal that corresponds to the dc spectrum component inherent to the system.

The raw signal from the APD is then band-pass filtered by the Krohn-Hite filter-amplifier to produce a signal similar to that shown in Figure 3.14. Following the suggestions of Durst *et al*. (1981), a high-pass filter was used to pass frequencies corresponding to greater than one quarter of the expected velocity. The expected velocity of the *x*-component was taken to be the volumetrically averaged nozzle exit velocity U_o. The expected velocity of the *z*-component was taken to be the shift velocity, $U_{shift} = d_{fr} \times f_{shift}$. The low pass filter had a fixed maximum value of 2 MHz and was thus not used in these experiments so as not to filter out the Doppler signal. The signal was also amplified by 20 dB both before and after being filtered, for an effective total amplification of 40 dB. A trigger value of 0.4 V (in a voltage range of 3 V) was set to assure a good signal-to-noise ratio and minimize any remaining background noise from the signal.

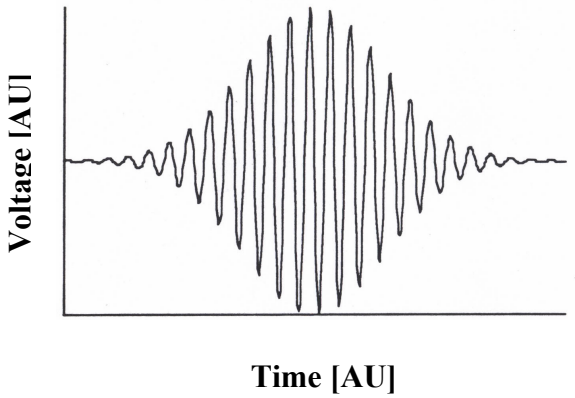

Figure 3.14. Sample of an ideal Doppler burst after signal filtering.

A sample of 1,000 readings was collected at each spatial location. The mean and rms fluctuations of velocity were determined and recorded by the data processing software. The data collection rate was typically between 1 to 100 Hz, so that the

sampling time or period is typically between 10 and 1000 seconds. Defining a convective time scale, τ, as:

$$\tau = \delta / U_o \tag{3.3}$$

where δ is the nozzle thickness and U_o is the average velocity at the nozzle exit, the largest convective time scale is expected to be approximately 2 ms. Therefore, the samples were acquired over a minimum of 5,000 convective time scales during the smallest sampling period of 10 seconds.

The filtered Doppler burst signal is converted to a digital signal onto the hard drive of a PC by the National Instruments digitizer card. The digitizer has a bandwidth of 100 MHz and a maximum output data rate of 10 kHz which is 5 orders of magnitude greater than the data rates acquired in these experiments. VioBP-1.19 software using a Fast Fourier Transform (FFT) then determines the Doppler frequency from the digital signal. The instantaneous velocity can then be calculated using the fringe spacing as a proportionality factor in equation 3.4.

$$u = d_{fr} \times f_D \tag{3.4}$$

Here, d_{fr} is the fringe spacing in the probe volume and f_D is the Doppler frequency. In these experiments, d_{fr} = 2.55 μm. The signal to noise ratio (SNR) is also determined from the Doppler frequency, and the data are then validated. Once a set of statistical results is collected, the mean velocity and rms fluctuation can be accurately measured.

The LDV sensor head was mounted atop two perpendicular linear translation stages. The top stage (Newport URM8.51) had a maximum travel of 25 mm and allowed the sensor head to travel along the *z*-axis. The bottom stage (Newport 433/Newport SM-50) moved the sensor head along the *y*-axis with a maximum travel of 50 mm. The two

stages were mounted on a horizontal aluminum T-slotted beam attached to the rigid frame of the open test section. The height of the aluminum crossbeam could be adjusted to position the probe volume along the *x*-axis. Figure 3.15 shows a photograph of the LDV sensor head mounted on top of the linear stages.

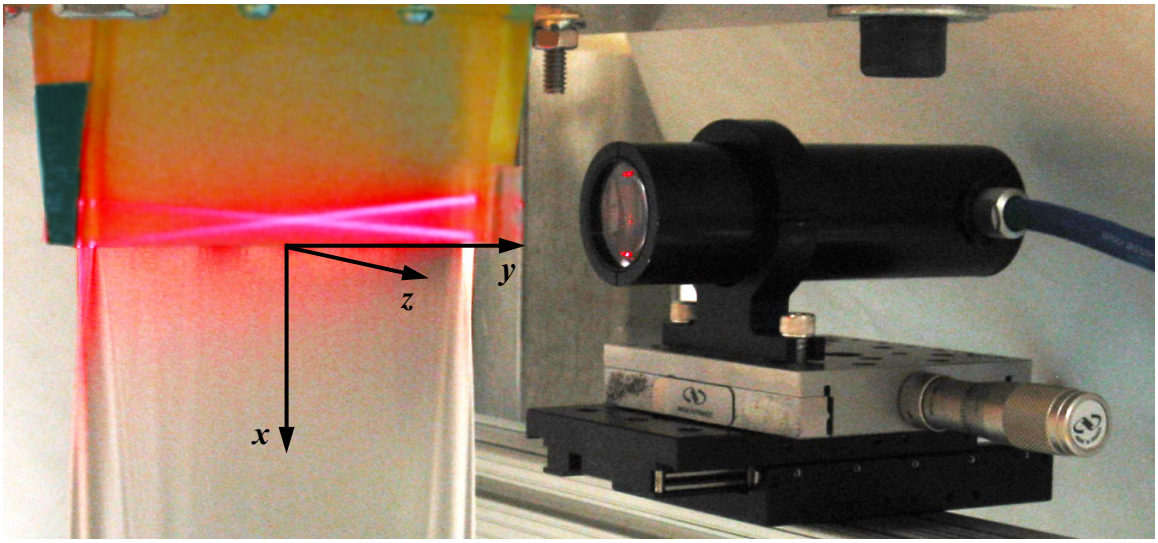

Figure 3.15. Photograph of the LDV sensor head aligned to measure streamwise (*x*-component) velocity.

3.2.3 LDV Procedures

Before any data acquisition, the LDV sensor head was positioned and aligned. First, the aluminum mounting beam was adjusted such that the two stages were level and the *x*-location of the probe volume corresponded to x = -6 mm. Second, a piece of masking tape was temporarily placed on the interior of the optical window. With the frequency shift on, the beams were brought almost to the point of convergence on the tape. The high pass filter was then set to 800 kHz with amplification of 20 dB before and after filtering. The second filter channel was set to bypass with no amplification. The

trigger value was set to 5 V (with a voltage range of 20 V). The stage positions were recorded when the frequency shift signal of 1.3 MHz was first detected and subsequently lost (Figure 3.16). This procedure was repeated three times for three different *z*-locations. The average of these values was used to determine the *y*-location of the probe volume center and to assure the probe volume was inside the optical window.

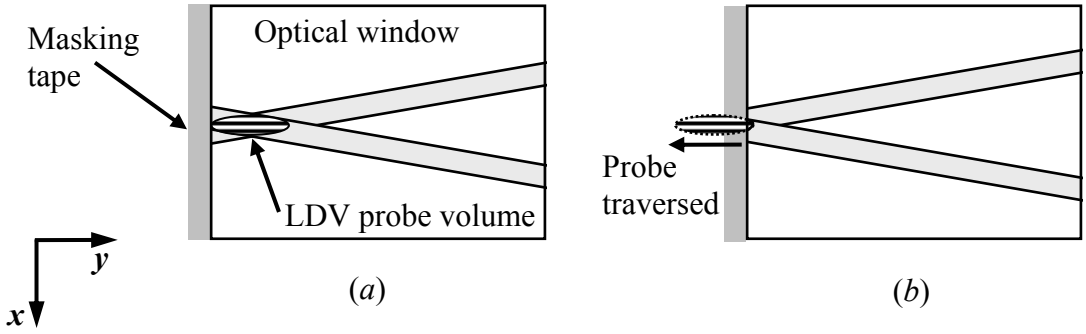

Figure 3.16. Schematic demonstrating procedure for determining LDV probe volume center with respect to the *y*-axis. Stage positions are recorded when (*a*) the shift signal is first detected, and (*b*) the signal is lost.

To determine the *z*-location of the probe, the masking tape was removed so that the beams could propagate through the window. The *z*-stage was then traversed until optical interference with the laser beams and the nozzle walls was encountered. The location of interference was recorded for both nozzle walls, effectively fixing the location of $z = 0$ as the average of these stage values. This procedure was followed for both the streamwise and transverse setups.

The absolute *y*-position of the probe volume can be determined using Snell's Law in conjunction with geometrical relationships. The *y*-location of the probe volume is dependent on the indices of refraction of air ($n_a = 1.00$), Lexan ($n_L = 1.586$), and water

(n_w = 1.33). The incident angle of the laser on the optical window was κ = 7.44°. Figure 3.17 shows the geometry used to determine the location of the probe inside the nozzle.

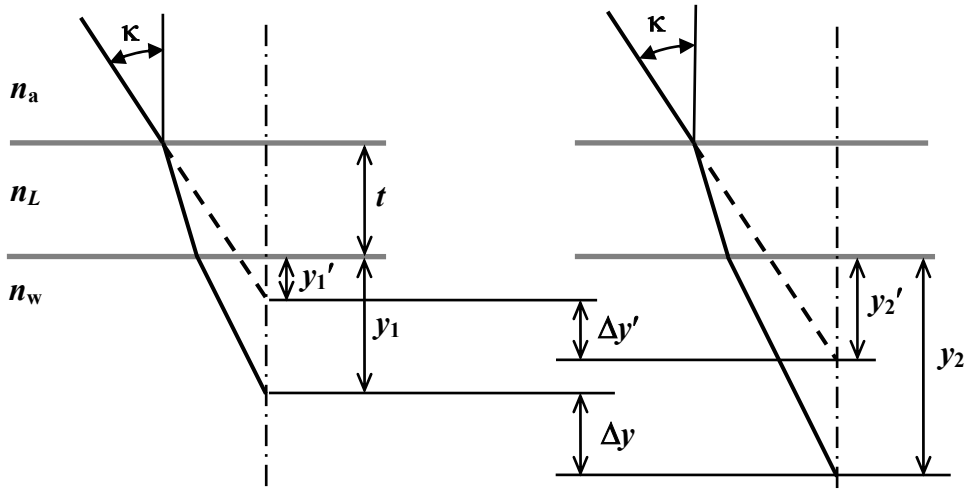

Figure 3.17. Geometry of the probe volume location (only one beam shown at exaggerated angles for emphasis).

The relationship between y and y' can then be used to determine how a given stage displacement is related to the actual probe volume displacement. Equation 3.5 defines the relationship between y and y' based on Snell's Law and trigonometry.

$$y = \left[y' + t\left(1 - \frac{\cos\kappa}{\sqrt{\left(\frac{n_L}{n_a}\right)^2 - \sin^2\kappa}} \right) \right] \frac{1}{\cos\kappa} \sqrt{\left(\frac{n_w}{n_a}\right)^2 - \sin^2\kappa} \qquad 3.5$$

The difference in positions is of particular importance, as $\Delta y'$ is the quantity measured by the micrometer of the stage. The term relating to refraction through the Lexan (second term in bracket) cancels by subtraction. Making use of small-angle

approximations for the sine and cosine terms, the relationship for Δy and $\Delta y'$ may be written as

$$\Delta y \cong \left(\frac{n_w}{n_a} \right) \Delta y' \qquad 3.6$$

Thus, a traverse of 1 mm on the *y*-stage translates into the probe volume moving 1.33 mm in the flow.

Once the desired *y*-position was fixed, the bottom translation stage was used to traverse the probe volume out along the *z*-axis. The first point at which no signal was obtained is then defined as the nozzle wall. The center of the probe volume was moved approximately 0.25 mm in from the contracting nozzle wall at this point. A sample of 1,000 readings was taken at this location, and the relevant statistical data (*i.e.* mean velocity, rms velocity, etc.) were recorded. The probe volume was traversed along the *z*-axis in small increments, and subsequent samples were collected until the probe volume approached the other side of nozzle, where the signal was again lost. Near the walls, increments of 0.05 mm were used, and larger increments of up to 1 mm were used in the region of the flow where the mean velocity profile can be assumed to be uniform. The samples taken by this method constitute velocity and rms fluctuation profiles along the *z*-direction of the jet. The probe volume was then traversed by the upper stage along the *y*-axis and set to the next desired *y*-location. The above process was repeated to obtain profiles along the *z*-direction at different *y*-locations. To avoid any backlash in the translation stages, the micrometer was turned only in one direction once a profile was started. Typically, the profiles were started near the optical window and subsequent profiles were obtained as the probe volume was traversed toward the center of the flow ($y = 0$). Velocity and rms fluctuation profiles were acquired along the *z*-direction for $3.38 \leq$

$y \leq 48.38$ mm. Stray reflections and interference with the optical window made $y = 48.38$ mm the maximum y-location at which data could be obtained. Figure 3.18 shows typical profile locations in the flow.

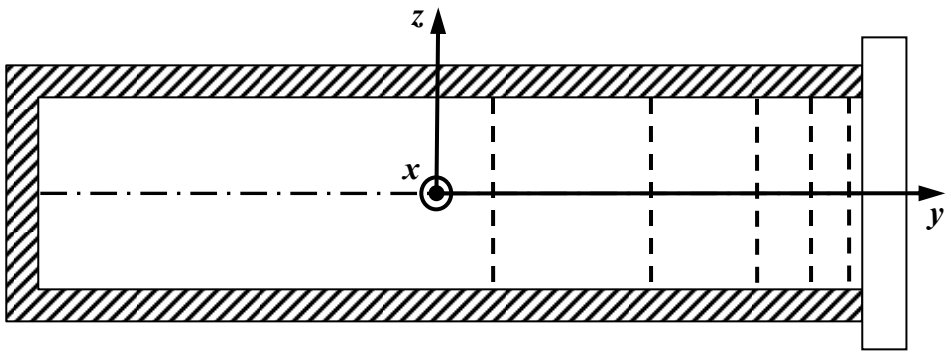

Figure 3.18. Schematic showing orientation of typical profile locations. Profiles are indicated by dashed lines.

Velocity profiles were taken at two Reynolds numbers, Re = 53,000 and 120,000. The Reynolds number was calculated in these studies using equation 3.7.

$$Re = \frac{U_o \delta}{\nu} \tag{3.7}$$

δ is the nozzle thickness (δ = 10 mm), ν is the kinematic viscosity of the fluid ($\nu = 9.12 \times 10^{-7}$ m^2/s at the maintained temperature of 24°C), and U_o is the average fluid velocity determined from the volumetric flow rate.

3.3 Planar Laser-Induced Fluorescence

3.3.1 Experimental Setup for PLIF

The technique used to examine the free surface geometry and fluctuations of the liquid sheet is based on the common flow visualization technique of planar laser-induced

fluorescence (PLIF). Merzkirch (1987) describes the principles of the laser-induced fluorescence in detail. The turbulent liquid sheet was illuminated at various downstream (x) locations by a 0.2 cm thick argon-ion laser light sheet, and the resultant interface between fluorescing water and non-fluorescing air (which corresponds to the free surface) was imaged obliquely from below. Figure 3.19 shows a photo of the components used in the PLIF arrangement. The apparatus used in this process are described in the following paragraphs.

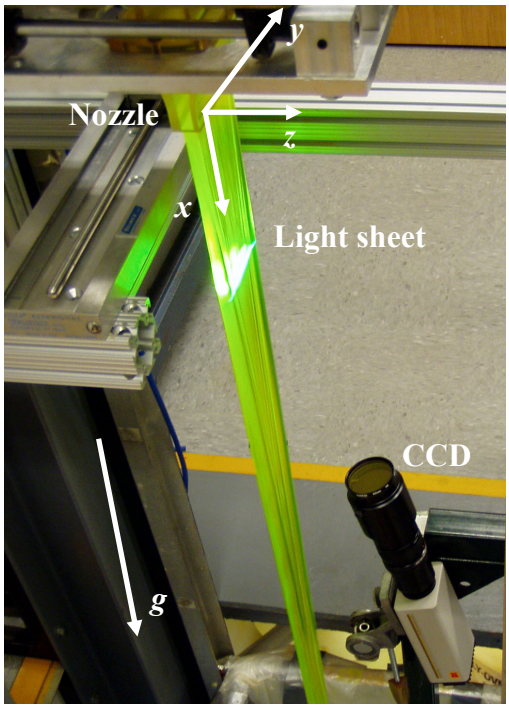

Figure 3.19. Free-surface visualization setup. An argon-ion laser light sheet illuminates the uranine-doped jet, with the resulting fluorescence obliquely imaged from below by a CCD camera.

The water in the flow loop was dyed with disodium fluorescein (uranine), a dye which fluoresces in the yellow-green when illuminated by argon-ion laser light at 488 nm

at a nominal concentration of 71 μmoles per liter (26 mg/L). This relatively high concentration ensured that all laser light was absorbed near the free surface. The surface tension of aqueous solutions of uranine at concentrations up to 53 mg/L concentration was measured and found to be identical to that of distilled water. The spectra for absorption and stimulated emission for disodium fluorescein are shown in Figure 3.20.

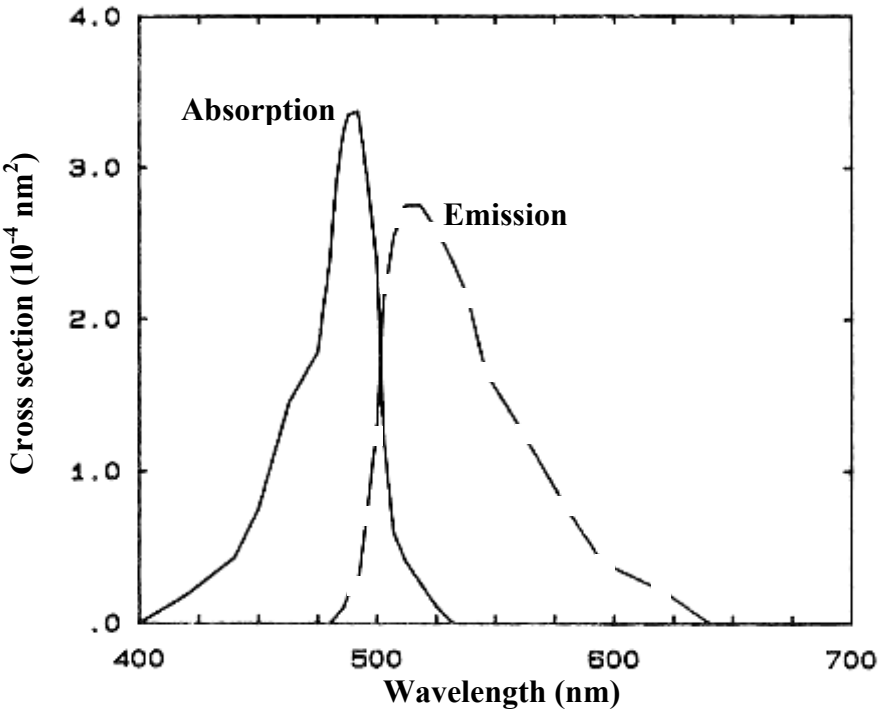

Figure 3.20. Spectra for absorption and emission by disodium fluorescein dye. Adapted from Figure B-1 in Dahm (1985).

The illumination source was a 500 mW multiline argon-ion laser (Omnichrome 543-MA-A03). The laser was passed through a notch filter (Edmund Scientific NT30-907) to obtain about 0.2 W at 488 nm. Two adjustable mirrors were used to steer the laser beam to the focusing lenses. The beam then passed through a 400 mm focal length bi-convex lens (Melles Griot 01LDX243) and a 19 mm focal length cylindrical lens

(Melles Griot 01LCN002) positioned approximately 200 and 250 mm from the liquid sheet, respectively. The light sheet is approximately 5 cm wide (y-dimension) and 2 mm thick (x-dimension) at the intersection with the liquid jet.

The free surface was imaged as the interface between fluorescing water and non-fluorescing air by an obliquely mounted B/W CCD camera (Kodak Model ES 1.0) from below at 30 Hz with a close-focusing macro video lens (Navitar Zoom 7000). A high-pass wavelength filter (Sunpak Yellow-8) with a cut-off frequency of 500 nm was mounted to the camera lens to ensure only fluorescence was imaged. The camera was fixed to a two-axis mill table allowing positioning in the y- and z-axis.

3.3.2 PLIF Procedures

The free surface was visualized using 4 – 5 overlapping segments that span one side of the entire y-extent of the flow. The field of view for each image is about 3.0 cm (y) × 3.0 cm (z) with a spatial resolution of 30 μm/pixel. Each segment was composed of 134 consecutive images, each with an exposure of $\tau = \delta / U_o$, with an entire segment spanning at least 5200τ. The individual frames were stored as 8-bit 1008 × 1008 image bitmaps on a PC hard drive using digital video recording software (Video Savant 3.0).

The free surface is found in each image using a threshold-based edge detection algorithm written in MATLAB. Figure 3.21 illustrates the various steps involved in determining the free surface from the raw PLIF images. The grayscale threshold value was chosen based upon the grayscale histogram for the entire dataset. This grayscale value was chosen such that it was the first grayscale value to the right of the background peak to be 1% of the number of background peak pixels. For every segment, the

instantaneous free-surface locations are determined for each of 134 thresholded frames using a standard edge detection scheme and used to calculate the average location and *z*-direction standard deviation of the free surface.

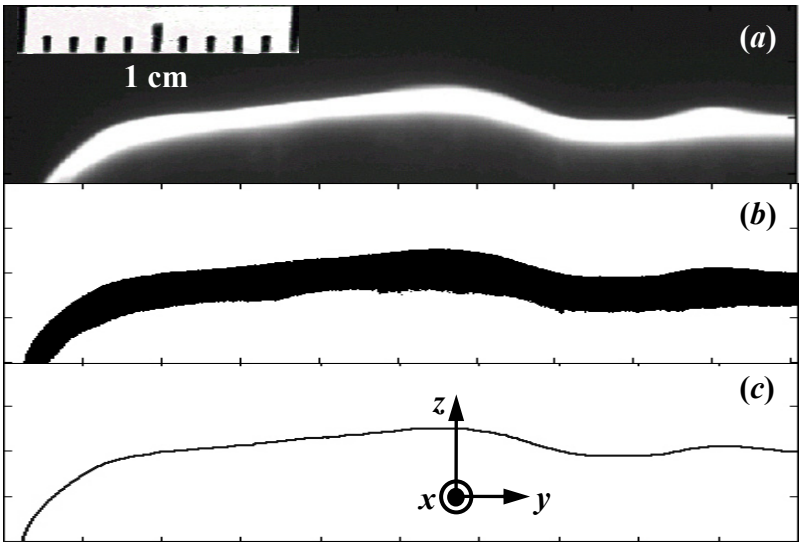

Figure 3.21. Image processing steps for identifying the liquid sheet free surface: (*a*) Raw PLIF image; (*b*) Thresholded image; and (*c*) Free surface obtained with edge detection.

A scale was positioned 1 cm away from the nominal free surface in each image. The scale was mounted on a linear stage allowing control in the *z*-axis. With the flow off, the nominal free surface was determined by fixing two monofilament lines to the inner wall of the nozzle with a plumb bob attached at the ends. The monofilament lines then formed a reference plane corresponding to the nominal free surface, *i.e.* the inner wall of the nozzle. The scale was then traversed towards the monofilament lines until contact was visually observed. The *z*-position of the jet was then established with respect to the original nozzle wall by referencing to the scale, which was 1 cm away from the nominal free surface.

Each segment of the free surface has a slight overlap with neighboring segments. The extent of the overlap region is known from a reference scale imaged in each frame. In all cases, the average position and free surface fluctuations in this overlap region are taken to be those calculated for the left segment. No significant discontinuities were observed using this procedure.

3.4 Primary Turbulent Breakup

3.4.1 Mass Collection Experimental Setup

The ejected mass from the free surface was measured using a simple mass collection technique. Square cuvettes with inner open dimension of 1 cm and wall thickness of 1 mm were placed in the proximity of the free surface at the furthest downstream location of $x / \delta = 25$ (Figure 3.22). The cuvette standoff distance, Δz_s, was measured from the nominal free surface of the jet, which corresponds to the downstream location of the inner nozzle wall. A series of five cuvettes were centered with respect to the y-axis and maintained at a fixed z–location for $t_{coll} = 30 – 60$ minutes. An angle of $\theta = 6.5°$ from the vertical was imposed on the cuvettes to accommodate the correlation-based droplet trajectories. The cuvettes were weighed on a digital scale (OHAUS GT 210) to 1 mg accuracy before and after each trial so that the mass difference provides an estimate of the mass ejected from the free surface. These measurements do not account for any mass lost to evaporation during the collection time.

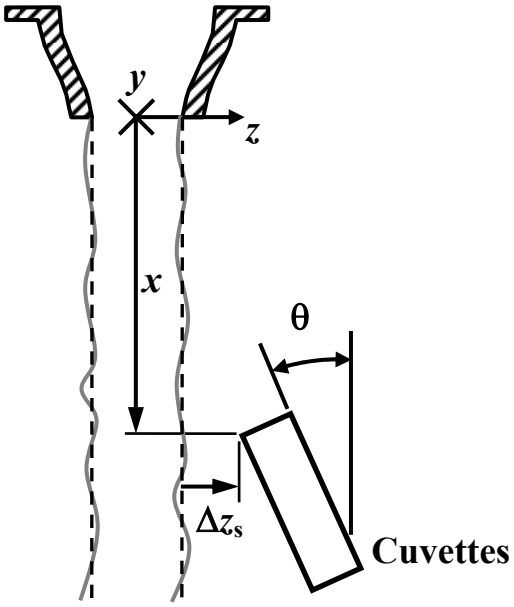

Figure 3.22. Schematic of mass collection technique. The cuvettes are brought to a distance Δz_s from the nominal free surface (dashed lines) at angle $\theta = 6.5°$ from the vertical.

The cuvette holder consisted of an aluminum bar machined to accept and secure the five cuvettes. The holder was cantilevered from two linear translational stages allowing adjustments in the *y*- and *z*-directions. The two stages were mounted on a horizontal aluminum T-slotted beam attached to the rigid frame of the open test section. The height of the aluminum crossbeam could be adjusted to set the *x*-position of the cuvettes. The *y*-stage (Newport 433/Newport SM-50) had a maximum travel of 50 mm and was used to center the cuvettes with respect to the *y*-axis. The *z*-position was controlled by a screw-driven linear stage (UniSlide A4012-S4-TL) with a travel of 30.5 cm. The cuvettes were held in place with two clamping plates as shown in Figure 3.23. The angle of the cuvettes was measured at the base of the cuvette holder to within 0.1° using the SmartTool™ Builders Angle Finder.

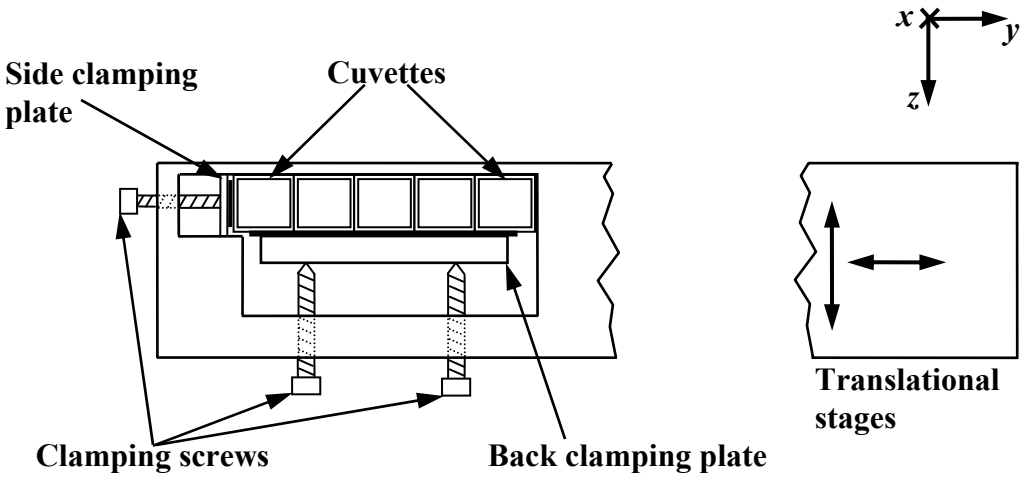

Figure 3.23. Detail view of the cuvette holder.

3.4.2 Mass Collection Procedures

The nominal free surface was determined by the following procedure. Two monofilament lines were attached symmetrically about the *y*-axis 5 cm apart to the inner wall of the nozzle with masking tape. A plumb bob was fixed to the bottom of these lines thus forming a reference plane corresponding to the nozzle wall. With the cuvettes in place, the *z*-stage was advanced until the cuvettes were visually observed to contact the monofilament lines. This position was recorded as the nominal free surface, and all subsequent positioning of the cuvettes was made relative to this reference value. The cuvettes were then centered with respect to the *y*-axis by aligning the left and right cuvettes with the monofilament lines.

The droplet collection apparatus was positioned at the desired downstream distance *x* measured from the nozzle exit. Each cuvette used in the experiment was individually numbered and weighed using a digital scale (OHAUS GT 210). Once the flow was initiated, the set of cuvettes were placed and secured in the cuvette holder. The

cuvettes were translated along z to the desired standoff distance from the nominal free surface. With the cuvettes in position, droplets were allowed to collect in them over a time t_{coll} = 30 – 60 min. At the end of the collection time, the cuvettes were withdrawn along z away from the flow. The cuvettes were then removed from the cuvette holder and cleaned of any droplets accrued on the outside of the cuvettes with a paper towel. The total mass of each cuvette and collected water within, m_{tot}, was measured using the digital scale. Again, any mass lost to evaporation is unaccounted for with this procedure. The mass collected is then defined as:

$$m_{coll} = m_{tot} - m_{cuv} \tag{3.8}$$

The mass flux due to droplet ejection G is defined as the amount of mass of droplets collected in the cuvettes per unit area per unit time.

$$G = \frac{m_{coll}}{A_{cuv} \cdot t_{coll}} \tag{3.9}$$

Two other quantities of interest, the effective line density and the equivalent number density, were derived from the mass flux of droplets. The effective line density, ρ_{eff} (kg/m^3), was defined using the experimental mass flux and the magnitude of the droplet velocity

$$\rho_{eff} = \frac{G}{\sqrt{\tilde{u}^2 + \tilde{v}^2}} \tag{3.10}$$

with $\tilde{u}$ and $\tilde{v}$ given in Sallam (2002). The equivalent average number density, N (m^{-3}), was then defined as

$$N = \frac{\rho_{eff} \cdot N_A}{M} \tag{3.11}$$

where M and N_A are molecular weight and Avogadro's number, respectively.

3.4.3 Droplet Visualizations

Droplets were visualized using a digital camera (Nikon CoolPix 950) attached to a standard microscope with a 5× objective. A microscope slide treated with Rain-X® was placed approximately 5 mm from the free surface for ~10 sec. The slide was then viewed under the microscope with the image recorded by the digital camera. Images were captured at a resolution of 1600 × 1200 with a resulting spatial resolution of 1 μm / pixel.

The time taken to transfer the slide from the experiment to the microscope was minimized, ~10 sec. However, droplet evaporation was observed even during this short time. Estimates of evaporation indicated that a droplet with an initial radius of 1 μm evaporates within ~ 3 sec at lab conditions. These visualizations are therefore provided as a qualitative reference, since the actual droplet sizes are not represented with this technique.

CHAPTER 4

RESULTS AND DISCUSSION

This chapter presents the initial conditions and resulting near-field behavior of a turbulent liquid sheet. In this thesis, "initial conditions" refer to z-profiles of the x- and z-velocity components obtained using LDV just upstream of the nozzle exit. Free-surface geometry and fluctuations are next quantified by means of the PLIF technique. Finally, the breakup of the jet is estimated using a mass collection method.

4.1 LDV Measurements

4.1.1 Effect of *Re*

Streamwise (x) and transverse (z) velocity profiles were taken at Reynolds numbers Re = 53,000 and 120,000 just inside the nozzle exit at $x / \delta = -0.6$. The mean and rms fluctuations of velocity are normalized by the average velocity at the nozzle exit U_o, where U_o = 5.21 and 10.85 m/s for Re = 53,000 and 120,000, respectively. The profiles were all taken along the z-axis with the z-position normalized by the local nozzle thickness, b. At $x / \delta = -0.6$, the nozzle thickness is b = 10.95 mm (Figure 4.1). The profile location with respect to the y-axis was normalized by the width of the nozzle W_o = 10 cm. Representative profile locations are also shown in Figure 4.1.

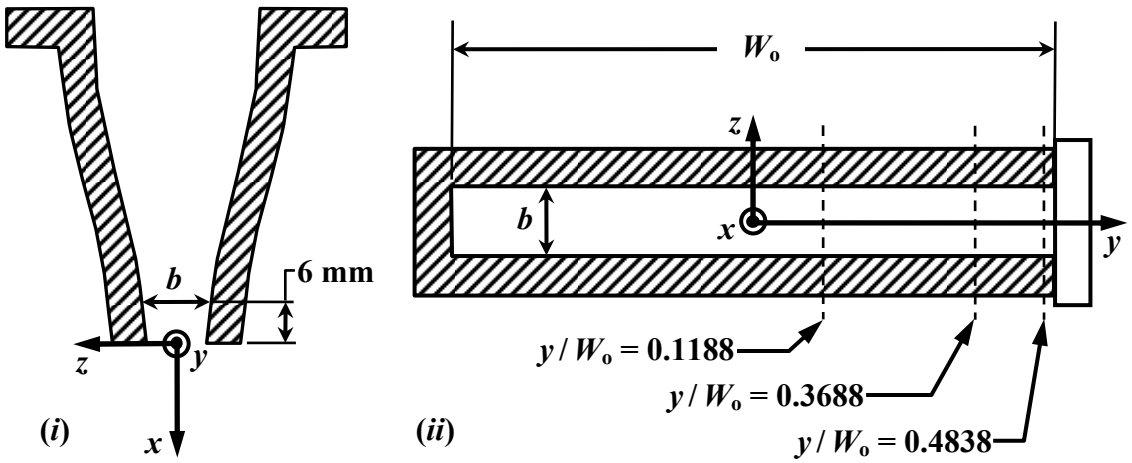

Figure 4.1. Schematic showing *i*) local nozzle thickness, b, at x = -6 mm and *ii*) three representative profile locations at y / W_o = 0.1188, 0.3688, and 0.4838.

Figures 4.2 and 4.3 show the mean x- and z-velocity components u and w, respectively, at Reynolds number Re = 53,000 and 120,000 for flow conditioning Type I.A. The profiles shown were acquired at y / W_o = 0.1188 (+), 0.3688 (●), 0.4163 (▲), 0.4438 (◆), and 0.4838 (■). Only a w profile was measured at y / W_o = 0.1188. The open and closed symbols represent u / U_o and w / U_o, respectively. The 95% confidence intervals for these data are comparable to the symbol size. Profiles of u indicate nearly uniform flow across the thickness of the nozzle for both Reynolds numbers. The volumetrically-averaged values of velocity are plotted as dashed lines. The expected average value of u / U_o was based on the area contraction ratio δ / b = 0.913. A linear regression for the expected transverse velocity shows that it spans $|w/U_o| \leq \tan(5.5°)(\delta/b)$, where 5.5° is the local nozzle contraction angle at x / δ = -0.6, corresponding to a slope of -0.176.

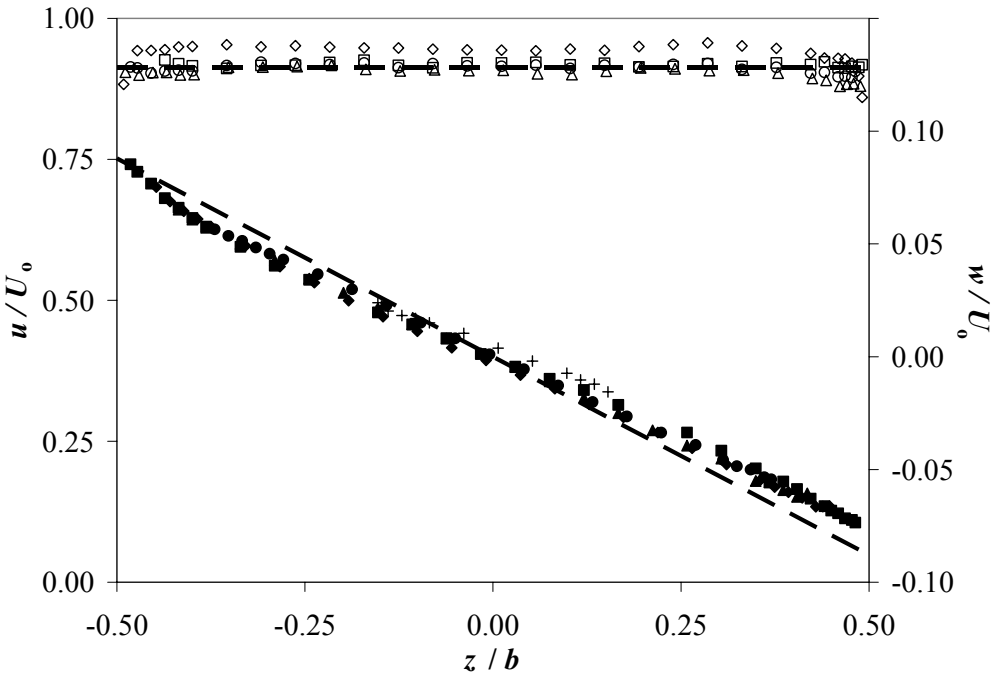

Figure 4.2. Mean velocity profiles for Type I.A flow conditioning and Re = 53,000 and y / W_o = 0.1188 (+), 0.3688 (●), 0.4163 (▲), 0.4438 (◆), and 0.4838 (■). The open and closed symbols represent u / U_o and w / U_o, respectively, while the dashed lines indicate the expected velocity values.

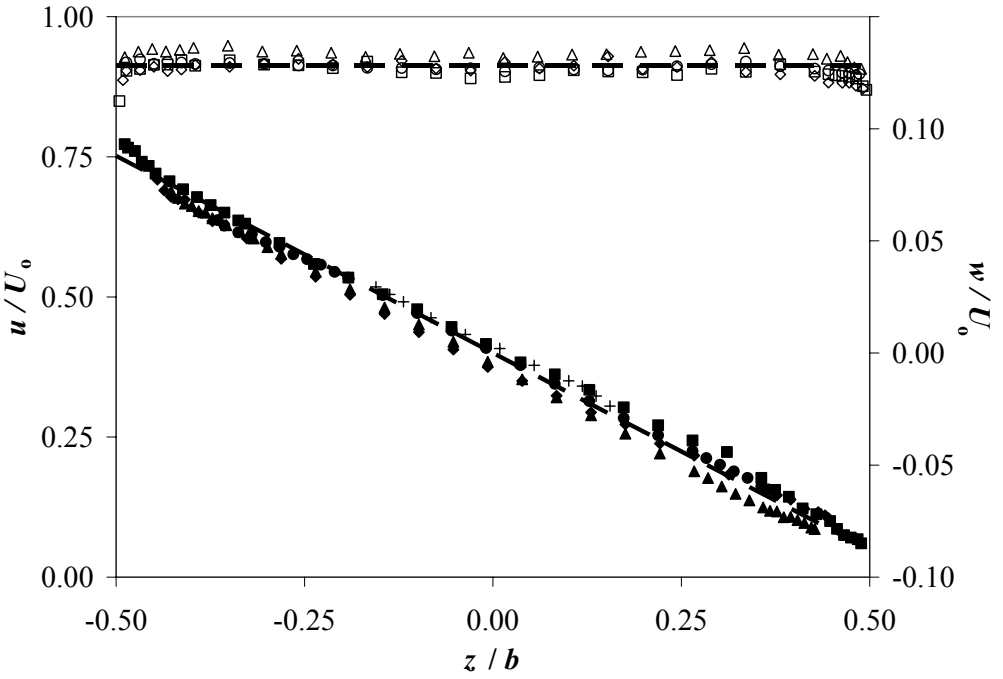

Figure 4.3. Mean velocity profiles, similar to Figure 4.2, for Type I.A flow conditioning and Re =120,000.

A spatially-averaged value of u, u_{avg}, is defined for each profile using the data lying within $|z/b| \leq 0.375$, or the central 75% of the profile. The values of u_{avg}/U_o are within ±3.5% and 2.2% of the expected value for Re = 53,000 and 120,000, respectively. A least squares fit to the transverse velocity data gives slopes of -0.153 and -0.172 for Re = 53,000 and 120,000, respectively. The magnitude of transverse velocities at Re = 53,000 are slightly less than the linear regression away from $z/b = 0$.

The boundary-layer thickness δ_{BL} is defined in these experiments as the z-distance from the nozzle wall where $u \leq 0.95 \cdot u_{avg}$. This criterion based upon 95% (*vs.* 99%) was chosen since the streamwise velocity profiles varied by about 3 – 4% over $|z/b| \leq 0.375$. The spatial resolution of each LDV data point and uncertainties in the probe volume position introduce errors in estimating the boundary-layer thickness from the measurements of $u(z)$. The boundary-layer thickness was estimated to be δ_{BL} = 0.19 and 0.11 mm for Re = 53,000 and 120,000, respectively.

The rms velocity fluctuations of the x- and z-velocity components u' and w', respectively, for Type I.A flow conditioning at Re = 53,000 and 120,000 are presented in Figures 4.4 and 4.5. The profiles shown were acquired at y/W_o = 0.1188 (+), 0.3688 (●), 0.4163 (▲), 0.4438 (◆), and 0.4838 (■). Again, only a w' profile was acquired at y/W_o = 0.1188. The open and closed symbols represent normalized values of u' and w', respectively. The velocity fluctuations are relatively constant over the bulk of the flow and increase near the nozzle walls due to the presence of a turbulent boundary layer. The profiles for y/W_o = 0.4838 show marked increase in w', due most likely to the influence of the optical sidewall. The 95% confidence level for all these data is less than 0.14%.

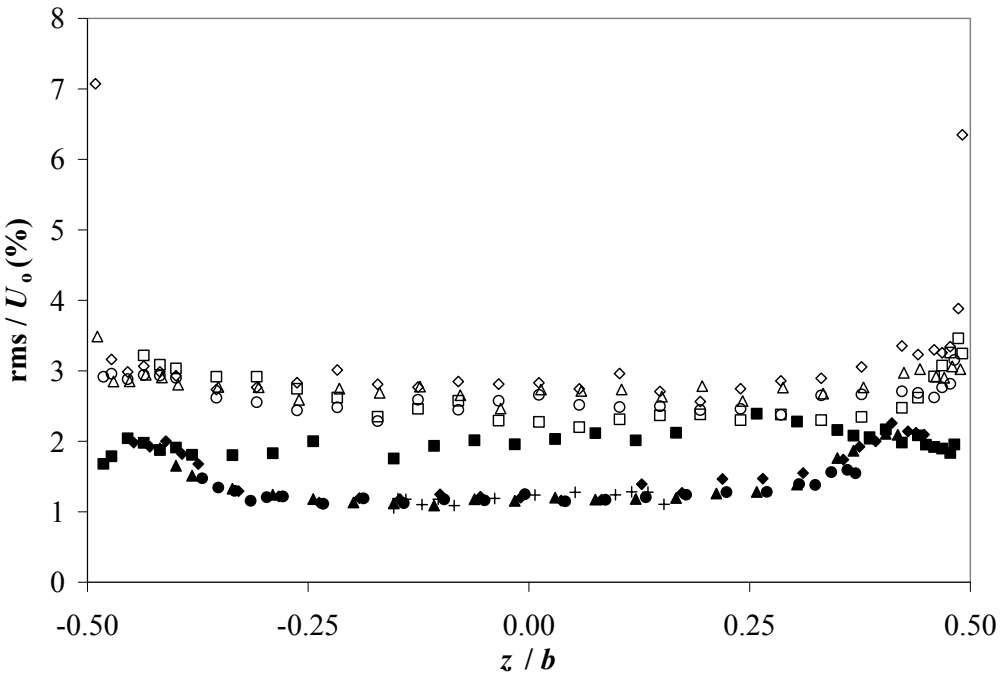

Figure 4.4. Rms velocity fluctuation profiles for Type I.A flow conditioning and Re = 53,000 and y / W_o = 0.1188 (+), 0.3688 (●), 0.4163 (▲), 0.4438 (◆), and 0.4838 (■). The open and closed symbols represent u' / U_o and w' / U_o, respectively.

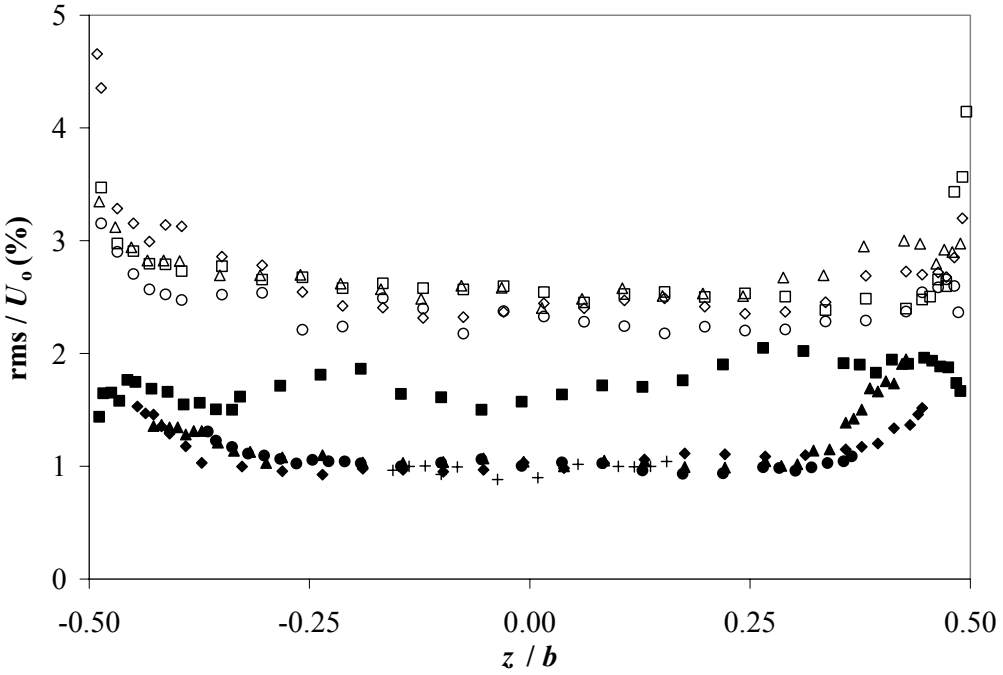

Figure 4.5. Rms velocity fluctuation profiles, similar to Figure 4.4, for Type I.A flow conditioning and Re =120,000.

The streamwise velocity fluctuations are on average approximately twice the transverse measurements. This result may be due to the acceleration of the flow in the streamwise direction, although some researchers have observed decreases in streamwise fluctuations through linear contractions (Parsheh *et al.*, 2005). Figure 4.6 shows the definition of a control volume inside the nozzle. Assuming uniform flow and making use of the Reynolds decomposition in the continuity equation gives the following relationship.

$$u(x,t) = \frac{A_{in}}{A(x)}\left(u_{in,avg} + u'(t)\right) \tag{4.1}$$

The streamwise mean and rms fluctuations of velocity both increase along the *x*-axis as the nozzle contracts. This relationship ignores any transfer of turbulent kinetic energy between velocity components. Koehler (2004) confirmed this behavior for the nozzle geometry studied here at multiple upstream locations inside the nozzle.

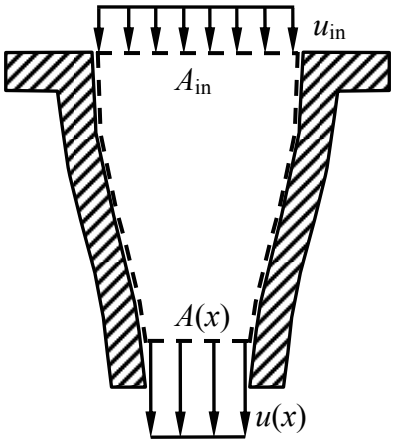

Figure 4.6. Definition of the nozzle control volume.

Similar to u_{avg}, spatially-averaged values of velocity fluctuations were calculated for u' and w' over the central 75% of the profile and are shown in Tables 4.1 and 4.2. The fluctuations of the x-component are all within the 95% confidence interval at all y-locations and both Reynolds numbers. The transverse measurements show some discrepancy with the values measured at Re = 120,000 slightly lower than those at Re = 53,000. The absolute values of w' are nevertheless greater at the higher Re.

Table 4.1. Streamwise and transverse rms fluctuations averaged over $|z/b| \leq 0.375$ for Type I.A flow conditioning and Re = 53,000.

y/W_o	u'_{avg}/U_o (%)	w'_{avg}/U_o (%)
0.4838	2.7	2.0
0.4438	2.8	1.4
0.4163	2.7	1.3
0.3688	2.5	1.3
0.1188	–	1.2
Average	2.7	1.4

Table 4.2. Streamwise and transverse rms fluctuations averaged over $|z/b| \leq 0.375$ for Type I.A flow conditioning and Re = 120,000.

y/W_o	u'_{avg}/U_o (%)	w'_{avg}/U_o (%)
0.4838	2.6	1.7
0.4438	2.5	1.0
0.4163	2.6	1.1
0.3688	2.3	1.1
0.1188	–	1.0
Average	2.5	1.2

The turbulent fluctuations near the walls are higher for both the *x*- and *z*-velocity components compared to the relatively constant central 75% of the flow. The regions of elevated fluctuation extend well beyond the boundary layer thickness δ_{BL} as determined from the streamwise velocity profiles, an effect that is particularly noticeable for w'. Averaging over profiles $y / W_o < 0.4838$, the transverse velocity fluctuations are $\geq 1.2 \cdot (w'_{avg} / U_o)$ for $|z / b| \geq 0.3806$ and 0.3898 at Re = 53,000 and 120,000, respectively. These marked transverse fluctuations may be due to the presence of vortex rings outside the boundary layer.

4.1.2 Effect of Flow Conditioning

Three flow conditioning configurations, Types I.A, I.N, and II.A,B, were used to determine the downstream influence of conditioning elements on velocity and rms fluctuations at the nozzle exit. The previous section dealt exclusively with the Type I.A configuration. Now, the influence of the fine screen(s) element is closely examined. The fine screen element in a flow conditioner is a critical feature; it is the last element the flow encounters and imposes the smallest scale on the turbulent structures that pass through the conditioner. Farrel and Youssef (1996) recommend the addition of a second screen for the optimal suppression of turbulence. This design is reflected by the Type II.A,B configuration. However, fine screens are also the most restrictive elements in the flow conditioner, introducing significant pressure drop and likely trapping debris. Removal of these elements would be attractive from a reactor design standpoint and is studied in the Type I.N configuration.

The pumping power required to drive the flow scales with the losses across the entire system; here, the flow conditioner / nozzle assembly is a significant source of loss.

The impact of adding screens to the flow conditioner was therefore experimentally quantified in terms of the loss coefficient across the flow conditioner / nozzle assembly $K_L = [2(\Delta P) + \rho U_{in}^2]/(\rho U_o^2)$, where ΔP is the pressure loss across the flow conditioner / nozzle, ρ is the fluid density, and U_{in} is the mean velocity at the inlet of the assembly. As expected, adding screens increases ΔP. Table 4.3 shows the pressure loss data and the corresponding loss coefficients at $Re = 1.2\times10^5$ for the three flow conditioning configurations studied here.

Table 4.3. Pressure loss coefficients across three different flow conditioning schemes for Re = 120,000.

Conditioning Type	**ΔP (kPa)**	**U_{in} (m/s)**	**U_o (m/s)**	**K_L**
I.N	69	2.35	10.72	1.25
I.A	103	2.36	10.75	1.84
II.A,B	121	2.38	10.84	2.11

Figures 4.7 and 4.8 show the mean velocity profiles at y / W_o = 0.3688 and 0.4438 for Re = 120,000 and flow conditioning Type I.A (▲), Type I.N (◆), and Type II.A,B (■). The open and closed symbols represent normalized values of u and w, respectively. These measurements are well outside the influence of the optical sidewall and indicate the bulk behavior of the flow. The streamwise measurements are nearly uniform and in good agreement with the volumetrically-averaged velocity for all flow conditioning schemes. Types I.A and II.A,B follow the linear regression established in the previous section for w. The magnitude of transverse velocity for Type I.N flow conditioning is slightly less than the regression away from z / b = 0.

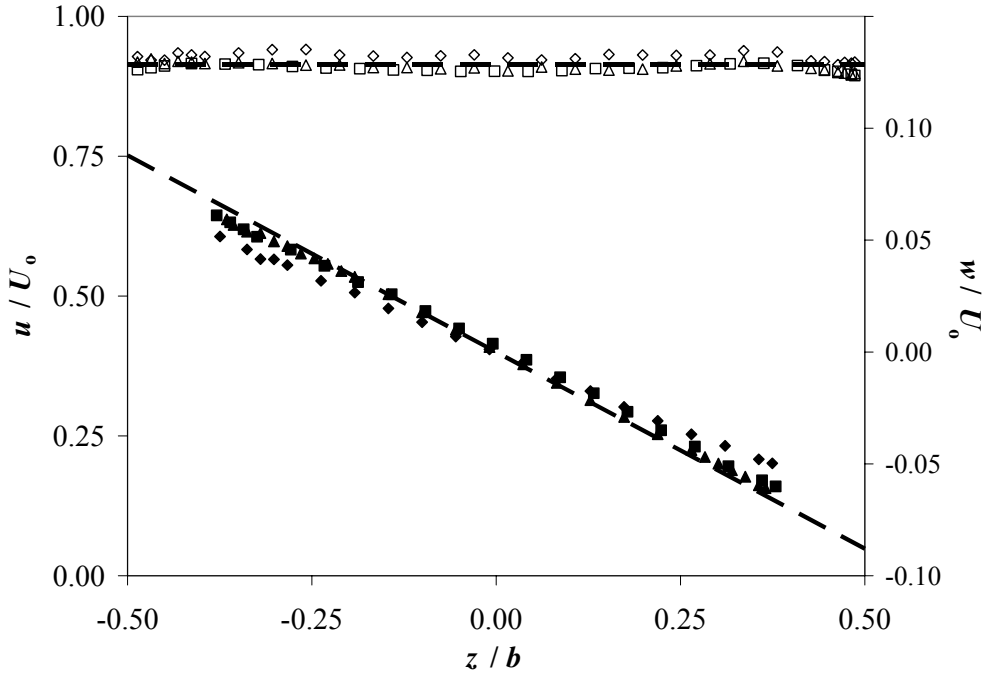

Figure 4.7. Mean velocity profiles at $y / W_o = 0.3688$ for $Re = 120{,}000$ and Type I.A (▲), Type I.N (◆), and Type II.A,B (■). The open and closed symbols represent u / U_o and w / U_o, respectively. Dashed lines indicate the expected velocity values.

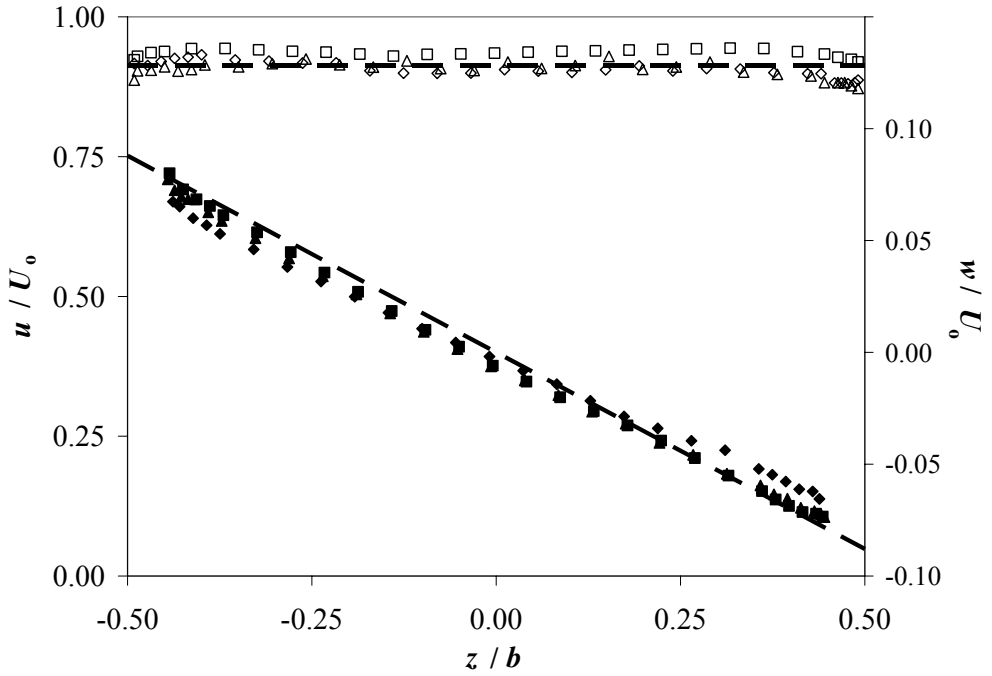

Figure 4.8. Mean velocity profiles, similar to Figure 4.7, at $y / W_o = 0.4438$.

Figure 4.9 shows the mean velocity profiles closest to the optical window at y / W_o = 0.4838 for the three flow conditioning configurations. These profiles are again similar to those in the previous Figures, except that the streamwise velocity profiles are slightly lower than the average velocity. Again, transverse measurements indicate a linear relationship for Types I.A and II.A,B, while the magnitude of transverse velocities for Type I.N are somewhat less than the regression.

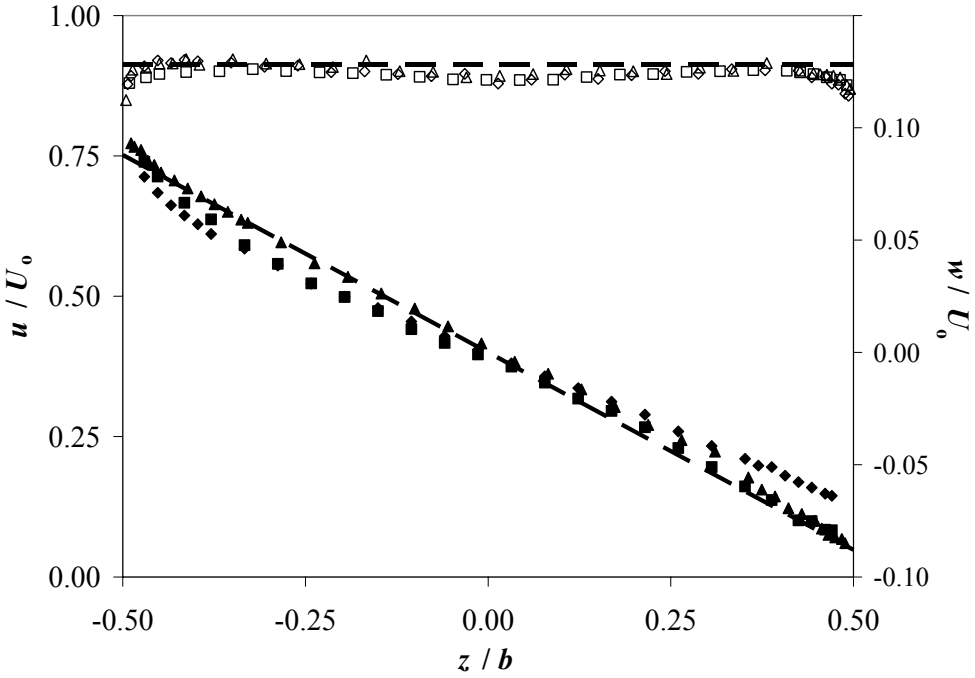

Figure 4.9. Mean velocity profiles, similar to Figure 4.7, at y / W_o = 0.4838.

Figures 4.10 through 4.12 show the rms fluctuations of the *x*- and *z*-velocity components for *Re* = 120,000 at y / W_o = 0.3688, 0.4438, and 0.4838, respectively. The open and closed symbols represent u' / U_o and w' / U_o, respectively. These profiles indicate that for $y / W_o < 0.4838$, or the bulk of the flow, the addition of fine screens to the

flow conditioner reduces streamwise velocity fluctuations. Streamwise turbulence is particularly decreased with the addition of the second fine screen in Type II.A,B flow conditioning, though the differences in u' between Type I.A and Type I.N configurations are within the 95% confidence interval of the data. The transverse fluctuations also lie within the 95% confidence interval, but the Type I.N configuration exhibits consistently higher rms values. In fact, a central disturbance characterized by a significant increase in w' was observed for $y / W_o \leq 0.1188$. The influence of the side wall in terms of increased transverse velocity fluctuations near the optical window at $y / W_o = 0.4838$ can be seen in Figure 4.12.

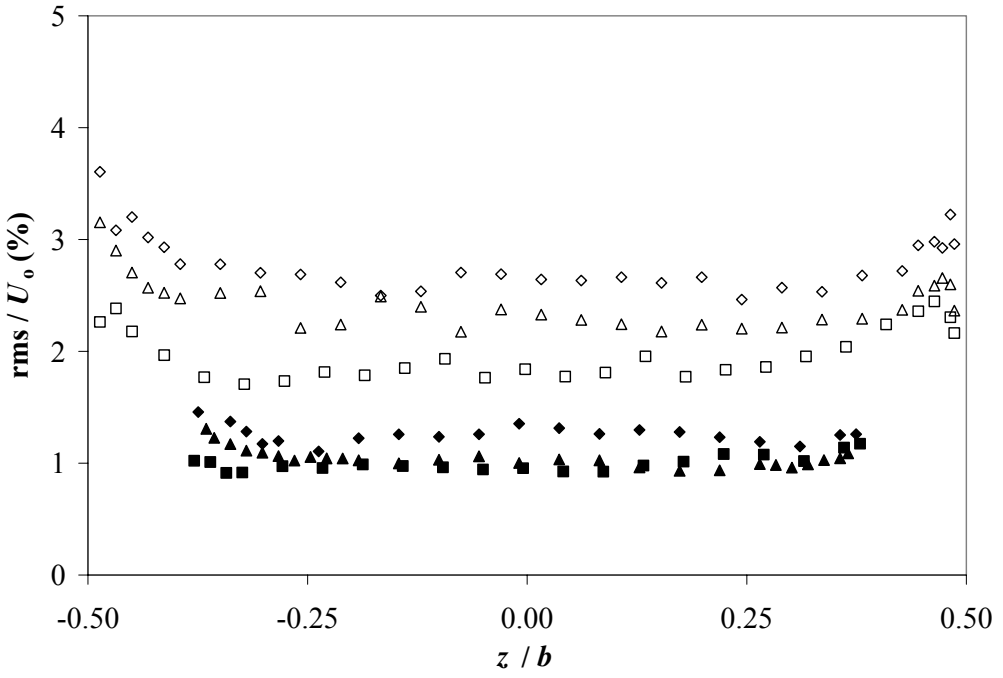

Figure 4.10. Rms velocity fluctuation profiles at $y / W_o = 0.3688$ for Re = 120,000 and Type I.A (▲), Type I.N (◆), and Type II.A,B (■). The open and closed symbols represent u' / U_o and w' / U_o, respectively.

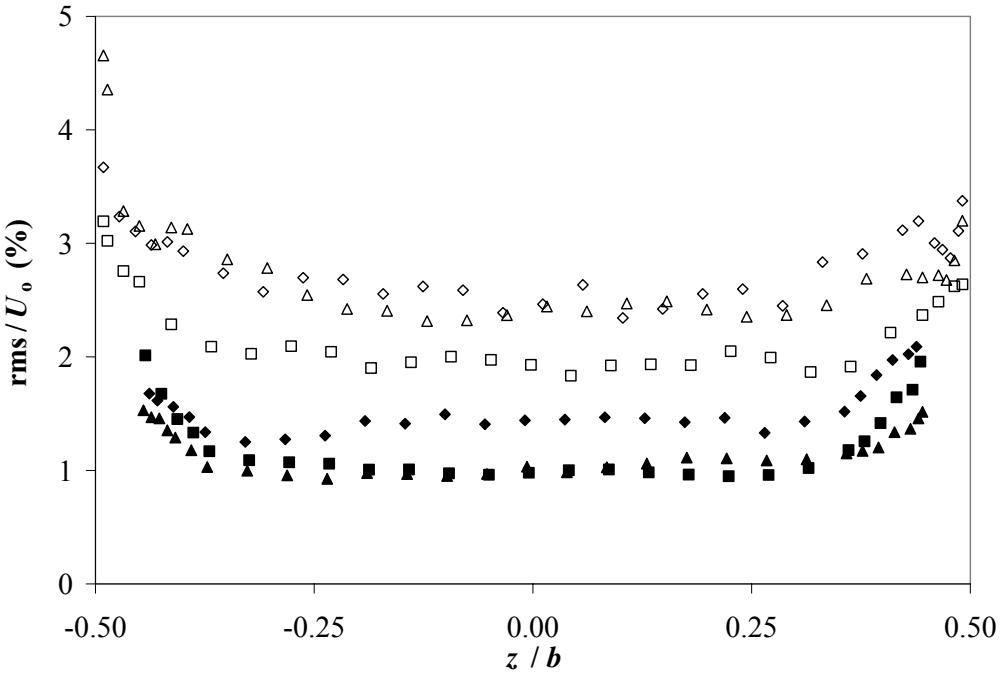

Figure 4.11. Rms velocity fluctuation profiles, similar to Figure 4.10, at $y / W_o = 0.4438$.

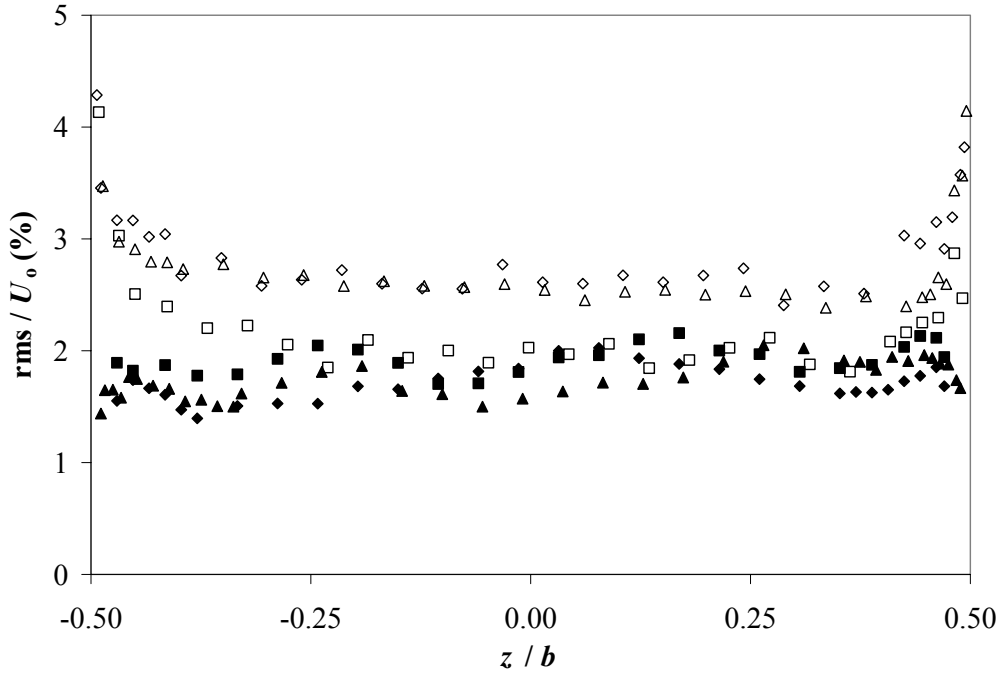

Figure 4.12. Rms velocity fluctuation profiles, similar to Figure 4.10, at $y / W_o = 0.4838$.

Figure 4.13 summarizes the effects of the different flow conditioning schemes on the centrally-averaged x- and z-component of rms velocity fluctuations as a function of y / W_o. As defined in the previous section, values of u'_{avg} and w'_{avg} are averaged over $|z / b| \leq 0.375$, or the central 75% of the profile. The addition of the second screen (FS-B) reduces overall streamwise rms fluctuations by no less than 0.6% of U_o. However, the presence or absence of a single screen (FS-A) has no experimentally measurable impact on the overall streamwise turbulent fluctuations of the flow. The resulting transverse fluctuations from flow conditioning Types I.A and II.A,B are identical within experimental error at all y / W_o. The case with no fine screen, Type I.N, demonstrates somewhat elevated values of w'_{avg}, particularly towards the center of the flow, or $y / W_o = 0$. These elevated levels of transverse turbulence are likely due to entrance effects associated with the abrupt geometry change (circular-to-rectangular) at the beginning of the flow conditioner. This central disturbance in the flow was observed in flow visualizations as well.

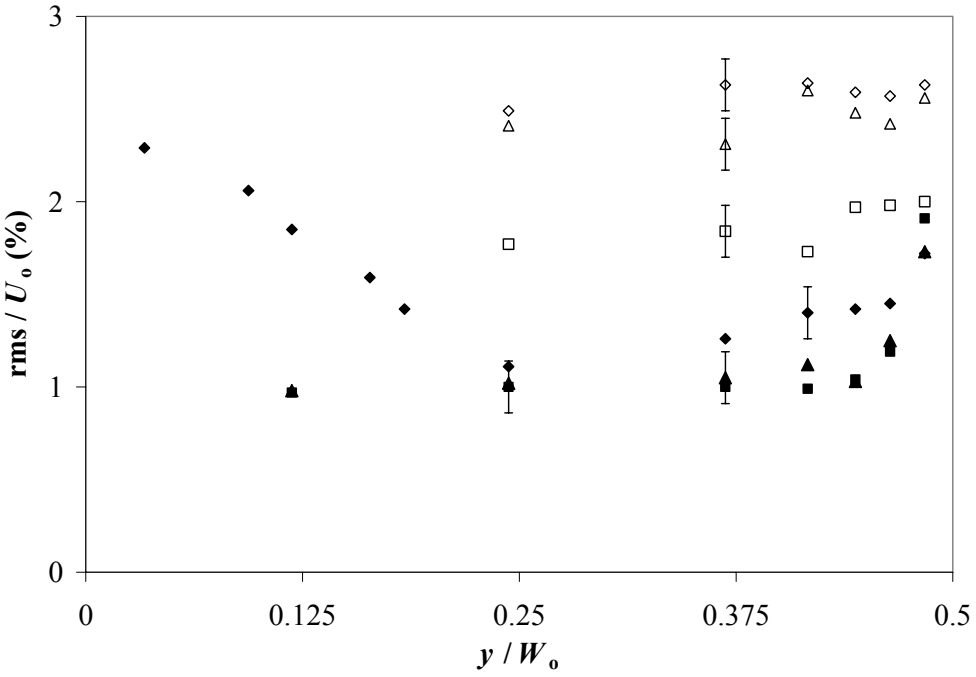

Figure 4.13. Rms velocity fluctuation profiles as a function of y / W_o for Re = 120,000 and Type I.A (▲), Type I.N (◆), and Type II.A,B (■). The open and closed symbols represent u'_{avg}/U_o and w'_{avg}/U_o, respectively.

4.2 PLIF Measurements

4.2.1 Effect of *Re*

The free surface was visualized up to $x / \delta = 25$ for Type I.A flow conditioning and Re = 53,000 and 120,000. The mean and rms of the z-position of the free surface were measured directly with the PLIF technique. Only one side of the jet was accessible for imaging given the nature of the PLIF technique, so these profiles depict the free-surface behavior of approximately half the liquid sheet. These mean free-surface profiles are presented here to demonstrate the geometric transition of the free surface. The mean position is reported as jet cross-sections versus downstream distance. The rms of

position, σ_z, is a measure of the free-surface fluctuations and is normalized by the nozzle exit thickness, δ.

Figure 4.14 shows the mean free surface for Re = 53,000 at downstream distances of x / δ = 5, 10, 15, 20, and 25. The vertical axis is magnified 5× with the scale bars in the upper left corner of the figure representing 1 cm in each direction. The sheet changes geometry significantly downstream of the imposed rectangular exit condition. The jet width decreases slightly with downstream distance due to surface tension forces and gravitational acceleration of the flow. The face of the jet is nearly flat (5× vertical magnification) with protrusions along the edges growing along the x-axis. The inner protrusions are wake structures emanating from the corners of the nozzle.

Half sheet cross-sections for Re = 120,000 as a function of downstream distance are shown in Figure 4.15. Optical dropout and high curvature at the edges limit the extent to which the mean free-surface profiles are accurate. The profiles are therefore truncated on the edges. Unlike Re = 53,000, the sheet width increases with downstream distance due to the jetting of "fingers" along the y-axis. This condition likely arises from the inwardly directed momentum imposed at the nozzle exit (4° contraction). A degree of asymmetry is noticeable from these composite profiles but is reasonable given the 5× magnification of the vertical axis. The center of the jet appears to "bulge" with noticeable curvature increasing downstream of the nozzle. Deformations in the nozzle up to 5% of δ, observed after these data were obtained, are likely the reason for this distortion of the free surface. This problem was avoided in subsequent investigations with the use of the redesigned nozzle and external clamping.

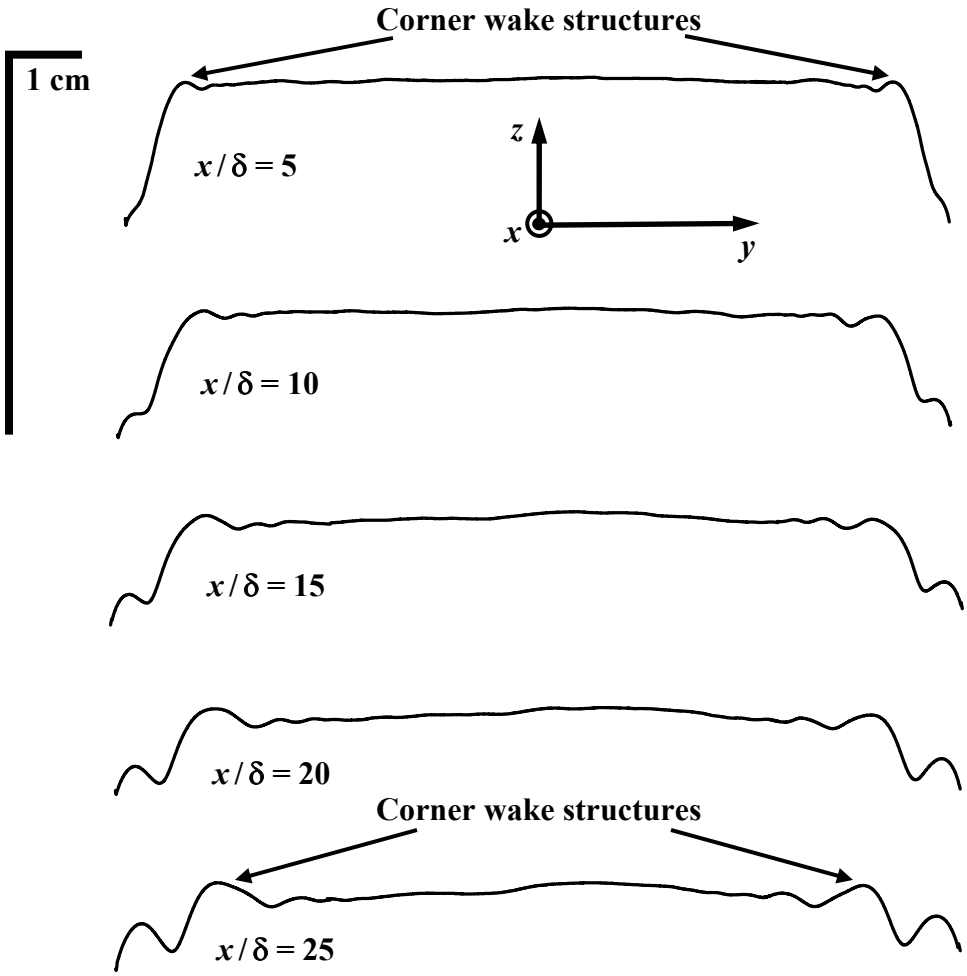

Figure 4.14. Free surface of the liquid sheet for *Re* = 53,000 at different downstream distances. Note: Flow is out of page and vertical axis is magnified 5×.

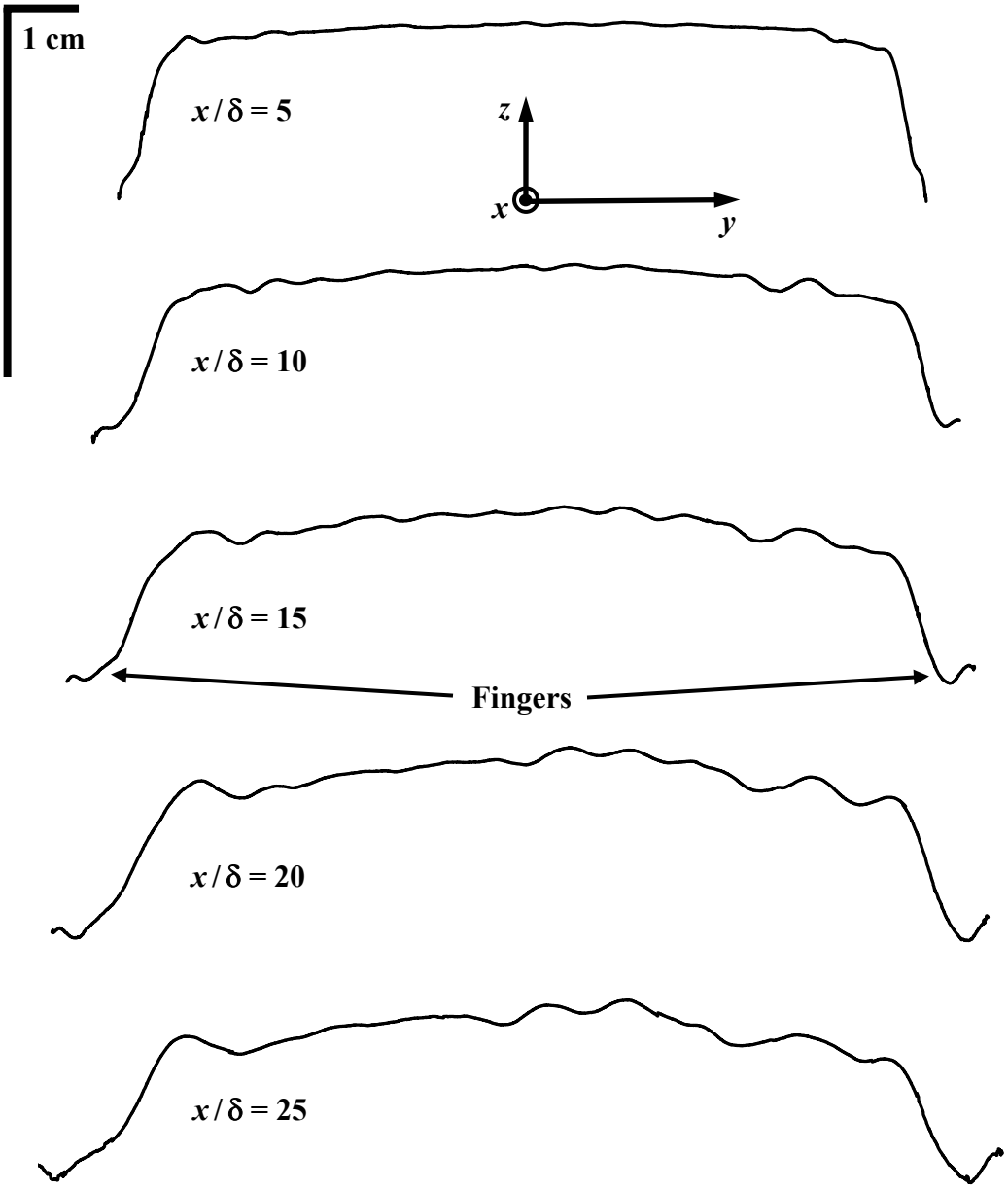

Figure 4.15. Free surface of the liquid sheet for *Re* = 120,000 at different downstream distances. Note: Flow is out of page and vertical axis is magnified 5×.

The rms fluctuations in the *z*-position of the free surface were calculated with respect to the *x*- and *y*-axes. Figure 4.16 plots the normalized free-surface fluctuations with respect to the *z*-axis for *Re* = 120,000 at $x / \delta = 25$. These results are typical of the

flow, with fluctuations relatively constant in the center of the sheet and sharply increasing near the edges of the sheet. This sharp increase corresponds to optical drop out of the sheet in the images.

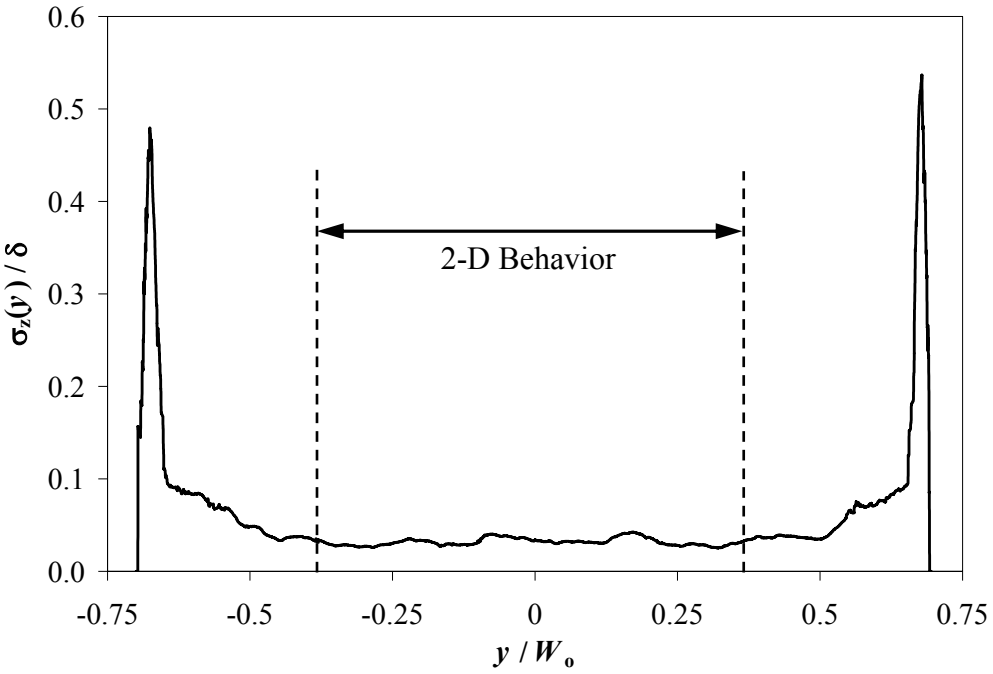

Figure 4.16. Normalized free-surface rms fluctuations as a function of y / W_o for x / δ = 25 and *Re* = 120,000. The jet exhibits nearly 2-D behavior in the region marked in the graph.

In order to compare fluctuation data, a spatial average was applied to the fluctuations for $| y / W_o | < 0.375$, *i.e.*, over the central 75 % of the original flow width. The behavior of the jet in this section was essentially constant, indicating 2-D behavior. Figure 4.17 shows the centrally-averaged σ_z / δ data for *Re* = 53,000 (gray) and 120,000 (black) as a function of x / δ. The fluctuations increase in a linear manner with downstream distance. Although the normalized streamwise and transverse velocity

fluctuations were comparable for both Reynolds numbers, surface ripple increases with *Re*.

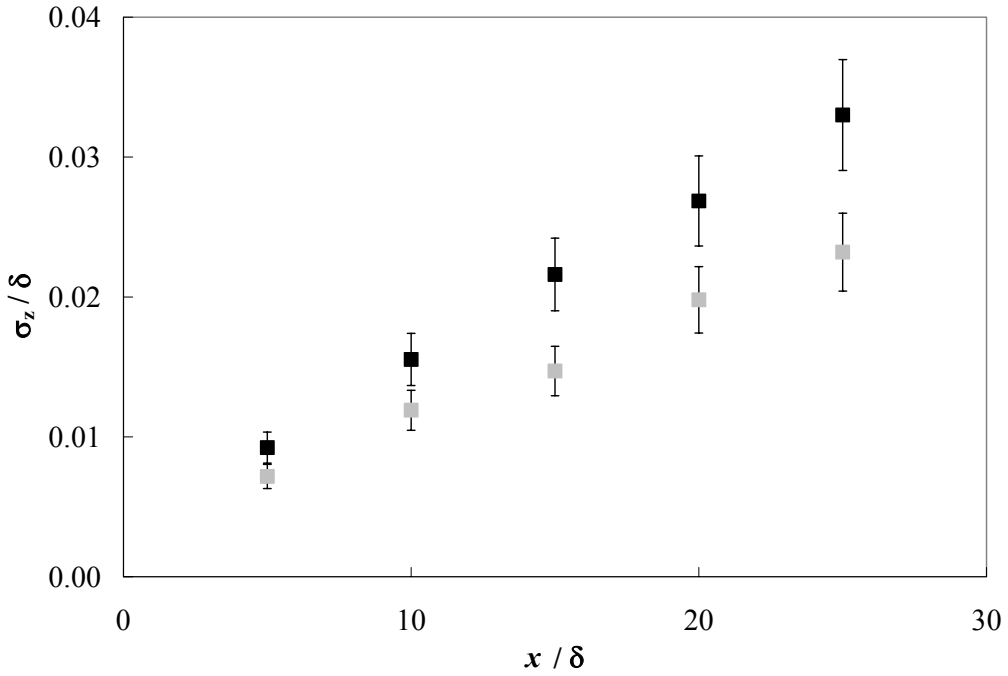

Figure 4.17. Graph of σ_z / δ *vs.* x / δ for *Re* = 53,000 (gray) and 120,000 (black).

4.2.2 Effect of Flow Conditioning

Flow conditioning was altered by the insertion and removal of fine screens. Type I and II flow conditioning are capable of holding one and two fine screens, respectively. The fine screens used in these investigations are described in Table 3.3. The Type I.A configuration was the standard design and studied extensively in the previous section. The following discussion will focus on flow conditioning for which the initial conditions were quantified, namely Types I.A, I.N, and II.A,B. In addition, a summary of PLIF results at $x / \delta = 25$ for all flow conditioning configurations is also presented.

The free surface profiles at $x / \delta = 25$ for flow conditioning Types I.A, I.N, and II.A,B are shown in Figure 4.18. The nozzle exit (dashed lines) and center line (about the *y*-axis) are indicated in the profiles. These flows were produced with the redesigned nozzle and external clamping to avoid elastic deformation of the nozzle under flow conditions. The three flow conditioning configurations produced flows with relatively similar free surfaces. The *z*-extent of the jet is always inside the original nozzle exit with "fingers" jetting outward in the *y*-direction. The width of the jet is within ±1 mm for the three types of flow conditioning. Type I.N shows a central "bulge" in the flow extending towards the nozzle exit. The asymmetry of the bulge is likely due to secondary flows generated at the turning elbows upstream. This feature corresponds to a central disturbance of the flow, which was observed in the transverse velocity fluctuations and is discussed next.

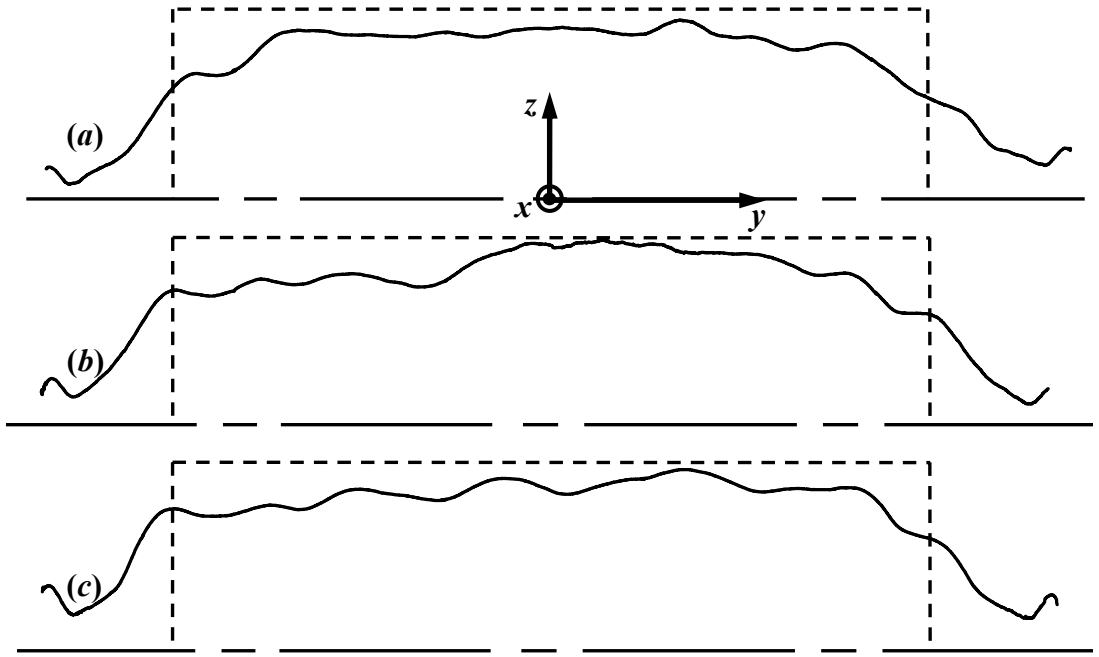

Figure 4.18. Free surface profiles at $x / \delta = 25$ for Re = 120,000 and flow conditioning (*a*) Type I.A, (*b*) Type I.N, and (*c*) Type II.A,B. Dashed lines indicate the nozzle exit. Note: Flow is out of page and vertical axis is magnified 5×.

Figure 4.19 shows the normalized surface ripple for Type I.N (gray) and Type I.A (black) *vs.* y / W_o at $x / \delta = 25$ and Re = 120,000. A large central peak in free-surface fluctuations is evident for flow conditioning Type I.N. This central disturbance in the flow was also observed in the transverse velocity rms fluctuations and to a certain degree in the mean free-surface profile. The sharp transition from round-to-rectangular at the beginning of the flow conditioner is likely the source of the increased flow fluctuations, which survive the perforated plate and honeycomb elements. The addition of the screen to the flow conditioner acts to damp the downstream impact of the sudden contraction and eliminates any "flow memory" of entry into the calming chamber. A tailored inlet transition may also improve this condition but was not explored.

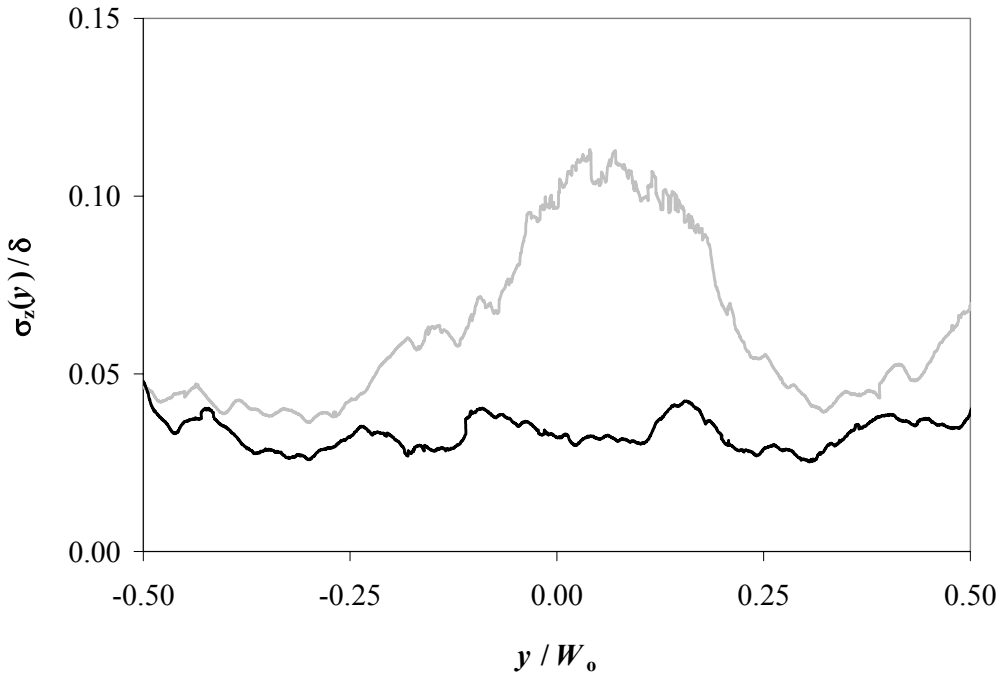

Figure 4.19. Normalized free-surface rms fluctuations for flow conditioning Type I.N (gray) and Type I.A (black) *vs.* y / W_o at $x / \delta = 25$ and Re = 120,000. Note the central peak in fluctuations for Type I.N flow conditioning.

Figure 4.20 plots the centrally-averaged free-surface standard deviation as a function of downstream distance for Re = 53,000 (gray) and 120,000 (black) and flow conditioning Type I.A (▲), Type I.N (◆), and Type II.A,B (■). Flow conditioning without a fine screen (Type I.N) exhibited the highest levels of free-surface fluctuation at Re = 120,000, due to the central disturbance discussed earlier. Velocity rms fluctuations at Re = 120,000 for Type I.A and II.A,B were comparable in the z-component but significantly higher in the x-component for Type I.A conditioning. However, measurements of surface ripple for Type I.A and II.A,B conditioning were within experimental uncertainty at Re = 120,000, although Type II.A,B was consistently higher. Velocity fluctuations at Re = 53,000 demonstrated similar trends (comparable w', higher

u') for Type I.A compared to Type II.A,B, but the resulting free-surface fluctuations were significantly higher for Type II.A,B. Moderate increases in streamwise turbulence may actually provide a stabilizing effect by increasing the turbulent viscosity, whereas strong transverse turbulent fluctuations translate to increased free-surface fluctuations.

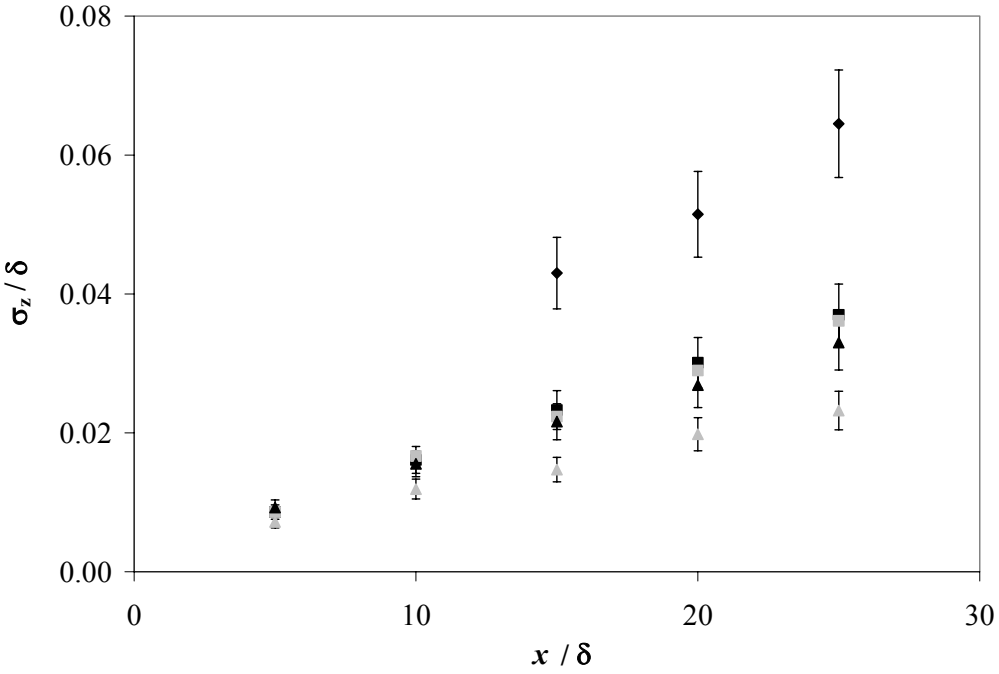

Figure 4.20. Graph of σ_z / δ *vs.* x / δ for *Re* = 53,000 (gray) and 120,000 (black) and flow conditioning Type I.A (▲), Type I.N (◆), and Type II.A,B (■).

Figure 4.21 shows the average (black) and fluctuations corresponding to one standard deviation (gray) of the free surface for the Type I.A and Type I.N flow conditioning at $x / \delta = 25$. A beam-to-jet standoff of 0.07δ is indicated by the dotted lines in the plots. The *z*-position of the sheet produced with Type I.A conditioning is nearly inside the original nozzle exit at all *y*-locations and meets the proposed standoff distance.

The central disturbance of the Type I.N conditioning is again evident with the surface ripple entering the beam pathline.

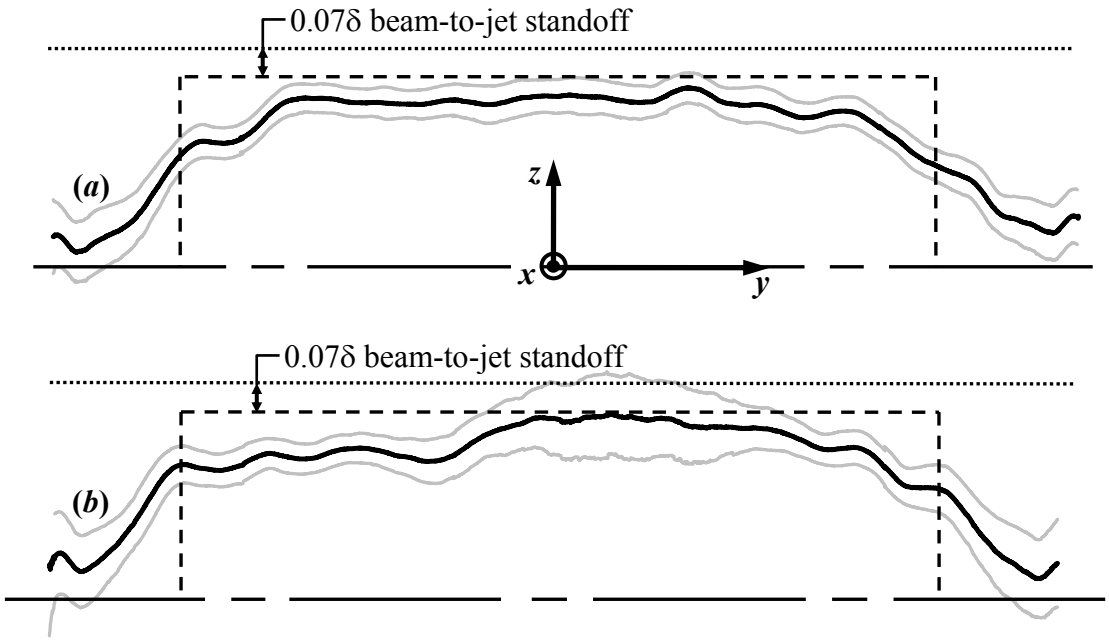

Figure 4.21. Plot showing the average (black) and ± 1·σ_z fluctuations (gray) of the sheet free surface for (*a*) Type I.A and (*b*) Type I.N flow conditioning at $x / \delta = 25$. The recommended 0.07δ beam-to-jet standoff of Latkowski and Meier (2001) is superimposed for each case.

The centrally-averaged standard deviation, σ_z, is plotted in Figure 4.22 for all flow conditioning configurations at the farthest downstream location $x / \delta = 25$ with *Re* = 53,000 (gray) and 120,000 (black). The standard configuration, Type I.A, exhibited the lowest free-surface fluctuations at both Reynolds numbers. The roughest flows were produced by flow conditioning without any screen, Type I.N. The case of Type II.N,A suggests the spacing between the honeycomb element and the fine screen are important to the optimization of flow conditioning. The addition of a second screen did not improve

surface ripple; indeed, the free surface fluctuated more as compared to flows produced with the "standard" Type I.A conditioning.

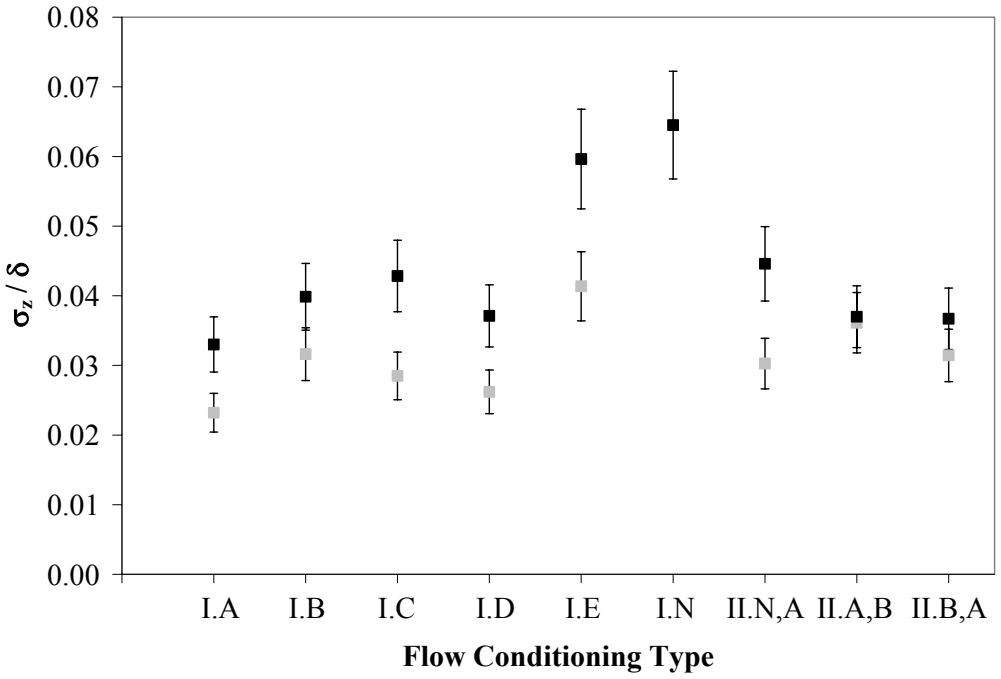

Figure 4.22. Surface ripple of the free surface at $x / \delta = 25$ for different flow conditioning configurations with Re = 53,000 (gray) and 120,000 (black).

The influence of screen design in Type I flow conditioning is shown in Figure 4.23. The surface ripple is plotted as a function of the wire diameter (d_{wire}) of the fine screen at $x / \delta = 25$ and Re = 53,000 (gray) and 120,000 (black). The case for $d_{wire} = 0$ at Re = 120,000 corresponds to Type I.N flow conditioning. The free-surface fluctuations tend to decrease with increasing wire diameter. The screens in these studies operated well above the critical wire-based Reynolds number of Re_{cr} = 30-70, *i.e.* in the supercritical regime (Shubauer *et al.*, 1950). In fact, fine screens "A" and "B" both produced an audible pitch at Re = 120,000, probably due to shedding from the mesh

wires of von Karmen vortex streets in the auditory range. Indeed, the frequency predicted from a shedding analysis of a cylinder with a diameter of 0.33 mm (FS-A) gives a shedding frequency of 6.2 kHz. Since the turbulence spectrum of the flow was not resolved with the LDV, the impact of this "singing" condition on the flow is unknown.

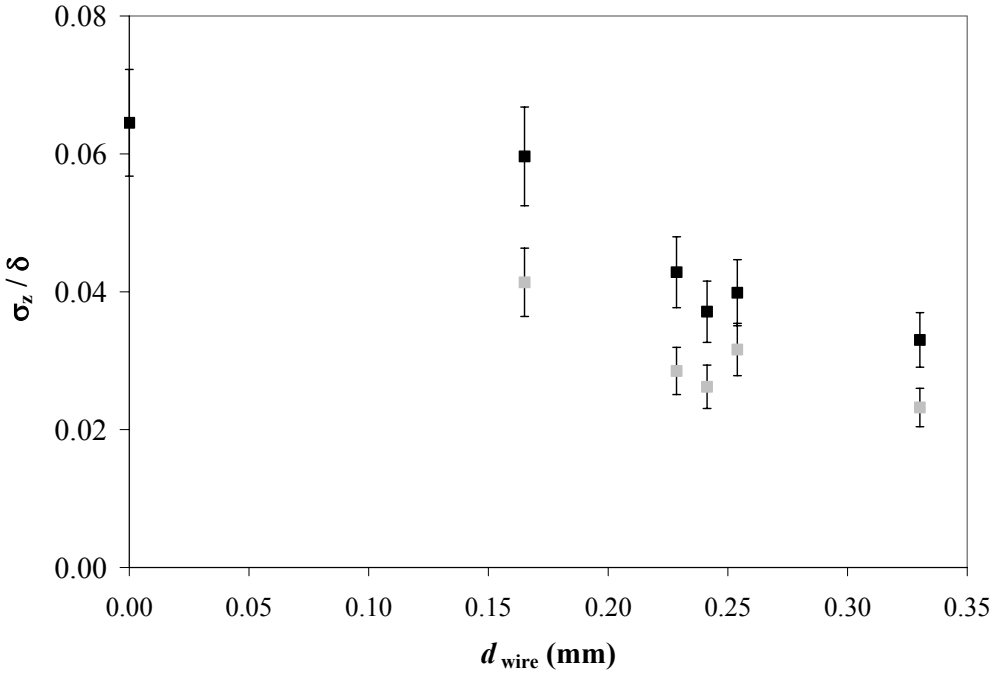

Figure 4.23. Surface ripple *vs.* the wire diameter of fine screen for Type I flow conditioning at $x / \delta = 25$ and $Re = 53{,}000$ (gray) and 120,000 (black).

4.2.3 Effect of Boundary-Layer Cutting

The effect of boundary-layer cutting on the free surface was evaluated at $Re = 120{,}000$. The free surface was visualized at $x / \delta = 15$, 20, and 25 for Type I.A flow conditioning. The mean and rms of the z-position of the free surface were measured directly with the PLIF technique. A range of different levels of BL cutting ranging

from $\dot{m}_{cut} / \dot{m}_{fl}$ = 0 to 1.9% ($\dot{m}_{cut}$ is the diverted mass flow rate)—were evaluated for the highest jet mass flow rate, $\dot{m}_{fl}$ = 10.82 kg/s.

Figure 4.24 shows the amount of fluid cut from one side of the free surface as a function of cut depth for two calibration data sets. The cut depth was measured from the downstream location of the inner nozzle wall. Uncertainty in the cut depth (estimated here to be ~ 0.05 mm) is clearly reflected in the two trials. The flow rate data follow a nearly linear relationship (thus confirming uniform exit velocity) with a non-zero intercept. Possible reasons for the non-zero intercept include inaccuracies in the *z*-stage lead screw and/or the actual free surface of the jet lying inside the original *z*-location of the jet. Since the cut depth proved difficult to reproduce, the fractional cut in mass flow rate was chosen to match between experiments for reasons of repeatability.

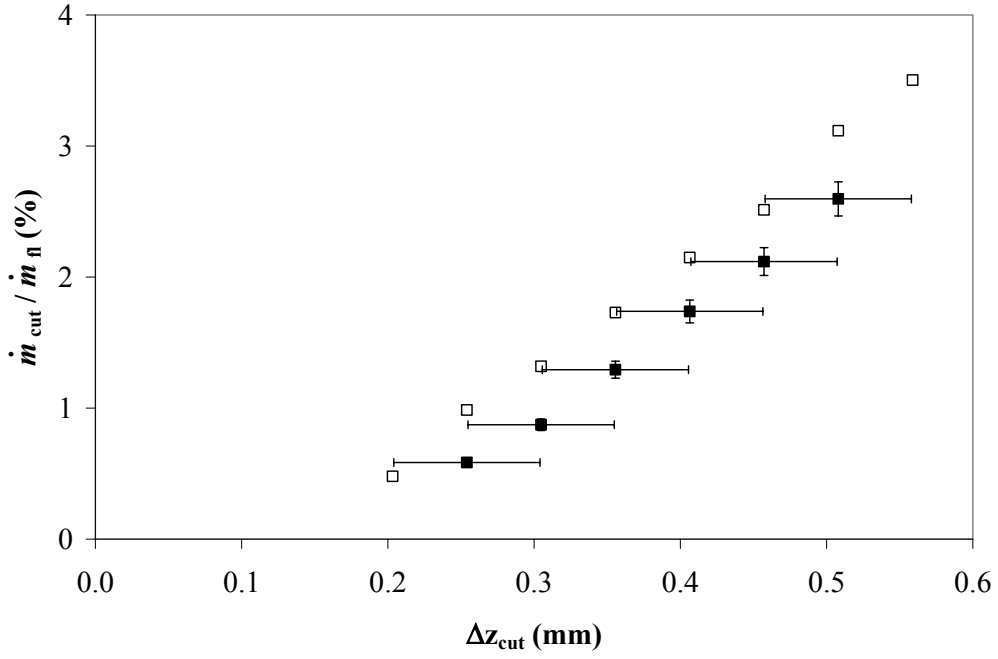

Figure 4.24. Normalized cut flow rate as a function of cut depth, Δz_{cut}. Two calibration data sets obtained 8 weeks apart are shown, Trial 1 (open) and Trial 2 (closed).

Figure 4.25 gives the mean free-surface profiles for sheets with various levels of BL cutting at Re =120,000 and x/δ =25. The free surface is altered significantly by the introduction of the cutter blade to the flow, depicted by the case of $\dot{m}_{cut}/\dot{m}_{fl}$ = 0.0%. The protrusions near the original nozzle corners are a result of wake from the interface of the sheet and the blade. Similar corner wake structures were observed at Re = 53,000 (*cf.* Figure 4.14). Between these structures, the free surface of flows with BL cutting is further inside the original nozzle exit compared to flow without cutting. Also, the y-extent of the "cut" jet was less than that for the "uncut" flow at all downstream locations due to the sheet being confined in the y-axis by its attachment to the cutter blade; at x/δ = 25, this difference in the y-dimension was about 0.6 cm for all cut rates. These changes to the free surface are possibly due to removing fluid from only one side of the sheet, but BL cutting may re-introduce the corner wake structures even with symmetric fluid removal.

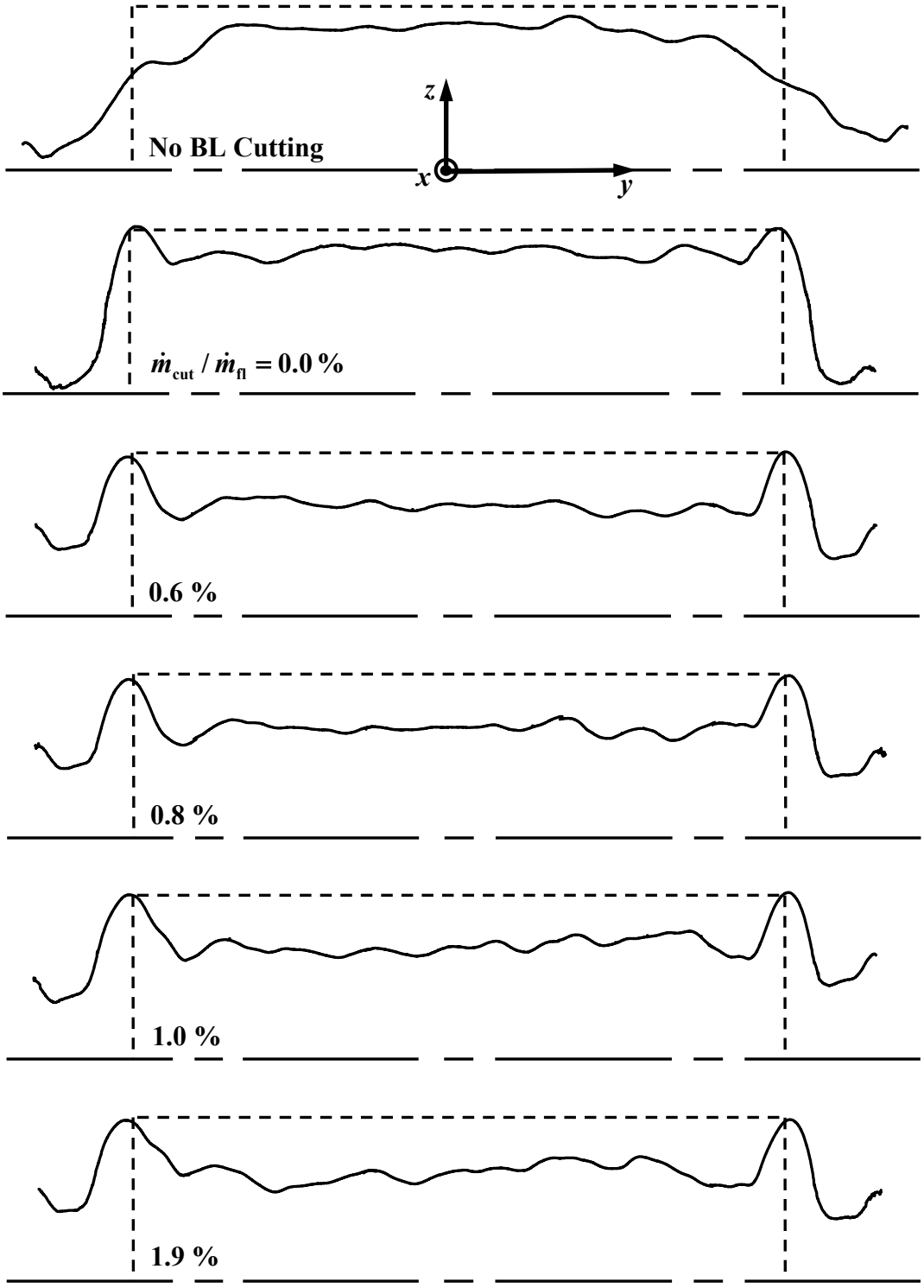

Figure 4.25. Free-surface profiles at $x / \delta = 25$ for Re =120,000 and BL cutting ranging from 0.0–1.9 %. Dashed lines indicate the nozzle exit. Note: Flow is out of page and vertical axis is magnified 5×.

Figure 4.26 shows the impact of BL cutting on the centrally-averaged free-surface fluctuations at x / δ = 15 (▲), 20 (◆), and 25 (■). Surface ripple decreases at all downstream locations as $\dot{m}_{cut} / \dot{m}_{fl}$ increases; σ_z is reduced significantly even at BL cutting levels as low as $\dot{m}_{cut} / \dot{m}_{fl}$ = 0.6%. Increasing $\dot{m}_{cut} / \dot{m}_{fl}$ provides diminishing improvements in surface smoothness. The normalized surface ripple at x / δ = 25 is 0.0317 and 0.0295 for $\dot{m}_{cut} / \dot{m}_{fl}$ = 0.6 and 1.9%, respectively. This behavior indicates the edge of the cutter blade is positioned in the bulk of the flow for even the lowest removal rate.

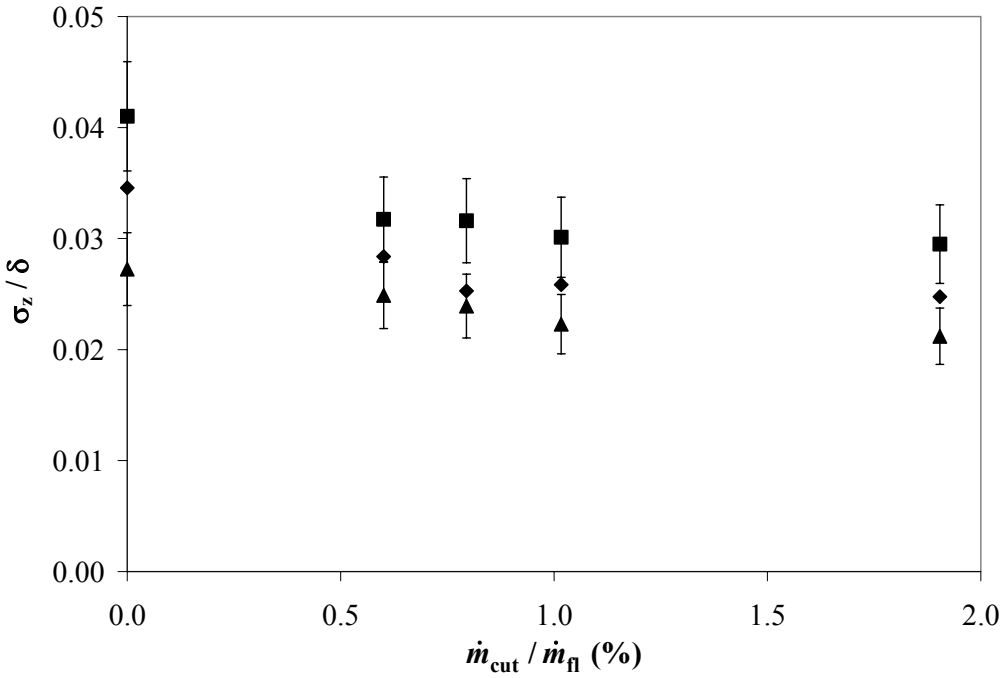

Figure 4.26. Graph of σ_z / δ *vs.* $\dot{m}_{cut} / \dot{m}_{fl}$ at x / δ = 15 (▲), 20 (◆), and 25 (■).

Finally, the relative impact of BL cutting and "traditional" flow conditioning elements on the free-surface smoothness was examined. Figure 4.27 shows the centrally-

averaged standard deviation of the free surface for flow conditioning Type I.N (gray) and Type I.A (black) with symbols indicating no BL cutting (closed) and $\dot{m}_{cut} / \dot{m}_{fl}$ = 1.9% (open). Removing 1.9% of the overall mass flow rate from the surface reduced σ_z on average by about 33% and 10% for Type I.A and Type I.N configurations, respectively. In the absence of BL cutting, the standard deviation of the Type I.A configuration was about 67% lower than that for the Type I.N configuration. BL cutting clearly reduces surface ripple, but the fine screen has a larger overall impact on free-surface smoothness. BL cutting is less effective in Type I.N conditioning because the central disturbance observed in transverse velocity fluctuations extends into the center of the jet, beyond the range of the cutter blade.

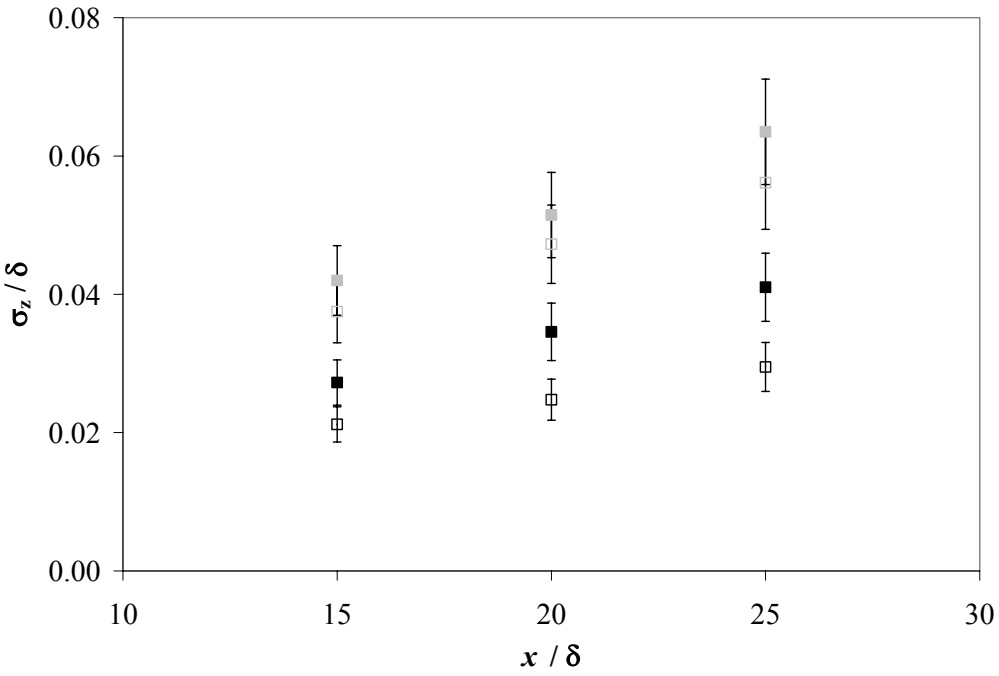

Figure 4.27. Graph of σ_z / δ *vs.* x / δ for flow conditioning Type I.N (gray) and Type I.A (black). Symbols indicate no cutting (closed) and $\dot{m}_{cut} / \dot{m}_{fl}$ = 1.9% (open).

4.3 Mass Collection Measurements

4.3.1 Effect of Initial Conditions

Turbulent breakup of the liquid sheet was studied at $x / \delta = 25$ for Re = 120,000 and We = 19,000. Figure 4.28 gives the normalized collected mass rate (left axis) and resulting equivalent number density (right axis) as a function of cuvette standoff distance, Δz_s, for Type I.A (black) and Type I.N (gray) flow conditioning at $\dot{m}_{cut} / \dot{m}_{fl}$ = 0 (■), 1.0 (◆), and 1.9% (▲). The proposed beam-to-jet standoff is shown in the graph in gray. Any droplets to the right of this limit could attenuate the driver beam. The background density of the HYLIFE-II chamber (5×10^{19} m^{-3}) is also shown in the graph (Moir, 2001). The density of drops due to turbulent breakup at the jet free surface increases as Δz_s decreases. Not surprisingly, there are more drops near the source of breakup, namely the jet surface. Note that any measurement below the sensitivity limit indicates a collected mass of zero within experimental error. Secondary effects such as aerodynamic shear, drop re-entrainment, and evaporation limit the spatial distances over which drops can be detected or collected. Approaching the jet, N should therefore increase from zero at a sufficiently large standoff value with a sharp increase as the free surface. Confidence intervals for these data are estimated to be within ±42% of the measurement.

BL cutting reduces the primary turbulent breakup; a marked reduction in breakup is already observed for the Type I.A configuration at a cut rate of 1.0% over all standoff distances. Moreover, breakup is completely suppressed at $\dot{m}_{cut} / \dot{m}_{fl}$ = 1.9%. For the Type I.N configuration, breakup is observed farther from the nominal free surface. In addition, BL cutting appears to have less impact on the Type I.N configuration, with smaller reductions in breakup compared with the Type I.A cases. The dominant impact

of the fine screen seen here is consistent with the trends observed in the PLIF data; in all cases, the (absence of the) fine screen has a much more significant impact upon jet quality than BL cutting. The elevated transverse velocity fluctuations observed at the nozzle exit for Type I.N flow conditioning appear to be directly related to both increased free-surface fluctuations and increased turbulent breakup.

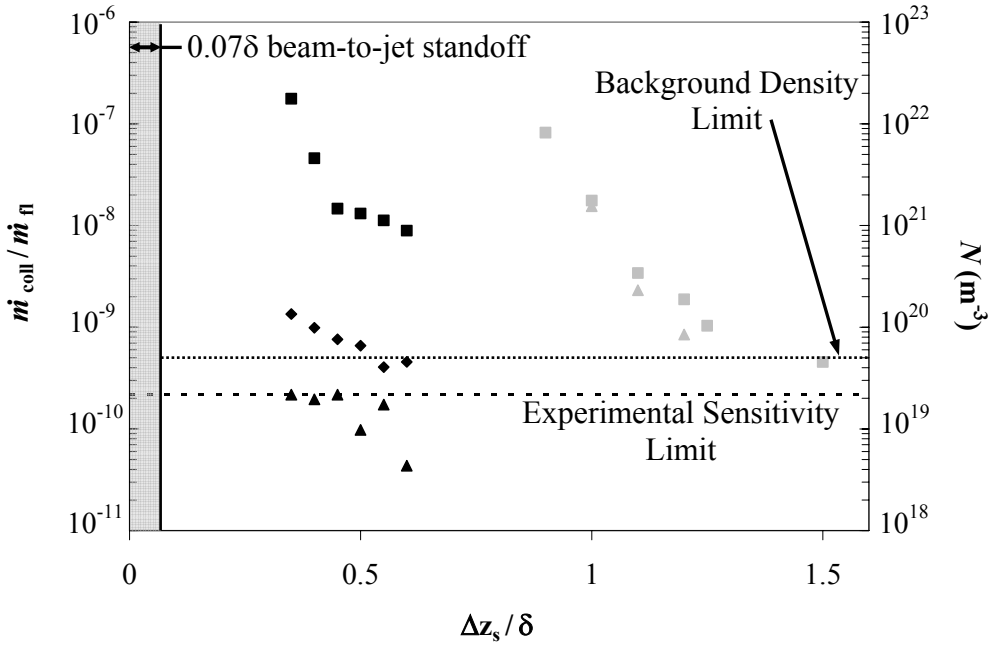

Figure 4.28. Normalized collected mass rate and the resulting equivalent number density *vs.* $\Delta z_s / \delta$ for Type I.A (black) and Type I.N (gray) configurations with $\dot{m}_{cut} / \dot{m}_{fl}$ = 0.0% (■), 1.0% (◆), and 1.9% (▲).

Given the simple nature of these mass collection experiments, these results are presented only as a relative measure of the impact of initial conditions on the turbulent breakup of a liquid sheet. In this context, the capability of BL cutting to reduce or even eliminate breakup was clearly demonstrated, consistent with the findings of Wu *et. al*

(1995). The relationship between elevated free-surface fluctuations and breakup are also reinforced.

4.3.2 Droplet Visualizations

Droplet visualizations were performed for the cases of Type I.A and Type I.N flow conditioning at a downstream distance of $x / \delta = 25$ (Figure 4.29). These images indicate droplet sizes are on the order of 1 – 100 μm. The maximum observed droplet diameter is greater for the Type I.N configuration. Although not quantified, the mean droplet diameter appears to also be greater for Type I.N conditioning. However, the number of droplets observed in the field of view is greater for the Type I.A configuration. These observations indicate the scale of breakup is "finer" for flows produced with the fine screen.

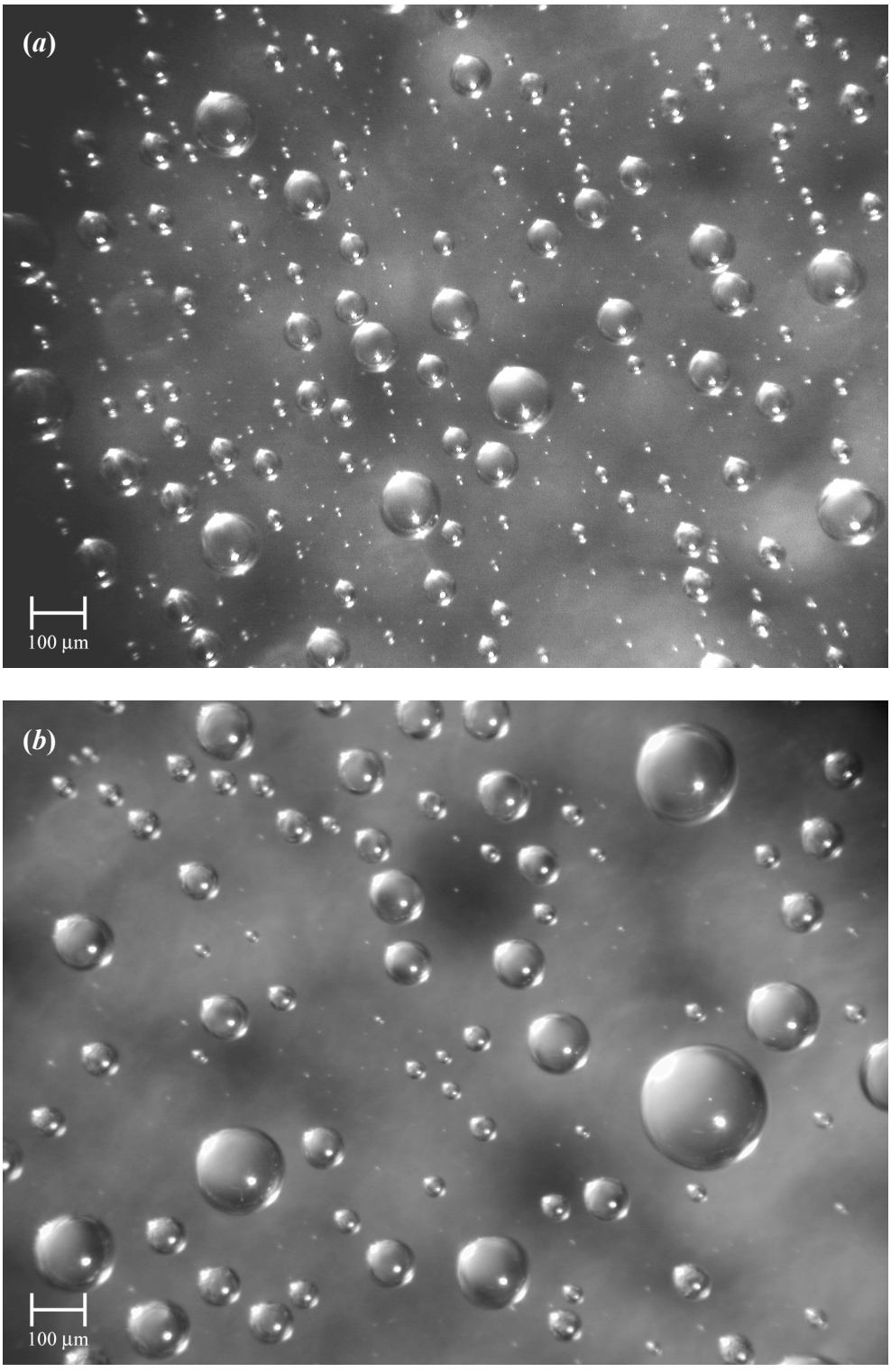

Figure 4.29. Droplets collected from jet with (*a*) Type I.A and (*b*) Type I.N flow conditioning at $x / \delta = 25$. Scale in lower left corner represents 100 μm.

4.3.3 Comparison to Correlations

The breakup correlations of Sallam *et al.* (2002) were applied to a turbulent liquid sheet matching the experimental Weber number. Model predictions of Sauter mean diameter (SMD) range from 0.6 to 2.1 mm for downstream distances of x / δ from 3.7 to 25, respectively. The observed droplets were considerably smaller, even considering losses due to evaporation. The droplets from a conditioned jet are understandably smaller, since the turbulent energy has been forced to smaller scales via the flow conditioner.

Next, the ratio of the mass flux from the experiments and correlations is shown as a function of standoff distance in Figure 4.30 for Type I.N (gray) and Type I.A (black) flow conditioner configurations at $\dot{m}_{cut} / \dot{m}_{fl}$ = 0.0% (■), 1.0% (◆), and 1.9% (▲). See Appendix A for details on the calculation of the correlation mass flux. Based upon these results, flow conditioning and a contracting nozzle already reduce the mass flux by 3–5 orders of magnitude. Since the experimental conditions in these studies are not identical to those used to establish the correlations, reductions in breakup with respect to the correlations should be considered qualitative. Nevertheless, this discrepancy again demonstrates the sensitivity of these types of flows to initial conditions.

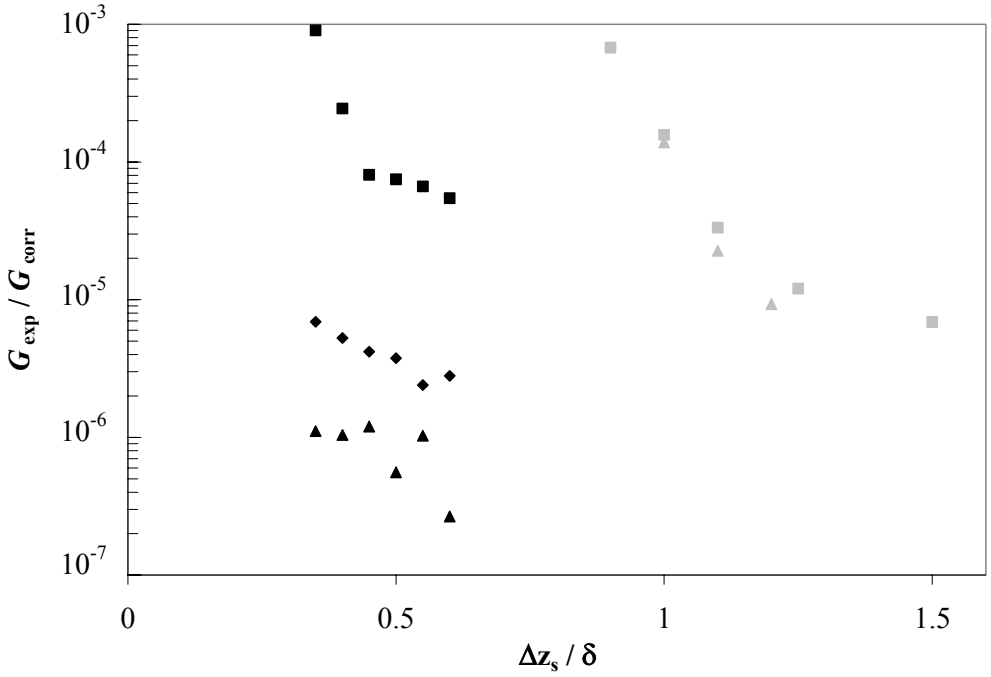

Figure 4.30. G_{exp} / G_{corr} *vs.* Δz_s / δ for Type I.A (black) and Type I.N (gray) flow conditioner configurations at $\dot{m}_{cut}$ / $\dot{m}_{fl}$ = 0.0% (■), 1.0% (◆), and 1.9% (▲).

CHAPTER 5

CONCLUSIONS AND RECOMMENDATIONS

The purpose of this investigation is to examine the effect of initial conditions, defined by velocity profiles near the nozzle exit, on the downstream dynamics of turbulent liquid sheets. These initial conditions, free-surface behavior, and turbulent breakup of water sheets issuing into ambient air were studied experimentally at the Georgia Tech Large-Scale Test Facility. Initial conditions were modified upstream of the forming nozzle using different combinations of fine screen elements in the flow conditioner and just downstream of the nozzle with various levels of boundary-layer cutting. The resulting free-surface profiles and fluctuations were quantified in the near-field $x / \delta \leq 25$. In addition, the breakup of the sheet was measured in terms of the collected mass of ejected drops as a function of standoff distance from the nominal free surface. Data were collected for turbulent sheets with average nozzle exit velocities of 5.21 and 10.85 m/s corresponding to Reynolds numbers of $Re = 5.3 \times 10^4$ and 1.2×10^5, respectively.

5.1 Conclusions

The conclusions derived from the data are presented in the following section. The conclusions are grouped according to the type of data obtained, namely, mean and rms

velocity profiles characterizing initial conditions, free-surface profiles and fluctuations, and mass collection of turbulent primary breakup.

5.1.1 Initial Conditions

5.1.1.1 Effect of *Re*

Normalized mean streamwise and transverse velocity profiles for Type I.A flow conditioning were independent of Reynolds number. As shown in Appendix C, this trend was also observed for Types I.N and II.A,B flow conditioning. In all cases, the streamwise velocities were nearly uniform in the bulk flow with values within ±3.5% of the volumetrically-averaged velocity u_{avg}. The boundary layer δ_{BL}, determined based upon a criterion of $0.95 \cdot u_{avg}$, decreased from 0.19 to 0.11 mm as Reynolds numbers increased from 53,000 and 120,000, respectively. The transverse velocity increases nearly linearly with z-position due to the nozzle geometry.

For both Reynolds numbers, the rms fluctuations of the x-velocity component at a given location in the flow were approximately twice those of the z-velocity component on average. This result is expected given the acceleration of the flow along the x-axis, which forces energy into the streamwise component. The rms fluctuations of velocity were consistently higher by ~0.2% of U_o on average for Re = 53,000. However, the absolute values of u' and w' were greater for Re = 120,000. These observations indicate that a source of fluctuations other than turbulence exists in the overall rms signal. Pressure fluctuations due to pump surge, which are independent of Re, are the most likely source of these secondary velocity fluctuations.

5.1.1.2 Effect of Flow Conditioning

The mean velocity profiles for Re = 120,000 were not significantly affected by the removal or addition of fine screens to the flow conditioner. Streamwise velocity profiles were nearly uniform and agreed with the volumetrically-averaged velocity for Types I.A, I.N, and II.A,B flow conditioning. The transverse velocity was again found to vary linearly as a function of the z-coordinate. The magnitude of transverse velocity for Type I.N flow conditioning was slightly less than the linear regression away from $z / b = 0$.

Flow conditioning had a significant impact on the rms fluctuations of velocity, however. The addition of the second screen (FS-B) reduced overall streamwise rms fluctuations by no less than 0.6% of U_o. This behavior is consistent with the observations of Loehrke and Nagib (1976), as well as Farell and Youssef (1996). However, the presence or absence of a single screen (FS-A) had no experimentally measurable impact on the overall streamwise turbulent fluctuations of the flow. The resulting transverse fluctuations from flow conditioning Types I.A and II.A,B were identical within experimental error for the bulk of the flow. The case with no fine screen, Type I.N, demonstrated somewhat elevated values of w'_{avg}, particularly towards the center of the flow, or $y / W_o = 0$. These elevated levels were likely due to entrance effects associated with the abrupt geometry change (circular-to-rectangular) at the beginning of the flow conditioner. This central disturbance in the flow translated into increased free-surface fluctuations, which is discussed later in more detail.

5.1.2 Free-Surface Behavior

5.1.2.1 Effect of *Re*

The geometry of the liquid sheet evolved as a function of downstream distance from the nozzle exit. The center of the sheet, where jet behavior was essentially 2-D, was nearly flat for both Reynolds numbers. The cross-sections for Re = 53,000 showed prominent corner wake structures and revealed that the y-dimension of the sheet was decreasing slightly with downstream distance. At Re = 120,000, the corner wakes were much less noticeable. The sheet also increased in width downstream, due to protrusions jetting along the y-axis from the edges of the sheet. These protrusions, or fingers, resulted because of the inwardly directed momentum imposed on the flow at the nozzle exit (4° contraction in the z-direction).

Free-surface fluctuations, or surface ripple, for flow conditioning Type I.A increased by greater than 3× over a range of normalized downstream distances x / δ = 5–25 at both Reynolds numbers. Surface ripple also increased with Re, although the normalized streamwise and transverse velocity fluctuations were comparable at both Reynolds numbers. This trend was observed with other flow conditioning configurations as well. The fluctuations were essentially constant across the center of the sheet, which is consistent with the 2-D behavior observed in the mean free-surface profiles.

5.1.2.2 Effect of Flow Conditioning

Free-surface geometry at Re = 120,000 was relatively unaffected by changes to the flow conditioning. The z-extent of the jet was always inside the original nozzle exit with finger-like protrusions jetting outward along the y-axis. The width of the jet was within ±1 mm for Types I.A, I.N, and II.A,B flow conditioning. A slightly off-center

"bulge" in the sheet free surface was observed for Type I.N conditioning. The asymmetry of the bulge was likely due to secondary flows generated at the turning elbows upstream. This free-surface feature corresponded to a central disturbance of the flow, which was observed in the transverse velocity fluctuations and is discussed next.

A large central peak in free-surface fluctuations was evident for flow conditioning Type I.N. This central disturbance in the flow, as mentioned earlier, was also detected in the transverse velocity rms fluctuations and to a certain degree in the mean free-surface profile. Again, this flow disturbance was likely caused by the sudden inlet contraction and led to increased transverse fluctuations in velocity and the free surface. The addition of screens to the flow conditioner acted to dampen the impact of the inlet condition and eliminates any "flow memory" of entry into the calming chamber.

Overall, surface ripple at Re = 120,000 was highest for flow conditioning without a fine screen (Type I.N), due to the central disturbance. Transverse velocity rms fluctuations for Type I.A and II.A,B were comparable, but streamwise fluctuations were significantly higher for Type I.A conditioning. However, measurements of surface ripple for Type I.A and II.A,B conditioning were within experimental uncertainty at Re = 120,000, although Type II.A,B was consistently higher. Velocity fluctuations at Re = 53,000 demonstrated similar trends (comparable w', higher u') for Type I.A compared to Type II.A,B, but the resulting free-surface fluctuations were significantly higher for Type II.A,B. Moderate increases in streamwise turbulence may actually provide a stabilizing effect by increasing the turbulent viscosity, whereas strong transverse turbulent fluctuations translate to increased free-surface fluctuations. This explanation was first

suggested by Heukelbach (2003), who was unable to confirm this hypothesis since he could not obtain transverse velocity data.

Free-surface fluctuations generally decreased with increasing wire diameter of the fine screen element in the flow conditioner. All screens in these investigations were operated in the supercritical regime, whereby eddies are shed by the screen. Indeed, fine screens "A" and "B" both produced a high-pitched audible tones at Re = 120,000, likely due to the shedding of von Karmen vortex streets in the auditory range. Unfortunately, the sampling limitations of the LDV system precluded confirming the presence of these frequencies in the flow.

5.1.2.3 Effect of Boundary-Layer Cutting

Boundary-layer cutting in liquid sheets at Re = 120,000 introduced wake structures to the free surface, which emanated from the free interface between the sheet and the cutter blade. These protrusions were similar to the corner wake structures observed at Re = 53,000. With the exception of the protrusions, the bulk of the sheet was contained well within the original nozzle exit cross-section with respect to the z-axis. The cutter blade also acted to confine the spreading of the sheet in the y-axis; the sheet width was decreased by as much as 0.6 cm at $x/\delta = 25$ for all cut rates.

Surface ripple decreased at all downstream locations as the extent of BL cutting was increased. Free-surface fluctuations were reduced significantly even at BL cutting levels as low as $\dot{m}_{cut}/\dot{m}_{fl}$ = 0.6%. Increasing $\dot{m}_{cut}/\dot{m}_{fl}$ provided diminishing improvements in surface smoothness; the normalized surface ripple at $x/\delta = 25$ was 0.0317 and 0.0295 for $\dot{m}_{cut}/\dot{m}_{fl}$ = 0.6 and 1.9%, respectively. This behavior indicates the

edge of the cutter blade was positioned in the bulk of the flow for even the lowest removal rate, which is consistent with the estimated BL thickness of $\delta_{BL} = 0.11$ mm.

BL cutting was less effective in improving surface fluctuations for sheets with poor flow conditioning, specifically the Type I.N configuration. Even at the highest removal rate of $\dot{m}_{cut} / \dot{m}_{fl} = 1.9\%$, surface ripple was only reduced by 10% on average compared to the 33% reduction for Type I.A configuration. BL cutting clearly decreases free-surface fluctuations, but the fine screen has a larger overall impact on free-surface smoothness. Type I.N conditioning was less affected by BL cutting because the central disturbance observed in transverse velocity fluctuations extended into the center of the jet $z = 0$, beyond the range of the cutter blade.

5.1.3 Turbulent Breakup

5.1.3.1 Effect of Initial Conditions

The density of drops due to turbulent breakup decreased with increasing standoff distance from the liquid sheet at $Re = 120{,}000$ and $We = 19{,}000$. Not surprisingly, there are more drops near the source of breakup, namely the free surface. The equivalent number density of the breakup spray increased from zero at a sufficiently large standoff value with a sharp increase at the free surface. Finally, the accuracy of the mass collection measurements was limited by secondary effects such as aerodynamic shear, drop re-entrainment, and evaporation. Therefore, the following conclusions must be considered qualitative in nature.

Flow conditioning design had a significant impact on the breakup characteristics of the sheet. Breakup was reduced with the addition of a fine screen (Type I.A) to the flow conditioner for a given standoff distance from the free surface. Additionally, the

scale of the breakup appeared to be smaller for the Type I.A configuration O(1-100 μm). The dominant impact of the fine screen is consistent with previous observations of free-surface behavior and velocity fluctuation profiles. The elevated transverse velocity fluctuations recorded near the nozzle exit for Type I.N flow conditioning appear to be directly related to both increased free-surface fluctuations and increased turbulent breakup.

BL cutting reduced the primary turbulent breakup. A marked decrease in breakup was observed for the Type I.A configuration at a cut rate of 1.0% of the sheet flow rate over all standoff distances. Moreover, breakup was completely suppressed at $\dot{m}_{cut} / \dot{m}_{fl}$ = 1.9%. BL cutting had less impact on the Type I.N configuration, with smaller reductions in breakup compared to Type I.A conditioning. In all cases, the (absence of the) fine screen has a much more significant impact upon jet quality than BL cutting.

5.1.3.2 Comparison to Breakup Correlations

The correlations of Sallam *et al.* (2002) as applied to a turbulent liquid sheet matching the experimental Weber number did not agree with the measurements of breakup in this investigation. This disagreement was somewhat expected given the disparity in initial conditions between the fully-developed turbulent flows used in the correlation studies and the highly-conditioned sheets considered here. Model predictions of Sauter mean diameter ranged from 0.6 to 2.1 mm for downstream distances of x / δ from 3.7 to 25, respectively. The observed droplets were noticeably smaller, even considering losses due to evaporation. The droplets from a conditioned jet are understandably smaller, since the turbulent energy has been forced to smaller scales via the flow conditioner.

Based upon these results, flow conditioning and a contracting nozzle already reduce the breakup mass flux by 3–5 orders of magnitude. Since the experimental conditions in these studies are not identical to those used to establish the correlations, reductions in breakup with respect to the correlations should again be considered qualitative. Nonetheless, this discrepancy again demonstrates the sensitivity of these types of flows to initial conditions.

5.2 Implications for Thick Liquid Protection

The experimental work presented in this thesis provides a basis for the successful implementation of thick liquid protection. Reynolds and Weber numbers of the scaled experiments were approximately 50% and 20% of the prototypical values, respectively. Free-surface fluctuations and turbulent breakup are likely to increase at prototypical values. Nevertheless, the methodology developed from these studies to improve the flow control of turbulent liquid sheets is valid. The impact of initial conditions, particularly transverse velocity fluctuations, on downstream free-surface and breakup behavior was clearly demonstrated. The experience gained in this investigation leads to the following design recommendations for turbulent sheets in thick liquid protection schemes.

1. The introduction of transverse velocity fluctuations and secondary flows must be minimized. Manifold and flow conditioner inlet designs should be tailored to prevent these types of disturbances to the flow. In terms of minimizing free-surface fluctuations, the flow is less sensitive to and may actually benefit from moderate increases in streamwise velocity fluctuations.
2. Flow conditioning based around a single screen operating in the supercritical regime is the optimal configuration for liquid sheets in the range of interest. The

flows produced with Type I.A flow conditioning would meet the standoff requirement of 0.07δ, or 5 mm, given in Latkowski and Meier 2001 for final focus magnet lifetimes of 30 years. Based on the experimental results of $1{\cdot}\sigma_z$ from this study, surface ripple of a prototypical HYLIFE-II flow would be less than 0.04δ, or 2.9 mm, at the bottom of the protective flow $x / \delta = 25$. The addition of a second screen does not appear to improve surface ripple and would increase pumping power due to additional pressure loss across the flow conditioner.

3. Based on driver and target propagation requirements, boundary-layer cutting can be customized to reduce turbulent breakup to acceptable levels. BL cutting should be used only as necessary given the complexity of implementation and the pumping penalty incurred (fluid removal rates of up to 4% of the overall mass flowrate).

5.3 Contributions

This work is the first in the available literature to detail the connection between initial conditions and the resulting free-surface flow of turbulent liquid sheets at such high Reynolds numbers. The main contributions of this doctoral research on the dynamics of turbulent liquid sheets are listed below.

1. Implementation of boundary-layer cutting device for the removal of low-momentum fluid from one face of the liquid sheet. This apparatus allowed the controlled removal of fluid to determine the relative effectiveness of different cutting rates on free-surface and breakup characteristics.

2. Measurement of the free-surface dynamics of the liquid sheet in the near-field. Free-surface geometry and fluctuations were acquired for a variety of different conditioning schemes and BL cutting configurations as a function of downstream distance.
3. Statistical quantification of the initial conditions by a non-intrusive LDV technique to obtain both the streamwise and transverse velocity components. Initial conditions were manipulated by the insertion and removal of fine screens in a modularly designed flow conditioner.
4. Characterization of turbulent breakup with a simple mass collection technique. This method allowed the different forms of passive flow control, namely flow conditioning and BL cutting, to be evaluated for effectiveness in reducing breakup.
5. Establishment of design guidelines for the creation of robust turbulent sheets compatible with thick liquid protection schemes.

5.4 Recommendations

This doctoral thesis represents an extensive effort to characterize turbulent liquid sheets. This work is the first in the available literature to track the influence of initial conditions on the free surface of a free plane jet in the near-field region. Based on the experience gained in this study, the following recommendations for future research are recommended:

1. Data for free-surface geometry and fluctuations should be extended to include prototypical Reynolds numbers Re = 240,000 and Weber number We = 100,000.

Since water is unsuitable to match Reynolds and Weber simultaneously, an alternative working fluid may need to be considered for true dynamic similarity.

2. Extensive velocity information before and after the flow conditioner would be useful for optimizing the design and interaction of conditioning elements. The turbulent spectral content of the flow would be of particular interest, especially for determining the shedding characteristics of different screen designs.
3. A smooth transition at the flow conditioner inlet may eliminate the need for a fine screen element and should be investigated. However, it is likely that the combination of a smoothed entry length in conjunction with a fine screen would prove superior to the use of either alone.
4. Further investigation of nozzle design is warranted. The contraction ratio of three used in this study does not allow for an ideal packing fraction for shielding purposes. Therefore, similar studies at smaller contraction ratios (*e.g.* CR = 1.5) would be useful.
5. Pointwise techniques such as particle dynamic analysis (PDA) or pulsed shadowgraphy should be employed to more accurately measure the turbulent breakup of the liquid sheet. These methods would provide an instantaneous representation of both droplet size and velocity.
6. Improvements to the BL cutting apparatus should be developed to permit symmetric fluid removal from all sides of the sheet. This step would be necessary for the practical implementation of the cutting technique in future applications.

APPENDIX A

PRIMARY TURBULENT BREAKUP CORRELATIONS

This appendix outlines the turbulent breakup correlations as adapted from Sallam *et al.* (2002). These correlations were derived from experiments using pulsed shadowgraphy and holography for round and annular jets with a fully-developed turbulent pipe flow velocity profile at the "nozzle" exit. Therefore these flows incorporate no flow conditioning or contracting nozzle. The downstream location for the onset of breakup measured from the nozzle exit, x_i, is given by the following empirical power-law correlation

$$\frac{x_i}{d_h} = 4403 \cdot We_d^{-0.74} \qquad \text{A.1}$$

where the Weber number We_d is defined here with the hydraulic diameter, d_h, as the characteristic length. Equation A.1 is valid for We_d = 13,000 – 151,000. As We_d increases for a given jet diameter, x_i decreases, *i.e.*, the onset of breakup occurs closer to the nozzle exit.

The Sauter mean diameter (SMD), defined as the diameter of a droplet having the same volume to surface area ratio of a representative sample of the spray, is often used to characterize the "average" size of droplets in a spray. Droplet size as given by SMD is described by the power-law relationship

$$\frac{\mathrm{SMD}}{d_\mathrm{h}} = 0.65 \cdot \left(\frac{x}{d_\mathrm{h} \cdot We_d^{0.5}} \right)^{2/3} \qquad \text{A.2}$$

This equation illustrates that droplet size increases with downstream distance.

The streamwise and cross-stream components of the drop velocity after breakup or $\tilde{u}$ and $\tilde{v}$, respectively, were measured using pulsed shadowgraphy. The streamwise components were found to be relatively independent of downstream location, while the cross-stream components were found to decrease with increasing x, with:

$$\frac{\tilde{u}}{U_0} = 0.78 \qquad \frac{\tilde{v}}{U_0} \le 0.089 \qquad \text{A.3}$$

The relative cross-stream droplet velocity measured with respect to the jet free-surface is then $\tilde{v}_r / U_\mathrm{o} = 0.04$. The values for this velocity are comparable to the rms turbulence intensities near the wall in fully-developed turbulent pipe flow.

The derivation of an expression for the mass flux of droplets measured relative to the liquid surface due to turbulent primary breakup, denoted as G [kg/(m^2·s)], is described next. The droplet mass flux was measured directly by single-pulse holography and normalized in terms of the surface efficiency factor, ε. This factor is given as $\varepsilon = G / \left(\rho_\mathrm{L} \cdot \tilde{v}_r \right)$, where the limit of ε = 1 denotes the case when droplets are being emitted over the entire surface of the jet. Based on measurements of G and $\tilde{v}_r$, the surface efficiency factor as a function of downstream distance is given by the following correlation

$$\varepsilon = 0.272 \left[\frac{x}{d_\mathrm{h} \cdot We_d^{0.5}} \right] \qquad \text{A.4}$$

Equations A.2 – A.4 are valid for We_d = 235 – 270,000.

The correlation mass flux G_{corr} reported in Section 4.3.3 is derived from the breakup correlations with the following assumptions. Neglecting aerodynamic effects and gravitational acceleration, Equation A.3 shows that the droplets follow a linear trajectory at an angle $\theta = \tan^{-1}(\tilde{v}/\tilde{u}) = 6.5°$ measured with respect to the jet free surface for all x-locations downstream of x_i. All droplets ejected by the jet due to primary breakup should therefore fall within a "breakup halo" bounded by a line starting at the jet free surface at $x = x_i$ at an angle of θ with respect to the x-axis (Figure A.1).

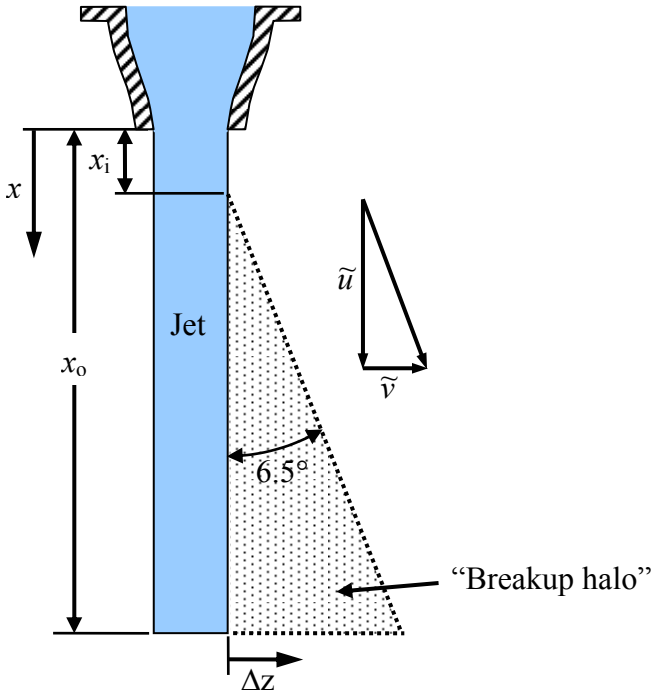

Figure A.1. Schematic of droplet trajectories based on correlations. The standoff from the nominal free surface and downstream cuvette location are denoted by Δz and x_o, respectively.

There exist two cases for the position of the cuvettes with respect to the bounding halo, as shown in Figure A.2: 1) The cuvettes are completely inside the droplet halo; or

2) Part or all of the cuvettes are outside the halo. The droplets following the dashed trajectory lines are predicted to enter the cuvettes in the Figure.

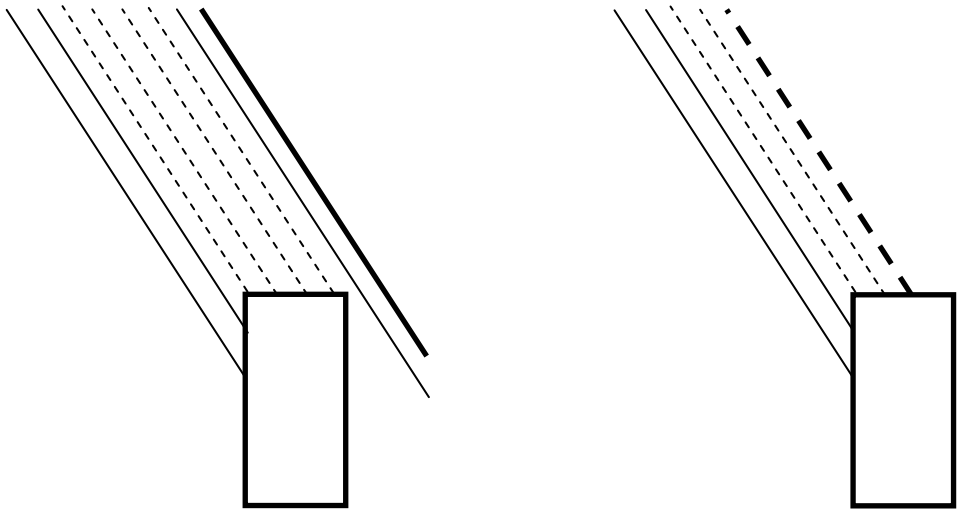

Figure A.2. Schematic of cuvettes inside (Case 1) and partially inside droplet halo (Case 2). Droplets following dashed lines are predicted to enter cuvettes. The bold trajectories indicate the boundary of the halo.

Equation A.5 gives the mass flux due to primary breakup *at the jet free surface* at a given x-location.

$$G = \left[0.272 \left(\frac{x}{d_{\mathrm{h}} \cdot We_d^{0.5}} \right) \right] \cdot \rho_{\mathrm{L}} \, \tilde{v}_r \qquad \text{A.5}$$

Since $G \propto x$, the average mass flux sampled inside the halo (Case 1) in our experiments should correspond to that sampled in the center of the cuvette open aperture, or at a z-location $z_{\mathrm{o}} = \Delta z_{\mathrm{s}} + 6$ mm and an x-location x_{o} from the nozzle exit (Figure A.3). Tracing back from this location along a line at angle θ gives the x-location at the free surface:

$$x = x_{\mathrm{o}} - \frac{z_{\mathrm{o}}}{\tan\theta} \qquad \text{A.6}$$

where $x > x_i$. Using this value of x in Equation A.5 then gives:

$$G_{corr} = G(x_o) - (0.272)\frac{z_o}{d_h\sqrt{We_d}}\frac{\rho_L \tilde{v}_r}{\tan\theta} \qquad \text{A.7}$$

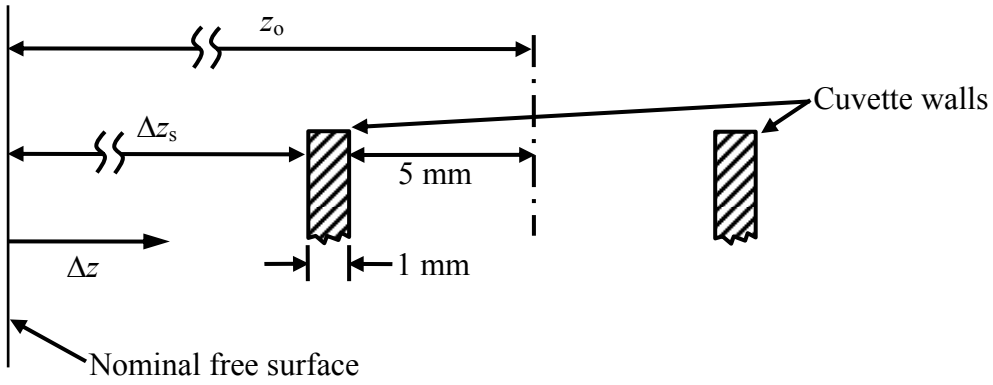

Figure A.3. Schematic of cuvette centerline position, z_o.

If Δz_s is large enough so that only part of the cuvette opening falls within the breakup halo (Case 2), the z-extent of the cuvette opening that falls within the breakup halo is given by $\zeta = (x_o - x_i)\tan\theta - (\Delta z_s + 1\text{ mm})$. The z-location of the center of the cuvette opening portion that falls within the breakup halo is then

$$\zeta_o = \frac{x_o - x_i}{2}\tan\theta + \frac{\Delta z_s + 1\text{ mm}}{2} \qquad \text{A.8}$$

Finally, the mass flux predicted by the correlation for this case is.

$$G_{corr} = \left(\frac{\zeta}{1\text{ cm}}\right) G(\zeta_o) \qquad \text{A.9}$$

APPENDIX B

ERROR ANALYSIS

The error and uncertainty inherent to an experimental result are critical to the accurate interpretation of the data. Therefore, the uncertainties in the experimental measurements are estimated in this section. Results of this analysis are given followed by a general description of the method used and a brief explanation of the source of each reported measurement uncertainty.

B.1 Error Propagation Analysis

The overall standard uncertainty of an indirect measurement y, dependent on N indirect measurements x_i, is defined in Equation B.1. The standard uncertainty associated with an indirect measurement is analogous to the standard deviation of a statistical population.

$$\tilde{u}^2 = \sum_{i=1}^{N} \left(\frac{\partial y}{\partial x_i} \tilde{u}_i \right)^2 \qquad \text{B.1}$$

Here, $\tilde{u}$ is used to define standard uncertainty (not to be confused with streamwise velocity u).

The expanded uncertainty U is reported in this appendix and defines the bounds that include 95% of the possible data. The expanded uncertainty is usually defined as some multiple of the standard uncertainty. Equation B.2 shows the definition of the expanded uncertainty as used in the following sections.

$$U = 2 \cdot \tilde{u} \qquad \text{B.2}$$

B.1.1 Uncertainty in Mean Nozzle Exit Velocity

The uncertainty in the nozzle exit velocity U_o was determined using error propagation analysis (EPA). The nozzle exit velocity was determined from Equation B.3 in which Q is the volumetric flow rate, δ is the nozzle thickness, and W_o is the nozzle width.

$$U_o = \frac{Q}{\delta W_o} \qquad \text{B.3}$$

Equation B.4 gives the relation between the overall uncertainty of U_o and the contributions from the measurement uncertainties of Q, δ, and W_o.

$$\tilde{u}_{U_o}^2 = \left(\frac{1}{\delta W_o} \tilde{u}_Q \right)^2 + \left(-\frac{Q}{\delta^2 W_o} \tilde{u}_\delta \right)^2 + \left(-\frac{Q}{\delta W_o^2} \tilde{u}_{W_o} \right)^2 \qquad \text{B.4}$$

Table B.1 summarizes the values used to determine the overall uncertainty of the nozzle exit velocity. The overall uncertainty in U_o was found for two volumetric flow rates Q = 0.00479 m^3/s and 0.01085 m^3/s corresponding to Re = 53,000 and 120,000. The standard uncertainty was determined to be $\tilde{u}_{U_o}$ = 0.034 m/s and 0.077 m/s for Re = 53,000 and 120,000, respectively. The uncertainty was most affected by Q which contributed 98% of the overall uncertainty.

Table B.1. Measurement uncertainties and intermediate calculations for U_o.

Measurement, i	Standard Uncertainty, $\tilde{u}_i$	Influence Coefficient $\frac{\partial(Q/\delta W_o)}{\partial i}$	Section Containing Explanation
Volumetric Flow Rate, Q	7.6×10^{-5} m^3/s	$\frac{1}{\delta W_o}$	B.1.1.1
Nozzle thickness, δ	0.013 mm	$-\frac{Q}{\delta^2 W_o}$	B.1.1.2
Nozzle width, W_o	0.013 mm	$-\frac{Q}{\delta W_o^2}$	B.1.1.3

B.1.1.1 Uncertainty in Volumetric Flow Rate Q

The uncertainty of the volumetric flow rate was determined from ten independent timed trials in which the volume change in the supply tank was measured after the desired flow rate was established. In these tests, the overflow tank was cut out of the flow loop, so that the water level in the supply tank could be monitored. The flow rate was set by the bypass valve and the drainage valves were closed once the flow rate was established. Thus all the water was collected in the receiving tank. A timer was started once the water level in the supply tank reached an indicated mark on the tank. When the water level had significantly decreased, the pump was turned off, and the water level and total elapsed time were recorded. The standard uncertainty was determined for the two flow rates corresponding to the two Reynolds numbers used in these experiments. The standard uncertainty of the flow rate was then assumed to be the standard deviation of each set of trials. For Q = 0.00479 m^3/s and 0.01085 m^3/s, the standard uncertainty was found to be $\tilde{u}_Q$ = 3.3×10^{-5} m^3/s and 7.6×10^{-5} m^3/s, respectively. The value shown in

Table B.1 represents the largest standard uncertainty associated with the volumetric flow rate.

B.1.1.2 Uncertainty in Nozzle Thickness δ

The nozzle thickness was measured using a standard caliper. Thus, the source for the uncertainty in the nozzle exit thickness was the resolution on the caliper. The measurements of the nozzle thickness were made within 0.025 mm, corresponding to a standard uncertainty of 0.013 mm.

B.1.1.3 Uncertainty in Nozzle Width W_o

The nozzle width was also measured using the caliper within 0.025 mm. Thus the source of uncertainty was again the resolution of the caliper, and the standard uncertainty of the nozzle width is the same as the nozzle exit of 0.013 mm. Recall from Chapter 3 that surface roughness tests found the average peak-to-valley height to be about 5 μm, or 0.005 mm. Thus, the standard uncertainty in both the width and height of the nozzle is larger than the average surface roughness.

B.1.2 Uncertainty in LDV Results

B.1.2.1 Normalized Mean Streamwise Velocity

The uncertainty in normalized mean streamwise velocity is developed in this section. The values used to calculate the uncertainties were chosen to reflect conservative limits. The uncertainties reported here are therefore the maximum values obtained for the entire data set. The uncertainty of the normalized mean is given by Equation B.5.

$$\tilde{u}^2_{u/U_o} = \left(\frac{1}{U_o}\,\tilde{u}_u\right)^2 + \left(-\frac{u}{U_o^2}\,\tilde{u}_{U_o}\right)^2 \qquad \text{B.5}$$

Table B.2 summarizes the values used to calculate the overall uncertainty. Again, the values of the largest uncertainties are used to obtain a conservative estimate of the overall uncertainty. The mean exit velocity was U_o = 10.85 m/s, and the mean profile velocity was u = 9.79 m/s. The largest overall standard uncertainty in normalized mean velocity was found to be 0.65% of the nozzle exit velocity. The maximum expanded uncertainty is then 1.3% of U_o and was due predominantly to the uncertainty of the nozzle exit velocity, which contributed in excess of 98% to the overall uncertainty.

Table B.2. Measurement uncertainties and intermediate calculations for u / U_o.

Measurement, i	Standard Uncertainty, $\tilde{u}_i$	Influence Coefficient $\frac{\partial(u/U_o)}{\partial i}$	Section Containing Explanation
Mean Streamwise Velocity, u	0.010 m/s	$\frac{1}{U_o}$	B.1.2.1.1
Nozzle Exit Velocity, U_o	0.077 m/s	$-\frac{u}{U_o^2}$	B.1.1

B.1.2.1.1 Uncertainty in Mean Streamwise Velocity

Statistical estimates of uncertainty for turbulent data are conveniently summarized in Benedict and Gould (1996). Here, the quantity of interest is the mean streamwise velocity. Equation B.6 gives the standard uncertainty for the mean velocity as

$$2\cdot\tilde{u}_u = \pm 1.96\left[\frac{(u')^2}{S}\right]^{1/2} \qquad \text{B.6}$$

where S is the number of samples.

A conservative value of $u' = 0.28$ m/s was chosen to calculate the uncertainty of the mean velocity. Substituting this value and a validated sample size of $S = 773$ yields a standard uncertainty of $\tilde{u}_u = 0.010$ m/s. Traditionally, sample sizes in LDV studies range up to 10,000 samples per location in the flow. However, the low sampling rates (~ 5 Hz) in these investigations prohibited large sample sizes but also insured each sample to be statistically independent.

B.1.2.2 Normalized RMS Fluctuations of Streamwise Velocity

The uncertainty in normalized rms velocity fluctuations is developed in this section. The values used to calculate the uncertainties were chosen to reflect conservative limits. The uncertainties reported here are therefore the maximum values obtained for the entire data set. The uncertainty of the normalized rms fluctuations is given by equation B.7.

$$\tilde{u}^2_{u'/U_o} = \left(\frac{1}{U_o}\,\tilde{u}_{u'}\right)^2 + \left(-\frac{u'}{U_o^2}\,\tilde{u}_{U_o}\right)^2 \qquad \text{B.7}$$

Table B.3 summarizes the values used to calculate the overall uncertainty. Again, the values of the largest uncertainties are used to obtain a conservative estimate of the overall uncertainty. The mean exit velocity was $U_o = 10.85$ m/s, and the rms fluctuations of velocity was $u' = 0.28$ m/s. The largest overall standard uncertainty in normalized rms fluctuations was found to be 0.068% of the nozzle exit velocity. The maximum expanded uncertainty is then 0.14% of the nozzle exit velocity and was due predominantly to the uncertainty of the velocity fluctuations, which contributed about 95% of the overall uncertainty.

Table B.3. Measurement uncertainties and intermediate calculations for u'/U_o.

Measurement, i	Standard Uncertainty, $\tilde{u}_i$	Influence Coefficient $\frac{\partial(u'/U_o)}{\partial i}$	Section Containing Explanation
RMS Fluctuations of Velocity, u'	0.007 m/s	$\frac{1}{U_o}$	B.1.2.2.1
Nozzle Exit Velocity, U_o	0.077 m/s	$-\frac{u'}{U_o^2}$	B.1.1

B.1.2.2.1 Uncertainty in RMS Fluctuations of Velocity

Again, the statistical estimates of Benedict and Gould (1996) for turbulent data are used to quantify uncertainty. Equation B.8 gives the standard uncertainty for the rms fluctuations of velocity.

$$2 \cdot \tilde{u}_{u'} = \pm 1.96 \left[\frac{(u')^2}{2S} \right]^{1/2} \qquad \text{B.8}$$

Similar to the previous section, a conservative value of $u' = 0.28$ m/s was chosen to calculate the uncertainty. Substituting this value and a validated sample size of $S = 773$ yields a standard uncertainty of $\tilde{u}_{u'} = 0.007$ m/s.

B.1.2.3 Normalized Transverse Velocity Measurements

The uncertainty in the transverse velocity measurements was evaluated with the same techniques as described above. The results of this EPA analysis are presented in Tables B.4-5, where conservative values of $w = 1.0$ m/s, $w' = 0.22$ m/s, and $S = 790$ were used. The maximum expanded uncertainties in the normalized mean and rms transverse velocity measurements were then 0.20% and 0.10% of the mean exit velocity,

respectively. The uncertainties reported for all velocity measurements in this thesis were taken to be the more conservative values calculated for the streamwise component.

Table B.4. Measurement uncertainties and intermediate calculations for w / U_o.

Measurement, i	Standard Uncertainty, $\tilde{u}_i$	Influence Coefficient $\frac{\partial(w/U_o)}{\partial i}$	Section Containing Explanation
Mean Transverse Velocity, w	0.008 m/s	$\frac{1}{U_o}$	B.1.2.1.1
Nozzle Exit Velocity, U_o	0.077 m/s	$-\frac{w}{U_o^2}$	B.1.1

Table B.5. Measurement uncertainties and intermediate calculations for w'/ U_o.

Measurement, i	Standard Uncertainty, $\tilde{u}_i$	Influence Coefficient $\frac{\partial(w'/U_o)}{\partial i}$	Section Containing Explanation
RMS Velocity Fluctuations, w'	0.005 m/s	$\frac{1}{U_o}$	B.1.2.2.1
Nozzle Exit Velocity, U_o	0.077 m/s	$-\frac{w'}{U_o^2}$	B.1.1

B.1.2.4 Uncertainty in Normalized Probe Position

The probe volume location was controlled by two linear stages, each with a resolution of 0.01 mm. However, these measurements were made relative to the location of the inner walls of the nozzle and optical window, which were determined through a zeroing procedure described in Section 3.2.3. The standard deviation of these

measurements was taken to be the standard uncertainty in the probe location. The standard deviations of the y- and z-location measurements were 0.12 mm and 0.087 mm, respectively. The uncertainty calculations are summarized in Tables B.6-7. The maximum expanded uncertainty for the normalized probe location was then 0.0024 and 0.016 for the y- and z-coordinate, respectively. These conservative values of uncertainty were calculated for y = 50 mm and z = 5.475 mm.

Table B.6. Measurement uncertainties and intermediate calculations for y / W_o.

Measurement, i	Standard Uncertainty, $\tilde{u}_i$	Influence Coefficient $\frac{\partial(y/W_o)}{\partial i}$	Section Containing Explanation
Probe location, y	0.12 mm	$\frac{1}{W_o}$	B.1.2.4
Nozzle Exit Width, W_o	0.013 mm	$-\frac{y}{W_o^2}$	B.1.1.3

Table B.7. Measurement uncertainties and intermediate calculations for z / b.

Measurement, i	Standard Uncertainty, $\tilde{u}_i$	Influence Coefficient $\frac{\partial(z/b)}{\partial i}$	Section Containing Explanation
Probe location, z	0.087 mm	$\frac{1}{b}$	B.1.2.4
Local Nozzle Width, b	0.013 mm	$-\frac{z}{b^2}$	B.1.2.4.1

B.1.2.4.1 Uncertainty in Local Nozzle Thickness

The local nozzle thickness was not measured directly. The uncertainty reflected in the Table B.7 was chosen based on the uncertainty in the nozzle exit thickness and is presented only as an estimate. However, the uncertainty in local nozzle thickness did not significantly influence the overall uncertainty of the measurement.

B.1.3 Uncertainty in PLIF Results

B.1.3.1 Uncertainty in Normalized Downstream Location x / δ

Table B.8 outlines the terms influencing the uncertainty in the normalized downstream location. It was found that the overall uncertainty for the normalized downstream location was 0.1δ for all downstream locations with the uncertainty in nozzle thickness negligible. The maximum expanded uncertainty for all normalized downstream distances was then 0.2δ.

Table B.8. Measurement uncertainties and intermediate calculations for x / δ.

Measurement, i	Standard Uncertainty, $\tilde{u}_i$	Influence Coefficient $\frac{\partial(x/\delta)}{\partial i}$	Section Containing Explanation
Downstream Location, x	1 mm	$\frac{1}{\delta}$	B.1.3.1.1
Nozzle Exit Thickness, δ	0.013 mm	$-\frac{x}{\delta^2}$	B.1.1.2

B.1.3.1.1 Uncertainty in x

The downstream position was measured with a lab yardstick with a resolution of 2 mm. The standard uncertainty in the measurement was then 1 mm. These measurements

were taken with the laser light sheet intersecting the ruler. The laser sheet was centered on the desired downstream location.

B.1.3.2 Uncertainty in Mean Free-Surface Position

The uncertainty in the mean free-surface position was determined from the surface ripple data. In the center of the sheet, the free-surface profiles for all flow conditioning are accurate to within the maximum expanded uncertainty of 0.11 mm. These error bars were not plotted since they were undistinguishable from the mean profile at the chosen scale. The expanded uncertainty was calculated using Equation B.9, with σ_z = 0.64 mm and S = 135. The spatial resolution of the images was considerably smaller with a value of 0.030 mm/pixel.

$$U_{FS} = \pm 1.96 \left[\frac{(\sigma_z)^2}{S} \right]^{1/2} \qquad \text{B.9}$$

B.1.3.3 Uncertainty in Normalized Free-Surface Fluctuations

The uncertainties in the normalized free-surface fluctuation measurement are summarized in Table B.9. The maximum expanded uncertainty based on these values was 0.0076, or 12% of the measurement of σ_z. This uncertainty estimate is almost completely dependent on the uncertainty of the fluctuation measurement. Estimates of uncertainty for other flow conditioning schemes, Reynolds numbers, and downstream locations yielded slightly lower results. Therefore, the error bars shown in Chapter 4 reflect the upper limit of 12% of the measurement of σ_z.

Table B.9. Measurement uncertainties and intermediate calculations for σ_z / δ.

Measurement, i	Standard Uncertainty, $\tilde{u}_i$	Influence Coefficient $\frac{\partial(\sigma_z/\delta)}{\partial i}$	Section Containing Explanation
Free-Surface Fluctuations, σ_z	0.038 mm	$\frac{1}{\delta}$	B.1.3.3.1
Nozzle Exit Thickness, δ	0.013 mm	$-\frac{\sigma_z}{\delta^2}$	B.1.1.2

B.1.3.3.1 Uncertainty in Free-Surface Fluctuations

The uncertainty in the free-surface fluctuations was calculated using the statistical estimates of Benedict and Gould (1996) for turbulent data. Equation B.9 gives the standard uncertainty for the rms free-surface fluctuations.

$$2 \cdot \tilde{u}_{\sigma_z} = \pm 1.96 \left[\frac{(\sigma_z)^2}{2S} \right]^{1/2} \qquad \text{B.10}$$

For Type I.N flow conditioning at Re = 120,000 and x / δ = 25, a value of σ_z = 0.64 mm was chosen to calculate the uncertainty. Substituting this value and a validated sample size of S = 135 yields a standard uncertainty of $\tilde{u}_{\sigma_z}$ = 0.038 mm. This relatively small sample size was chosen based on the number of images used to calculate each value of $\sigma_z(y)$.

B.1.4 Uncertainty in Normalized Mass Collection Results

The uncertainty of the normalized mass collection measurements was dominated by the uncertainty in the average collected mass, $\tilde{u}_{\dot{m}_{coll}}$. This high uncertainty was a direct

result of the limited number of trials that could be conducted per standoff distance, given the relatively long collection times. The maximum expanded uncertainty was 8.3×10^{-9}, or 42% of average value of $\dot{m}_{\text{coll}}$.

Table B.10. Measurement uncertainties and intermediate calculations for $\dot{m}_{\text{coll}}/\dot{m}_{\text{fl}}$.

Measurement, i	Standard Uncertainty, $\tilde{u}_i$	Influence Coefficient $\frac{\partial\left(\dot{m}_{\text{coll}}/\dot{m}_{\text{fl}}\right)}{\partial i}$	Section Containing Explanation
Mass Collection Rate, $\dot{m}_{\text{coll}}$	4.5×10^{-8} kg/s	$\frac{1}{\dot{m}_{\text{fl}}}$	B.1.4.1
Mass Flow Rate, $\dot{m}_{\text{fl}}$	0.076 kg/s	$-\frac{\dot{m}_{\text{coll}}}{\dot{m}_{\text{fl}}^2}$	B.1.4.2

B.1.4.1 Uncertainty in Mass Collection

The mass collection experiments were repeated at each standoff distance for a minimum of six trials. The standard uncertainty of these measurements was taken to be the standard deviation of this data set. The maximum uncertainty found with this method was $\tilde{u}_{\dot{m}_{\text{coll}}} = 4.5 \times 10^{-8}$ kg/s.

B.1.4.2 Uncertainty in Mass Flow Rate

The uncertainty in the mass flow rate of the jet was determined from the uncertainty in the volumetric flow rate. Uncertainty in the density was assumed to be negligible. Therefore, the maximum standard uncertainty in the mass flow rate was $\tilde{u}_{\dot{m}_{\text{fl}}} =$ 0.076 kg/s for Re = 120,000.

B.1.5 Uncertainty in Normalized Mass Cut Rate

The uncertainty in the normalized mass cut rate of the BL cutter is summarized in Table B.11. The overall uncertainty in the normalized measurement was 5.0×10^{-4} and was due predominantly to uncertainty in the mass cut rate. Therefore, the maximum expanded uncertainty was 1.0×10^{-4}, or 5.3% of $\dot{m}_{\text{cut}}$. These values reflect the maximum experimental uncertainty for the entire range of cut rates.

Table B.11. Measurement uncertainties and intermediate calculations for $\dot{m}_{\text{cut}} / \dot{m}_{\text{fl}}$.

Measurement, i	Standard Uncertainty, $\tilde{u}_i$	Influence Coefficient $\frac{\partial\left(\dot{m}_{\text{cut}}/\dot{m}_{\text{fl}}\right)}{\partial i}$	Section Containing Explanation
Mass Cut Rate, $\dot{m}_{\text{cut}}$	5.2×10^{-3} kg/s	$\frac{1}{\dot{m}_{\text{fl}}}$	B.1.5.1
Mass Flow Rate, $\dot{m}_{\text{fl}}$	0.076 kg/s	$-\frac{\dot{m}_{\text{cut}}}{\dot{m}_{\text{fl}}^2}$	B.1.4.2

B.1.5.1 Uncertainty in Mass Cut Rate

The mass cut rate was measured a minimum of 5 times for each experiment. The standard uncertainty of these measurements was taken to be the standard deviation of this data set. The maximum uncertainty found with this method was $\tilde{u}_{\dot{m}_{\text{cut}}} = 5.2 \times 10^{-3}$ kg/s. The cut rate of this experiment was $\dot{m}_{\text{cut}} = 202.4$ g/s, corresponding to the highest normalized cut rate of 1.9%.

B.2 Experimental Reproducibility

B.2.1 Reproducibility of LDV Results

The mean and rms of streamwise velocity were obtained for two independent test runs under identical experimental conditions to verify experimental reproducibility. These two tests were performed for profiles at $y / W_o = 0.4438$ and $Re = 120{,}000$ with Type I.A flow conditioning (Figure B.1). For each point, 1000 instantaneous velocity samples were recorded at a data rate of approximately 5 Hz. The error bars shown in the graph indicate the experimental uncertainty in the mean and rms data as determined in Sections B.1.2.1 and B.1.2.2, respectively. The average of these data over the central 75% of b are presented in Table B.12 and are analyzed in this section for experimental reproducibility.

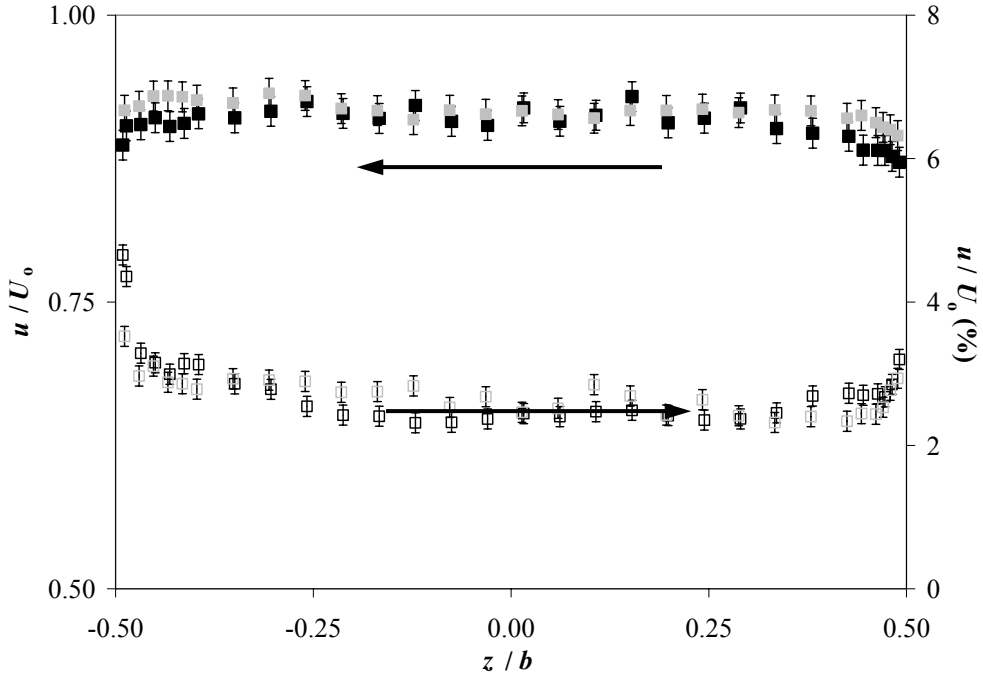

Figure B.1. Two independent normalized mean velocity and rms fluctuation profiles Test 1 (■) and Test 2 (■) at $y / W_o = 0.4438$ and $Re = 120{,}000$ with Type I.A flow conditioning. The open and closed symbols represent u / U_o and u' / U_o, respectively. Note: Error bars indicate 95% experimental uncertainty.

Table B.12. Statistical results obtained from reproducibility tests of mean velocity.

	u_{avg}/U_o	u'_{avg}/U_o
Test 1	0.912	0.0248
Test 2	0.918	0.0265

A two-sample *t*-test was used to test the null hypothesis that the mean velocities found in both tests are equal. The null hypothesis is an assumption made about the population characteristics that is initially considered to be true (Hayter, 1995). In this case, the null hypothesis is H_o: $u_{avg,1} = u_{avg,2}$. Note that the subscripts used here and in the rest of this section refer to the test population corresponding with the variable they follow. It is also assumed that the 1000 data points in each set follow a normal distribution. The appropriate *t*-statistic for the null hypothesis is given by Equation B.11.

$$t_s = \frac{u_{avg,1} - u_{avg,2}}{\sqrt{\frac{\left(u'_{avg,1}\right)^2}{1000} + \frac{\left(u'_{avg,2}\right)^2}{1000}}} = -5.23 \qquad \text{B.11}$$

Choosing $\alpha/2$ to be 0.025, which corresponds to a 95% confidence interval for a two-sided hypothesis test, the null hypothesis is rejected if Equation B.12 is true.

$$|t_s| > t_{\alpha/2,1000+1000-2} = 1.96 \qquad \text{B.12}$$

Because $t_s > 1.96$, the test rejects the null hypothesis and indicates that the two population means are not statistically identical. However, recall that the maximum expanded uncertainty in the normalized streamwise component was 1.3% of U_o. This confidence bound on the mean streamwise velocities contradicts the *t*-test and implies the two population means are reproducible to within experimental error.

A directional, or one-sided, F-test was used to test the null hypothesis that the two sample variances are equal. The null hypothesis for this test is then H_o: $\left(u'_{\text{avg},1}\right)^2 = \left(u'_{\text{avg},2}\right)^2$. Since this test is directional, a confidence level of $\alpha = 0.05$ is appropriate for a 95% confidence level in the hypothesis test. The null hypothesis is rejected if Equation B.13 is true.

$$F_s \geq F_{\text{critical}} = 1.033 \qquad \text{B.13}$$

As determined from a two-sample F-test, the data from these two experimental samples give $F_s = 1.127$. This result rejects the null hypothesis and indicates that the variances are statistically different. However, the maximum experimental uncertainty in these results was 0.14% of U_o. This confidence interval signifies that the variances, while statistically different, are reproducible within experimental error.

B.2.2 LDV System Noise in Transverse Measurements

As described in Chapter 3, all measurements of the transverse velocity (z-component) were conducted with a frequency shift $f_{\text{shift}} = 1.3$ MHz. This relatively high frequency shift was necessary in order to measure this component of velocity. However, imperfections in mechanical alignment of the rotating diffraction grating and slight inconsistencies in motor rotation speeds introduced a "system noise" into the measured signal. The resulting signal will have a variance equal to sum of the variances due to turbulence and system noise.

$$(\text{rms})^2_{\text{meas}} = (\text{rms})^2_{\text{turb}} + (\text{rms})^2_{\text{sys}} \qquad \text{B.14}$$

If the turbulence is of sufficient strength compared to the system noise, the measured signal rms will be dominated by the turbulent signal. Figure B.2 shows the

relationship for $(rms)_{turb}$ / $(rms)_{meas}$ as a function of the signal-to-noise ratio. The turbulent signal accounts for over 90% of the overall signal for SNRs greater than ~ 2, which means the measured and actual signals are within 10%.

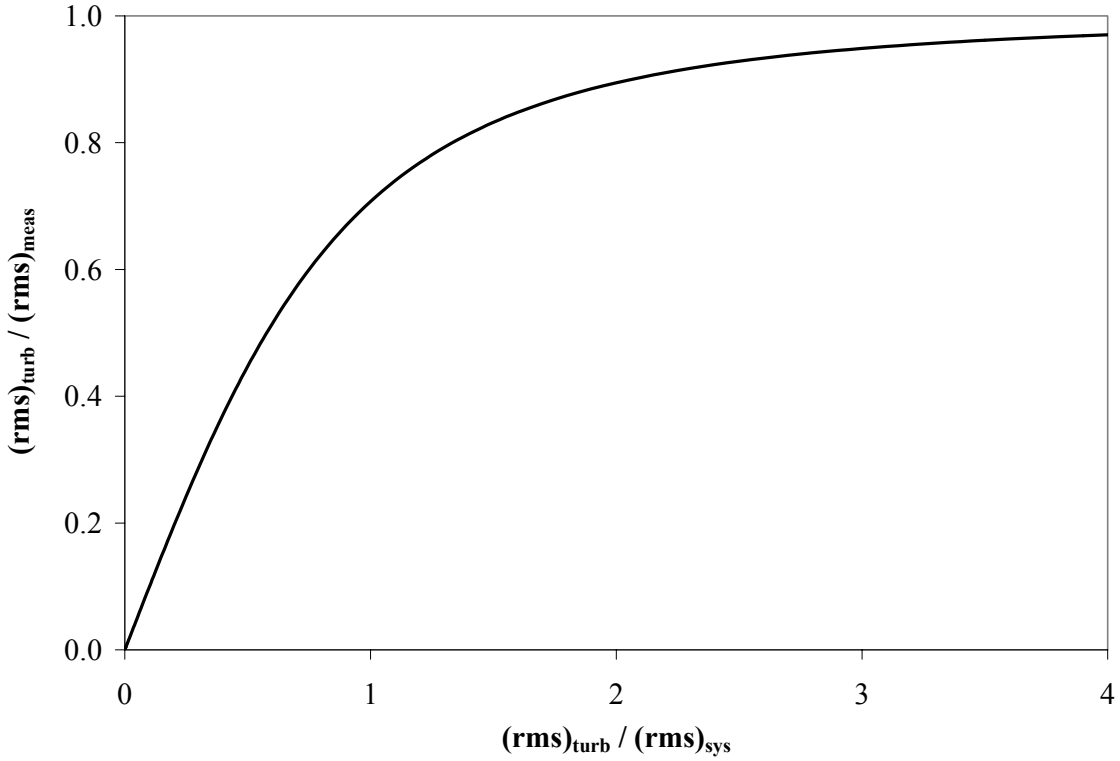

Figure B.2. Ratio of turbulent rms to measured rms as a function of the signal strength-to-noise.

Typical values of the measured transverse rms velocity fluctuations at *Re* = 120,000 are ≥ 3% of the frequency shift, *vs.* the manufacturer's quoted value of 1% of the frequency shift. For these values, the measured and actual turbulent rms values are within 5%. Calibrations were performed to verify the claim of 1% f_{shift} system noise. Figure B.3 shows a histogram of the system signal with the probe volume intersecting a stationary wall. The sample size was kept constant at 1000. The system noise was

estimated to be ~1.2% of the shift frequency from this particular calibration. Other calibrations indicate the system noise to be $0.9 < (\text{rms})_{sys} < 1.5\%$ of f_{shift}. Even wth system noise fluctuations of 1.5%, the overall system signal will be dominated by the turbulence signal.

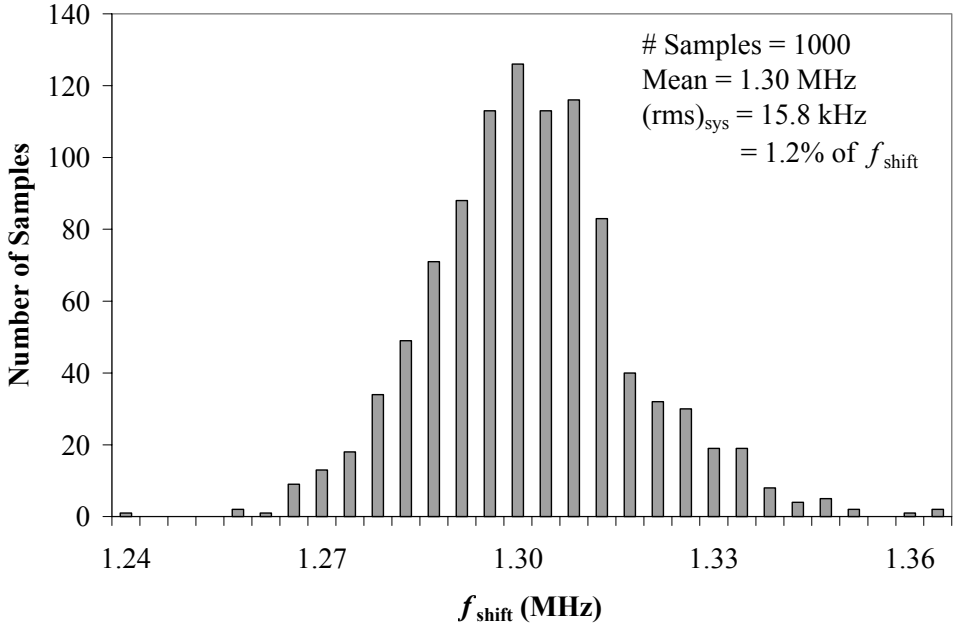

Figure B.3. Histogram of f_{shift} calibration data.

B.2.3 Reproducibility of PLIF Results

The mean and rms fluctuations of the free surface were obtained for two independent test runs under identical experimental conditions to verify experimental reproducibility. These two tests were performed for profiles at $x / \delta = 15$–25 and $Re = 120{,}000$ with Type I.A flow conditioning. Figure B.4 shows the mean free-surface profiles for the two trials at $x / \delta = 15$ and 25. These profiles deviate from each other at certain locations by more than six times the calculated maximum experimental

uncertainty. However, the overall geometry of the sheet is in good qualitative agreement, given the sensitivity of these flows to slight changes in initial conditions.

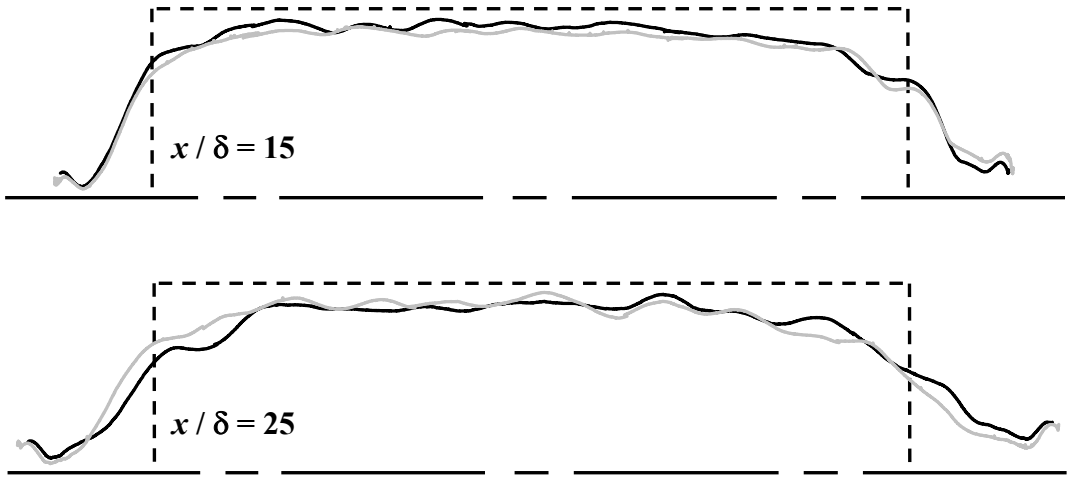

Figure B.4. Two independent free-surface profiles, Test 1 (—) and Test 2 (—) for *Re* = 120,000 and Type I.A flow conditioning.

Figure B.5 shows the normalized free-surface fluctuations of the two independent trials for *Re* = 120,000 and Type I.A flow conditioning. The error bars shown in the graph indicate the 95% experimental uncertainty in each data point. Table B.13 gives the values of σ_z / δ for both trials at each downstream location. To test the statistical repeatability of the free-surface fluctuation measurements, a directional *F*-test was used to test the null hypothesis that the two sample variances are equal. The null hypothesis for this test is then H_o: $\left(\sigma_{z,1}\right)^2 = \left(\sigma_{z,2}\right)^2$. A confidence level of $\alpha = 0.05$ was chosen to determine a 95% confidence in the evaluation of the null hypothesis. For the given data sets, the null hypothesis is rejected if Equation B.15 is true.

$$F_s > F_{\text{critical}} = 1.330 \qquad \text{B.15}$$

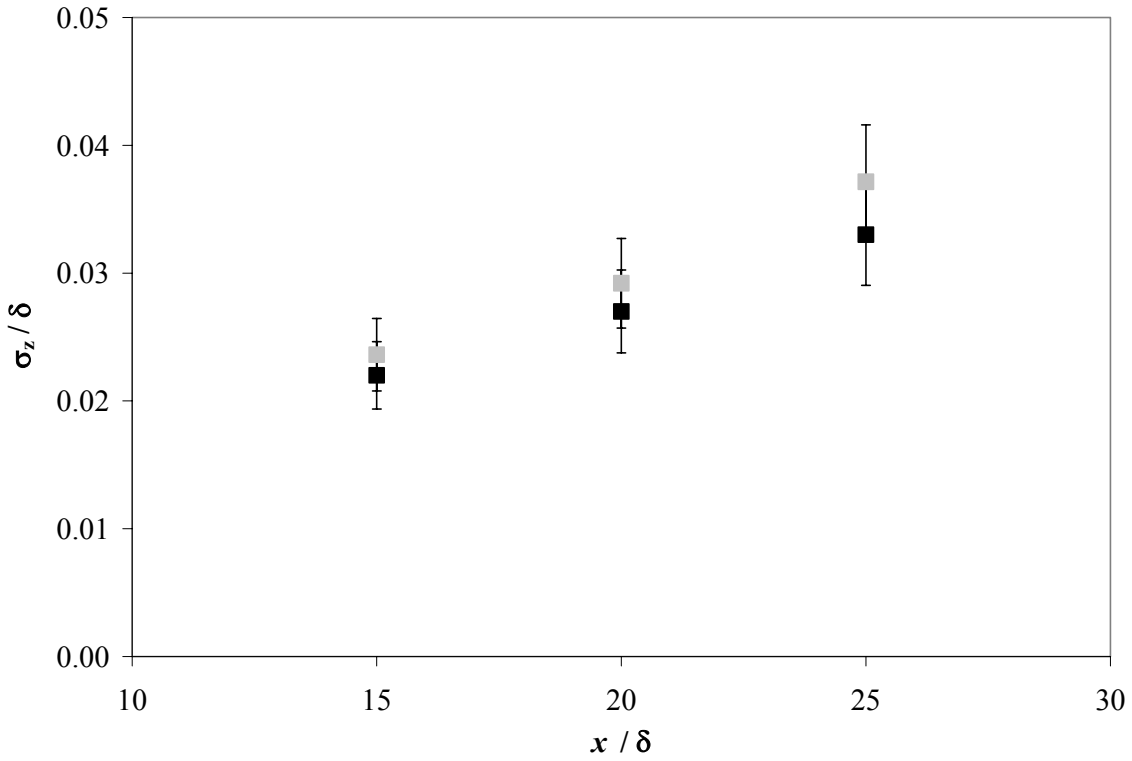

Figure B.5. Two independent normalized free-surface fluctuation measurements, Test 1 (■) and Test 2 (■) for *Re* = 120,000 and Type I.A flow conditioning. Note: Error bars indicate 95% experimental uncertainty.

Table B.13. Statistical results obtained from reproducibility tests of σ_z / δ.

	$x / \delta =$		
	15	20	25
Test 1	0.022	0.027	0.033
Test 2	0.024	0.029	0.037

The two-sample *F*-tests yielded F_s = 1.137, 1.091, and 1.125 at x / δ = 15, 20, and 25, respectively. Therefore, these results accept the null hypothesis and indicate that the variances are statistically repeatable. These data sets also fall within the experimental uncertainty as determined in Section B.1.3.3.

APPENDIX C

ADDITIONAL EXPERIMENTAL DATA

The following appendix presents experimental data not included in Chapter 4. These results are comprised of velocity and free-surface data for the remaining flow conditioning types. Sections are organized according to the type of data obtained, namely, mean and rms velocity profiles and mean free-surface profiles.

C.1 LDV Measurements

This section details the LDV results for flow conditioning Types I.N and II.A,B. For all plots, the profiles shown were acquired at y / W_o = 0.1188 (+), 0.3688 (●), 0.4163 (▲), 0.4438 (◆), and 0.4838 (■). First, the mean streamwise and transverse velocity profiles are presented. Next, the rms velocity fluctuations are given for the corresponding flow conditioning scheme. These data are consistent with the trends outlined in Chapter 4.

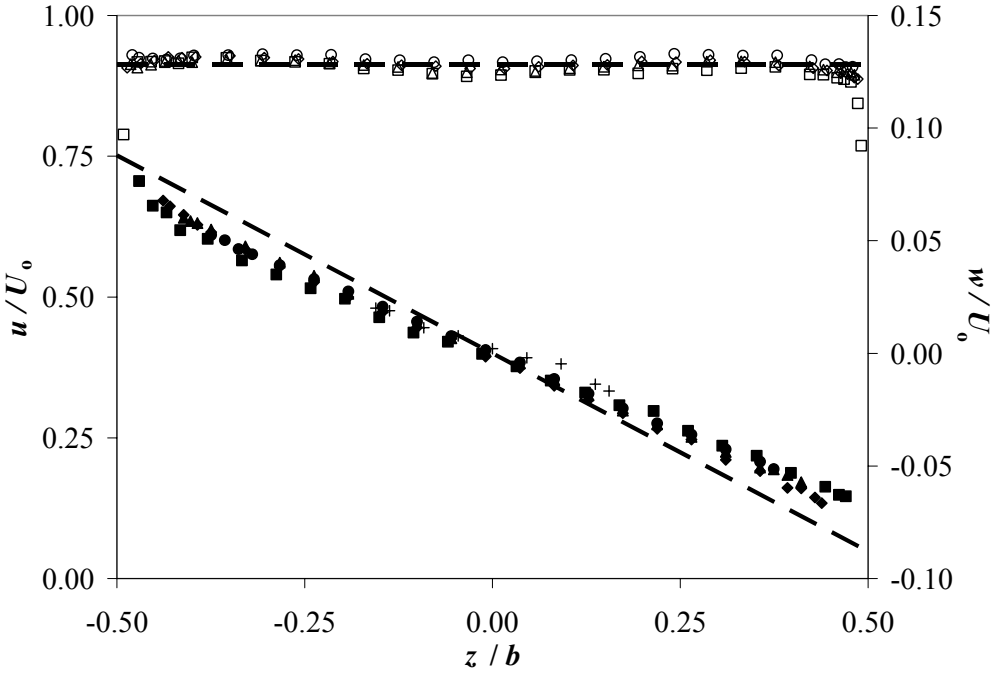

Figure C.1. Mean velocity profiles for Type I.N flow conditioning and Re = 53,000 and y / W_o = 0.1188 (+), 0.3688 (●), 0.4163 (▲), 0.4438 (◆), and 0.4838 (■). The open and closed symbols represent u / U_o and w / U_o, respectively, while the dashed lines indicate the expected velocity values.

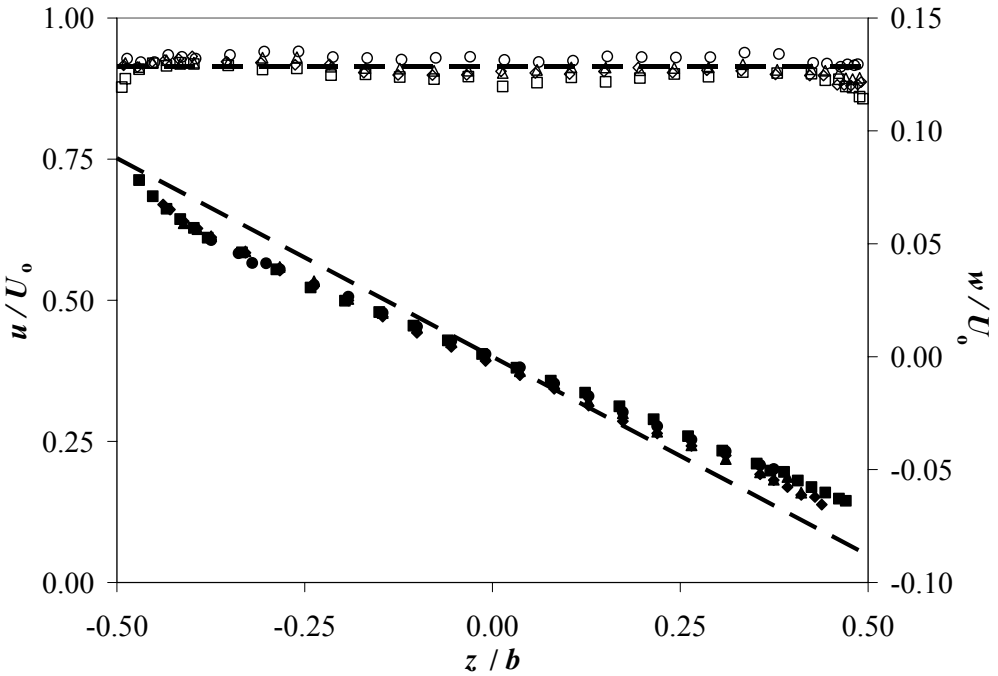

Figure C.2. Mean velocity profiles, similar to Figure C.1, for Type I.N flow conditioning and Re = 120,000.

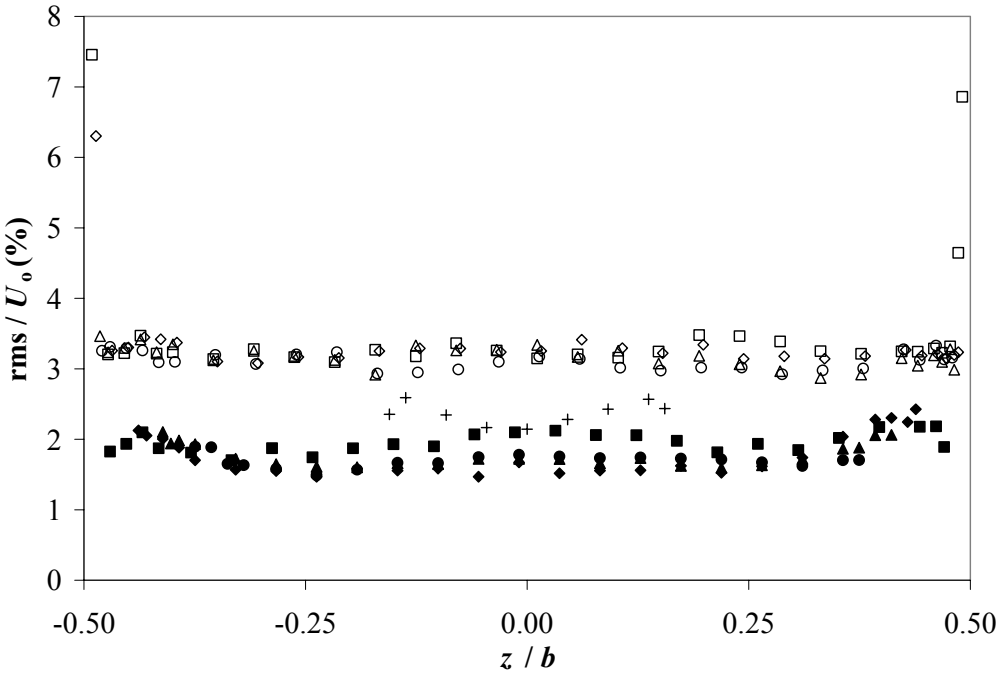

Figure C.3. Rms velocity profiles for Type I.N flow conditioning and Re = 53,000 and y / W_o = 0.1188 (+), 0.3688 (●), 0.4163 (▲), 0.4438 (◆), and 0.4838 (■). The open and closed symbols represent u' / U_o and w' / U_o, respectively.

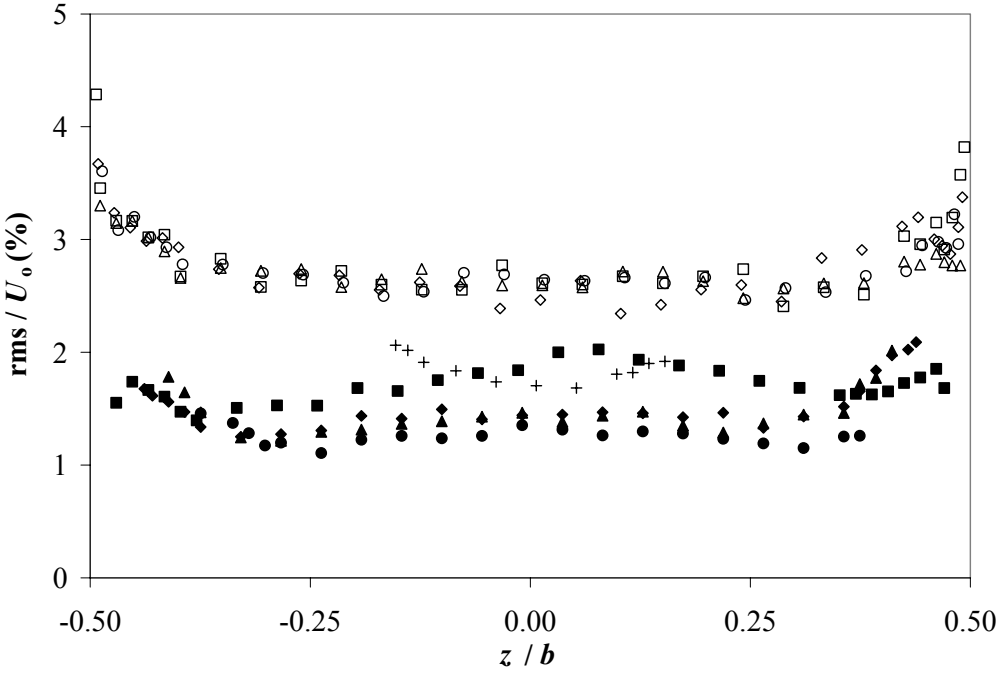

Figure C.4. Rms velocity profiles, similar to Figure C.5, for Type I.N flow conditioning and Re = 120,000.

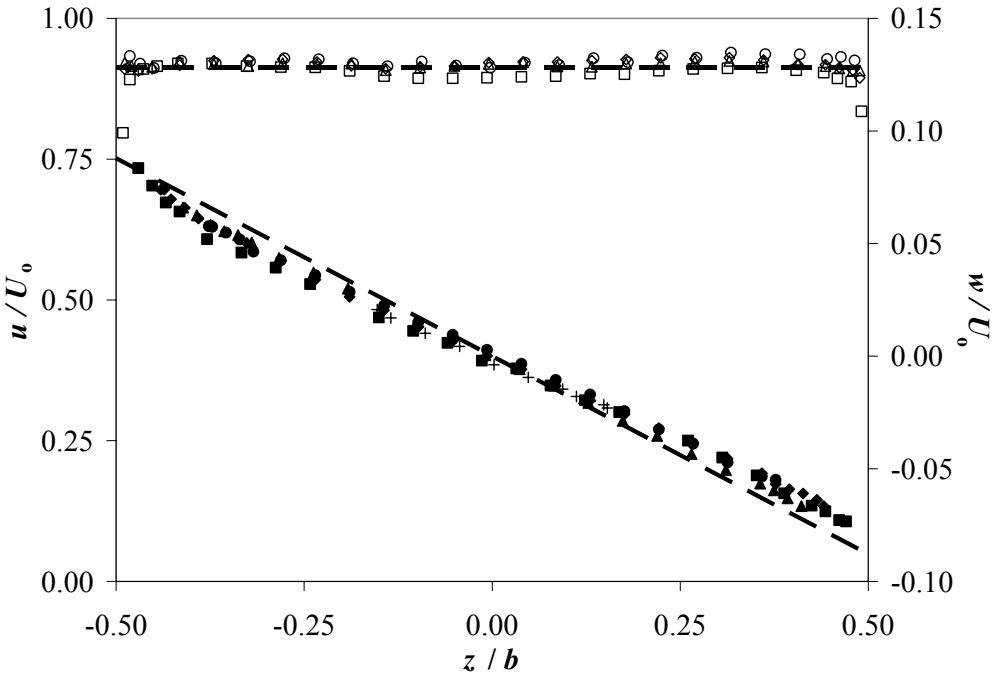

Figure C.5. Mean velocity profiles for Type II.A,B flow conditioning and Re = 53,000 and y / W_o = 0.1188 (+), 0.3688 (●), 0.4163 (▲), 0.4438 (◆), and 0.4838 (■). The open and closed symbols represent u / U_o and w / U_o, respectively, while the dashed lines indicate the expected velocity values.

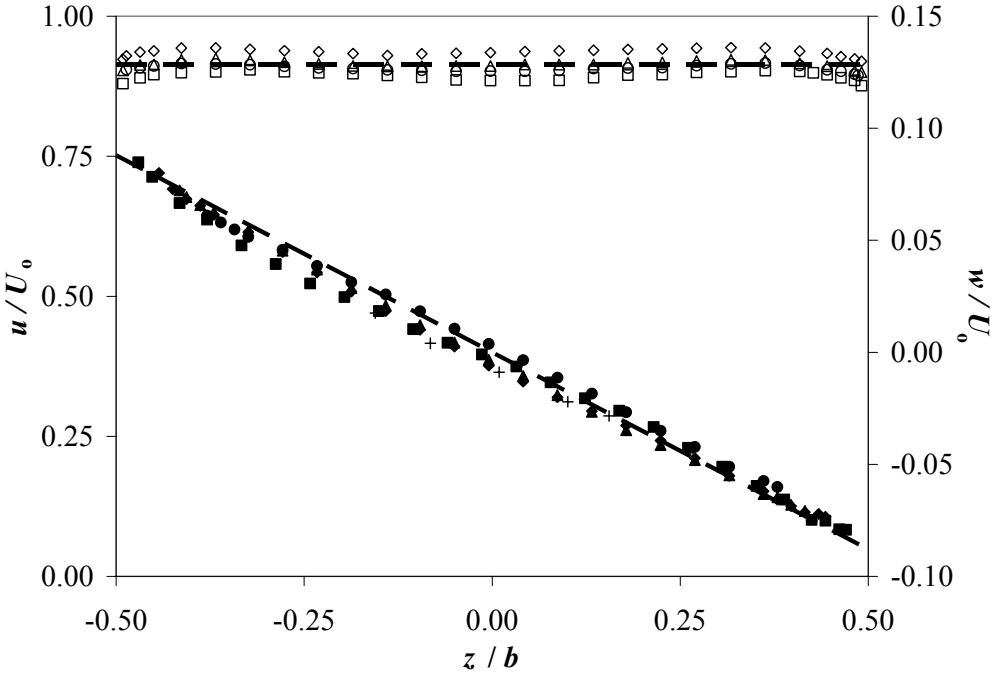

Figure C.6. Mean velocity profiles, similar to Figure C.5, for Type II.A,B flow conditioning and Re = 120,000.

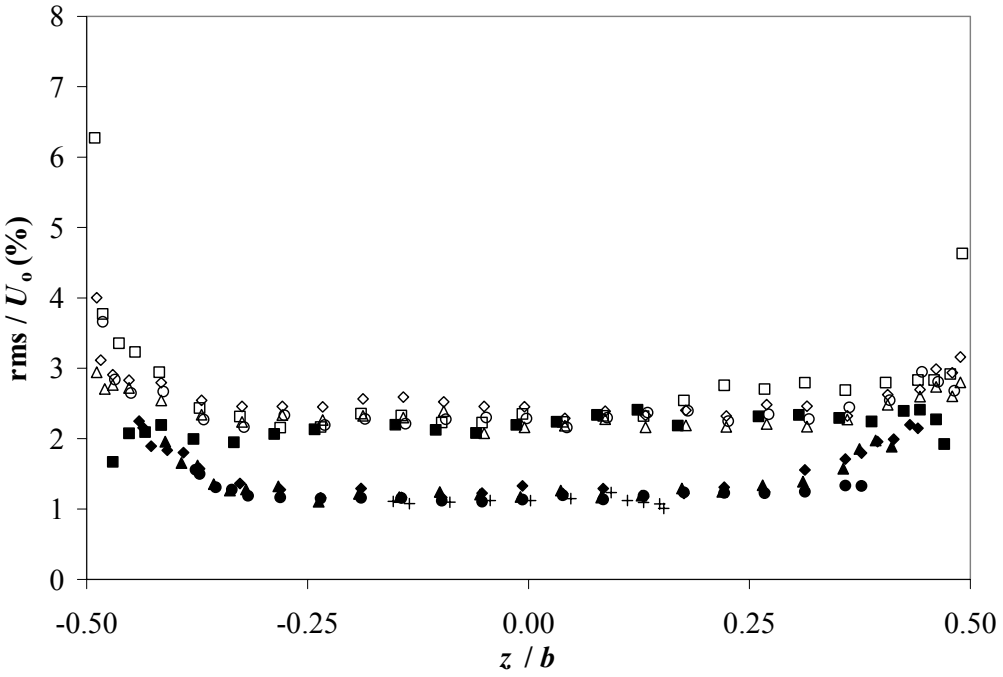

Figure C.7. Rms velocity profiles for Type II.A,B flow conditioning and Re = 53,000 and y / W_o = 0.1188 (+), 0.3688 (●), 0.4163 (▲), 0.4438 (◆), and 0.4838 (■). The open and closed symbols represent u'/ U_o and w'/ U_o, respectively.

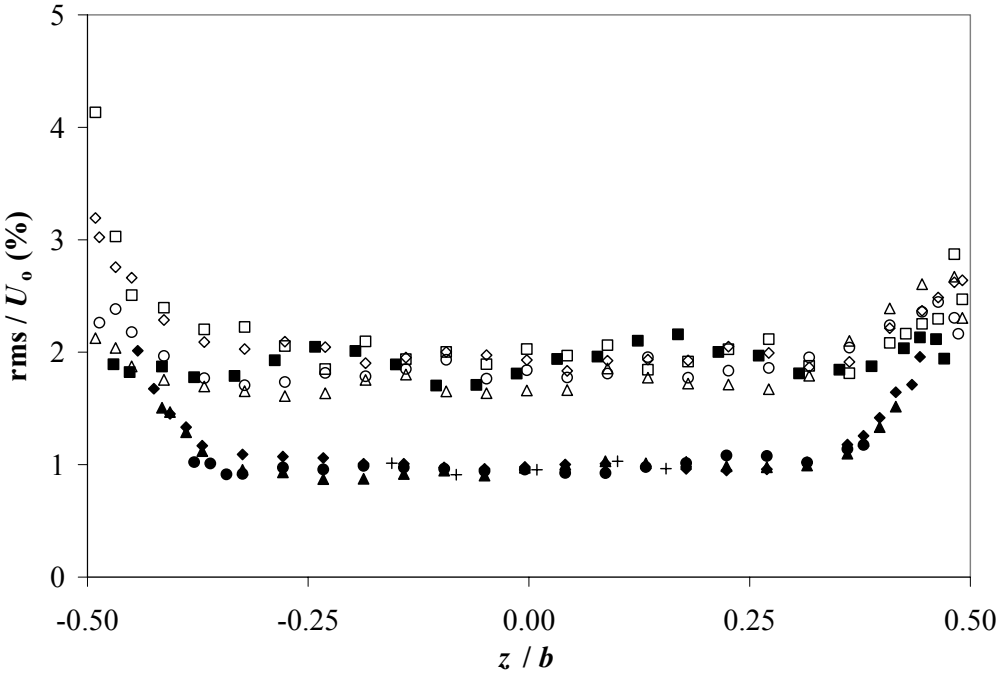

Figure C.8. Rms velocity profiles, similar to Figure C.7, for Type II.A,B flow conditioning and Re = 120,000.

C.2 PLIF Measurements

The following section presents additional free-surface profiles for various flow conditioning schemes. Figures C.9 and C.10 show the free surface for flow conditioning Types I.A, I.N, and II.A,B at $x / \delta = 15$ and 20, respectively. These profiles are similar to those shown in Chapter 4 at $x / \delta = 25$. The central bulge in the sheet for Type I.N conditioning is still evident, even at $x / \delta = 15$.

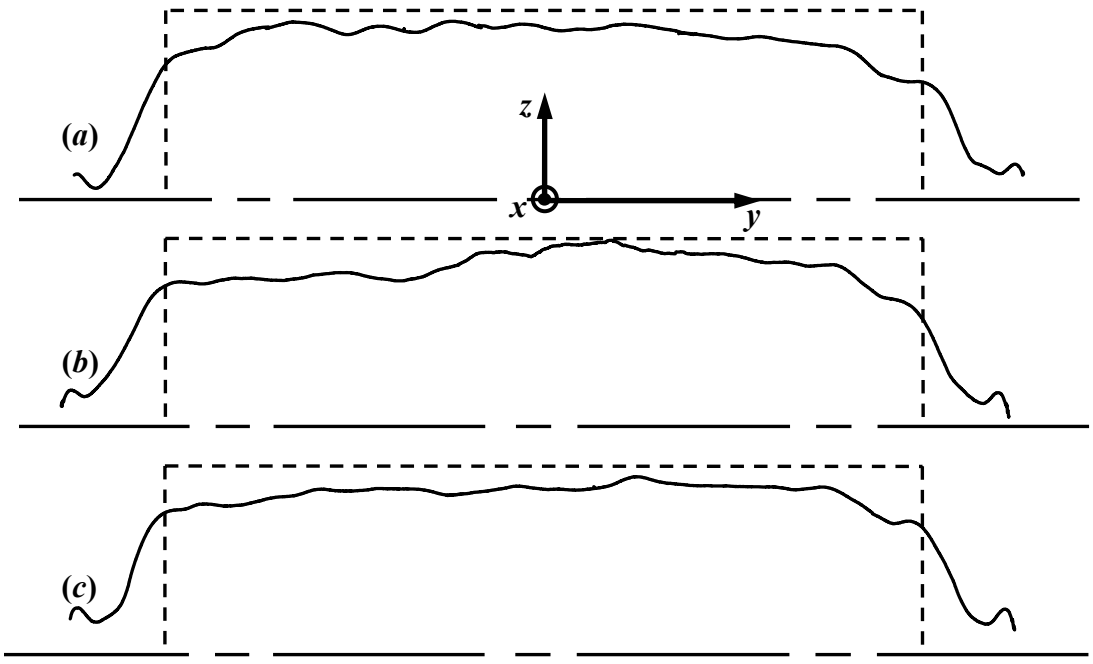

Figure C.9. Free surface profiles at $x / \delta = 15$ for Re = 120,000 and flow conditioning (*a*) Type I.A, (*b*) Type I.N, and (*c*) Type II.A,B. Dashed lines indicate the nozzle exit. Note: Flow is out of page and vertical axis is magnified 5×.

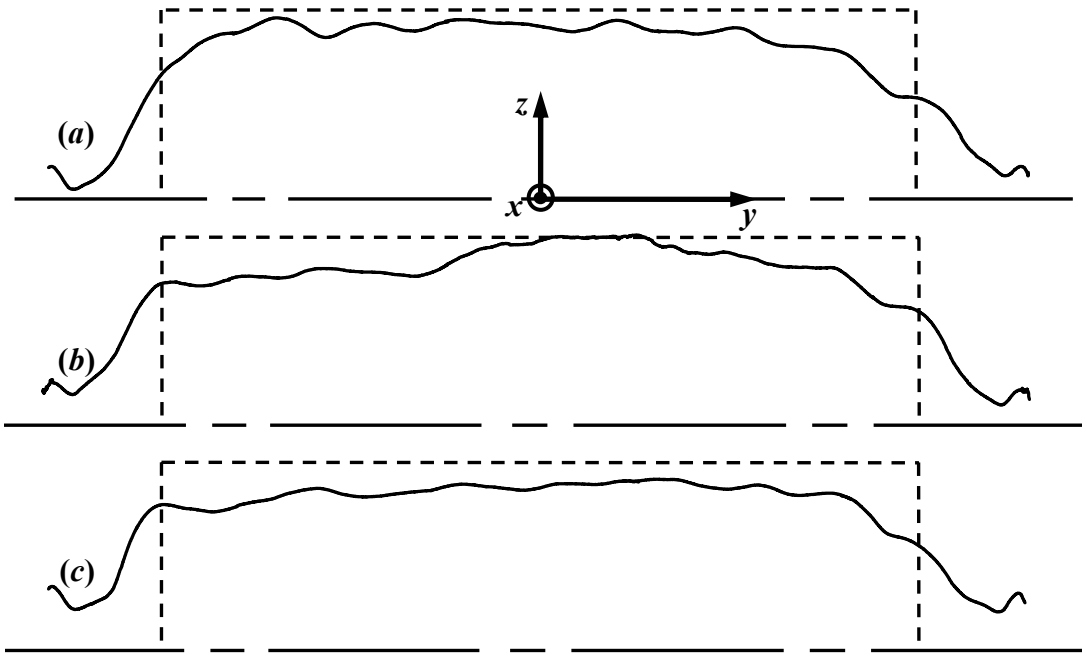

Figure C.10. Free surface profiles at $x / \delta = 20$ for Re = 120,000 and flow conditioning (a) Type I.A, (b) Type I.N, and (c) Type II.A,B. Dashed lines indicate the nozzle exit. Note: Flow is out of page and vertical axis is magnified 5×.

Figures C.11 and C.12 show the free-surface profiles for Type II.A,B flow conditioning at downstream locations of x / δ = 5–25 for Re = 53,000 and 120,000, respectively. These profiles are similar in appearance to those for Type I.A, except for the absence of prominent corner wake structures at Re = 53,000.

Finally, profiles for the remaining flow conditioning schemes are shown in Figures C.13 and C.14 at Re = 53,000 and 120,000, respectively. Again, the sheet free surface is relatively unaffected by changes to the flow conditioner. The only prominent difference in these profiles is a noticeable bulge in the center of the sheet for Type I.E conditioning. This is similar in appearance to flows produced with Type I.N conditioning.

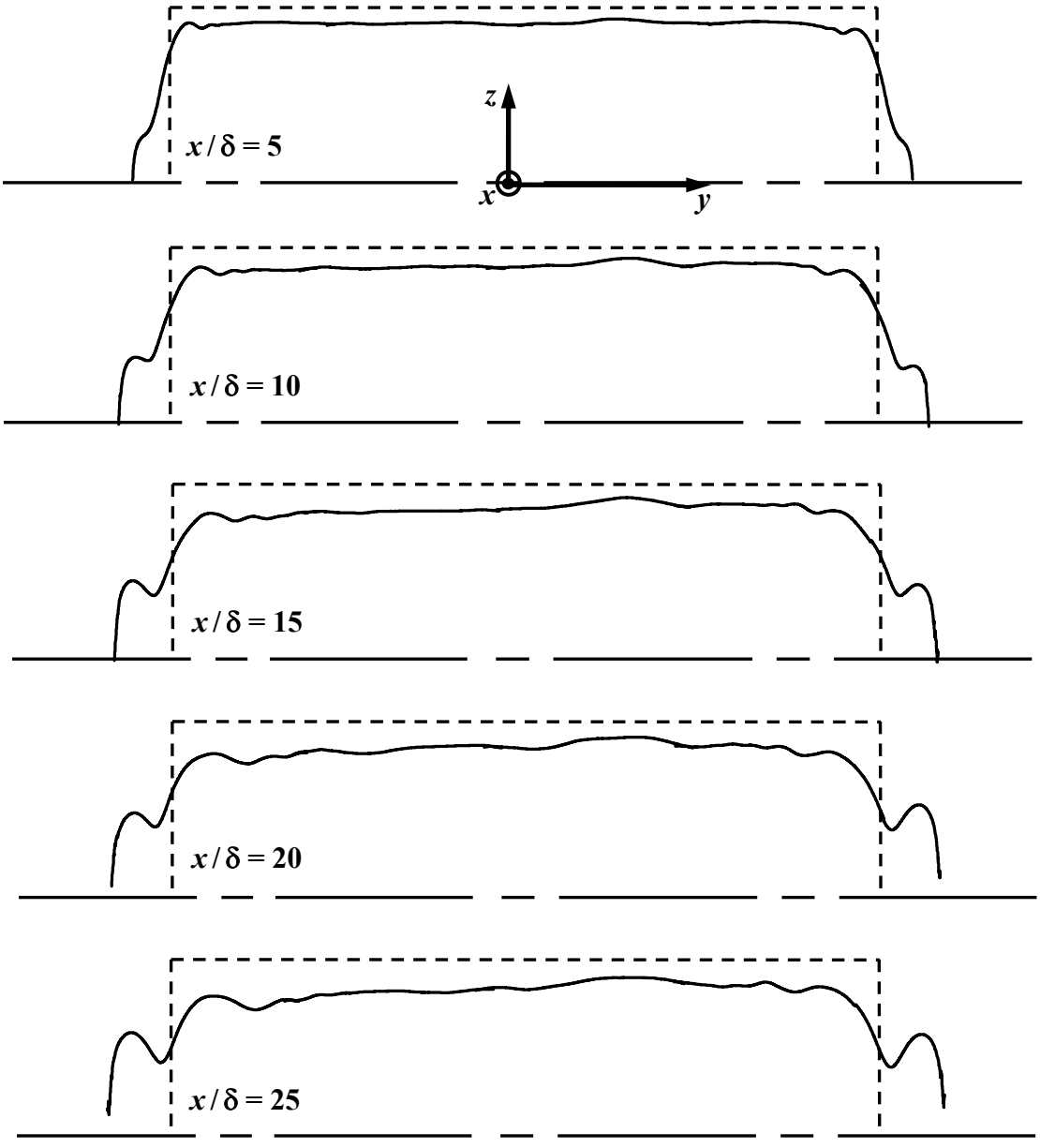

Figure C.11. Free surface of the liquid sheet for Type II.A,B flow conditioning and *Re* = 53,000 at different downstream distances. Note: Flow is out of page and vertical axis is magnified 5×.

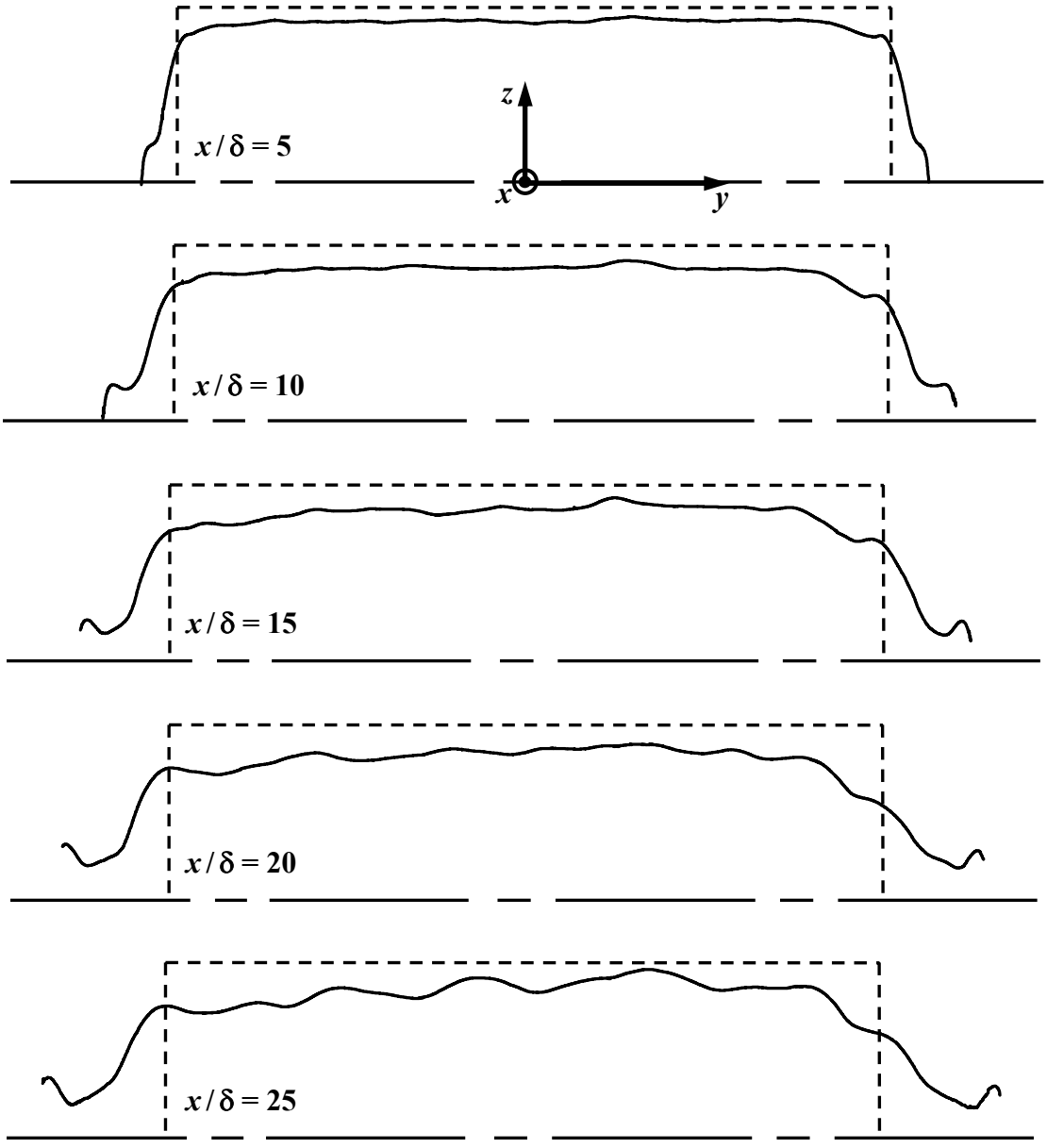

Figure C.12. Free surface of the liquid sheet for Type II.A,B and *Re* = 120,000 at different downstream distances. Note: Flow is out of page and vertical axis is magnified 5×.

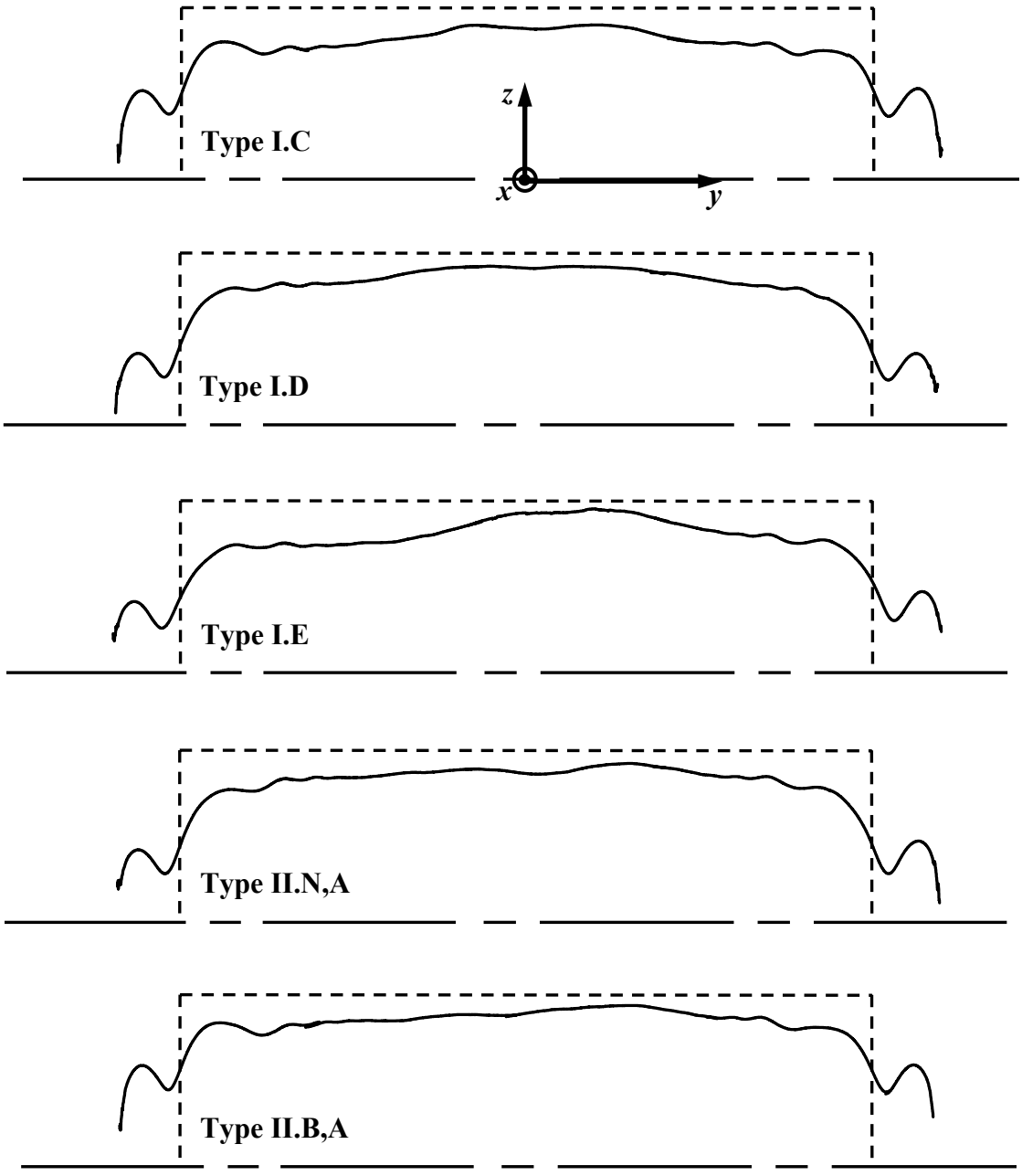

Figure C.13. Free surface of the liquid sheet for different flow conditioning types and Re = 53,000 at $x/\delta = 25$. Note: Flow is out of page and vertical axis is magnified 5×.

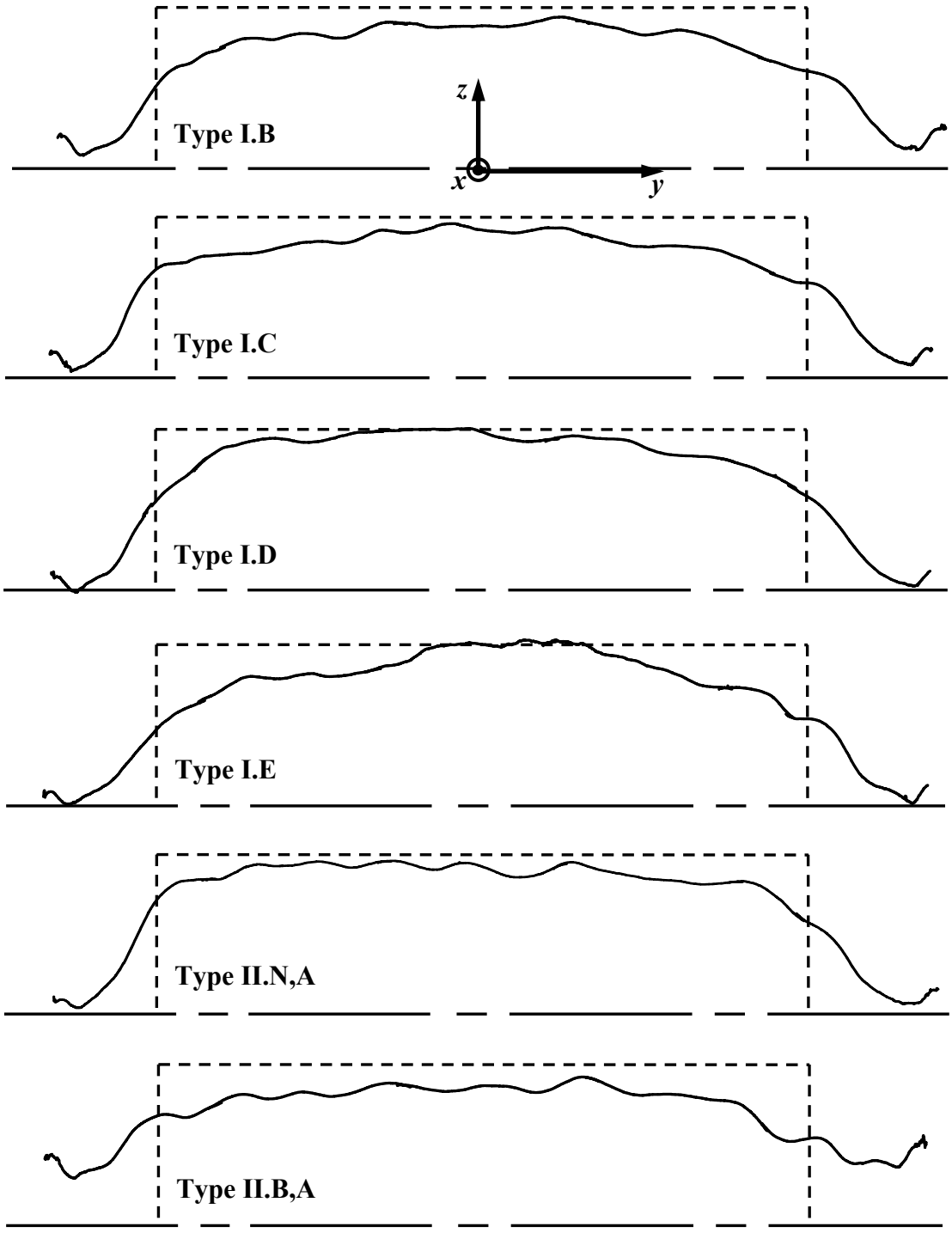

Figure C.14. Free surface of the liquid sheet for different flow conditioning types and Re = 120,000 at $x/\delta = 25$. Note: Flow is out of page and vertical axis is magnified 5×.

APPENDIX D

JOURNAL PUBLICATIONS

This section contains copies of the refereed journal publications authored in the course of this doctoral research project, reproduced here with the permission of the American Nuclear Society. These publications include articles generated directly from this doctoral work and related experimental investigations. The articles in chronological order are:

Anderson, J.K., Durbin, S.G., Sadowski, D.L., Yoda, M. and Abdel-Khalik, S.I., "Experimental studies of high-speed liquid films on downward facing surfaces for inertial fusion energy wet wall concepts", *Fusion Sci. and Technol.*, **43**, 401-407, 2003.

Durbin, S.G., Yoda, M., Abdel-Khalik, S.I., and Sadowski, D.L., "Turbulent liquid sheets for protecting IFE reactor chamber first walls," *Fusion Sci. and Technol.*, **44**, 307-311, 2003.

Durbin, S.G., Koehler, T.P., Reperant, J.J.R., Yoda, M., Abdel-Khalik, S.I. and Sadowski, D.L., "Surface fluctuation analysis for turbulent liquid sheets," *Fusion Sci. and Technol.*, **45**, 1-10, 2004.

Shellabarger, B.T., Durbin, S.G., Yoda, M., Abdel Khalik, S.I., and Sadowski, D.L., "Primary turbulent breakup in turbulent liquid films on downward-facing surfaces," *Fusion Sci. and Technol.*, **46**, 571-576, 2004.

Durbin, S.G., Yoda, M., Abdel-Khalik, S.I., Sadowski, D.L., Koehler, T.P., and the ARIES Team, "Assessment and control of primary turbulent breakup of thick liquid sheets in IFE reactor cavities – the 'hydrodynamic source term'," *Fusion Sci. and Technol.*, **47**, 16-26, 2005.

Durbin, S.G., Yoda, M., and Abdel-Khalik, S.I., "Impact of boundary-layer cutting and flow conditioning on free-surface behavior in turbulent liquid sheets," Accepted for publication *Fusion Sci. and Technol.*, 2005.

Durbin, S.G., Yoda, M., and Abdel-Khalik, S.I., "Flow conditioning design in thick liquid protection," Accepted for publication *Fusion Sci. and Technol.*, 2005.

EXPERIMENTAL STUDIES OF HIGH-SPEED LIQUID FILMS ON DOWNWARD-FACING SURFACES FOR INERTIAL FUSION ENERGY WET WALL CONCEPTS

JONATHAN K. ANDERSON, SAMUEL G. DURBIN II, DENNIS L. SADOWSKI, MINAMI YODA,* SAID I. ABDEL-KHALIK, and the ARIES TEAM
Georgia Institute of Technology, G. W. Woodruff School of Mechanical Engineering
Atlanta, Georgia 30332-0405

Received August 13, 2002
Accepted for Publication September 13, 2002

The fusion event in inertial fusion energy (IFE) reactors creates neutrons, photons, and charged particles that can damage the chamber first walls. The Prometheus design study used a high-speed thin film of molten lead injected tangential to the wall to protect the upper endcap of the reactor chamber from damaging X rays and target debris. To assure full chamber coverage, the film must remain attached. Film detachment under the influence of gravity is most likely to occur on the downward-facing surfaces over the upper endcap of the reactor chamber. Accurate numerical predictions of detachment length are effectively impossible in this turbulent flow because of difficulties in determining appropriate boundary conditions near the detachment point.

As part of the ARIES-IFE study, experimental investigations of high-speed water films injected onto downward-facing planar surfaces at angles of inclination up to 45 deg below the horizontal were therefore performed. The initial growth and subsequent detachment of films with initial thickness up to 2 mm and injection speed up to 11 m/s were measured. To our knowledge, these experiments are the first to investigate the detachment of turbulent liquid films on downward-facing surfaces. The implications of these initial results on thin liquid protection and the "wet wall" concept are discussed.

KEYWORDS: *thin liquid protection, high-speed liquid films, inertial fusion energy*

I. INTRODUCTION

A number of inertial fusion energy (IFE) power plant design studies have been considered using a sacrificial layer to protect the first wall. In thin liquid protection, a sacrificial liquid film flowing along the reactor chamber walls absorbs essentially all the X rays and charged particles from the fusion event, protecting the first wall from damaging radiation and thermal stresses. The Prometheus study,[1,2] which considered thin liquid protection for both heavy-ion beam and laser ignition reactors, proposed using a film of liquid lead to protect the silicon carbide first walls of the reactor chamber, a vertical cylinder with hemispherical upper and lower endcaps with a radius of curvature of 5 m. The film was created using two different systems: (a) a "wetted wall" with a 0.5-mm-thick layer of liquid lead supplied through a porous SiC structure and (b) a "wet wall" with a "film injector" injecting liquid lead through slots at the top of the chamber to create a film a few millimeters thick in contact with the first wall over the upper chamber endcap. The sacrificial lead layer was vaporized by each fusion microexplosion, requiring recondensation and reestablishment of a fresh layer before the next microexplosion.

Both the wetted and wet wall concepts are currently under investigation as part of the ARIES-IFE study.[3] The work described here focuses on the basic hydrodynamics of the wet wall concept. There are several major design issues for robust and effective protection of the upper endcap of the reactor chamber using the wet wall concept. The most important design issue is prevention of the formation of "dry patches" on the first wall, or patches with no protective liquid layer. Consider dry patch formation in a film flow driven by forces tangential to the surface (e.g., thermocapillary and surface forces). Recent results using minimum total energy criteria show that for an isothermal liquid film flowing down a vertical adiabatic wall,[4] the minimum film thickness required

*E-mail: minami.yoda@me.gatech.edu

to rewet any dry patch is <1 mm for most IFE coolants of interest with contact angles ranging from 0 to 90 deg (Ref. 5). Moreover, the minimum film speed (based upon a minimum wetting rate) required for a stable fully wetted liquid film is <1 m/s under the same conditions. The minimum required film thickness is proportional to the square of the gravitational acceleration component along the flow direction.[4] The minimum required film speed, on the other hand, is weakly dependent on gravity ($\sim g^{-0.2}$, where g is gravitational acceleration) and strongly dependent on surface tension ($\sim \sigma^3$, where σ is the surface tension). Hence, at the expected liquid film velocities in IFE systems (which are much greater than 1 m/s), dry patch formation in a film flowing over a vertical wall is the "worst case" from a purely hydrodynamic viewpoint since the streamwise component of gravity is greatest for this orientation.

In the absence of dry patches, preventing detachment of the film from the first wall—which would partially uncover the surface, thereby negating its effectiveness as a wall protectant—is then the most important design issue, inasmuch as it will dictate the spacing of liquid injection and extraction points on the cavity surface. If the curvature of the first wall is negligible, a reasonable assumption given that the radius of curvature for the Prometheus chamber upper endcap is 5 m, or at least three orders of magnitude greater than the film thicknesses of $O(10^{-3}$ m) and film radii of curvature at the detachment point of $O(10^{-2}$ m), the appropriate model problem is a film flowing over a flat surface at various angles of inclination with respect to the horizontal. Detachment is most likely to occur on films flowing over downward-facing surfaces (i.e., surfaces at a negative angle of inclination with respect to the horizontal), where the component of gravity normal to the surface promotes film detachment. Moreover, this flow geometry—where a denser "heavy" liquid flows above a less dense "light" near-vacuum—may be susceptible to droplet and even dry patch formation due to Rayleigh-Taylor instability.

As the first part of our study of the wet wall concept, turbulent films on downward-facing surfaces were therefore experimentally studied by injecting water through rectangular slot nozzles tangentially onto the underside of a glass plate in atmospheric pressure air. The effect of initial film (i.e., nozzle) thickness δ, initial film injection velocity U, and plate inclination angle below the horizontal θ was characterized in terms of the Froude, Reynolds, and Weber numbers, or $\mathrm{Fr} = U/\sqrt{g(\cos\theta)\delta}$, $\mathrm{Re} = U\delta/\nu$, and $\mathrm{We} = \rho U^2\delta/\sigma$, respectively. Here, g is the gravitational acceleration, ν is the fluid kinematic viscosity, and σ is the surface tension between the fluid and the surrounding gas. In these initial studies, $\delta = 1$ to 2 mm, $U = 1.9$ to 11 m/s, and $\theta = 0$ to 45 deg, giving Fr = 15 to 121, Re = 3700 to 21 000, and We = 100 to 3200.

To our knowledge, there have been few studies of turbulent liquid films on downward-facing surfaces. Hashidate et al.[6] studied films on a downward-facing acrylic surface for Re = 10 to 500 and $\theta = 0$ to 30 deg for water with surfactants to vary the surface tension, and they concluded that surface roughness had a major impact on detachment length. These results on film detachment and lateral spread—the first to our knowledge for such high Reynolds number turbulent liquid films—will help provide an experimental design database for wet wall concepts in thin liquid protection of IFE reactor chamber first walls.

II. EXPERIMENTAL APPARATUS AND PROCEDURES

II.A. Flow Loop

The pump-driven recirculating flow loop used to produce the thin liquid films is shown in Fig. 1. Water is driven by a 0.5-hp centrifugal pump (Teel 2P39C) through an adjustable butterfly valve and a flexible coupling (A). The water passes through a flow straightening section (B) and exits through a rectangular nozzle (C) at an adjustable angle with respect to the horizontal. The water is injected by the nozzle tangentially onto the underside of a tempered float glass plate of width 0.4 m extending a distance $x = 0$ to 183 cm downstream of the nozzle exit. The flow, which either detaches from the glass surface or hits a vertical splash guard at the downstream end of the glass plate, then falls into an 840 ℓ (220-gal) receiving tank below, where it is recirculated by the pump. The coordinate system for this flow is defined as follows: x along the flow direction, y along the long dimension of the film or parallel to the glass surface, and z downward along the short dimension of the film or normal to the glass surface.

Three different nozzles, all fabricated using stereolithography rapid prototyping at the Georgia Institute of Technology Rapid Prototyping and Manufacturing Institute from DSM Somos® 7110 resin, were used in these

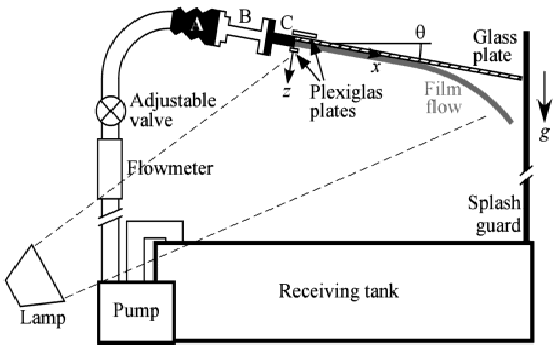

Fig. 1. Schematic of flow loop (side view).

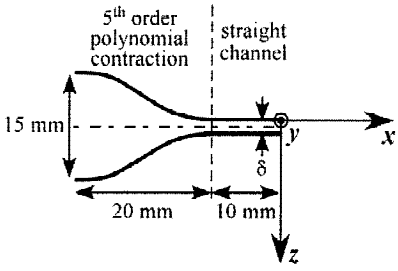

Fig. 2. Nozzle cross section.

experiments. The fabrication tolerance was 0.1 mm, based upon the spatial resolution of the rapid prototyping machines. All the nozzles have a two-dimensional fifth-order polynomial contraction in their z dimension from 1.5 cm upstream to δ over an x extent of 2 cm, followed by a straight channel with an x extent of 1 cm (Fig. 2). This type of contraction is extensively used in wind tunnels and water channels to produce uniform flow with thin boundary layers. The nozzles have a y dimension at their exit of 5 cm, giving rectangular exits with aspect ratios of 50, 33, and 25 for nominal initial film thicknesses at the nozzle exits of $\delta = 1$, 1.5, and 2 mm, respectively. In all experiments, the water was injected parallel to the glass plate by clamping the nozzle along its entire y extent at its straight channel exit section parallel to and flush with the underside of the glass plate using two parallel Plexiglas plates.

The flow straightening section, also fabricated from DSM Somos® 7110 resin, consisted of a perforated plate (53.6% open area ratio, 0.21-cm-diam staggered holes), followed by a 1.8-cm section of honeycomb with cell diameter 0.16 cm, both of stainless steel. The edge-to-edge spacing between the perforated plate and honeycomb and the honeycomb and the nozzle inlet was 7 and 50 mm, respectively. The butterfly valve adjusts the flow rate and hence initial film velocity U at the nozzle exit. In all cases, U is determined using a Rotameter-type flowmeter just upstream of the butterfly valve (see Fig. 1).

II.B. Flow Visualization

The film first spreads laterally (i.e., along the surface of the glass plate) and then detaches from the glass plate some distance downstream of the nozzle exit. This film "detachment length" x_d and the lateral dimension, or width, of the film W were studied as a function of various flow parameters. Although droplet formation was typically observed at the film free surface upstream of the detachment point, no dry patch formation was observed before detachment. Detachment length x_d was measured by imaging the turbulent water films from the side to obtain x-z planes ("side views") of the flow, which was illuminated obliquely from below (see Fig. 1) by a 425-W lamp. Individual images were recorded at an exposure of 8 ms by a progressive scan charge-coupled-device camera (Pulnix TM-9701) onto the random access memory of a personal computer using a framegrabber card (ImageNation PX610A) as 8-bit grayscale 640 col × 480 row images. Each individual image spans 7τ to 90τ, where the flow convective timescale $\tau = \delta/U = 0.09$ to 1.1 ms. A ruler attached to the upper side of the glass plate was used to measure the detachment length x_d (in inches), defined here as the distance measured along x from the nozzle exit where the film detaches from the plate surface (Fig. 3a) on each image. The film detaches at slightly different x locations across the lateral (y) extent of the film at low U, and the largest value of δ = 2 mm (Fig. 3b). In all cases, the detachment distance on each image was therefore taken to be the smallest x value, or the location farthest upstream, at which film detachment occurred. Since the detachment distance on a single image can vary by up to ±3.5 cm for this turbulent flow, the values reported here for x_d are the average of 20 independent realizations obtained from images taken of the flow over ~60 s.

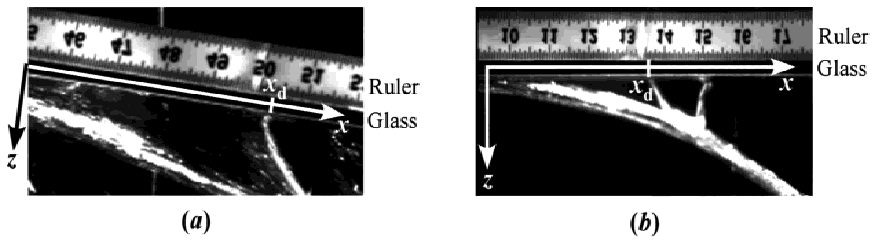

Fig. 3. Typical side view images near the film detachment point showing an x-z plane of the flow and the detachment distance x_d for (a) $\delta = 0.1$ cm, $\theta = 10$ deg, Fr = 90, Re = 8600, and We = 1070 and for (b) $\delta = 0.2$ cm, $\theta = 0$ deg, Fr = 13.5, Re = 3600, and We = 98. Note the detachment of the water from the glass plate on the lower right side of both images and the multiple detachment points in (b). The ruler on the top of both images is in inches.

The film width, or y extent, $W(x)$ was measured through the top of the glass plate as a function of distance downstream of the nozzle by direct visual inspection (Fig. 4), with data obtained every 5 cm for $x < x_d$. In all the experimental cases studied here, $W(x)$ varied by less than ± 1 mm over time at any given downstream location. Initially, the film spreads along and normal to the glass surface after leaving the nozzle, with lateral (i.e., along the y direction) spreading rates dW/dx much greater than those normal to the surface, or along the z direction. The lateral spreading rate then decreases, with W (versus dW/dx) decreasing at lower Fr, before gravitational effects overcome surface tension effects and the film detaches from the underside of the glass plate.

III. RESULTS AND DISCUSSION

III.A. Detachment Distance x_d

The average detachment distance normalized by initial film thickness x_d/δ is shown as a function of Fr for $\delta = 1$ mm (open symbols), 1.5 mm (black symbols), and 2 mm (gray symbols); and $\theta = 0$ deg (squares), 10 deg (diamonds), 30 deg (triangles), and 45 deg (circles) in Fig. 5. In the cases where gravitational effects normal to the plate are weakest (large θ, small δ, and large Fr), film detachment was not observed over the entire glass plate, implying that $x_d > 183$ cm; obviously no data are presented for these cases. In the cases where detachment was observed, the nondimensional detachment distance increases with Fr, as expected, since gravitational effects normal to the plate become smaller as Fr increases. Although the actual value of x_d/δ varies with both δ and θ, the slope of the various x_d/δ curves for each δ and θ appears to be similar, suggesting that the growth rate of nondimensional detachment length with Fr is independent of initial film thickness and inclination angle. A "virtual origin," such as those used in various types of turbulent flows, may then be used to account for different initial conditions between various experimental runs. There also appears to be a slight "leveling off" of the x_d/δ curves at higher Fr (see open triangles and diamonds, for example). These detachment distance data were also plotted as functions of Re and We, but no clear trends were observed. The Froude number therefore appears to be the only significant dimensionless group for characterizing detachment distance. This result is hardly surprising since Fr is the only one of these three dimensionless groups that includes the effects of gravity and plate inclination angle—parameters that both have a significant impact on film detachment.

In the Prometheus design, $\delta = 0.5$ mm and $U > 8$ m/s, giving Fr > 120. Extrapolation of the detachment length data in Fig. 5 suggests that a film injected at the top of the endcap ($\theta \approx 0$ deg) will have a mean detachment length $x_d > 1600\delta = 0.8$ m. Given that the hemispherical upper endcap of 5-m radius will have a dimension along its colatitude of 7.9 m from top to bottom, the protective film will detach and form droplets

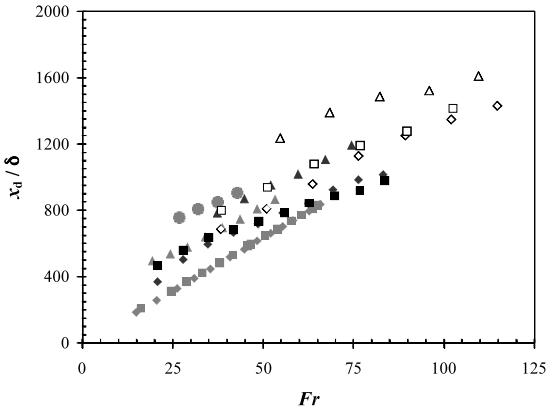

Fig. 5. Plot of nondimensional detachment distance x_d/δ versus Froude number Fr for $\delta = 1$ mm (open symbols), 1.5 mm (black), and 2 mm (gray) and $\theta = 0$ deg (squares), 10 deg (diamonds), 30 deg (triangles), and 45 deg (circles).

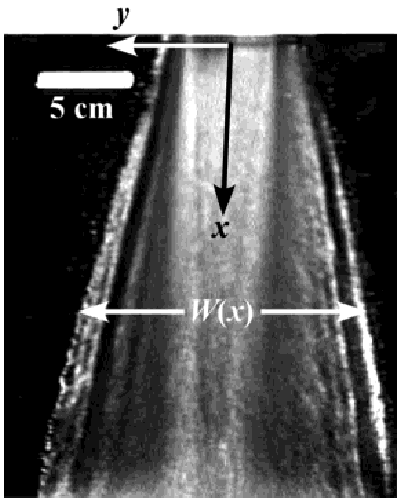

Fig. 4. Image of the turbulent film viewed at an oblique angle through the glass plate for $\delta = 0.1$ cm, $\theta = 30$ deg, Fr = 81, Re = 7200, and We = 790. Here, the sheet width $W(x)$ increases from ~7.5 to 18 cm over a downstream extent of 23 cm. Although not evident in this view, the film is essentially symmetric around its centerline (the x axis).

well before the end of the endcap. Maintaining an attached film over the entire upper endcap will therefore require some type of "composite" structure, possibly involving several injection slots over the colatitude of the endcap and some type of suction downstream of each injection slot to remove the film before it detaches.

We hypothesize that the major sources of error in these data are slight misalignments between the nozzle and the glass plate and variations in the initial film thickness δ due to our fabrication tolerances. The maximum misalignment between the y axis of the nozzle and the surface of the glass plate is ~1 deg, resulting in a height difference of 0.9 mm, or 0.45 to 0.9δ, across the 5-cm y extent of the nozzle exit. The minimum geometric tolerance for these nozzles, based upon the spatial resolution of the rapid prototyping machine used to fabricate these components, is 0.1 mm absolute, or 5 to 10% of δ. The resultant variation in initial film thickness over the y extent of the nozzle with respect to the glass surface due to these two factors can affect the detachment distance and film width by introducing local variations in pressure gradient and flow speeds.

Other potential sources of error in these data include local variations in the wettability of the glass plate due to surface and liquid contamination. The contact angle of water on the glass plate used in these experiments was estimated by visual inspection to lie between 30 and 35 deg. Although the glass plate was cleaned with a commercial ammonia-based glass cleaner at the beginning of each experimental run, the contact angle varies over the glass surface by at least a few degrees because of contamination of the water (which remained in the facility for up to a week) and the glass plate. Nevertheless, little variation was observed in either mean detachment length or film width over independent experimental runs under otherwise identical conditions. The geometry of the glass plate is not considered to be a significant source of error in these experiments since the overall curvature of tempered glass should be minimal and the average surface roughness of glass manufactured using the float process is typically $<10^{-6}$ m.

The trends observed in Fig. 5 are most consistent for $\delta = 2$ mm (gray symbols), where variations in initial film thickness due to nozzle-plate misalignment and nozzle fabrication tolerances are the smallest for the cases studied. Data obtained for the $\delta = 2$ mm nozzle were therefore used to characterize the lateral spreading rate of the film, as discussed in Sec. III.B.

III.B. Average Film Width *W*

Figure 6 shows the film width or y extent along the glass surface normalized by the exit width W/W_o as a function of distance downstream of the nozzle exit normalized by the initial film thickness x/δ for $\delta = 2$ mm and Re = 18 000 at $\theta = 0$ deg (squares), 10 deg (diamonds), 30 deg (triangles), and 45 deg (circles). The

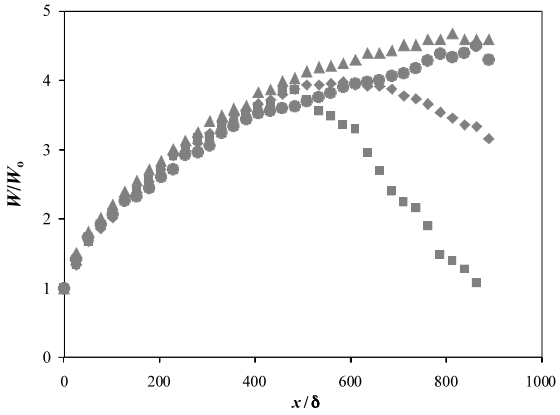

Fig. 6. Plot of normalized average film width as a function of the ratio of distance downstream of the nozzle exit to initial film thickness for $\theta = 0$ deg (squares), 10 deg (diamonds), 30 deg (triangles), and 45 deg (circles) for $\delta = 2$ mm, Re = 18 000, and We = 2450.

initial width of the film at the nozzle exit $W_o = 5$ cm in all cases. For $x/\delta \leq 400$, the film width is essentially independent of θ, probably because the effects of initial conditions are dominant in this "near-field" region of the flow, and the film spreads until it is more than 3.5 times its initial width. In the "far-field" region ($x/\delta > 400$), however, dW/dx increases with θ. The film width actually decreases for $\theta = 0$ and 10 deg, suggesting that the film must have significant growth normal to the plate to conserve linear momentum. At higher angles of inclination, namely $\theta = 30$ and 45 deg, the sheet continues to grow in the far-field region, reaching widths nearly quintuple its initial value. The marked lateral growth observed for these films is in agreement with previous experimental results for three-dimensional turbulent wall jets, where fluid is injected through a rectangular slot into a large quiescent reservoir of the same fluid. Recent simulations show that the remarkable lateral spread of these flows is primarily due to the creation of streamwise vorticity.[7] The W/W_o curves for both angles are essentially the same, suggesting that the film reaches an asymptotic shape (at least in the y dimension) at higher values of inclination angle. Finally, the film does not separate until $x/\delta > 400$ in all cases.

Figure 7 shows dimensionless film width W/W_o plotted as a function of normalized downstream distance x/δ at $\delta = 2$ mm and $\theta = 30$ deg for Re = 7500 ($\times$), 12 400 (∇), and 18 600 ($+$). Here, W is independent of Re (versus θ in Fig. 6) for $x/\delta \leq 400$. The film width also appears to be independent of Re at the two higher Re, suggesting that the film reaches an asymptotic shape (at least along the y direction) above a certain Re.

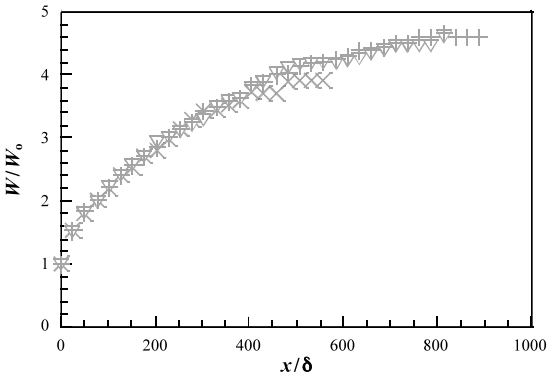

Fig. 7. Normalized average film width versus normalized downstream distance at $\delta = 2$ mm, $\theta = 30$ deg for Re = 7500 ($\times$), 12 400 (∇), and 18600 ($+$).

Defining the streamwise extent of the near-field region as x_c, and the mean width of the film at the end of the near-field region as W_c [i.e., $W(x_c) = W_c$], Figure 8 shows a graph of W_c/W_o as a function of Fr for all experimental cases studied here: $\delta = 1$ mm (open symbols), 1.5 mm (black symbols), and 2 mm (gray symbols); and $\theta = 0$ deg (squares), 10 deg (diamonds), 30 deg (triangles), and 45 deg (circles). For Froude numbers above ~40, W_c, which is an indication of the maximum y dimension of the flow, is essentially independent of Fr and δ. However, W_c appears to increase slightly with $W_c/W_o \approx 3.6$ to 4.5 for $\theta = 0$ to 45 deg. Although not shown here, similar trends were observed for W_c/W_o as a function of Re. The marked lateral spread of these film flows suggests that the longitudinal spacing of injection slots in the Prometheus design can be three to four times their longitudinal dimension while still maintaining adequate coverage, assuming that adjacent films merge smoothly.

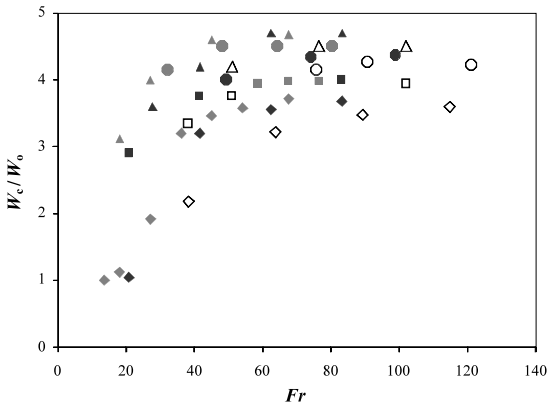

Fig. 8. Plot of normalized film width at the end of the near-field region W_c/W_o as a function of Froude number Fr for $\delta = 1$ mm (open symbols), 1.5 mm (black), and 2 mm (gray) and $\theta = 0$ deg (squares), 10 deg (diamonds), 30 deg (triangles), and 45 deg (circles).

IV. SUMMARY

Mean detachment distance and average film width (i.e., dimension along the plate) were experimentally characterized for thin turbulent liquid films on downward-facing surfaces for various flowrates, initial film thicknesses, and angle of inclination. In many cases, droplet formation was observed at the film free surface upstream of the detachment point. In all cases, dry patch formation was not observed. Although the absolute value of detachment distance is determined by the initial flow conditions, change in mean detachment distance was found to be a function only of Froude number, a dimensionless group characterizing the relative importance of inertial and gravitational effects. The flow has a large lateral spread along the surface, growing up to fivefold in the y dimension. Based upon this lateral growth, we define a near-field region of the turbulent film where the lateral growth is determined by initial conditions and appears independent of other flow parameters such as Reynolds number. The lateral dimension of the flow at the end of this region appears to be essentially independent of Froude number and initial film thickness but appears to depend weakly upon inclination angle. The lateral growth of the flow in the far-field region farther downstream is a strong function of inclination angle, with the film lateral dimension actually decreasing at small angles of inclination. In all cases, the film detaches in the far-field.

In terms of implications for the wet wall concept, the initial results from this experimental study of turbulent liquid films flowing over downward-facing surfaces suggest the following:

1. Any film injected at the top of the upper endcap of the reactor chamber in the Prometheus design will detach well before the bottom of the endcap. At a minimum, the wet wall concept will therefore require multiple injection slots and some mechanism to remove liquid before the film forms droplets or detaches.

2. The injected films will spread to at least 3.5 times their initial width, improving the lateral (presumably longitudinal) spacing requirements for the injection slots.

The aim of this study is to provide "design windows" for thin liquid protection schemes. Given that the Prometheus study reported that liquid lead did not wet silicon carbide, and suggested that this issue required further consideration, we intend next to characterize the

effect of wettability or contact angle on film detachment and lateral spread by studying turbulent films of water on downward-facing surfaces of various chemical compositions (e.g., Teflon). Studies of how turbulent liquid film flows recover around cylindrical dams protecting penetrations into the chamber first wall for target injection and ignition beam propagation are also planned. Since this flow is likely to separate around the dam and possibly form droplets and then "reattach" some distance downstream of the trailing edge of the dam (much like uniform flow around a circular cylinder), some type of aerodynamic fairing may be required on the downstream end of the penetrations to protect the first wall in the neighborhood of a beam or target injection port.

ACKNOWLEDGMENTS

This work was performed as part of the ARIES-IFE study supported by the U.S. Department of Energy Office of Fusion Energy Sciences through contract DE-FG02-01ER54656. We thank the members of the ARIES project team for numerous discussions and helpful suggestions.

REFERENCES

1. L. M. WAGANER et al., "Inertial Fusion Energy Reactor Design Studies: Prometheus Final Report," MDC 92E0008 (DOE/ER-54101), U.S. Department of Energy (1992).

2. L. M. WAGANER, "Innovation Leads the Way to Attractive Inertial Fusion Energy Reactors—Prometheus-L and Prometheus-H," *Fusion Eng. Des.*, **25**, 125 (1994).

3. S. SHIN, F. ABDELALL, D. JURIC, S. I. ABDEL-KHALIK, M. YODA, D. SADOWSKI, and the ARIES TEAM, "Fluid Dynamic Aspects of the Porous Wetted Wall Protection Scheme for Inertial Fusion Energy Reactors," *Fusion Sci. Technol.*, **43**, paper #269702 (2003).

4. M. S. EL-GENK and H. H. SABER, "Minimum Thickness of a Flowing Down Liquid Film on a Vertical Surface," *Int. J. Heat Mass Transfer*, **44**, 2809 (2001).

5. S. I. ABDEL-KHALIK and M. YODA, "Design Considerations for Thin Liquid Film Wall Protection Scheme," presented at ARIES Project E-Meeting; available on the Internet (⟨http://aries.ucsd.edu/ARIES/MEETINGS/0110/⟩) (Oct. 24, 2001).

6. Y. HASHIDATE, K. SHIODA, and S. NONAKA, "Experimental Study on the Flow Behavior of a Liquid Film on an Inclined Downward-Facing Plate," *Trans. Jpn. Soc. Mech. Eng. B*, **59**, 770 (1993) (in Japanese with English abstract).

7. T. J. CRAFT and B. E. LAUNDER, "On the Spreading Mechanism of the Three-Dimensional Turbulent Wall Jet," *J. Fluid Mech.*, **435**, 305 (2001).

Jonathan K. Anderson (MS, mechanical engineering, Georgia Institute of Technology, 2002) is a graduate research assistant in the George W. Woodruff School of Mechanical Engineering, Georgia Institute of Technology. His research is in the area of high-speed liquid films on downward-facing surfaces.

Samuel G. Durbin II (MS, mechanical engineering, Georgia Institute of Technology, 2002) is a graduate research assistant and Fusion Energy Sciences Fellow in mechanical engineering at the Georgia Institute of Technology. His research is in the area of turbulent liquid sheets for thick liquid protection applications.

Dennis L. Sadowski (MS, mechanical engineering, University of Illinois, Chicago, 1986) is a research engineer in mechanical engineering at the Georgia Institute of Technology. His current research interests are in the areas of thermal hydraulics and the construction of complex experimental systems.

Minami Yoda (PhD, aeronautics and astronautics, Stanford University, 1993) is associate professor in mechanical engineering at the Georgia Institute of Technology. Her research interests are in the areas of experimental fluid mechanics and optical diagnostic techniques.

Said I. Abdel-Khalik (PhD, mechanical engineering, University of Wisconsin, 1973) is Southern Nuclear Distinguished Professor at the George W. Woodruff School of Mechanical Engineering at the Georgia Institute of Technology. His research interests are in the areas of reactor engineering and thermal hydraulics.

TURBULENT LIQUID SHEETS FOR PROTECTING IFE REACTOR CHAMBER FIRST WALLS

S.G. Durbin†, M. Yoda, S.I. Abdel-Khalik and D.L. Sadowski
G. Woodruff School of Mechanical Engineering
Georgia Institute of Technology
Atlanta, GA 30332-0405 USA
†(404) 385-1891 gte397r@prism.gatech.edu

ABSTRACT

Turbulent liquid sheets have been proposed to protect solid structures in fusion power plants by absorbing damaging radiation. Establishing an experimental design database for this flow would therefore be valuable in various thick liquid protection schemes. The effect of initial conditions on the flow free-surface fluctuation was studied experimentally for vertical turbulent sheets of water issuing downwards from nozzles of thickness (small dimension) δ = 1 – 1.5 cm into ambient air. Sheets issuing from nozzles with both two- and three-dimensional fifth-order polynomial contractions with exit aspect ratios of 6.7 and 10 were investigated at Reynolds numbers ranging from 2×10^4 to 1×10^5. Mean velocity and turbulence intensity profiles were measured just upstream of the nozzle exit using laser-Doppler velocimetry to quantify initial conditions. Planar laser-induced fluorescence was used to visualize the free surface geometry of the liquid sheet in the near-field region up to 25δ downstream of the nozzle exit. Fluctuations of the free surface, or surface ripple, are characterized by the standard deviation in the position of the gas/liquid interface.

I. INTRODUCTION

Inertial fusion energy (IFE) requires novel solutions to address the issues of first wall protection and heat removal in the reactor chamber. The High-Yield Lithium-Injection Fusion Energy (HYLIFE-II) conceptual IFE power plant proposed using liquid sheets, or slab jets, of molten Flibe (Li_2BeF_4) for cooling and attenuation of damaging radiation and target debris.[1] A lattice of stationary jets forms a protective grid that allows target injection and heavy-ion driver beam propagation, while protecting the reactor chamber first walls from the fusion event. Thick liquid protection can therefore help make fusion energy commercially attractive by reducing chamber size and prolonging chamber lifetime, thus reducing the cost of electricity produced by fusion by at least 30%.[2]

Designing nozzles and flow straighteners that create smooth stationary jets is a crucial issue for effective protection of the first walls and final focus magnets. Minimizing surface ripple in, or free-surface fluctuations, of, liquid sheets will minimize driver beam clipping while maximizing protection. For effective thick liquid protection, the distance between the driver beam and the free surface of the liquid sheet should not exceed 0.5 cm, or about 7% of the short dimension of the nozzle exit δ.[3]

Moreover, little is known from a fundamental fluid physics perspective about turbulent liquid sheets, or rectangular jets with a very high jet to surrounding fluid density ratio. Turbulent flows are highly sensitive to initial conditions. Understanding the impact of initial conditions such as nozzle geometry on surface ripple is hence a critical design issue for thick liquid protection. These turbulent free-surface flows cannot at present be accurately computed, given the prohibitively high computational cost of tracking moving interfaces and directly simulating flows at Reynolds numbers above 10^4.

This work experimentally studied turbulent sheets of water issuing vertically downwards into ambient air from three different nozzle geometries at Reynolds numbers ranging from 2×10^4 to 1×10^5. The liquid sheets proposed for HYLIFE-II have an initial thickness δ = 7 cm

and Reynolds numbers of about 2.4×10^5. The results here are at about half the prototypical Reynolds numbers for smaller jets. Initial conditions are quantified by measuring velocity and turbulence intensity profiles just upstream of the nozzle exit using laser-Doppler velocimetry (LDV). The free surface ripple is directly studied using the planar laser-induced fluorescence (PLIF) technique.

II. APPARATUS AND PROCEDURES

A. Flow Loop

A pump-driven recirculating flow loop was used in these experiments. Water was supplied by a 7.5 hp centrifugal pump from the bottom receiving tanks (total volume 2800 L) 5.5 m below the test section. The flow from the pump passed through the flow conditioning section and nozzle, forming the liquid sheet in the open test section.

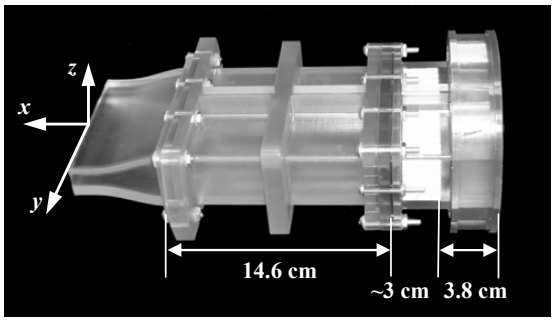

Figure 1 Flow straightener assembly (shown with Nozzle I).

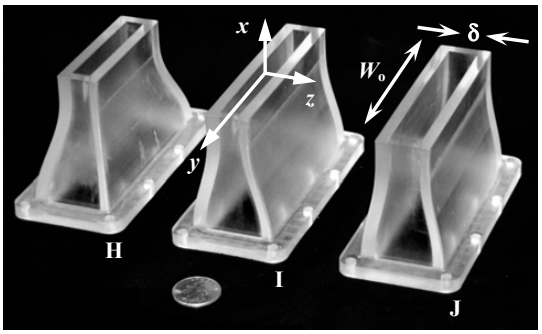

Figure 2 Photo of nozzles H, I and J .

The flow straightener was produced in three sections using stereolithography rapid prototyping (Figure 1). Flow conditioning elements consisted of a stainless steel perforated plate PP (50% open area ratio, 4.8 mm diameter staggered holes) followed by a 2.5 cm section of polycarbonate honeycomb HC with 0.32 cm cell diameter and a stainless steel fine screen FS (30 × 30 mesh size, 37.1% open area ratio, 0.33 mm wire diameter, 0.51 mm open cell width). The streamwise edge-to-edge spacings between the PP and HC and the HC and FS were 3.8 cm, and 0.5 cm, respectively, with the FS 14.6 cm above the nozzle inlet. The overall x-dimension of the flow straightener was 21.6 cm. The jet exited into the 1500 L top receiving tank 1.9 m downstream of the nozzle exit and drained into the bottom receiving tanks, where it was recirculated by the pump. The pump frequency was 60 Hz, well below the measured natural frequency of the flow loop of approximately 8.6 kHz.

Three different nozzle geometries (Figure 2), produced in DSM® Somos WaterClear™ resin using rapid prototyping, were studied:

- H had 3D 5th order polynomial contractions along both z and y and exit dimensions δ =1 cm × W_o = 6.7 cm (z × y), for an exit aspect ratio $AR = W_o / \delta = 6.7$.
- Nozzle I had a 2D 5th order polynomial contraction along z with δ =1 cm and W_o = 10 cm, giving AR = 10.
- Nozzle J was similar to I except that δ =1.5 cm, W_o = 10 cm and AR = 6.7.

All nozzles had a 1 cm long (x-dimension) straight channel section just upstream of the exit for acquiring LDV data.

B. Measurement of Initial Conditions

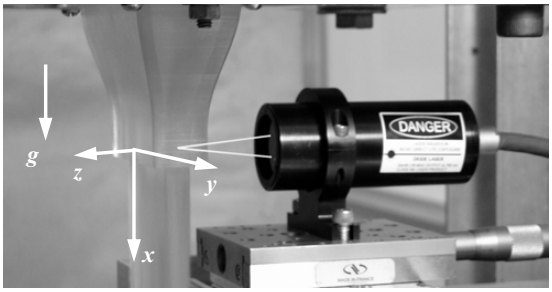

Figure 3 Photo of the LDV probe head (shown with simulated laser beams).

Velocity and turbulence intensity profiles were measured directly at the nozzle exit using a single-component LDV system (Viosense MiniLDV-50) in backscatter mode with a working distance of 46 mm and a probe volume with nominal dimensions of 20 μm (x) × 40 μm (y) × 100 μm (z) (Figure 3). Data were acquired about 2 mm above the nozzle exit to allow propagation of both laser beams through the nozzle wall. The water was seeded with TiO_2 particles having a 10 μm nominal diameter. The

Doppler bursts were converted to voltage signals by an avalanche photo-diode (APD), bandpass filtered by a Krohn-Hite 3940, digitized by a National Instruments 5112 onto a PC HD, and converted to velocity using a FFT. The resultant velocity data were then used to calculate mean velocity and turbulence intensity (standard deviation). Profiles of the mean x-velocity component U and its rms fluctuation U' were acquired along the y-axis of the jet (*i.e.*, for $z = 0$) working inwards from the nozzle wall. Velocities were sampled at a mean rate of 20 Hz with 500 velocity samples used to calculate average and standard deviation. In all cases, the averaged velocity data were acquired over at least 3000τ, where the convective time scale $\tau = \delta / U_o$.

C. Free Surface Visualization

PLIF was used to visualize the free surface of the liquid sheet.[4] The water in the flow loop was dyed with 19.1 mg/L (about 51 μM) disodium fluorescein (uranine), a dye that fluoresces in the yellow-green when illuminated at 488 nm. A 0.5 W multiline argon-ion laser beam was passed through a notch filter (Edmund Scientific NT30-907) to obtain about 0.2 W at 488 nm. The flow was illuminated at various downstream (x) locations by the 488 nm laser light sheet with a thickness (x-dimension) of 0.2 cm.

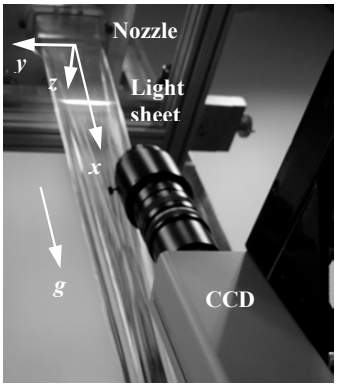

Figure 4 Photo of PLIF setup.

The free surface, which is the interface between fluorescing water and non-fluorescing air, was imaged obliquely from below at 30 Hz by a B/W CCD camera (Kodak Model ES 1.0) with a close-focusing macro video lens (Navitar Zoom 7000) (Figure 4). A high-pass wavelength filter (Sunpak Yellow-8) with a cut-off frequency of 500 nm was used to image only fluorescence, and reject the shorter-wavelength illumination.

The field of view for each image is about 3.1 cm (y) × 3.1 cm (z). The free surface is e visualized using 3–4 overlapping segments that span one side of the entire y-extent of the flow. Each segment was composed of 100 consecutive images, each with an exposure of τ, with an entire segment spanning at least 650τ. The individual frames were stored as 8-bit 1008 × 1008 image bitmaps on a PC hard drive using digital video recording software (Video Savant 3.0).

In each image, the free surface is found using a threshold-based edge detection algorithm written in MATLAB. Figure 5 illustrates the various steps involved in processing the raw images to determine the free surface. The threshold grayscale was chosen based upon the grayscale histogram for the entire dataset. In all cases, it was the first grayscale value to the right of the histogram background (dark) peak where the number of pixels at that value fell to 5% that of the background peak maximum. For every segment, the instantaneous free-surface locations are determined for each of 100 thresholded frames using a standard edge detection scheme and used to calculate the standard deviation of the z-position of the free surface. This standard deviation was spatially averaged over the central 75% of the flow (based on W_o) to obtain σ_z.

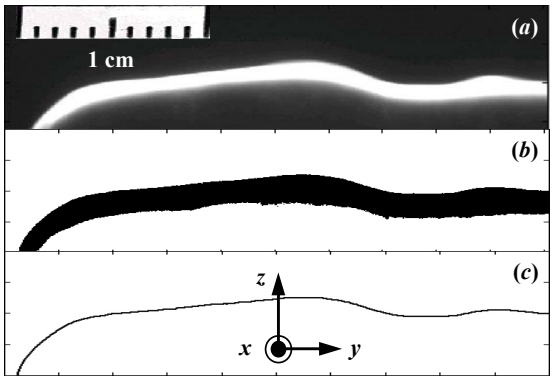

Figure 5 Images processing steps for identifying the liquid sheet free surface: (*a*) Raw PLIF image; (*b*) Thresholded image; and (*c*) Free surface obtained with edge detection.

Each segment of the free surface has a slight overlap with neighboring segments. In all cases, the free surface fluctuations in this overlap region are taken to be those calculated for the left segment. The extent of the overlap region is known from a reference scale imaged in each frame. No significant discontinuities were observed using this procedure, since the central portion of the jet exhibits nearly constant surface fluctuations.

III. RESULTS AND DISCUSSION

A. Mean Velocity and Turbulence Intensity Profiles

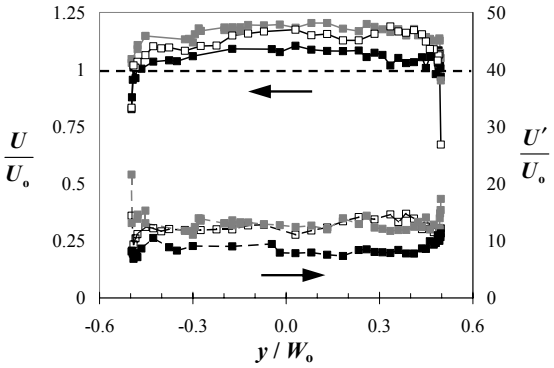

Figure 6 Normalized mean velocity (solid lines) and turbulence intensity (dashed lines) profiles for nozzle J at *Re* = 25,000 (white), 50,000 (gray) and 97,000 (black symbols).

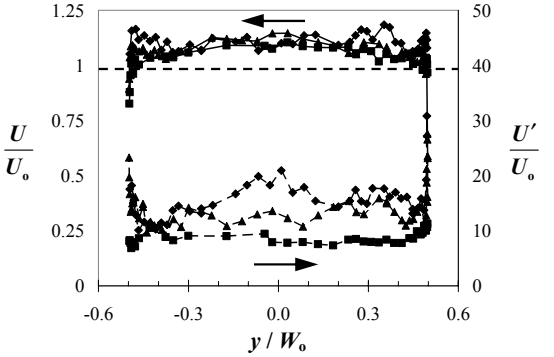

Figure 7 Plot of normalized mean velocity (solid lines) and turbulence intensity (dashed lines) for nozzles H (◆), I (▲) and J (■) at *Re* = 97,000.

Profiles were acquired for the three nozzles at Reynolds numbers $Re = U_o\delta / \nu$ = 25,000, 50,000, and 97,000. The average velocity $U_o = Q / (W_o \delta)$, where Q is the volumetric flowrate. Measurements were taken at x/δ = 5, 10, 15, 20, and 25. Figure 6 shows mean velocity (solid lines) and turbulence intensity (dashed lines) characterized by rms fluctuations, both normalized by U_o, as a function of y-location normalized by W_o for nozzle J at *Re* = 25,000 (white), 50,000 (gray) and 97,000 (black symbols). Both the average velocity and turbulence intensity are essentially constant across the central portion of the jet, suggesting that the flow at these *Re* is close to plug, or uniform, flow. The dashed line at unity indicates the expected velocity value for uniform flow. The turbulence intensity increases rapidly near the nozzle walls, suggesting the presence of a turbulent boundary layer.

Figure 7 compares U / U_o (solid lines) and U' / U_o (dashed lines) profiles for nozzles H (◆), I (▲) and J (■) at *Re* = 97,000.. The mean velocity profiles indicate that the flow is uniform for all nozzles. Nozzle H has the highest turbulence intensity, with $U' / U_o \approx 0.2$ at $y / W_o \approx 0$, while nozzles I and J have U' / U_o values up to 0.14 and 0.1, respectively.

B. Free Surface Fluctuations

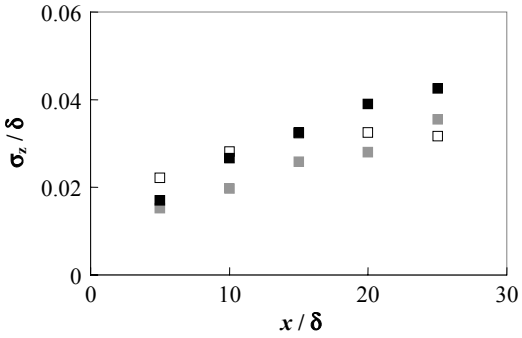

Figure 8 Graph of σ_z / δ *vs.* x / δ for nozzle J at *Re* = 25,000 (white), 50,000 (gray) and 97,000 (black symbols).

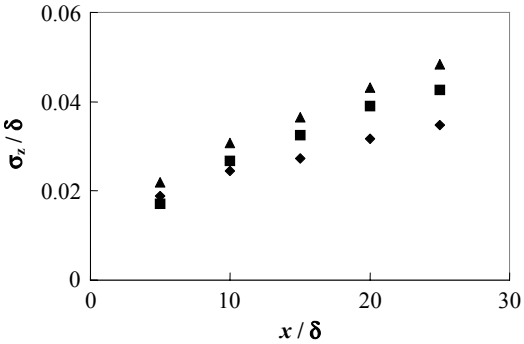

Figure 9 Plot of σ_z / δ as a function of x / δ for nozzles H (◆), I (▲) and J (■) at *Re* = 97,000.

Figure 8 shows σ_z / δ as a function of x / δ for nozzle J at *Re* = 25,000 (white), 50,000 (gray), and 97,000 (black symbols). Although surface ripple (characterized by σ_z) increases for the most part with downstream location. *Re* appears to have a minor effect on surface ripple, with σ_z / δ varying by less than 1.5% over a fourfold increase in *Re*. In all cases, $\sigma_z / \delta < 4.3\%$. The liquid sheets produced by nozzle J appear (albeit at *Re* below prototypical values) to

meet the current criterion for the prototypical HYLIFE-II jets restricting surface ripple to less than 7% of δ. [3]

Figure 9 compares σ_z / δ as a function of x / δ for nozzles H (◆), I (▲) and J (■) at *Re* = 97,000. Surface ripple again increases with downstream distance, with higher σ_z / δ levels for nozzles I and J. For all nozzle geometries, $\sigma_z / \delta < 5\%$; for nozzle H, $\sigma_z / \delta < 3.5\%$ over this range of x / δ.

IV. CONCLUSIONS

A. Summary

Initial conditions were quantified for three different nozzle geometries in terms of the mean *x*-component of velocity and its rms fluctuations. Profiles of both parameters along *y* at *z* = 0 were obtained using LDV at *x* = –2 mm. Nozzle geometry has a marked impact on turbulence intensity. A nozzle with a three-dimensional contraction (H) has a peak turbulence intensity at the center of the jet at least 50% greater than that of the other two nozzles at the largest *Re* studied here of 97,000. The mean velocity profiles indicate that the flow near the exit of all three nozzles is nearly uniform, or plug, flow.

Surface ripple was quantified as a function of distance downstream of the nozzle exit using PLIF. Surface ripple increases with downstream distance, with a maximum standard deviation for nozzle H below 0.035δ. Although the prototypical value is twice the maximum *Re* studied here, the normalized surface ripple values were similar for all three nozzle geometries over a fourfold change in *Re*. Standard dimensional analysis arguments indicate that results in water accurately model a Flibe slab jet.

Assuming that the data for *Re* = 25,000–97,000 can then be extrapolated to the HYLIFE-II value of about 200,000, these results suggest that a slab jet issuing from a nozzle with a three-dimensional contraction and exit aspect ratio of 6.7 (*i.e.*, nozzle H) will easily meet current surface ripple requirements for a single slab jet over the entire extent of the protective lattice in HYLIFE-II. Even if the surface ripple increases suddenly between *Re* = 97,000 and 200,000 (unlikely given that these Reynolds numbers are both well above the minimum value for turbulent flow of about 3,000), the surface ripple at the lower *Re* for nozzle H is half the maximum specified in the current design.

B. Future Work

These studies are, to our knowledge, the first characterizations of initial conditions in nearly prototypical turbulent liquid sheets proposed for thick liquid protection schemes. We plan next to quantify the impact of blockage in the flow straightener (due, for example, to debris in the coolant) upstream of the nozzle. Even modest blockage can drastically increase surface ripple.[4]

Velocity profiles at other *z*-locations (and profiles along the *z*-axis at various *y*-locations) would also be of interest to determine the extent of plug flow near the nozzle exit. The LDV system is also capable of measuring the *y*- and *z*-components of the velocity (*V* and *W*, respectively), which are known to have a significant impact upon the fluid dynamics and cross-sectional geometry of rectangular jets.

Finally, "axis switching", where the cross-section of the jet "rotates" by 90° so that the long axis of the jet eventually becomes perpendicular to the long axis of the nozzle, has also been observed in turbulent liquid sheets. Understanding the initial conditions that promote axis switching and its origins would be of interest for both IFE applications and in terms of fluid mechanics.

ACKNOWLEDGEMENTS

This research was sponsored by the Office of Fusion Energy Sciences, US DOE, under award DE-FG02-98ER54499. S.G. Durbin was under an appointment to the Fusion Energy Sciences Fellowship Program, administered by Oak Ridge Institute for Science and Education under a contract between the U.S Department of Energy and the Oak Ridge Associated Universities. We thank J.K. Anderson and T.P. Koehler for their help and support.

REFERENCES

1. R.W. MOIR, "The High-Yield Lithium-Injection Fusion-Energy (HYLIFE)-II Inertial Fusion Energy (IFE) Power Plant Concept and Implications for IFE," *Phys. Plasmas* **2**, 2447 (1995).

2. R.W. MOIR, ET AL, "HYLIFE-II: A Molten-Salt Inertial Fusion Energy Power Plant Design—Final Report," *Fusion Tech*. **25**, 5 (1994).

3. J.F. LATKOWSKI AND W.R. MEIER, "Heavy-Ion Fusion Final Focus Magnet Shielding Design", *Fusion Tech.* **39**, 798 (2001).

4. J.J.R. REPERANT, S.G. DURBIN, M. YODA, S.I ABDEL-KHALIK, AND D.L SADOWSKI, "Studies of Turbulent Liquid Sheets for Protecting IFE Reactor Chamber First Walls," *Fusion Eng. Des.* **63–64**, 627 (2002).

SURFACE FLUCTUATION ANALYSIS FOR TURBULENT LIQUID SHEETS

SAMUEL G. DURBIN II,* TIMOTHY P. KOEHLER, JEFFEREY J. R. REPERANT, MINAMI YODA, SAID I. ABDEL-KHALIK, and DENNIS L. SADOWSKI
Georgia Institute of Technology, G. Woodruff School of Mechanical Engineering, Atlanta, Georgia 30332-0405

Received June 13, 2003
Accepted for Publication July 28, 2003

A lattice consisting of arrays of stationary turbulent liquid sheets has been proposed for the HYLIFE-II inertial fusion energy reactor design to allow target injection and driver-beam propagation while protecting the first walls from damaging radiation. Interference between these sheets and the driver beams must be avoided, placing strict requirements on sheet free-surface fluctuations. Experiments were performed on nearly prototypical liquid sheets to determine the surface ripple and the absolute position of the free surface with respect to the nozzle exit. Planar laser-induced fluorescence was used to directly image the free surface at downstream distances up to 25 times the jet thickness (i.e., short dimension) at the nozzle exit δ for Reynolds numbers up to 130 000. Surface ripple, calculated using two different methods, was compared for two nozzle and two flow straightener designs. The surface ripple was found to be $<0.05\delta$ (versus the current HYLIFE-II requirement of 0.07δ). The mean thickness of the sheet was found to decrease with increasing x. This work should be useful in establishing the minimum distance between neighboring jets to avoid interference with the driver beams and to provide quantitative geometric data for shielding and neutronics analyses of such systems.

KEYWORDS: *turbulent liquid sheet, inertial fusion energy, liquid protection*

I. INTRODUCTION

Recent developments in heavy-ion-beam inertial fusion energy (IFE) reactor designs have renewed interest in thick liquid protection using high-speed liquid curtains or turbulent liquid sheets to shield reactor chamber first walls. The proposed HYLIFE-II conceptual power plant design uses molten Flibe (Li_2BeF_4) for both cooling and neutron attenuation.[1] Stationary and oscillating slab jets, or liquid sheets, form a protective pocket that allows target injection and driver beam propagation yet shields the chamber first walls from damaging neutrons, X rays, and target debris. Liquid protection can greatly reduce chamber size and prolong chamber lifetime, thereby potentially reducing the cost of electricity from IFE by >30% (Ref. 2).

In HYLIFE-II, the chamber walls and the heavy-ion driver arrays, including the final focus magnets, are protected by a lattice of stationary sheets that are positioned to allow target injection and implosion by driver beams propagating through the lattice openings. An alternative scheme consisting of an array of cylindrical jets within the reactor chamber in conjunction with vortex tubes just outside the chamber to shield the final focus magnets while allowing beam propagation has also been suggested.[3] The Robust Point Design (RPD-2002), an update to the HYLIFE-II chamber design, therefore uses a lattice of cylindrical (round) jets to shield the 120 driver beams.[4] Nevertheless, dynamically similar experiments in water have found that slab jets will also meet the stringent criteria on surface ripple, or sheet smoothness, in the HYLIFE-II chamber.[5] Surface ripple is a major concern for both cylindrical and slab jets since even moderate surface ripple will require more space between adjacent jets and increase irradiation of the final focus magnets. Alternatively, interactions between the driver beam, or the injected target, and the liquid may decrease fuel targeting and ignition efficiency.[6] Neutronic calculations for the slab jets proposed for HYLIFE-II show that the surface ripple should be <7% of the nozzle thickness at its exit to achieve final focus magnet lifetimes exceeding 30 yr (Ref. 7). Data that quantify surface ripple—and the probability over time of finding liquid within a given region in space—will provide design guidance on where to position the protective lattice of jets.

This paper describes a technique based on planar laser-induced fluorescence (PLIF) to directly measure

*E-mail: gte397r@mail.gatech.edu

time-averaged surface ripple in stationary turbulent sheets of water into air. The PLIF data are used to obtain two types of results for characterizing free-surface smoothness:

1. the standard deviation in the z position of the free surface (direction normal to the unperturbed free surface) spatially averaged over the central section of the sheet σ_z
2. the liquid cumulative distribution function (LCDF) for a central section of the sheet, given as the liquid volume fraction Φ within a "box" of a given size at a prespecified location in the flow.

Results are presented for downstream locations up to 25 times the original jet thickness downstream of the nozzle exit, at Reynolds numbers $\mathrm{Re} = U_o\delta/\nu = 50\,000$ and 130 000 and Weber numbers $\mathrm{We} = \rho U_o^2\,\delta/\sigma = 2900$ and 19 000, respectively. Here, the average jet speed $U_o =$ 4.5 and 12 m/s, and the jet thickness (short dimension) at the nozzle exit $\delta = 1$ cm. At the nozzle exit, the jet has a width $W_o = 10$ cm. The liquid kinematic viscosity, density, and surface tension are $\nu = 9.12 \times 10^{-7}$ m^2/s, $\rho = 997.4$ kg/m^3, and $\sigma = 7.22 \times 10^{-2}$ N/m, respectively. The maximum Reynolds and Weber numbers studied here, namely, $\mathrm{Re} = 130\,000$ and $\mathrm{We} = 19\,000$, are ~50 and 20%, respectively, of the prototypical values for HYLIFE-II.

II. FLOW LOOP

In these experiments, water passes through a flow straightener and nozzle, forming vertical turbulent sheets issuing downward into atmospheric pressure air in the open test section with a vertical extent of 1.9 m. The water is recirculated by a 7.5-hp pump. The flow rate is controlled by a bypass with an adjustable valve. Figure 1 is a schematic of the flow loop where A, B, C, and D denote the pump, the bypass, the nozzle, and a 20-kW chiller, respectively. The apparatus is identical to that of Reperant[8] except for the addition of the chiller to maintain a constant water temperature of ~21°C. In this paper, the coordinate system is defined so that the origin is at the center of the nozzle exit, with the x-axis along the flow direction, the y-axis along the long dimension of the rectangular nozzle exit cross section, and the z-axis along the short dimension of the nozzle cross section. A spectral analysis of the signal from an accelerometer attached to the nozzle gave the natural frequency of the flow loop as ~8.6 kHz. We therefore expect minimal excitation of the flow by the pump since this value is well above the pump frequency of 60 Hz.

Two different flow straighteners were used in these experiments to break up large-scale eddies and minimize the cross-stream velocity components. Flow straightener A (FSA) consisted of a perforated plate (50% open area ratio and 4.8-mm-diam staggered holes) followed by a section of stainless steel honeycomb of 1.5-cm length with 0.32-cm cell diameter and a fine screen (30 × 30 mesh size, 37.1% open area ratio, 0.33-mm wire diameter, and 0.51-mm open cell width)—all of stainless steel. The streamwise edge-to-edge spacing between the perforated plate and honeycomb section was 4.2 cm, with the screen 13.2 cm above the nozzle inlet.[8] Flow straightener B (FSB) was produced using stereolithography rapid prototyping in three separate sections. The perforated plate and fine screen were identical to those used in FSA. The honeycomb section in FSB was made of polycarbonate plastic with a 2.5-cm length with circular (versus hexagonal) cells. The streamwise edge-to-edge spacing between the perforated plate and honeycomb was 3.8 cm, while the fine screen was located 14.6 cm above the upstream end of the nozzle.[5] In both flow straighteners, the honeycomb-to-fine-screen spacing was 0.5 cm.

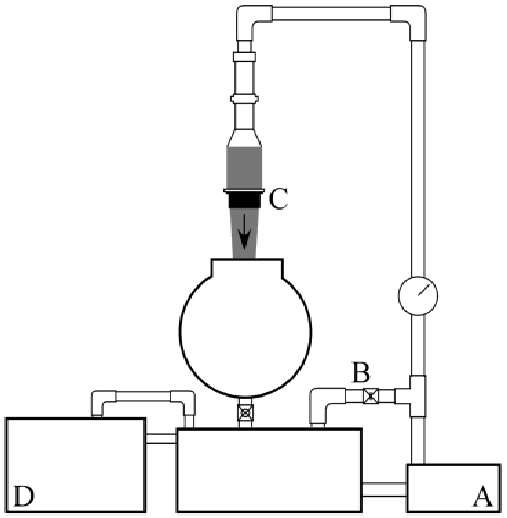

Fig. 1. Schematic of the flow loop.

The two nozzles, I and II, used in these experiments were produced using stereolithography rapid prototyping from Vantico SL 7510 and DSM Somos WaterClear resins, respectively. Both nozzles had two-dimensional contractions along their z dimension consisting of a fifth-order polynomial from a rectangular upstream cross section of 3 × 10 cm ($z \times y$) to a 1 × 10 cm ($\delta \times W_o$) rectangular exit cross section (giving an aspect ratio $AR = 10$). Nozzle II had a slight taper at its exit with a slope of 4 deg, while nozzle I had a straight channel with an x extent of 1 cm just upstream of its exit. The overall x dimensions of nozzles I and II were 7.3 and 6.3 cm, respectively. The fifth-order polynomial $f_1(x)$ describing the contraction for nozzle I was determined from the following boundary conditions:

Inlet ($x = -7.3$ cm):

$$f_{\mathrm{I}} = 1.5 \text{ cm} \; ; \quad \frac{df_{\mathrm{I}}}{dx} = 0 \; ; \quad \frac{d^2 f_{\mathrm{I}}}{dx^2} = 0$$

Exit ($x = -1$ cm):

$$f_{\mathrm{I}} = 0.5 \text{ cm} \; ; \quad \frac{df_{\mathrm{I}}}{dx} = 0 \; ; \quad \frac{d^2 f_{\mathrm{I}}}{dx^2} = 0 \; .$$

Note that the section of nozzle I where $-1 \text{ cm} \leq x \leq 0$ cm is a straight section with identical boundary conditions. The polynomial $f_{\mathrm{II}}(x)$ describing the contraction for nozzle II was determined from the following conditions:

Inlet ($x = -6.3$ cm):

$$f_{\mathrm{II}} = 1.5 \text{ cm} \; ; \quad \frac{df_{\mathrm{II}}}{dx} = 0 \; ; \quad \frac{d^2 f_{\mathrm{II}}}{dx^2} = 0$$

Exit ($x = 0$ cm):

$$f_{\mathrm{II}} = 0.5 \text{ cm} \; ; \quad \frac{df_{\mathrm{II}}}{dx} = -\tan(4^\circ) \; ; \quad \frac{d^2 f_{\mathrm{II}}}{dx^2} = 0 \; .$$

Figure 2 gives a plot of $f_{\mathrm{I}}(x)$ and $f_{\mathrm{II}}(x)$.

A two-dimensional optical profilometer (Taylor Hobson, Ltd., Form Talysurf) was used to determine the surface roughness of the rapid prototyped nozzles. The surface roughness, characterized by average peak-to-valley height, was ~ 10 μm for nozzle II; we expect that nozzle I, which was manufactured using the same process, has similar surface roughness characteristics. The surface roughness of the nozzles is hence negligible compared with the surface ripple results (Sec. VI).

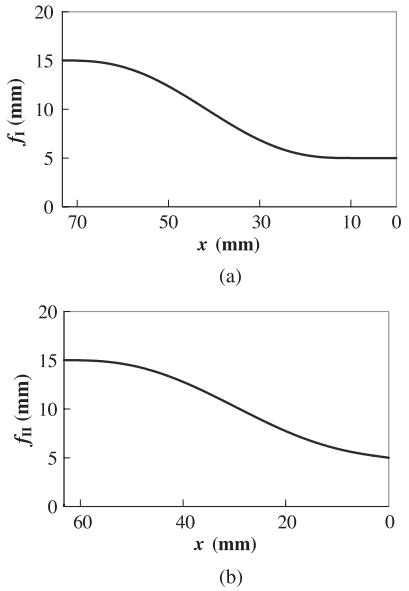

Fig. 2. Graphs depicting the fifth-order polynomial contractions for nozzles I and II, or (a) $f_{\mathrm{I}}(x)$ and (b) $f_{\mathrm{II}}(x)$, respectively.

III. FREE-SURFACE FLUCTUATIONS

A nonintrusive PLIF technique was used to directly image the free surface of the turbulent liquid sheet in the open test section. The water in the flow loop contained 25 mg/ℓ, which corresponds to a concentration of $\sim$66 μM, of disodium fluorescein (uranine). This relatively high dye concentration was chosen so that most of the illuminating light was absorbed within a few millimeters inside the flow (and hence from the free surface) to minimize refraction of spurious fluorescence—which could then interfere with imaging the flow free surface—out from the flow interior. Since even slight impurities can greatly affect the surface tension of water, σ for water containing fluorescein at concentrations exceeding those used in these experiments was measured by visualizing a pendant drop of the liquid. The measured values for σ were found to be identical (within measurement error) to those for pure water.

The turbulent flow was illuminated by a horizontal laser light sheet from a 0.5-W multiline argon-ion laser (Omnichrome 543-MA-A03). A laser band-pass filter with a transmission peak centered $\sim$488 nm and full-width at half-maximum of 7.2 nm was placed in the laser beam to ensure that only the 488-nm laser line illuminated the flow. Since uranine has an absorption maximum at a wavelength of 488 nm and an emission maximum at 514 nm, illuminating at only this wavelength maximized the fluorescence signal and prevented reabsorption of the red-shifted fluorescence resulting from the illumination at 488 nm by the dye.

An 8-bit B/W 1008 pixel $\times$ 1008 pixel charge-coupled device (CCD) camera (Kodak Megaplus ES 1.0) with a zoom lens (Navitar® Zoom 7000) was placed obliquely at an angle $\theta \approx 20$ deg with respect to the vertical below the illuminated area of the liquid sheet to image the free surface (Fig. 3). A high-pass photographic filter (Edmund Industrial Optics® 30907) transmitting wavelengths above 500 nm was placed in front of the lens to image only the longer-wavelength fluorescence (versus the illumination). The images were recorded at 30 Hz as 1008 $\times$ 1008 bitmaps directly onto the hard drive of a personal computer using imaging software (Video Savant 3.0). For the experiments using FSA, the field of view of each image was $\sim$4.8 $\times$ 4.8 cm, and one side of the entire jet along the y-axis was imaged over three separate sections. For the experiments using FSB, the field of

Fig. 3. Photograph showing the liquid sheet illuminated by the laser light sheet imaged obliquely from below by CCD camera.

view was $\sim 3.1 \times 3.1$ cm, and the long side of the jet was imaged over four to five sections. For each section, 100 consecutive images were acquired at exposure times of τ, where the convective timescale $\tau = \delta/U_o$. The overall data acquisition time for each set of 100 images was at least 650τ in all cases.

In all cases, the absolute location of the free surface at each downstream (x) location was determined with respect to the nozzle exit using the following procedure. First, the camera was placed so that the left edge of the liquid sheet was just at the edge of the camera field of view. A long rectangular insert was then placed in the nozzle with the flow off, and the edges of the insert were aligned with the long and short sides of the nozzle exit, or the y- and z-axes, respectively. A single digital image was taken of the insert, which had an x extent of $\sim$30 cm, as it was illuminated by the laser sheet at a given x position. The image of the insert illuminated by the laser sheet therefore gave the absolute location of one corner of the nozzle with respect to the camera position at that x location. The insert was removed, and the flow was turned on. A ruler was placed $\sim$5 mm from the free surface of the liquid sheet with the ruler edge parallel to the y-axis, and imaged with the camera in the same position used to acquire the image of the rectangular insert. This ruler, which extended over the entire y extent of the flow, then was used in conjunction with the image of the insert to determine the absolute position of all the adjacent sections spanning one side of the flow. After acquiring data at each section, the camera was traversed along the y-axis until the camera's field of view overlapped with 2 to 3 mm of the previous section without stopping the flow or moving the ruler. This procedure was repeated over the appropriate number of sections until the entire side of the liquid sheet was imaged. Finally, the flow was turned off, the insert was again placed inside the nozzle, and a second reference image was taken of the insert illuminated by the laser to determine the location of the opposite side of the nozzle on the other edge of the sheet at the final camera position. The images of the two opposite nozzle corners were then used by an image processing program to find the edge of the nozzle and its limits.

The oblique imaging introduces a slight difference in the magnification along the y and z directions (M_y, M_z) with $M_y = M_z/(\cos\theta) = 1.064M_z$. In all the image processing carried out in this work, however, this 6% difference in the magnification along the horizontal and vertical result affected the result by less than one pixel—or the minimum spatial resolution of a raw image. Hence, no attempt was made to correct for this difference in magnifications since it was beyond the spatial resolution of the imaging system.

IV. IMAGE PROCESSING

In-house software, implemented in MATLAB version 6.1, was used to find the spatially averaged standard deviation in the z position of the free surface, or σ_z, from the images. A grayscale histogram, or a graph of the number of pixels at each grayscale value as a function of that grayscale value, was used to threshold the raw images. The dark background of the images is a peak on the left of the histogram since darker pixels correspond to lower grayscale values. If the grayscale value for the maximum of this background peak is $G_{b,max}$ and the number of pixels with this value is $N_{b,max}$, the threshold grayscale was chosen to be the first grayscale value $>G_{b,max}$ with a number of pixels $<0.05N_{b,max}$. The location of the free surface—the interface between the bright fluorescing water and the dark air—was then determined for each image using a standard edge detection scheme. The standard deviation of the z position of the free surface was then calculated over the 100 images in each section, and σ_z was calculated by spatially averaging this standard deviation at each y location over the central 75% of the initial y extent of the flow, or $0.75W_0$ (Ref. 5). Because the central 75% of the y extent of the flow spans multiple viewing sections, the images are overlapped before performing the spatial average. Figure 4 shows representative images for each step in this procedure.

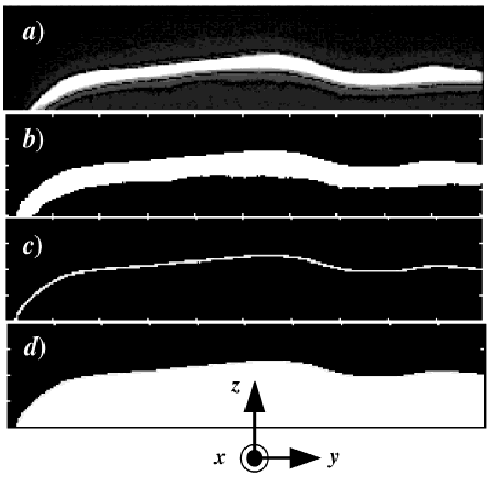

Fig. 4. Sample images illustrating the procedure used to find the liquid sheet free surface and calculate the LCDF: (a) raw PLIF image, (b) the image after thresholding, (c) the image after edge detection to find the free surface, and (d) the image with the all pixels inside the flow (i.e., below and to the right of the free surface) reset to white corresponding to liquid.

V. LIQUID CUMULATIVE DISTRIBUTION FUNCTION

The cumulative distribution function (CDF) $\Phi(\alpha)$ is a statistical function giving the net probability over time that a variable ξ is less than a given value α:

$$\Phi(\alpha) = P(\xi \leq \alpha) \ . \tag{1}$$

The CDF is a monotonic function with $0 \leq \Phi(\alpha) \leq 1$. A normal distribution is denoted by $N(\mu, \sigma)$, where μ represents the mean and σ is the standard deviation. The standard normal distribution is defined with $\mu = 0$ and $\sigma = 1$. Data within the range of $\mu \pm \sigma$ (i.e., $[\mu - \sigma : \mu + \sigma]$) correspond to $0.1587 \leq \Phi \leq 0.8413$, where Φ summarizes the probability that an event less than or equal to a value of α takes place. Data within the ranges $\mu \pm 2\sigma$ and $\mu \pm 3\sigma$ then correspond to $0.0228 \leq \Phi \leq 0.9772$, and $0.0013 \leq \Phi \leq 0.9987$, respectively.[9] The LCDF physically corresponds to the probability of finding liquid within a thin rectangular "box" at a specific distance from the nozzle centerline z, as z moves outward from the origin along the z-axis.

An Anderson-Darling normality test, which uses the null hypothesis that the data follow a normal distribution, was used to assess whether the free-surface position data were normally distributed.[10] This test showed that a normal distribution is plausible. Based upon this result, the data are assumed to be normally distributed, and 68% of the data will therefore fall within one standard deviation of the mean.

The LCDF was calculated using a MATLAB program with the following procedure. First, the reference images of the rectangular insert were used to locate the absolute position of the nozzle in each section. The ruler in each image was then used to determine the absolute position, and hence the edge and center of the nozzle exit, for each section. Next, the free surface of the liquid sheet was determined from the raw instantaneous images for each section using the same threshold-based edge detection algorithm described in Sec. IV. All the pixels in the area between the free surface and the nozzle centerline are set to a grayscale value of 255 (white), corresponding to liquid. We therefore assume that the area within the free surface is fully flooded by the liquid in the jet since neither cavitation nor entrainment of air has ever been observed in these and previous experiments.

The program then calculates the liquid volume fraction $\Phi(z)$ within a rectangular box with the inner edge at a z location of z, a width $\Delta z = 0.01\delta$, and a length Δy centered about the origin (Fig. 5) by dividing the number of white pixels (liquid) in the box by the total number of pixels in the box. A range of values of $\Delta y/\delta = 1$, 2, 4, 6, 8, and 10 were used in this work. By increasing z, the rectangular box was moved outward from the nozzle centerline until $\Phi \to 0$, or no liquid was observed within the box. Finally, Φ was averaged over the 100 overlapped images to calculate the LCDF.

The standard deviation was also calculated from the LCDF data. This standard deviation is denoted by σ' to distinguish these values from σ_z, or the standard deviation calculated directly from the z position of the free surface. Figure 6, which shows a typical LCDF, defines the standard deviation from the LCDF based upon one "sigma":

$$\sigma_1' = \frac{z(\Phi = 0.1587) - z(\Phi = 0.8413)}{2} \ .$$

Note that these values for Φ assume a normal distribution (see discussion at the beginning of this section). A similar procedure was used to calculate standard deviations from the LCDF values corresponding to two and three sigma, or σ_2' and σ_3', respectively. The local average jet thickness z_{50} was defined using the LCDF as twice the z value where $\Phi = 0.5$.

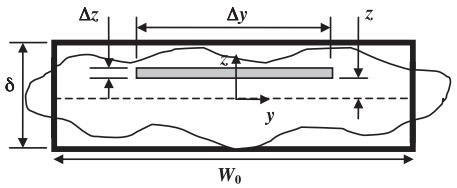

Fig. 5. Diagram showing the thin rectangular $\Delta y \times \Delta z$ box used to calculate the liquid volume fraction $\Phi(z)$.

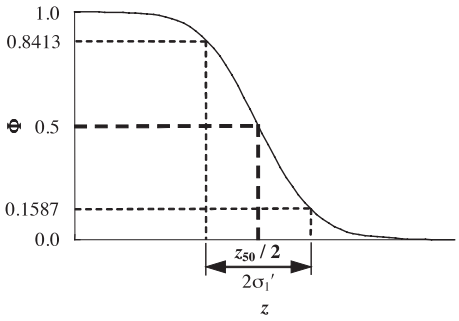

Fig. 6. Typical LCDF defining $2\sigma_1'$ and z_{50} assuming a standard normal distribution.

In general, the LCDF data are not symmetric about z_{50} because these data are a combination of two normally distributed datasets, namely, the surface ripple along z for the central portion of the sheet and that for the ends of the sheet. Although each of these distributions satisfies the null hypothesis of the Anderson-Darling normality test and can therefore be considered normally distributed, each distribution has a different standard deviation about a different mean. From a liquid protection perspective, however, "surface ripple" should reflect free-surface fluctuations over the entire extent of the flow. These two normally distributed datasets are therefore combined to determine z_{50}.

VI. RESULTS AND DISCUSSION

Figure 7 shows σ_z/δ as a function of x/δ at Re = 50 000 for the nozzle and flow straightener combination of nozzle II and FSB (■), nozzle II and FSA (◆), and nozzle I and FSB (▲). Surface ripple, characterized by σ_z, appears to increase with downstream location for all nozzle and flow straightener combinations. The standard deviation σ_z is <3% of δ for all cases. The combination of nozzle II and FSB has the smallest surface ripple at this Re.

Figure 8 shows a similar plot at Re = 130 000. The legend is the same as that in Fig. 7 with exposure times of τ and 5τ represented by gray and black symbols, respectively. The previously obtained σ_z values with an exposure time of 5τ (Ref. 8) are consistently smaller, most likely because the longer exposure averages the image of the free surface over a greater number of convective timescales, thus reducing the standard deviation calculated from these images. Surface ripple again increases with downstream location. Variations in flow straightener and nozzle design appear to have a negligible impact upon surface ripple at this higher Re. The results show that all nozzle and flow straightener combinations appear to meet the current design criterion for the HYLIFE-II slab jets or turbulent liquid sheets of $\sigma_z/\delta < 0.07$ (Ref. 7), although the Re here is only ~60% of the prototypical value for HYLIFE-II.

Though not shown here, z_{50} results at Re = 50 000 indicate that the local jet thickness decreases as downstream location increases. These data also suggest that the width of the rectangular box appears to have a negligible effect on the local jet thickness.

Figure 9 gives the LCDF Φ as a function of z/z_{50} for $\Delta y/\delta = 10$ and for $x/\delta = 5$ (heavy solid), 10 (light solid), 15 (heavy dotted), 20 (light dotted), and 25 (heavy dashed) at Re = 50 000. The slope of each line is indicative of the amount of surface ripple in the liquid sheet. A steep curve, or large slope, indicates that the amount of liquid in the rectangular box changes rapidly (i.e., over a small range of z) from a fully flooded box to an empty box as the normalized distance from the nozzle centerline is increased. A shallow curve, or smaller slope, indicates that a wider region of space is partially occupied by liquid, and hence, the flow has greater surface ripple. The slope of the Φ curves decreases as x/δ increases, which indicates surface ripple increases with downstream location. The point at which $\Phi \to 0$ at a given x/δ corresponds to the maximum value of z/z_{50}

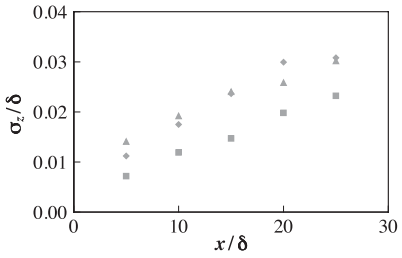

Fig. 7. Plot of σ_z/δ as a function of x/δ for nozzle II + FSA (◆), nozzle II + FSB (■), and nozzle I + FSB (▲).

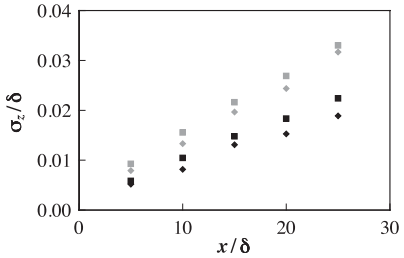

Fig. 8. Graph of σ_z/δ plotted against x/δ at Re = 130 000 for nozzle II + FSA (◆) and nozzle II + FSB (■); exposure times are indicated for τ (gray) and for 5τ (black symbols).

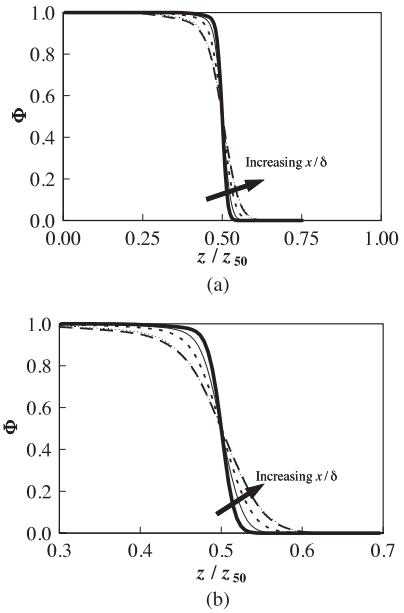

Fig. 9. (a) Graph of Φ as a function of z/z_{50} for $\Delta y/\delta = 10$ and for $x/\delta = 5$ (heavy solid), 10 (light solid), 15 (heavy dotted), 20 (light dotted), and 25 (heavy dashed) at Re = 50 000; (b) the same graph with an expanded horizontal scale showing more details of the free surface.

where any liquid is present over time. This "maximum jet thickness" appears to increase with x/δ, which suggests that liquid is present over a greater z extent in space farther downstream.

Figure 10 shows the local jet thickness z_{50}/δ plotted against x/δ for $\Delta y/\delta = 2$ (■), 4 (▲), 8 (◇), and 10 (△) at Re = 130 000. This thickness decreases as x/δ increases. Moreover, z_{50}/δ decreases as the width of the rectangular box increases; this effect is more marked farther downstream. This result suggests that the free surface of the jet "bulges" slightly outward in the central region of the liquid sheet farther downstream. We observed post priori that the nozzle had actually deformed up to 5% of the original nozzle thickness δ; this deformation probably caused the "bulge" evident in Fig. 10. Although it is possible that this bulge is due to so-called "axis switching" of liquid sheets,[11] axis switching is not observed at these high Re within the flow loop test section, which suggests that the jet crossover point, or the x location where the y and z dimensions of the jet become identical, occurs at $x/\delta > 300$. We therefore expect axis switching is negligible over the region of interest for these experiments, i.e., $x/\delta \leq 25$.

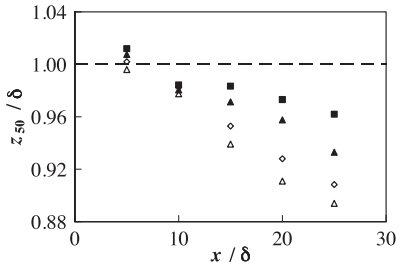

Fig. 10. Plot of z_{50}/δ versus x/δ for $\Delta y/\delta = 2$ (■), 4 (▲), 8 (◇), and 10 (△) at Re = 130 000.

Figure 11 shows Φ plotted against z/z_{50} for Re = 130 000 for various box widths, with a legend identical to that for Fig. 9. The trends in the LCDF are similar to those described and discussed in Fig. 9.

Figure 12 is a graph of the various standard deviations σ_1' (▲), σ_2' (■), σ_3' (♦), and σ_z (□)—all normalized by δ as a function of x/δ at Re = 130 000 for $\Delta y/\delta = 6$. Surface ripple, characterized here by the standard deviation, appears to increase with downstream location. Nevertheless, the values in all cases never exceed 5% of δ.

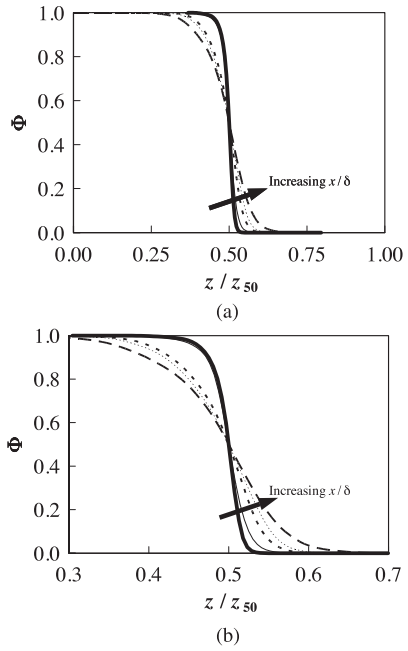

Fig. 11. Graph of Φ as a function of z/z_{50} for $\Delta y/\delta = 10$ and for $x/\delta = 5$ (heavy solid), 10 (light solid), 15 (heavy dotted), 20 (light dotted), and 25 (heavy dashed) at Re = 130 000; (b) the same graph with an expanded horizontal scale showing more details of the free surface.

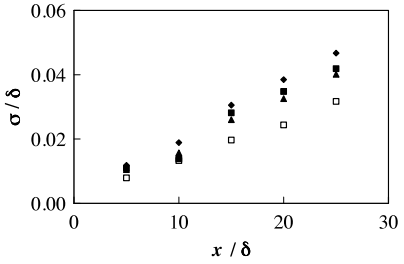

Fig. 12. Graph of σ/δ plotted against x/δ for $\Delta y/\delta = 6$ at Re = 130 000 where σ_1' (▲), σ_2' (■), σ_3' (♦), and σ_z (□).

For all downstream locations studied, $\sigma_3' > \sigma_2' > \sigma_1' > \sigma_z$; the σ' values exceed σ_z by as much as 50%. We hypothesize that the trend for σ' is due to inadequate sampling of the "tails" (i.e., more than one standard deviation away from the mean) of the normal distribution since the datasets of 100 images span only $O(10^3\tau)$. The differences between σ' and σ_z may be due to the additional data processing required to obtain σ', versus the relatively minimal processing required to calculate σ_z. This discrepancy may also be due to the bulge in the central region of the flow discussed previously. Given a nominally rectangular nozzle exit (and hence flow cross section), the LCDF calculation is based upon a rectangular box. Calculations of the LCDF with a rectangular box (not shown here) suggest that a flow with a convex cross section will have a larger value for σ' than a flow with a rectangular cross section.

Current requirements based on neutronics predictions for the slab jets proposed for HYLIFE-II suggest that the surface ripple be $<0.07\delta$ (Ref. 7). Since the values for free-surface fluctuations based upon σ' were consistently greater than those given by σ_z in these experiments, σ' is a more conservative estimate of surface ripple. Nevertheless, even the largest value of σ' gives a surface ripple of $<5\%$ of δ for liquid sheets at Re = 130 000 (versus the HYLIFE-II value of ~240 000).

Most experimental studies in thermal hydraulics are based upon dynamic similarity, where results for a geometrically scaled "model" situation can be extrapolated to the larger "prototypical" situation. Although the liquid sheets studied here are significantly smaller than those in HYLIFE-II, they should be dynamically similar to much larger liquid sheets as long as the important dimensionless groups—the Reynolds and Weber numbers, the flow aspect ratio, and the density ratio—for these flows are identical to those for HYLIFE-II.

The Reynolds and Weber numbers are 50 and 20%, respectively, of the prototypical values for HYLIFE-II. The aspect ratio of these liquid sheets ($AR = 10$) is less than that for HYLIFE II, where $AR = 17$, but is still large enough to ensure that the central 75% of the flow is essentially two-dimensional. The density ratio between the liquid and the surrounding fluid is $\sim 10^3$, or several orders of magnitude below the value for HYLIFE-II, since these studies are carried out in atmospheric pressure air (namely, the near vacuum of HYLIFE-II). Nevertheless, atomization studies in high-speed jets show that breakup behavior—the end result of the formation and growth of surface waves, or ripple—is independent of density ratio for values >500 (Ref. 12). The density ratio used here is twice this limiting value, which suggests that surface ripple data for liquid water sheets issuing into atmospheric pressure air are applicable to molten-salt sheets in a near vacuum. The dimensionless groups with the most impact upon surface ripple are therefore Re and We.

If these experimental results at lower Re and We can then be extrapolated to HYLIFE-II, liquid sheets produced by standard nozzle and flow straightener designs already meet current requirements for effective and robust protection of the first walls and the final focus magnet in HYLIFE-II over its 30-yr lifetime. Round jet (versus liquid sheet) arrays are currently used in RPD-2002 based upon analyses that suggest that jet "voids" eliminate the formation of high-speed liquid slugs (that could damage chamber structures) when adjacent jets are driven into each other by the shock waves from the fusion event.[13] Nevertheless, liquid sheets remain a viable candidate "building block" flow for liquid protection schemes in IFE reactors because they provide inherently more attenuation (i.e., liquid absorption thickness) over a given spatial distance.

VII. CONCLUSIONS

Surface ripple, i.e., free-surface fluctuations, were quantified using an LCDF describing the accumulated probability of finding liquid within a thin rectangular box at a distance z from the nozzle centerline for turbulent water sheets into air at Re = 50 000 to 130 000, We = 2900 to 19 000, and distances up to 25 cm downstream of the nozzle exit. LCDF data were obtained for nozzle II and FSA at Re = 50 000 and 130 000. In contrast with previous work, these studies give the surface ripple and its absolute position with respect to the nozzle exit. The surface ripple determined from the LCDF data was found to be greater than that found by our prior direct calculation method. In all cases, however, the surface ripple was still <5% of the nozzle exit thickness. We hypothesize that the difference between the LCDF-based and directly calculated standard deviation values is most likely a result of the additional data processing entailed in calculating the LCDF, and—especially for standard deviations obtained from the tails of the normal distribution—statistically undersampled data. These two independent determinations of the standard deviation give,

however, an estimate of the error in these surface ripple results. The higher standard deviations from the LCDF are therefore the most conservative estimate of surface ripple.

Local jet thickness, defined here as twice the distance from the nozzle centerline where the average liquid volume fraction is 50%, was found to decrease with downstream location and decrease with increasing rectangular box width. The maximum jet extent also increases with downstream location.

This paper describes ongoing work on the impact of initial conditions on free-surface smoothness in turbulent liquid sheets. We plan next to quantify how initial conditions such as different flow straightener and nozzle designs impact the turbulence intensities (i.e., velocity fluctuations) in these flows. An improved understanding of how different initial conditions affect turbulence intensities (and hence surface ripple) will improve technologies for producing smooth rectangular and round turbulent jets suitable for liquid protection of the chamber first walls in IFE reactors.

ACKNOWLEDGMENTS

This research was sponsored by the Office of Fusion Energy Sciences, U.S. Department of Energy (DOE), under award DE-FG02-98ER54499. Financial support for S. G. Durbin was provided by the Fusion Energy Sciences Fellowship Program, administered by Oak Ridge Institute for Science and Education under a contract between the DOE and the Oak Ridge Associated Universities.

REFERENCES

1. R. W. MOIR et al., "HYLIFE-II: A Molten-Salt Inertial Fusion Energy Power Plant Design—Final Report," *Fusion Technol.*, **25**, 5 (1994).

2. R. W. MOIR, "The High-Yield Lithium-Injection Fusion-Energy (HYLIFE)-II Inertial Fusion Energy (IFE) Power Plane Concept and Implications for IFE," *Phys. Plasmas*, **2**, 2447 (1995).

3. R. ABBOTT et al., "Cylindrical Liquid Jet Grids for Beam-Port Protection of Thick-Liquid Heavy-Ion Fusion Target Chambers," *Fusion Technol.*, **39**, 732 (2001).

4. S. J. PEMBERTON, R. P. ABBOTT, and P. F. PETERSON, "Thick-Liquid Blanket Configuration and Response for the HIF Point Design," *Fusion Sci. Technol.*, **44**, 294 (2002).

5. S. G. DURBIN, M. YODA, S. I. ABDEL-KHALIK, and D. L. SADOWSKI, "Turbulent Liquid Sheets for Protecting IFE Reactor Chamber First Walls," *Fusion Sci. Technol.*, **44**, 307 (2003).

6. A. YING and M. ABDOU, "Scaling Criteria for IFE Liquid Wall Protection Scheme Simulation," *Fusion Eng. Des.*, **42**, 555 (1998).

7. J. F. LATKOWSKI and W. R. MEIER, "Heavy-Ion Fusion Final Focus Magnet Shielding Design," *Fusion Technol.*, **39**, 798 (2001).

8. J. J. R. REPERANT, S. DURBIN, M. YODA, S. I. ABDEL-KHALIK, and D. L. SADOWSKI, "Studies of Turbulent Liquid Sheets in Protecting IFE Reactor Chamber First Walls," *Fusion Eng. Des.*, **63–64**, 627 (2002).

9. A. J. HAYTER, *Probability and Statistics for Engineers and Scientists*, PWS Publishing Company, Boston, Massachusetts (1995).

10. M. A. STEPHENS, "EDF Statistics for Goodness of Fit and Some Comparisons," *J. Am. Stat. Assoc.*, **69**, 730 (1974).

11. N. B. MORLEY, A. Y. YING, A. GAIZER, T. SKETCHLEY, A. I. KONKACHBAEV, and M. A. ABDOU, "Experimental Investigation of Free Liquid Metal Jets in Vacuum: Preliminary Results for IFE Chamber Wall Protection Applications," *Fusion Technol.*, **34**, 1035 (1998).

12. P. K WU and G. M. FAETH, "Aerodynamic Effects on Primary Breakup of Turbulent Liquids," *Atomization Sprays*, **3**, 265 (1993).

13. S. J. PEMBERTON, R. P. ABBOTT, and P. F. PETERSON, "Abatement of Shocks During Disruption of Porous Thick-Liquid Blankets in HYLIFE-Type Inertial Fusion Chambers," *Fusion Eng. Des.*, **63–64**, 641 (2002).

Samuel G. Durbin II [MS, mechanical engineering, Georgia Institute of Technology (Georgia Tech), 2002] is a graduate research fellow at the George W. Woodruff School of Mechanical Engineering at Georgia Tech. His research interests are in experimental investigations of thermal hydraulics with applications in thick liquid protection for inertial fusion energy (IFE) chambers.

Timothy P. Koehler (BS, mechanical engineering, Tulane University, 2002) is a graduate research assistant at the George W. Woodruff School of Mechanical Engineering at Georgia Tech. His research interests are in analytical and experimental studies of IFE-related fluid dynamics.

Jeffrey J. R. Reperant (MS, mechanical engineering, Georgia Tech, 2002) is a project engineer at Raytheon in El Segundo, California.

Minami Yoda (PhD, aeronautics and astronautics, Stanford University, 1993) is an associate professor at the George W. Woodruff School of Mechanical Engineering at Georgia Tech. Her research interests are in experimental fluid dynamics and optical diagnostic techniques.

Said I. Abdel-Khalik (PhD, mechanical engineering, University of Wisconsin, 1973) is the Southern Nuclear Distinguished Professor at the George W. Woodruff School of Mechanical Engineering at Georgia Tech. His research interests are in the areas of reactor engineering and thermal hydraulics.

Dennis L. Sadowski (MSME, University of Illinois, Chicago, 1987) is a research engineer at the George W. Woodruff School of Mechanical Engineering at Georgia Tech. His research interests are in the areas of thermal hydraulics and the construction of complex experimental systems.

PRIMARY BREAKUP IN TURBULENT LIQUID FILMS ON DOWNWARD-FACING SURFACES

Technical Note

B. T. SHELLABARGER, S. G. DURBIN,* M. YODA, S. I. ABDEL KHALIK, and D. L. SADOWSKI
Georgia Institute of Technology, George W. Woodruff School of Mechanical Engineering, Atlanta, Georgia 30332-0405

Received February 16, 2004
Accepted for Publication April 23, 2004

A number of thin liquid protection schemes involving a sacrificial thin liquid layer have been proposed to protect the first walls of inertial fusion energy reactor chambers from excessive radiation and energetic ion damage. The Prometheus study used a tangentially injected high-speed film of molten lead attached to the first wall to protect the upper endcap of the chamber reactor. Minimizing droplet formation and detachment from this film to avoid interference with beam propagation is a major design issue for such flows.

Experiments were conducted on turbulent films of water injected tangentially with a rectangular nozzle into ambient air onto the underside of a horizontal flat plate. Previous efforts were focused on the effect of various design and operational parameters on the film detachment distance. This study focuses on measurement of the "hydrodynamic source term," i.e., the rate of droplet formation due to primary turbulent breakup at the film surface. Droplet mass flux was measured using a simple collection technique at various standoff distances measured with respect to the plate surface and downstream distances measured from the nozzle exit. The data show that the ejected droplet mass flux increases as the standoff distance decreases and as both downstream distance and Weber number increase. Comparisons of the experimental data on the estimated ejected droplet mass flux with previously published correlations suggest that the correlations overpredict the ejected droplet mass flux by more than three orders of magnitude.

KEYWORDS: *thin films, inertial fusion energy, turbulent breakup*

I. INTRODUCTION

A number of inertial fusion energy (IFE) power plant design studies have considered using a sacrificial liquid layer to protect the first wall from excessive damage while maintaining practical cavity sizes. In thin liquid protection, a thin liquid film flowing along the reactor chamber walls absorbs essentially all the X rays and charged particles from the fusion event, thereby significantly reducing first-wall damage from radiation and thermal stresses. The Prometheus study[1,2] proposed using a 0.5-mm-thick "forced film" of liquid lead injected tangentially along the first wall with a minimum injection speed of 7 m/s to protect the 4.5-m-radius hemispherical upper endcap of the chamber. The film was partially vaporized by each fusion event, requiring recondensation (i.e., chamber clearing) and reestablishment of a fresh layer before the next event.

*E-mail: gte397r@mail.gatech.edu

The presence of liquid droplets within the cavity can interfere with the driver beam propagation and reduce the amount of energy delivered to the target in each shot. Formation and ejection of droplets due to turbulent primary breakup from the free surface is therefore a major design issue for all liquid protection schemes, including the forced thin liquid film concept. "Primary breakup" refers here to the formation of droplets at the free surface from ligaments created by flow disturbances, while "secondary breakup" refers to further breakup of these droplets after they leave the free surface.[3]

A number of previous experimental studies have examined turbulent primary breakup in liquid round jets and liquid sheets.[4] Pulsed shadowgraphy and holography were used in these studies to observe the free surface and droplet formation. The data were used to develop empirical correlations for mean droplet mass flux as a function of downstream distance measured from the jet nozzle exit.

Dai et al.[5] experimentally studied turbulent primary breakup on the outer surface of annular liquid wall jets, or annular liquid films flowing over a cylindrical rod, at

Reynolds numbers up to 840 000 and Weber numbers up to 57 000 for sheet thickness–to–rod radius ratios ranging from 0.09 to 2.2 and concluded that turbulent primary breakup along the free surface was caused by turbulence and shear due to the no-slip condition at the wall (versus aerodynamic shear). Nevertheless, they concluded that the general behavior of turbulent primary breakup for a wall jet was similar to that for round free jets. Although Ref. 4 suggests that the empirical correlations for estimating the mean droplet mass flux for turbulent liquid jets are also applicable to liquid films, it is likely that these correlations are a "worst-case" estimate for forced film flows typical of IFE thin liquid protection schemes since neither flow conditioning nor contracting nozzles were used to reduce the initial turbulence intensity—and hence delay the onset of breakup.

The objective of our studies was therefore to determine the mass flux of droplets from the free surface of a turbulent water film flowing over a horizontal downward-facing flat surface where standard techniques such as flow conditioning and a contracting nozzle were used to minimize the initial turbulence level in the flow and delay turbulent primary breakup. The droplet mass flux G was measured for various standoff distances measured from the horizontal flat surface Δz_s of 1.5 to 8.0 times the nominal film thickness (δ), downstream distances measured from the nozzle exit x of 50 to 150 times the nominal film thickness, and Weber numbers $\mathrm{We} = \rho U^2 \delta/\sigma =$ 1300 to 2800. Here, the initial film thickness at the nozzle exit $\delta = 2$ mm, the average speed at the nozzle exit $U = 6.9$ to 10.1 m/s, and the fluid surface tension $\sigma = 7.28 \times 10^{-2}$ N/m.

II. PRIMARY BREAKUP CORRELATIONS

The experimental data obtained in this study were compared with published correlations for droplet mass flux due to turbulent primary breakup in round and plane liquid jets (with fully developed turbulent pipe flow at the exit)[4] in the absence of flow conditioning and a contracting nozzle. The downstream distance for the onset of breakup x_i is given by[4]

$$\frac{x_i}{d_h} = 4403 \cdot \mathrm{We}_d^{-0.74} \ , \qquad (1)$$

where the Weber number is defined using the hydraulic diameter of the jet exit d_h. The streamwise and cross-stream velocity components of the droplets after breakup, $\tilde{u}$ and $\tilde{v}$, respectively, were measured using pulsed shadowgraphy. The streamwise component was found to be relatively independent of the downstream distance, with $\tilde{u}/U = 0.78$. The cross-stream velocity component decreases as the downstream distance x increases, with $\tilde{v}/U \leq 0.089$ for free jets. Ref. 4 uses these data to obtain a normalized cross-stream velocity relative to the jet free surface (whose velocity was also measured using pulsed shadowgraphy) of $\tilde{v}_r/U = 0.04$.

The mass flux of droplets due to turbulent primary breakup is then defined in terms of the surface efficiency factor ε as $G_{corr} = \varepsilon \rho_L \tilde{v}_r$, where the limit of $\varepsilon = 1$ corresponds to the case where droplets are emitted from the entire free surface of the jet. The surface efficiency factor is given by the following correlation as a function of the downstream distance and Weber number[4]:

$$\varepsilon = 0.272 \left[\frac{x}{d_h \mathrm{We}_d^{1/2}} \right] , \qquad (2)$$

which is valid for $\mathrm{We}_d = 235$ to 270 000.

III. EXPERIMENTAL DESCRIPTION

The turbulent films are produced by a recirculating flow loop that drives water through a flow straightening section with perforated plate and honeycomb, and a rectangular slot nozzle with a 7.5:1 area contraction ratio as outlined in Anderson et al.[6] A film of water exits the nozzle with an initial thickness $\delta = 2$ mm tangential and attaches to the underside of a flat glass plate. The flow coordinate system is defined as follows: The origin is at the center of the nozzle exit, with x along the flow direction, y along the long dimension of the film parallel to the glass plate, and z downward normal to the glass surface.

The mass ejected from the free surface was estimated using a simple collection technique where a series of five adjacent cuvettes centered with respect to the y axis with a cross-sectional inner dimension of 1×1 cm and wall thickness of 0.1 cm was placed with the openings of the cuvettes at an angle of 10 deg from the horizontal over a range of downstream distances $x = 10$ to 30 cm (Fig. 1). The angle of inclination of the cuvettes was based upon the droplet trajectories given by Ref. 4 and ensured that the droplets, once captured, would fall farther into the cuvette under the influence of gravity. The cuvette standoff distance measured from the glass plate surface was $\Delta z_s = 3$ to 16 mm, corresponding to a distance of at least 1 mm from the nominal film free surface. For each experimental realization, the mass ejected from the free surface was collected over 30 min. The mass of the five cuvettes was determined before and after collection using a digital scale (OHAUS GT 210) to an accuracy of ± 1 mg. The difference in mass then provides an estimate of the mass of collected droplets m_c, and the mass flux is then $G = m_c/(A\tau)$, where the collection area of the cuvettes was $A = 5$ cm^2 and the collection time was $\tau = 30$ min. Further details of the experiment are given in Shellabarger.[7]

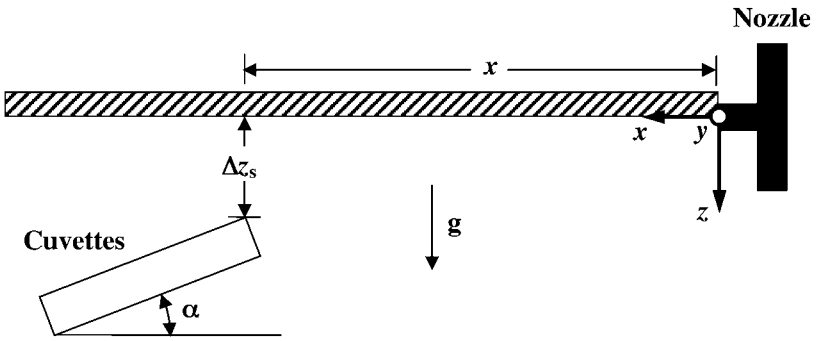

Fig. 1. Schematic of mass collection technique. The cuvettes are brought to a distance Δz_s from the glass surface at angle α = 10 deg with respect to the horizontal (x direction).

IV. RESULTS AND DISCUSSION

Figure 2 shows the mass flux G as a function of the standoff distance Δz_s at x = 10 cm for We = 1300 (△), 2000 (□), and 2800 (◇). As expected, G increases as the standoff distance decreases; i.e., more ejected droplets are collected closer to the free surface. The droplet mass flux increases rapidly near the nominal free surface of the jet, which is probably due to the cuvettes intermittently "clipping" ligaments on the free surface. The data suggest that clipping may be occurring at Δz_s = 3 mm. The mass flux also increases as We increases, which is in agreement with previous studies.

Figure 3 shows G (left axis) and the equivalent number density N (right axis) as functions of Δz_s at We = 2000 for x = 10 cm (□), 20 cm (■), and 30 cm (■). The data show that G and N increase with x since the density of the droplets increases downstream of the onset of breakup and that clipping (characterized by a rapid increase in G and N) occurs at greater Δz_s as x increases, as surface waves increase in amplitude.

A worst-case scenario for film breakup may now be examined to determine the importance of the hydrodynamic source term. Assuming that the entire upper endcap of the chamber is protected by a tangentially injected thin film and using the largest experimentally

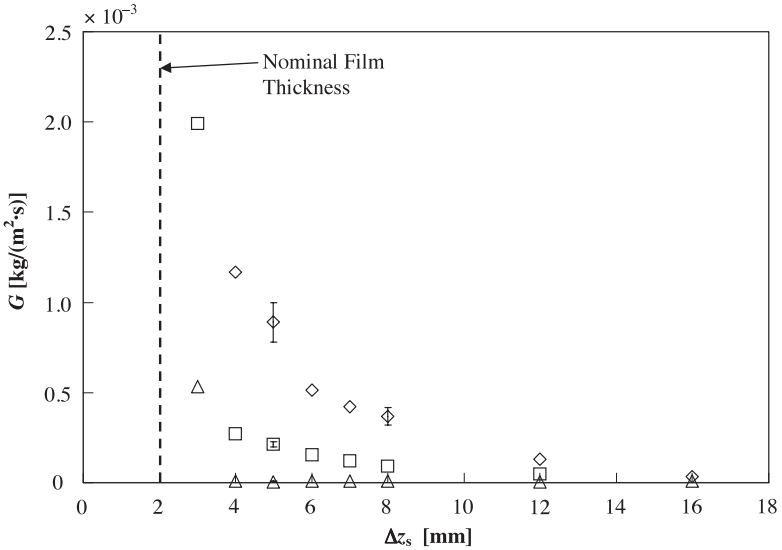

Fig. 2. Ejected droplet mass flux G [kg/(m^2·s)] versus standoff distance Δz_s (mm) at x = 10 cm for We = 1300 (△), 2000 (□), and 2800 (◇). The error bars denote 95% confidence intervals.

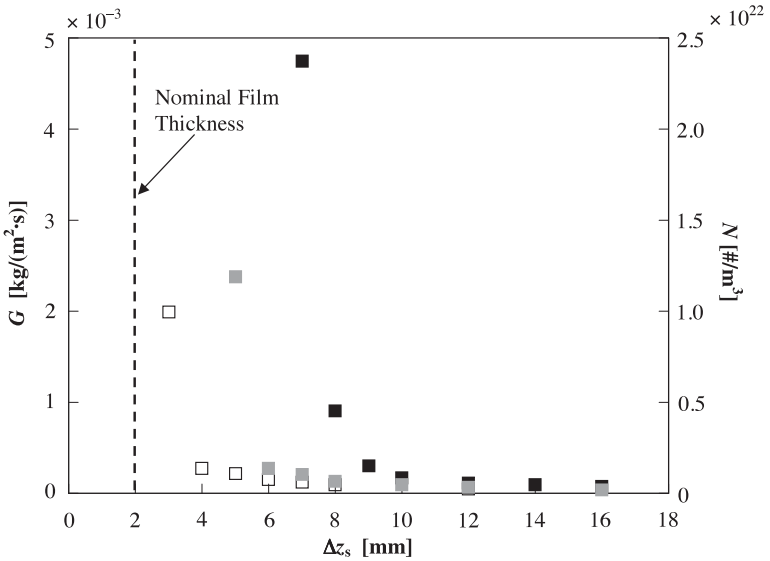

Fig. 3. Ejected droplet mass flux G [kg/(m$^2\cdot$s)] (left axis) and equivalent number density N (#/m^3) (right axis) versus standoff distance Δz_s (mm) at We = 2000 for x = 10 cm (□), x = 20 cm (■), and x = 30 cm (■). The error bars in these data are comparable to the size of the symbols.

measured mass flux value, the mass flux due to film breakup is given as

$$\text{Hydrodynamic Source Team} = (2\pi R^2)G = 0.636 \text{ kg/s} \quad (3)$$

for $R = 4.5$ m and $G = 5 \times 10^{-3}$ kg/(m$^2\cdot$s).

The amount of liquid vaporized by X rays and debris ions in a single shot is three orders of magnitude greater, ~1420 kg/s. This value was calculated assuming that the Prometheus heavy-ion target yield of 205 MJ in X rays and ions is completely deposited in the lead film at a repitition rate of 6 Hz, resulting in phase change of the liquid (h_{fg} = 0.866 MJ/kg). However, the background density limit for the Prometheus-H design was reported as 3.5×10^{21} m^{-3}, which is almost an order of magnitude below the experimentally measured maximum value of 2.5×10^{22} m^{-3}.

Figure 4 shows the mass flux predicted by the empirical correlation of Ref. 4 G_{corr} normalized by the experimental values of G as a function of Δz_s at We = 2000 and x = 10 cm (◆), 20 cm (■), and 30 cm (▲). Figure 4 illustrates that published empirical correlations for turbulent primary breakup overpredict the ejected droplet mass flux by at least three orders of magnitude. Clearly, the presence of both a flow straightening section and a contracting nozzle in the experimental apparatus greatly reduces turbulent primary breakup in these flows.

V. SUMMARY

The data presented in this investigation show that ejected droplet mass flux increases with decreasing standoff distance from the plate surface. The flux also increases with increasing Weber number and increasing distance downstream of the nozzle exit. Finally, existing empirical correlations for turbulent primary breakup appear to overpredict the ejected droplet mass flux by at least three orders of magnitude, which suggests that the presence of flow conditioning elements and a contracting nozzle have a huge influence upon turbulent primary breakup by creating a more uniform flow at the nozzle exit (versus fully developed turbulent channel flow).

Nevertheless, the ejected droplet mass flux results obtained in this study indicate that turbulent primary breakup may be a significant design issue for thin liquid protection schemes. These droplets will most likely remain in the immediate neighborhood of the film, i.e., in the upper hemispherical endcap of the chamber, or within 8δ of the first wall, as suggested by the experimental results. Given the symmetry requirements for laser ignition, beam ports are likely to be required in the upper endcap for laser ignition of direct-drive targets. Hence, such designs are more likely to be affected by the hydrodynamic source term from injected thin films. Based on target injection tracking requirements, an upper limit of $N = 6 \times 10^{21}$ m^{-3} has recently been suggested for an

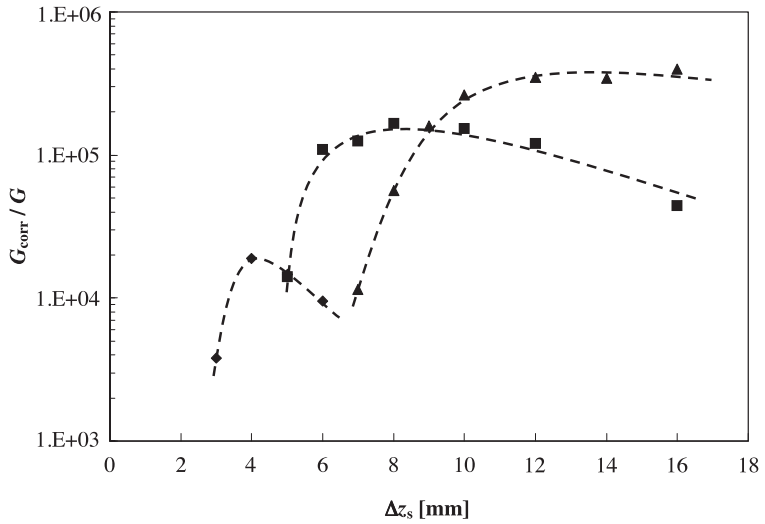

Fig. 4. Comparison between correlation and experimental droplet mass flux as a function of standoff distance from the downward-facing surface Δz_s for We = 2000, and downstream distances x = 10 cm (♦), 20 cm (■), and 30 cm (▲).

indirect-drive target design.[8] A more restrictive value of 3.5×10^{21} m^{-3} was given as the background density limit for the Prometheus heavy ion reactor design.[1] Even at the Weber numbers studied here (We = 1300 to 2800), which are significantly lower than prototypical values (We = 5900 to 190 000) and hence *underestimate* the droplet mass flux and number densities for Prometheus, the observed number densities exceed this upper limit.

While the hydrodynamic source term is likely to be much smaller than the evaporation rate due to photons and ions, the average number density from this "continuous" source may be sufficient to interfere with beam propagation and accurate target delivery. Therefore, the current acceptable limits for beam propagation and targeting may need to be reexamined. The results of these initial experiments suggest that turbulent breakup of the liquid film, and the resulting hydrodynamic source term, is a major design issue for tangentially injected thin liquid protection and could preclude the placement of beams in the upper portion of the chamber given current limits.

ACKNOWLEDGMENTS

The authors would like to thank the members of the ARIES team. This work was part of the ARIES-IFE study supported by the U.S. Department of Energy Office of Fusion Energy Sciences (contract DE-FG02-02ER54656).

REFERENCES

1. L. M. WAGANER et al., "Inertial Fusion Energy Reactor Design Studies: Prometheus Final Report," Vol. III, DOE/ER-4101, MDC 92E0008, McDonnell Douglas (1992).

2. L. M. WAGANER, "Innovation Leads the Way to Attractive Inertial Fusion Energy Reactors—Prometheus-L and Prometheus-H," *Fusion Eng. Des.*, **25**, 125 (1994).

3. J. C. LASHERAS, E. VILLERMAUX, and E. J. HOPFINGER, "Break-Up and Atomization of a Round Water Jet by a High-Speed Annular Air Jet," *J. Fluid Mech.*, **357**, 351 (1998).

4. K. A. SALLAM, Z. DAI, and G. M. FAETH, "Liquid Breakup at the Surface of Turbulent Round Liquid Jets in Still Gases," *Int. J. Multiphase Flow*, **28**, 427 (2002).

5. A. DAI, W. H. CHOU, and G. M. FAETH, "Drop Formation due to Turbulent Primary Breakup at the Free Surface of Plane Liquid Wall Jets," *Phys. Fluids*, **10**, 1147 (1998).

6. J. K. ANDERSON, S. G. DURBIN, M. YODA, S. I. ABDELKHALIK, D. L. SADOWSKI, and ARIES TEAM, "Experimental Studies of High-Speed Liquid Films on Downward Facing Surfaces for Inertial Fusion Energy Wet Wall Concepts," *Fusion Sci. Technol.*, **43**, 401 (2003).

7. B. T. SHELLABARGER, "Experimental Studies of High-Speed Liquid Films on Flat and Curved Downward-Facing Surfaces for IFE Applications," MS Thesis, Georgia Institute of Technology (2003).

8. R. PETZOLDT, B. RICKMAN, D. GOODIN, and L. BROWN, "Heavy Ion Fusion Target Materials Selection and Removal of Tungsten Carbide from Flibe," presented at ARIES September Meeting, Atlanta, Georgia, 2003.

Brian T. Shellabarger (MS, mechanical engineering, Georgia Institute of Technology, 2003) is a graduate research assistant in the George W. Woodruff School of Mechanical Engineering at the Georgia Institute of Technology. His research is in the area of high-speed liquid films on downward-facing surfaces.

Samuel G. Durbin II (MS, mechanical engineering, Georgia Institute of Technology, 2002) is a graduate research assistant at the George W. Woodruff School of Mechanical Engineering at the Georgia Institute of Technology. His research interests are in experimental investigations of thermal hydraulics with applications in thick liquid protection for IFE chambers.

Minami Yoda (PhD, aeronautics and astronautics, Stanford University, 1993) is an associate professor at the George W. Woodruff School of Mechanical Engineering at the Georgia Institute of Technology. Her research interests are in experimental fluid mechanics and optical diagnostic techniques.

Said I. Abdel-Khalik (PhD, mechanical engineering, University of Wisconsin, 1973) is the Southern Nuclear Distinguished Professor at the George W. Woodruff School of Mechanical Engineering at the Georgia Institute of Technology. His research interests are in the areas of reactor engineering and thermal hydraulics.

Dennis L. Sadowski (MSME, University of Illinois, Chicago, 1987) is a research engineer at the George W. Woodruff School of Mechanical Engineering at the Georgia Institute of Technology. His research interests are in the areas of thermal hydraulics and the construction of complex experimental systems.

ASSESSMENT AND CONTROL OF PRIMARY TURBULENT BREAKUP OF THICK LIQUID SHEETS IN IFE REACTOR CAVITIES: THE "HYDRODYNAMIC SOURCE TERM"

S. G. DURBIN,* M. YODA, S. I. ABDEL-KHALIK, D. L. SADOWSKI, T. P. KOEHLER, and ARIES TEAM *Georgia Institute of Technology, G. Woodruff School of Mechanical Engineering Atlanta, Georgia 30332-0405*

Received April 5, 2004
Accepted for Publication July 28, 2004

The "hydrodynamic source term" has been identified as a possible issue for thick liquid protection schemes in inertial fusion energy reactor cavities. The hydrodynamic source term refers to the ejected droplets due to the primary turbulent breakup of the jets themselves. Droplets are continuously ejected from the surface of the jets and spread about the chamber, possibly interfering with driver propagation and target injection. Published correlations are examined in order to estimate upper limits for the hydrodynamic source term in the case of the robust point design (RPD-2002), an update to the High-Yield Lithium Injection Fusion Energy II (HYLIFE-II) design. Experimental data for vertical turbulent sheets of water issuing into ambient air downward from nozzles of thickness (small dimension) $\delta = 1$ cm and aspect ratio of 10 are compared with the empirical correlations at near-prototypical Reynolds numbers of 1.3×10^5. A simple mass collection technique was developed to estimate the amount of ejected droplets from the jet surface. Boundary layer cutting is examined as a means of reducing the source term and improving surface smoothness. Alternate flow conditioning schemes are also explored to establish the relative importance of "traditional" flow straightening elements. Planar laser-induced fluorescence was used to visualize the free-surface geometry of the liquid sheet in the near-field region up to 25δ downstream of the nozzle exit. These results indicate that boundary layer cutting can suppress the hydrodynamic source term for a well-conditioned jet but is not a substitute for proper flow conditioning.

KEYWORDS: *liquid sheets, inertial fusion energy, turbulent breakup*

I. INTRODUCTION

Thick liquid protection provides an innovative solution that addresses the issues of first-wall protection and heat removal in an inertial fusion energy (IFE) reactor chamber. Liquid sheets, or slab jets, of molten flibe (Li_2BeF_4) are proposed for the cooling and attenuation of damaging radiation and target debris in the High-Yield Lithium-Injection Fusion Energy (HYLIFE-II) conceptual IFE power plant.[1] A lattice of stationary jets forms a protective grid that allows target injection and heavy-ion-driver beam propagation, while protecting the front and back reactor chamber first walls from the fusion event. In addition, a series of oscillating jets forms a pocket to shield the chamber sidewalls during ignition and dynamically clear the center of the chamber of jet fragments and debris between shots. Thick liquid protection can therefore help make fusion energy commercially attractive by reducing chamber size and prolonging chamber lifetime, thus significantly reducing the cost of electricity produced by fusion.[2]

Cylindrical liquid jets with boundary layer cutting have been proposed as an alternative for beamline shielding in the Robust Point Design (RPD-2002), an update to the HYLIFE-II design.[3] This design would use an array of cylindrical jets to shield the front and back walls (Fig. 1). Much effort and attention have been paid to the dynamics of these jets under chamber conditions. However, these analyses assume the thick liquid jets to be smooth, well-behaved entities.

*E-mail: gte397r@mail.gatech.edu

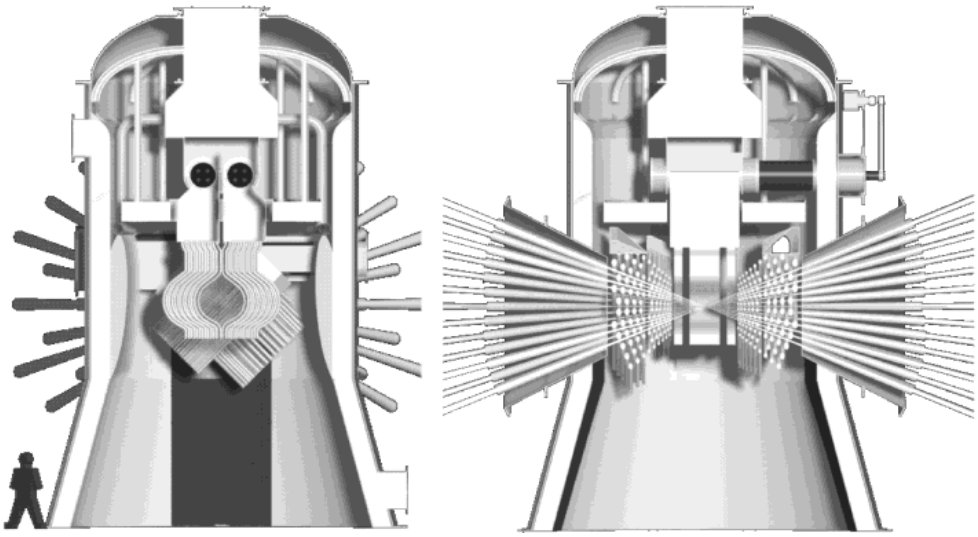

Fig. 1. Orthogonal views of the RPD-2002 chamber layout.

Close examination of the literature indicates that jets in the regime of interest are inherently unstable and susceptible to primary turbulent breakup.[4–6] Primary turbulent breakup, or primary atomization, is the breakup mechanism that involves only internal forces (i.e., turbulent, inertial, or those arising from vorticity in the flow). The fluid ejected along the surface of the jet due to turbulent breakup is again referred to as the "hydrodynamic source term." Correlations have been proposed to estimate the onset of primary breakup and mass flux from turbulent annular and round jets.[6] These relationships are valid for jet exit conditions corresponding to unconditioned, fully developed turbulent pipe flow.

Research has shown that turbulent breakup is suppressed in round jets with nearly uniform velocity profiles.[7,8] Wu et al. used a knife edge to remove the boundary layer from the flow near the nozzle exit. The boundary layer cutter had a relatively short reattachment length, to prevent substantial growth of a new boundary layer. The boundary layer cutting concept has also been employed for highly conditioned round jets with applications in fusion energy.[3] To our knowledge, boundary layer cutting has not heretofore been studied for use in turbulent liquid sheets.

Turbulent breakup correlations have been applied for the case of unconditioned round jets in the stationary protective lattice geometry in RPD-2002. Weber numbers of interest ranged from 6.8×10^4 to 23×10^4 for jet diameters of 46 to 156 mm, respectively. This analysis is expected to provide an upper limit for the hydrodynamic source term (overestimating by three to five orders of magnitude based on experimental evidence in this paper) since the correlations are based on jets produced without flow conditioning and with fully developed pipe flow conditions at the exit.

Liquid sheets of water issuing vertically downward into ambient air were studied experimentally to evaluate different flow conditioning schemes, including boundary layer cutting. These measurements were obtained in the near-field $x/\delta \leq 25$, where x is the streamwise coordinate measured from the nozzle exit. The Reynolds number $\mathrm{Re} = U_0 \delta/\nu$ and Weber number $\mathrm{We} = \rho_L U_0^2 \delta/\sigma$ for these flows were 1.3×10^5 and 1.9×10^4, respectively, where U_0 is the average jet speed and δ is the jet thickness (short dimension) at the nozzle exit. The liquid kinematic viscosity, density, and surface tension are denoted by ν, ρ_L, and σ, respectively. The Re and We for these investigations are about one-half and one-fifth of prototypical values for the HYLIFE-II concept. The free surface is visualized using planar laser-induced fluorescence (PLIF). The hydrodynamic source term is estimated using both the breakup correlations and a simple mass collection technique. The boundary layer cutter device in these experiments was used to cut 0.25 mm into the flow as measured from the nozzle wall since velocity measurements near the nozzle exit for similar flows at $\mathrm{Re} = 1 \times 10^5$ indicate that the boundary layer is $O(0.1\ \mathrm{mm})$ (Ref. 9). The effects of boundary layer cutting and flow conditioning are characterized by both measurement methods.

II. TURBULENT BREAKUP CORRELATIONS

Published correlations for the turbulent primary breakup of liquid jets were derived from experiments

using pulsed shadowgraphy and holography.[6,7,10] These correlations were developed for round and annular jets with a fully developed turbulent velocity profile at the nozzle exit. The flows incorporate no flow conditioning or contracting nozzle. The downstream location for the onset of breakup measured from the nozzle exit x_i is given by the following power law relationship[10]:

$$\frac{x_i}{d_h} = 4403 \cdot \mathrm{We}_d^{-0.74} \ , \tag{1}$$

where the Weber number is defined here with the hydraulic diameter d_h as the characteristic length. Equation (1) is valid for $\mathrm{We}_d = 13\,000$ to $151\,000$. As We_d increases for a given jet diameter, the onset of breakup occurs more closely to the nozzle exit.

The Sauter mean diameter (SMD) is often used to characterize the "average" size of droplets in a spray. The SMD is defined as the diameter of a droplet having the same volume-to-surface area ratio of a representative sample of the spray. Droplet size as given by SMD is described by the power law relationship[6]

$$\frac{\mathrm{SMD}}{d_h} = 0.65 \cdot \left(\frac{x}{d_h \cdot \mathrm{We}_d^{0.5}} \right)^{2/3} \ . \tag{2}$$

Equation (2) illustrates that droplet size increases with downstream distance.

The streamwise and cross-stream velocities of droplets after breakup were measured using pulsed shadowgraphy. Droplet streamwise velocities are relatively independent of downstream location and are given by $\tilde{u}/U_0 = 0.78$. The cross-stream velocities of droplets decrease with increasing downstream location and have values of $\tilde{v}/U_0 \leq 0.089$. The relative cross-stream droplet velocity to the surface of the jet takes on values of $\tilde{v}_r/U_0 = 0.04$, which is comparable to root-mean-square turbulence intensities near the wall in developed turbulent pipe flow. These velocities are used in calculating the ejected mass flux and in determining the trajectories of the droplets after breakup.

The mass flux of droplets relative to the liquid surface due to turbulent primary breakup, denoted as G [kg/(m$^2 \cdot$s)], is developed next. The droplet mass flux was measured directly by single-pulse holography and normalized in terms of the surface efficiency factor ε. This factor is given as $\varepsilon = G/(\rho_L \cdot \tilde{v}_r)$, where the limit of $\varepsilon = 1$ denotes the case when droplets are being emitted over the entire surface of the jet. Based on measurements of G and $\tilde{v}_r$, the surface efficiency factor as a function of downstream distance is given by the following correlation[6]:

$$\varepsilon = 0.272 \left[\frac{x}{d_h \cdot \mathrm{We}_d^{0.5}} \right] \ . \tag{3}$$

Equations (2) and (3) are valid for $\mathrm{We}_d = 235$ to $270\,000$.

III. EXPERIMENTAL APPARATUS AND PROCEDURES

III.A. Flow Loop

A recirculating flow loop driven by a 7.5-hp centrifugal pump was used for these experiments. The pump delivers water from the bottom receiving tanks (total volume 2800 ℓ) 5.5 m below the test section. The flow from the pump is then passed through the flow-conditioning section and nozzle forming the liquid sheet in the open test section.

The flow conditioner used in these experiments was manufactured in three sections by stereolithography rapid prototyping (Fig. 2). The three straightening elements consisted of a stainless steel perforated plate (50% open area ratio, 4.8-mm-diam staggered holes) followed by a 2.5-cm section of polycarbonate honeycomb with 0.32-cm cell diameter and a stainless steel fine screen (30 × 30 mesh size, 37.1% open area ratio, 0.33-mm wire diameter, 0.51-mm open cell width). The streamwise spacings between elements are 3.8 cm for perforated plate–honeycomb and 0.5 cm for honeycomb–fine screen with the nozzle inlet 14.6 cm downstream of the fine screen. The overall x extent of the flow conditioner was 21.6 cm. After exiting the nozzle, the flow was directed into the 1500-ℓ top receiving tank located 1.9 m below the nozzle exit and then drained into the bottom receiving tanks for recirculation by the pump.

The boundary layer cutter used in this study was independently mounted separate from the nozzle to allow

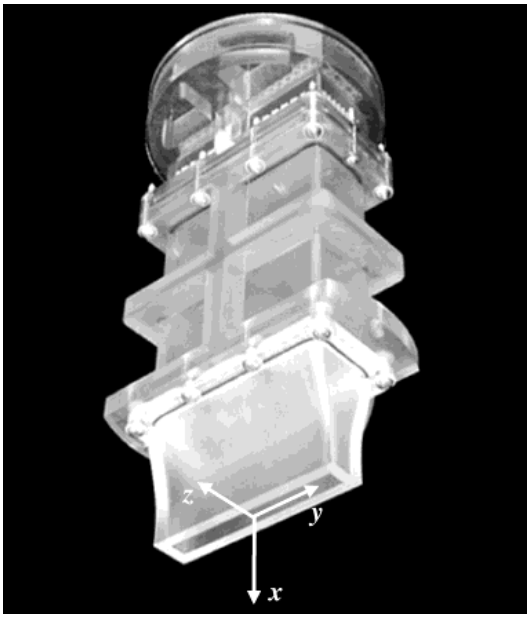

Fig. 2. Flow conditioner and nozzle assembly.

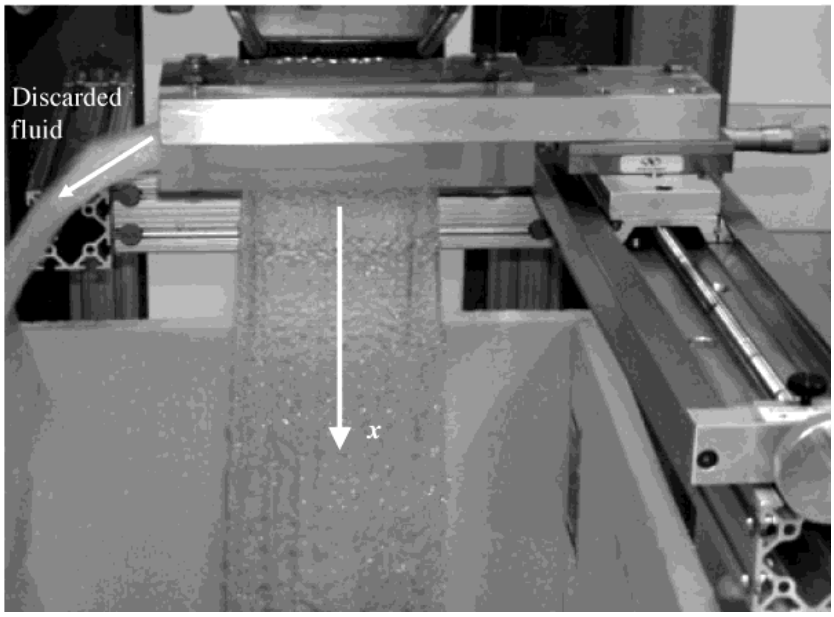

Fig. 3. Boundary layer cutter layout. Flow goes from top to bottom (along x).

the removal of fluid from one face of the jet. The cutter assembly was supported below the nozzle on a linear stage to allow control in the z direction (Fig. 3). The cutter blade was machined from aluminum with a reattachment length of 7.5 mm. Figure 4 is a schematic describing the arrangement of the cutter blade with respect to the nozzle. The width of the blade extended 1 cm beyond the width of the jet on each side for a total y extent of 12 cm. The edge of the blade was located 0.76 mm downstream of the nozzle exit. The cut depth for all experiments reported here was fixed at $\Delta z_{cut} = 0.25$ mm with the corresponding mass flow rate removed by the cutter being 0.18 kg/s or 1.5% of the total jet flow rate.

III.B. Free-Surface Visualization

PLIF was used to visualize the free surface of the liquid sheet. The water in the flow loop was dyed to a concentration of 26 mg/ℓ ($\approx$ 71 μmole/ℓ) with disodium fluorescein, a dye that fluoresces in the yellow-green when illuminated at 488 nm. This relatively high concentration ensured that all laser light was absorbed near the free surface. The surface tension of solutions up to 53 mg/ℓ concentration was measured and found to be identical to that of distilled water. The illumination source

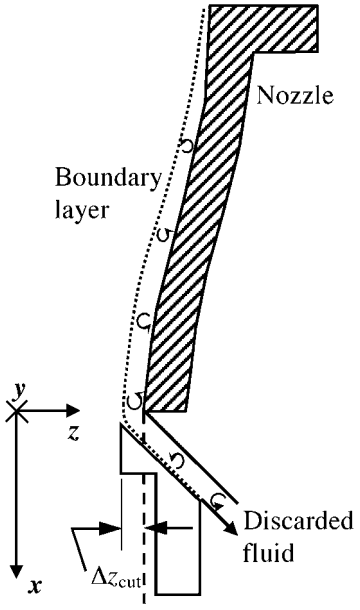

Fig. 4. Schematic of boundary layer cutter. (Note: Enclosure around cutter blade not shown.)

was a 0.5-W multiline argon-ion laser beam. The laser was passed through a notch filter (Edmund Scientific NT30-907) to obtain ~0.2 W at 488 nm. The flow was illuminated at various downstream (x) locations by the 488-nm laser light sheet with a thickness (x dimension) of 2 mm.

The free surface was imaged as the interface between fluorescing water and nonfluorescing air by an obliquely mounted black-and-white charge-coupled device camera (Kodak Model ES 1.0) from below at 30 Hz with a close-focusing macro video lens (Navitar Zoom 7000) (Fig. 5). A high-pass wavelength filter (Sunpak Yellow-8) with a cutoff frequency of 500 nm was mounted to the camera lens to ensure that only fluorescence was imaged.

The free surface was visualized using four to five overlapping segments that span one side of the entire y extent of the flow. The field of view for each image is ~3.0 cm (y) × 3.0 cm (z) with a spatial resolution of 30 μm/pixel. Each segment was composed of 134 consecutive images, each with an exposure of $\tau = \delta/U_0$, with an entire segment spanning at least 5200τ. The individual frames were stored as 8-bit 1008 × 1008 image bitmaps on a personal computer hard drive using digital video recording software (Video Savant 3.0).

The free surface is found in each image using a threshold-based edge detection algorithm written in MATLAB. The grayscale threshold value was chosen based upon the grayscale histogram for the entire dataset. This grayscale value was chosen such that it was the first grayscale value to the right of the background peak to be 1% of the number of background peak pixels. For every segment, the instantaneous free-surface locations are determined for each of 134 thresholded frames using a standard edge detection scheme and used to calculate the average location and z-direction standard deviation of the free surface.

Each segment of the free surface has a slight overlap with neighboring segments. The extent of the overlap region is known from a reference scale imaged in each frame. In all cases, the free-surface fluctuations in this overlap region are taken to be those calculated for the left segment. No significant discontinuities were observed using this procedure.

III.C. Measurement of Ejected Mass

The ejected mass from the free surface was measured using a simple mass collection technique. Square cuvettes with dimension of 1 cm were placed in the proximity of the free surface at the farthest downstream location of $x/\delta = 25$ (Fig. 6). The cuvette standoff distance Δz_s was measured from the nominal free surface of the jet, which corresponds to the downstream location of the inner nozzle wall. A series of five cuvettes were centered with respect to the y axis and maintained at a fixed z location for 30 to 60 min. An angle of 6.5-deg from the vertical was imposed on the cuvettes to accommodate the correlation-based droplet trajectories. The cuvettes were weighed on a digital scale (OHAUS GT 210) to 1-mg

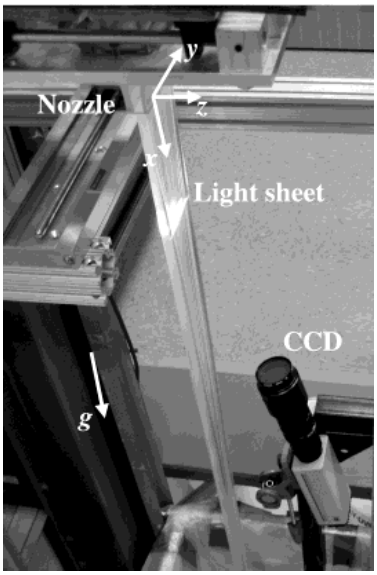

Fig. 5. Photograph of PLIF setup.

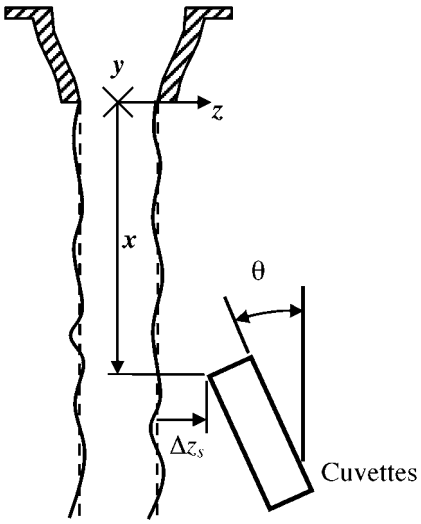

Fig. 6. Schematic of mass collection technique. The cuvettes are brought to a distance Δz_s from the nominal free surface (dashed lines) at angle θ from the vertical (typical 6.5 deg).

accuracy before and after each trial so that the mass difference provides an estimate of the mass ejected from the free surface.

Droplets were visualized using a digital camera (Nikon CoolPix 950) attached to a standard microscope with a 5× objective. A microscope slide treated with Rain-X® was placed near the free surface for ~10 s. The slide was then viewed under the microscope with the image recorded by the digital camera. Images were captured at a resolution of 1600 × 1200 with a resulting spatial resolution of 1 μm/pixel.

The quantities of interest for ion-beam propagation are the effective line density and the equivalent average number density. The experimental mass flux was calculated by dividing the collected mass by the collection time and total cuvette cross-sectional area (5 cm^2). The effective line density ρ_{eff} (kg/m^3) was then assumed to be

$$\rho_{eff} = \frac{G}{\sqrt{\tilde{u}^2 + \tilde{v}^2}} \tag{4}$$

with $\tilde{u}$ and $\tilde{v}$ given in the previous section. The equivalent average number density N (#/m^3) was defined as

$$N = \frac{\rho_{eff} \cdot N_A}{M} \ , \tag{5}$$

where N_A and M are Avogadro's number and molecular weight, respectively.

IV. RESULTS AND DISCUSSION

IV.A. Implications for HYLIFE-II and RPD-2002 Without Conditioning

The breakup correlations were applied to the geometry of the protective lattice of the RPD-2002 without flow conditioning or boundary layer cutting. One quadrant of the proposed lattice includes 12 rows of three to six cylindrical jets per row. Jet diameters range from 46 to 156 mm with U_o = 12 m/s for each jet.[3] The overall streamwise flow distance was assumed to be 2 m. Since the distance to the onset of breakup is small compared to the assumed flow length, an average downstream distance of x = 1 m was used for subsequent calculations of ejected mass flux and SMD. Table I summarizes the characteristic breakup values for the range of jet diameters in the RPD-2002 case.

The hydrodynamic source term was then estimated using the results for the entire jet lattice. The hydrodynamic source terms for selected rows of RPD-2002 are shown in Table II. These numbers reflect the breakup for all jets in these rows. The mass flow rate due to droplets being ejected from the free surface is given as $\dot{m}_{HST}$ (kg/s). The total hydrodynamic source term for the entire chamber lattice system was 1300 kg/s. This amount was ~3% of the total input flow rate on average. This is a substantial amount considering that the fast burn products from a typical heavy-ion indirect-drive target would vaporize only ~160 kg/s, based on a 6-Hz repetition rate.

TABLE I

Correlation Breakup Values for the Unconditioned RPD-2002 Protective Lattice

Row	d (mm)	x_i (mm)	$\mathrm{We}_d \times 10^{-4}$	SMD (x_i) (mm)	SMD (x = 1 m) (mm)	$G(x = 1\ \mathrm{m})$ (kg/(m^2·s))
0	46	54	6.8	0.82	5.7	21.4
11	156	74	23	1.0	5.7	3.44

Next, the influence of droplets in the beamlines was considered using the trajectories and mass fluxes as predicted by the correlations. Figure 7 shows the normalized effective line density and equivalent average number density for a first-row jet (row 0) from RPD-2002. The beam-to-jet standoff was taken to be 5 mm plus 10% of the jet radius. These results indicate that droplets penetrating into the beamlines would have equivalent number densities at the proposed beam standoff distance near the bottom of the lattice on the order of 10^{25} #/m^3, which would likely be incompatible with beam propagation requirements.

IV.B. Turbulent Liquid Sheet Experiments

IV.B.1. PLIF Experiments

Boundary layer cutting affects the mean free-surface position of turbulent liquid sheets. The appearance of protrusions near the edges of the jet was evident when boundary layer cutting was used (Fig. 8). These protrusions extend out to the nominal free surface with the bulk of the jet well within this boundary. Although not apparent in Fig. 8, the y extent of the cut jet was reduced for

TABLE II

Correlation-Predicted Hydrodynamic Source Terms of the Unconditioned RPD-2002 Case for Typical Rows and Lattice Total

Row	Total # Jets	$\dot{m}$ (kg/s)	$\dot{m}_{HST}$ (kg/s)	$f = \dfrac{\dot{m}_{HST}}{\dot{m}}$
0	24	944	149	0.15800
11	12	5 400	40.4	0.00748
Total	252	45 000	1300	0.02890

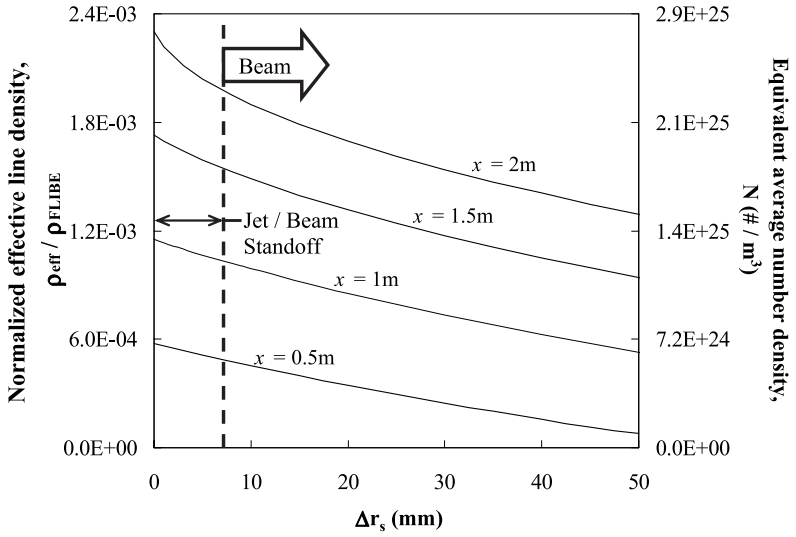

Fig. 7. Normalized line density and average equivalent number density as a function of beam standoff distance Δr_s for a typical RPD-2002 jet with $d = 46$ mm (row 0).

each downstream location with the cut jet width ~6 mm less at $x/\delta = 25$.

Two configurations of the flow conditioning were examined for this study: with and without the fine screen. The fine screen element is the most likely to trap debris and would therefore be the element of choice for designers to eliminate. Standard deviation as a function of y/δ is shown for both conditioning schemes with boundary layer cutting at $x/\delta = 25$ in Fig. 9. The case with no fine screen exhibits a marked increase in standard deviation near the center of the jet. These increased fluctuations are similar to those observed for the case of central blockage

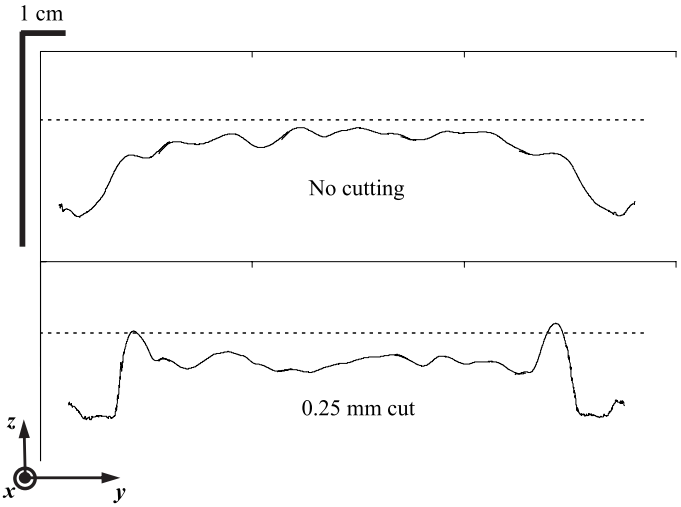

Fig. 8. Average free-surface position of a turbulent liquid sheet for Re = 130 000 and $x/\delta = 25$. Nominal free surface is indicated by dashed lines with flow out of the page. (Note: Vertical axis shown at 5× magnification.)

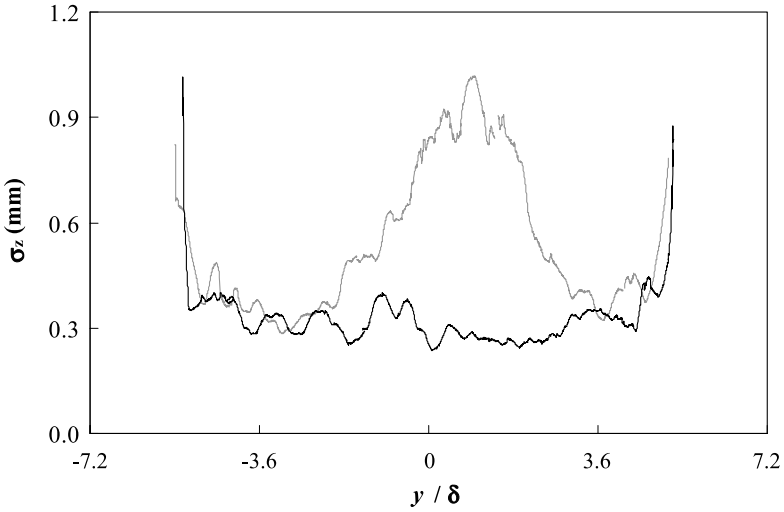

Fig. 9. Local free-surface standard deviation σ_z as a function of y/δ at $x/\delta = 25$. Results are for jets with 0.25-mm cut and flow conditioning with fine screen (black) and without (gray).

in the flow conditioner.[11] The sharp increases in σ_z at the edges of the jet are due to lateral fluctuations of the jet (y direction) and are indicative of the absence of the jet in some images.

For jets with boundary layer cutting, the surface standard deviation is reduced compared to those without cutting. This trend indicates that boundary layer cutting does improve surface smoothness, but the fine screen has a larger impact on overall jet fluctuations. Cutting 0.25 mm from the surface of the jet reduced the standard deviation on average 17% for the case with the fine screen and 10% for the case without (Fig. 10). The surface ripple for uncut jets was 75% greater for flow conditioning without the fine screen compared to the standard straightening

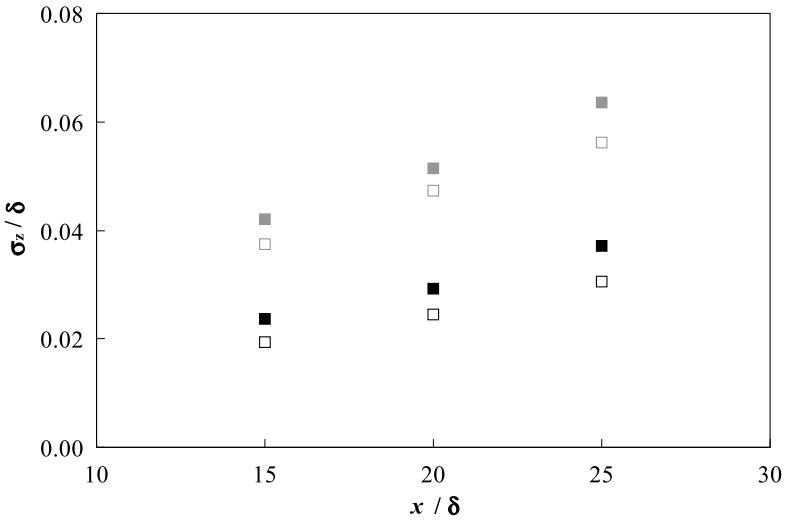

Fig. 10. Normalized average free-surface standard deviation σ_z/δ as a function of downstream distance. Results are for flow conditioning with fine screen (black) and without (gray). Symbols indicate with 0.25-mm cut (open) and without (closed).

design. For jets with boundary layer cutting, the standard deviation was reduced 90% by adding the fine screen to the flow conditioner.

IV.B.2. Mass Collection Experiments

The presence of droplets from turbulent breakup at the jet surface increases with decreasing standoff distance from the nominal free surface. Figure 11 shows the equivalent number density as a function of cuvette standoff for the two flow-conditioning arrangements at $x/\delta = 25$. Droplets are more prevalent near the source of breakup, the jet surface. Secondary effects such as aerodynamic shear, reentrainment, and evaporation act to limit the extent to which droplets can be collected. Therefore, the equivalent number density of the droplets will increase from zero at a sufficiently distant standoff with a sharp increase as the free surface of the jet is encountered. Droplets are confined to a region closer to the nominal free surface for flow conditioning with the fine screen. This trend is expected given the large increase in standard deviation at the free surface for conditioning without the fine screen.

Boundary layer cutting reduces the amount of turbulent breakup of the jet. For the case without a fine screen, the number density is decreased at each standoff distance but is not eliminated. Breakup is effectively suppressed for jets conditioned with the fine screen and boundary layer cutting at all standoff distances. These trends are consistent with those seen in the PLIF experiments with the absence of the fine screen having a larger impact on the quality of the jet than boundary layer cutting.

Droplet visualizations were performed for the case of standard flow conditioning at a downstream distance of $x/\delta = 25$ (Fig. 12). These images indicate that droplet sizes are on the order of 1 to 100 μm. Estimates indicate that a droplet with an initial radius of 1 μm evaporates within ~3 s at laboratory conditions. The images were taken within ~15 s of removing the microscope slide. Evaporation of droplets was visually detected while the slide was under inspection.

The breakup correlations were applied for a liquid sheet matching the experimental conditions. Model predictions of SMD range from 0.6 to 2.1 mm for downstream distances of x/δ from 3.7 to 25, respectively. The observed droplets were considerably smaller, even considering losses due to evaporation. Next, the ratio of the mass flux from the experiments and correlations is plotted as a function of standoff distance (Fig. 13). The contracting nozzle and flow conditioning alone reduce the mass flux by three to five orders of magnitude. Droplets are present at greater standoff distances away from the nominal free surface when the fine screen is absent from the flow conditioner. A ratio of 10^{-6} or less indicates a measured mass flux of zero to within experimental error.

V. CONCLUSIONS

Our work demonstrated the importance of flow conditioning and boundary layer cutting for jets of interest in the HYLIFE-II conceptual fusion reactor. Correlations from the literature were applied for a RPD-2002 stationary

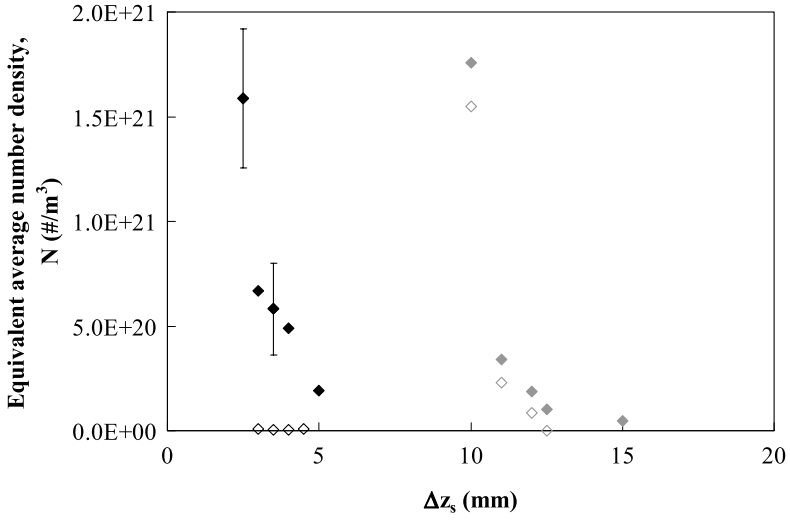

Fig. 11. Equivalent average number densities from turbulent liquid sheet experiments at $x/\delta = 25$ as a function of standoff distance from the nominal free surface Δz_s. Results are for flow conditioning with fine screen (black) and without (gray). Symbols indicate with 0.25-mm cut (open) and without (closed).

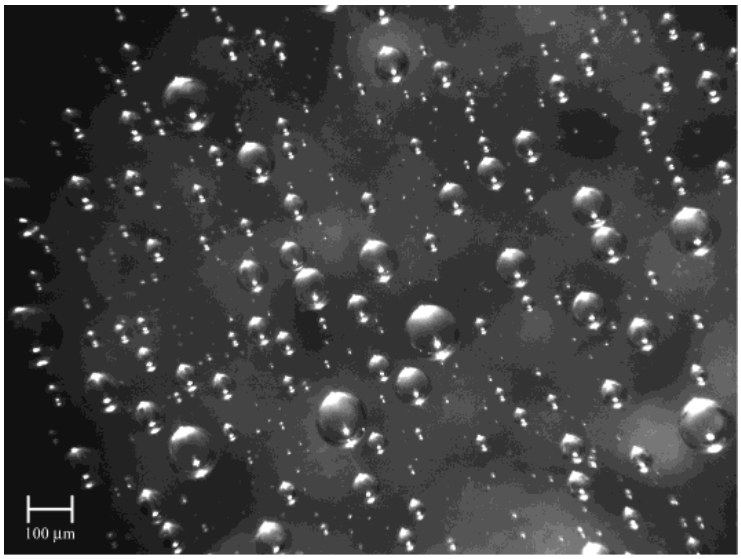

Fig. 12. Droplets collected from jet with standard flow conditioning at $x/\delta = 25$. Scale in lower left corner represents 100 μm.

lattice geometry of unconditioned cylindrical jets (without boundary layer cutting) to estimate the hydrodynamic source term. The mass flow rate due to the turbulent breakup of the lattice jets would account for up to 1300 kg/s, or 3% of the total flow rate for all jets. Equivalent number densities in the beamlines reach values comparable to air at atmospheric pressure near the bottom of the lattice. These estimates indicate that jets without any conditioning would be unsuitable for thick liquid protection applications in fusion chambers.

Experimental investigations of turbulent liquid sheets were conducted to compare actual jet breakup with the

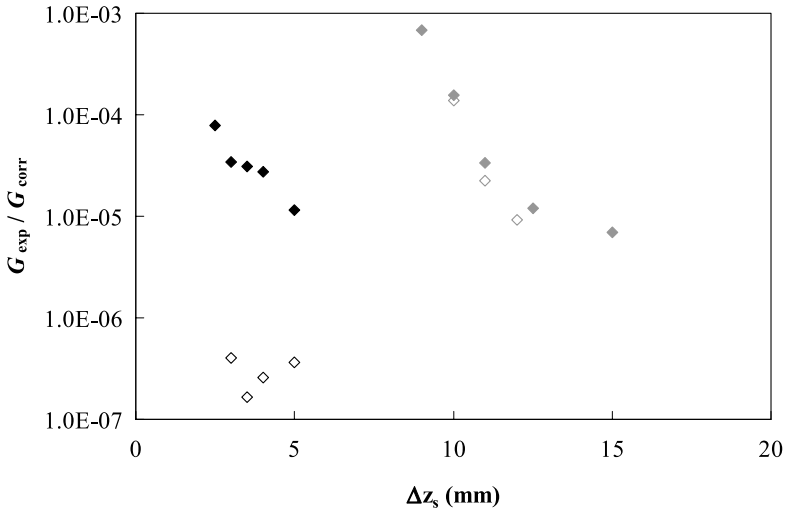

Fig. 13. Comparison of experimental and correlation results as a function of standoff distance from the nominal free surface Δz_s. Results are for flow conditioning with fine screen (black) and without (gray). Symbols indicate with 0.25-mm cut (open) and without (closed). (Note: Values below 10^{-6} are equivalent to a measured mass flux of zero within experimental error.)

predictions from the correlations. Since the experimental conditions in these trials are not identical to those used to establish the correlations, reductions in breakup with respect to the correlations should be considered preliminary. Standard flow conditioning and contracting nozzle reduce the predicted mass flux from turbulent breakup by three to five orders of magnitude. In addition, the size of the droplets from breakup is much smaller than the SMD predicted by the correlations. Removing the fine screen from the flow conditioner increases the hydrodynamic source term. Cutting for jets without the fine screen reduces but does not eliminate jet breakup. Boundary layer cutting does suppress turbulent breakup for jets with the fine screen included in the flow conditioning. Boundary layer cutting can be used in conjunction with "traditional" straightening elements to eliminate the hydrodynamic source term but is not a substitute for proper flow conditioning.

The dynamics of turbulent liquid sheets were quantified for different initial conditions using PLIF. The fine screen element of the flow conditioner has significant impact on surface ripple. The average standard deviation for jets produced without a fine screen is almost twice that of flows with all straightening elements in place. Flows conditioned without the fine screen produce surface fluctuations similar to those in which a central blockage was placed on the fine screen. Preventing blockages in the flow conditioner is therefore a major concern for thick liquid protection.

Boundary layer cutting reduces surface standard deviation for all cases. Cutting makes a more pronounced difference in surface ripple for jets with standard flow conditioning. These results are consistent with the mass collection experiments, demonstrating again that the fine screen in the flow conditioner has a larger impact on the downstream characteristics than the boundary layer cutter. The benefits of the boundary layer cutting technique are again secondary to proper flow conditioning.

The average free-surface profile of the jet was also measured with PLIF. These results indicate that boundary layer cutting produces sharp protrusions near the edges of the sheet. These protrusions extend to the nominal free surface, whereas the uncut sheet is always inside this limit. These end effects may be due to fluid being removed from only one side of the jet. Cutting also decreases the width (y extent) of the jet at all downstream locations with the width nearly 6 mm less for a cut jet at $x/\delta = 25$. The geometry of a rectangular jet continually evolves from the original cross section to a nonrectangular shape and must be understood to allow realistic beam-to-jet standoffs.

ACKNOWLEDGMENTS

This research was performed as part of the ARIES-IFE study supported by the U.S. Department of Energy (DOE) Office of Fusion Energy Sciences through contract DE-FG02-02ER54656. S. G. Durbin was under an appointment to the Fusion Energy Sciences Fellowship Program, administered by Oak Ridge Institute for Science and Education under a contract between the DOE and the Oak Ridge Associated Universities. We thank B. T. Shellabarger and R. Moir for their help and support. Figure 1 is courtesy of R. Abbott.

REFERENCES

1. R. W. MOIR, "The High-Yield Lithium-Injection Fusion-Energy (HYLIFE)-II Inertial Fusion Energy (IFE) Power Plant Concept and Implications for IFE," *Phys. Plasmas*, **2**, 2447 (1995).

2. R. W. MOIR et al., "HYLIFE-II: A Molten-Salt Inertial Fusion Energy Power Plant Design—Final Report," *Fusion Technol.*, **25**, 5 (1994).

3. S. J. PEMBERTON, R. P. ABBOTT, and P. F. PETERSON, "Thick-Liquid Blanket Configuration and Response for the HIF Point Design," *Fusion Sci. Technol.*, **44**, 294 (2003).

4. N. A. CHIGIER, "The Physics of Atomization," presented at 5th Int. Conf. Liquid Atomization and Spray Systems (ICLASS-91), Gaithersburg, Maryland, July 15–18, 1991.

5. S. P. LIN and R. D. REITZ, "Drop and Spray Formation from a Liquid Jet," *Annu. Rev. Fluid Mech.*, **30**, 85 (1998).

6. K. A. SALLAM, Z. DAI, and G. M. FAETH, "Liquid Breakup at the Surface of Turbulent Round Liquid Jets in Still Gases," *Int. J. of Multiphas. Flow*, **28**, 427 (2002).

7. P. K. WU, R. F. MIRANDA, and G. M. FAETH, "Effects of Initial Flow Conditions on Primary Breakup of Nonturbulent and Turbulent Round Liquid Jets," *Atomization Spray*, **5**, 175 (1995).

8. T. KARASAWA, M. TANAKA, K. ABE, S. SIGA, and T. KURABAYASHI, "Effects of Nozzle Configuration on the Atomization of a Steady Spray," *Atomization Spray*, **2**, 411 (1992).

9. S. G. DURBIN, M. YODA, S. I. ABDEL-KHALIK, and D. L. SADOWSKI, "Turbulent Liquid Sheets for Protecting IFE Reactor Chamber First Walls," *Fusion Sci. Technol.*, **44**, 307 (2003).

10. K. A. SALLAM, Z. DAI, and G. M. FAETH, "Drop Formation at the Surface of Plane Turbulent Liquid Jets in Still Gases," *Int. J. of Multiphas. Flow*, **25**, 1161 (1999).

11. J. J. R. REPERANT, S. G. DURBIN, M. YODA, S. I. ABDEL-KHALIK, and D. L. SADOWSKI, "Studies of Turbulent Liquid Sheets for Protecting IFE Reactor Chamber First Walls," *Fusion Eng. Des.*, **63–64**, 627 (2002).

MS #006: Presented at 16th Technology of Fusion Energy Meeting (Madison, WI)
Accepted for publication *Fusion Science and Technology* (2005)

IMPACT OF BOUNDARY-LAYER CUTTING AND FLOW CONDITIONING ON FREE-SURFACE BEHAVIOR IN TURBULENT LIQUID SHEETS

S.G. Durbin†, M. Yoda, and S.I. Abdel-Khalik

G. Woodruff School of Mechanical Engineering
Georgia Institute of Technology
Atlanta, GA 30332-0405 USA
†(404) 385-1891 gte397r@mail.gatech.edu

The HYLIFE-II conceptual design uses arrays of high-speed oscillating and stationary slab jets, or turbulent liquid sheets, to protect the reactor chamber first walls. A major issue in thick liquid protection is the hydrodynamic source term due to the primary turbulent breakup of the protective slab jets. During turbulent breakup, drops are continuously ejected from the surface of turbulent liquid sheets and convected into the interior of the cavity, where they can interfere with driver propagation and target injection. Experimental data for vertical turbulent sheets of water issuing downwards from nozzles of thickness (small dimension) δ = 1 cm into ambient air are compared with empirical correlations at a nearly prototypical Reynolds number Re = 1.2 × 10^5. A simple collection technique was used to estimate the amount of mass ejected from the jet surface. The effectiveness of boundary-layer cutting at various "depths" into the flow to reduce the source term and improve surface smoothness was evaluated. In all cases boundary-layer cutting was implemented immediately downstream of the nozzle exit. Planar laser-induced fluorescence (PLIF) was used to visualize the free-surface geometry of the liquid sheet in the near-field region up to 25δ downstream of the nozzle exit. Large-scale structures at the edges of the sheet, typically observed for Re < 5.0 × 10^4, reappeared at Re = 1.2 × 10^5 for sheets with boundary-layer cutting. The results indicate that boundary-layer cutting can be used to suppress drop formation, i.e. the hydrodynamic source term, for a well-conditioned jet but is not a substitute for well-designed flow conditioning.

I. INTRODUCTION

Thick liquid protection is potentially an innovative solution for first wall protection and heat removal for inertial fusion energy (IFE) reactor chambers. The High-Yield Lithium-Injection Fusion Energy (HYLIFE-II) IFE power plant design proposed using slab jets, or liquid sheets, of molten Flibe (Li_2BeF_4) for cooling and attenuation of damaging radiation and target debris.[1] However, jets in the range of interest for HYLIFE-II are susceptible to primary turbulent breakup[2,3], or breakup (atomization) involving only internal forces such as turbulent or inertial forces, or forces due to vorticity. The fluid ejected along the free surface of the jet due to turbulent breakup is here called the "hydrodynamic source term." Previous work on turbulent annular liquid sheets and round jets have proposed correlations for estimating the onset of and mass flux due to primary breakup.[3] These correlations were developed for jet initial conditions corresponding to unconditioned, fully-developed turbulent pipe flow.

A number of studies have shown that turbulent breakup is suppressed in round jets with nearly uniform initial velocity profiles.[4,5] Wu *et al.* used a knife-edge to remove the boundary layer (BL) from the flow near the nozzle exit. The boundary-layer cutter had a relatively short reattachment length, preventing substantial growth of a new BL. Our group has previously demonstrated that boundary-layer cutting can be used to eliminate breakup (within experimental error) for turbulent liquid sheets.[6]

In our previous study, a relatively large amount of BL cutting to a depth of 0.25 mm from the inner surface of the nozzle, corresponding to removing 1.5% of the total mass flux $\dot{m}_{fl}$, was used. BL cutting was found to be effective at suppressing breakup in only a "well-conditioned" flow. This subsequent work focuses upon optimizing the amount of BL cutting (in terms of the fraction of total mass flux removed) to suppress turbulent breakup while minimizing the amount of "cut" fluid, and exploring how changes in flow conditioner design impact the effectiveness of BL cutting.

Liquid sheets of water issuing vertically downwards into ambient air were studied experimentally in the near-field $x/\delta \leq 25$. The coordinate system used here has its origin at the center of the nozzle exit, with x along the flow direction, and y and z along the long and short dimensions of the nozzle, respectively. The Reynolds and Weber numbers are $Re = U_o\delta/\nu = 1.2\times10^5$ and $We = \rho_L U_o^2\delta/\sigma = 1.9\times10^4$, respectively. Here, U_o is the average jet speed and δ the z-dimension of the jet at the nozzle exit. The liquid kinematic viscosity, liquid density

and liquid-air surface tension are denoted by ν, ρ_L and σ, respectively. The *Re* and *We* for these investigations are about one-half and one-fifth of the HYLIFE-II prototypical values. The effectiveness of BL cutting at levels ranging from 0–1.9% of $\dot{m}_{fl}$, were evaluated for a standard flow conditioner design and an otherwise identical design without the fine screen.

II. TURBULENT BREAKUP CORRELATIONS

The hydrodynamic source term, measured by a simple mass collection technique, is compared to published correlations for turbulent primary breakup of liquid jets based upon pulsed shadowgraphy and holography data.[3] These correlations were developed for round and annular jets with fully-developed turbulent velocity profiles at the nozzle exit with neither flow conditioning nor a contracting nozzle upstream.

Using pulsed shadowgraphy to measure the streamwise and cross-stream droplet velocity components $\tilde{u}$ and $\tilde{v}$, respectively, Sallam *et. al.* reported values of $\tilde{u}/U_o = 0.78$ and $\tilde{v}/U_o \le 0.089$. They also concluded that $\tilde{v}_r$, the cross-stream velocity of the droplets measured with respect to the free surface, was proportional to the average speed at the nozzle exit, with $\tilde{v}_r/U_o = 0.04$.

The mass flux of droplets relative to the liquid surface due to turbulent primary breakup is denoted as *G* [kg/(m^2·s)]. The droplet mass flux was measured directly by single-pulse holography and normalized to give the surface efficiency factor $\varepsilon \equiv G/(\rho_L \tilde{v}_r)$. A 100% efficiency factor therefore corresponds to droplets emitted from the entire jet free surface. Based on measurements of *G* and $\tilde{v}_r$, the surface efficiency factor is then[3]

$$\varepsilon = \frac{0.272x}{d_h\sqrt{We_d}} \qquad (1)$$

where d_h is the hydraulic diameter of the jet and We_d is the Weber number based upon d_h. Eq. (1) is valid for We_d = 235–270,000.

III. APPARATUS AND PROCEDURES

III. A. Flow Loop

As detailed elsewhere,[6,7] water at 24°C was pumped through the flow conditioning section and contracting nozzle to form the liquid sheet in the open test section in the recirculating flow loop. The flow conditioner (Fig. 1) consisted of a stainless steel (SS) perforated plate (50% open area ratio, 4.8 mm diameter staggered holes), PP, followed by a 2.5 cm section of polycarbonate (circular cells of diameter 0.32 cm), HC 3.9 cm farther downstream. In the "standard" flow conditioner configuration, a SS fine screen (37.1% open area and 0.33 mm wire diameter), FS, was placed 0.5 cm downstream of the HC. In the "no screen" configuration, the FS was removed to evaluate the effectiveness of BL cutting for different flow conditioner configurations.

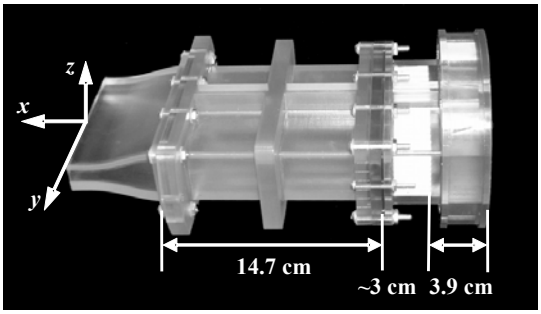

Fig. 1. Flow conditioner / nozzle assembly.

The nozzle downstream of the flow conditioner was a 5th order polynomial contraction with an area contraction ratio of 3 and exit *y*- and *z*- dimensions of δ = 1 cm and W_o = 10 cm, respectively. The nozzle exit had a slight contraction with a slope of 4°.[7]

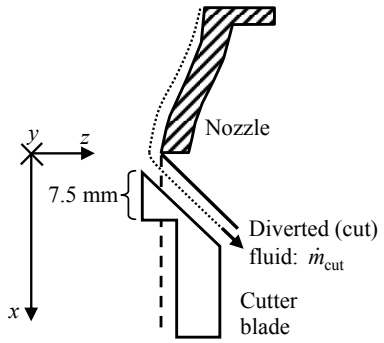

Fig. 2. Schematic of BL cutter (enclosure around cutter blade not shown).

Figure 2 shows the BL cutter and its placement with respect to the nozzle. The cutter used in this study, which was mounted independently from the nozzle, was used to remove fluid from only one face along the *y*-axis of the jet just downstream of the nozzle exit at *x* = 0.076 cm. The cutter assembly was supported on a linear stage that enabled fine adjustments along the *z*-direction. The cutter blade, machined from aluminum, had a reattachment length of 7.5 mm and a width (*y*-extent) of 12 cm that

extended 1 cm beyond the jet on both sides. A range of different levels of BL cutting ranging from $\dot{m}_{cut} / \dot{m}_{fl}$ = 0–1.9% ($\dot{m}_{cut}$ is the diverted mass flowrate)—were evaluated.

III. B. Measurement of Ejected Mass

The amount of drops ejected from the free surface was measured by collecting fluid in an array of square cuvettes.[6] A row of five square cuvettes (inner dimension 1 cm) centered with respect to the *y*-axis were placed just beyond the free surface at the furthest downstream location of x/δ = 25 (Fig. 3). The cuvette standoff distance Δz_s was measured from the nearest inner wall of the nozzle, or the nominal jet free surface. The row of cuvettes were tilted towards the free-surface at 6.5° with respect to the vertical; this tilt was based upon drop trajectories predicted by the correlations described in the previous section. The cuvettes were weighed on a digital scale to ±1 mg accuracy before and after each 30–60 minute collection period; the resultant mass difference is then an estimate of the mass of drops ejected from the free surface.

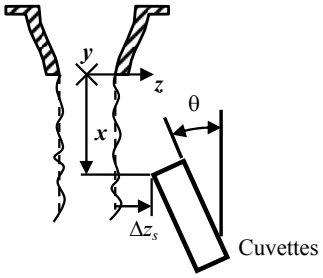

Fig. 3. Sketch of mass collection setup. The cuvettes are brought to a distance Δz_s from the nominal free surface (dashed line) at $\theta \approx 6.5°$.

The experimental mass flux G_{exp} is then the collected mass divided by the collection time and total cuvette cross-sectional area of 5 cm^2. The equivalent average number density *N* was then defined as

$$N = \frac{\rho_{eff} N_A}{M}, \quad \text{where } \rho_{eff} = \frac{G_{exp}}{\sqrt{\tilde{u}^2 + \tilde{v}^2}} \qquad (2)$$

Here, ρ_{eff} is the effective line density and N_A and M are Avogadro's number and molecular weight, respectively. This number density is provided to evaluate whether these flows are compatible with the requirements for a specific driver or target designs.

III. C. Free Surface Visualization

Planar laser-induced fluorescence (PLIF) was used to visualize the free surface of the liquid sheet.[7] The water in the flow loop contained 26 mg/L disodium fluorescein, a dye that fluoresces in the yellow-green when illuminated at 488 nm. This relatively high dye concentration was chosen so that most of the illuminating light was absorbed within a few millimeters of the free surface (*cf.* Fig. 5*a*). Refraction of spurious fluorescence that could interfere with imaging the flow free surface was thus minimized. The flow was illuminated at various *x*-locations by a ~0.2 cm thick 488 nm laser light sheet with a net power of about 0.2 W; the sheet was formed from a multiline argon-ion laser beam passed through a notch filter (Edmund Scientific NT30-907).

The free surface was imaged as the interface between fluorescing water and non-fluorescing air by an obliquely mounted B/W CCD camera (Kodak Model ES 1.0) from below at 30 Hz with a close-focusing macro video lens (Navitar Zoom 7000) (Fig. 4). A high-pass wavelength filter (Sunpak Yellow-8) with a cut-off frequency of 500 nm was mounted to the camera lens to ensure that the camera imaged only the longer-wavelength fluorescence.

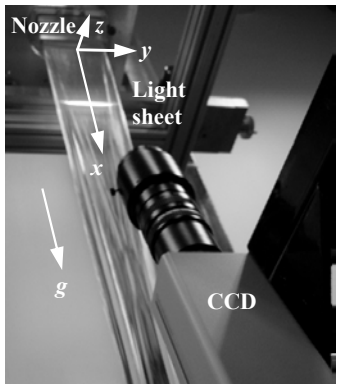

Fig. 4. PLIF experimental setup.

The field of view for each image is about 3.0 cm (*y*) × 3.0 cm (*z*). One side (*i.e.*, the entire *y*-extent) of the flow is then visualized by overlapping 4–5 segments, with each segment comprised of 134 consecutive images with an exposure of $\tau \equiv \delta / U_o$. The whole side then spans at least 5200τ. Individual images were stored as 8-bit 1008 × 1008 bitmaps on a PC HD using digital video recording software (Video Savant 3.0).

The free surface is found in each image using a threshold-based edge detection algorithm written in MATLAB (Fig. 5). The grayscale threshold value was chosen based upon a histogram of grayscale *vs.* number of pixels for the entire dataset. If M_p is the number of pixels

at the maximum of the background peak, the threshold grayscale is then the smallest grayscale above the background that contains at least 1% of M_p pixels. For every segment, the free-surface locations are determined for each of 134 thresholded images using a standard edge detection scheme and are used to calculate the average z-location of the free surface and its standard deviation. This standard deviation was spatially averaged over the central 75% of the flow ($|y/W_o| \le 0.375$) to obtain σ_z.

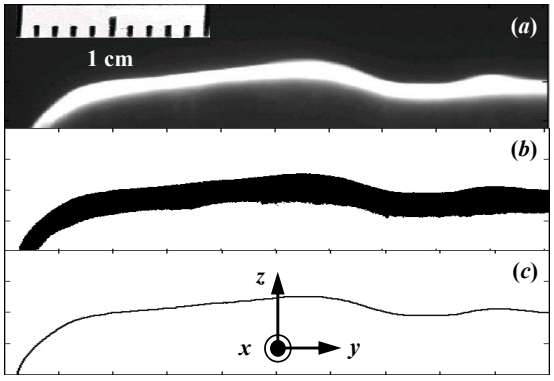

Fig. 5. Illustration of the process used to find the liquid sheet free surface: (*a*) Raw PLIF image; (*b*) Thresholded image; and (*c*) Free surface obtained by edge detection.

Each segment of the free surface has a slight overlap with neighboring segments. In all cases, the free surface fluctuations in this overlap region are taken to be those calculated for the left segment. The extent of the overlap region is known from a reference scale imaged in each frame. No significant discontinuities were observed using this procedure, since the central portion of the jet exhibits nearly constant surface fluctuations.

IV. RESULTS

IV. A. PLIF Experiments

Figure 6 shows σ_z / δ averaged over the central 75% of the flow ($|y/W_o| < 0.375$) as a function of x / δ for the standard (black) and no screen (grey symbols) flow conditioner configurations at $\dot{m}_{cut} / \dot{m}_{fl}$ = 0% (■), 1.0% (◆), and 1.9% (▲). As expected, BL cutting significantly reduces the standard deviation of the free surface. However, "cutting" more fluid has little discernible impact upon σ_z; the results at $\dot{m}_{cut} / \dot{m}_{fl}$ = 1.0% and 1.9% are virtually identical. Removing 1.9% of the overall mass flux from the surface reduced σ_z on average by about 33% and 10% for the standard and no screen configurations, respectively. In the absence of BL cutting, the standard deviation of the standard configuration was about 67% lower than that for the no screen configuration. BL cutting clearly reduces surface ripple, but the fine screen has a larger overall impact on free-surface smoothness.

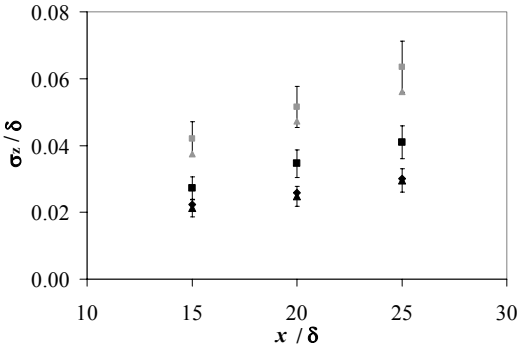

Fig. 6. σ_z / δ vs. x / δ for standard (black) and no screen (grey) flow conditioning configurations at $\dot{m}_{cut} / \dot{m}_{fl}$ = 0.0% (■), 1.0% (◆), and 1.9% (▲). The error bars in this and the following Figure represent 95% confidence intervals.

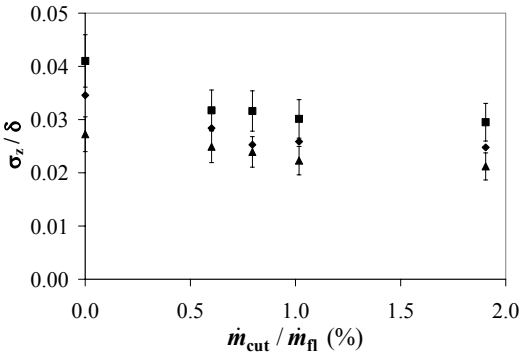

Fig. 7. σ_z / δ *vs.* $\dot{m}_{cut} / \dot{m}_{fl}$ for standard flow conditioning at x / δ = 15 (▲), 20 (◆), and 25 (■).

Figure 7 shows the effects of different levels of BL cutting on free-surface fluctuations for the standard flow configuration at x / δ = 15 (▲), 20 (◆), and 25 (■). Surface ripple decreases at all downstream locations as $\dot{m}_{cut} / \dot{m}_{fl}$ increases; σ_z is reduced significantly even at BL cutting levels as low as $\dot{m}_{cut} / \dot{m}_{fl}$ = 0.6%. Increasing $\dot{m}_{cut} / \dot{m}_{fl}$ provides diminishing improvements in surface smoothness.

BL cutting also alters the average free-surface geometry in turbulent liquid sheets, introducing protrusions near the edges of the flow (Fig. 8). Although

the entire "uncut" free surface at $x/\delta = 25$ lies well within the z-extent of the nozzle (Fig. 8*a*), the protrusions extend out to the nozzle while the rest of the flow moves even farther away from the nozzle walls (Figs. 8*b*–*c*). These end effects may be due to fluid being removed from only one side of the jet, but they clearly demonstrate the sensitivity of this flow to initial conditions. Though not shown here, the y-extent of the "cut" jet in both cases was less than that for the "uncut" flow at all downstream locations; at $x/\delta = 25$, this difference in the y-dimension was about 0.6 cm at $\dot{m}_{cut}/\dot{m}_{fl} = 1.9\%$.

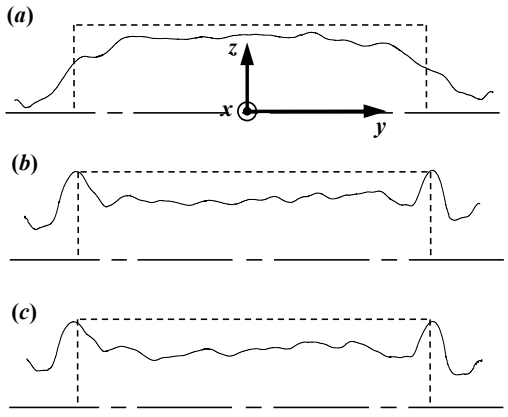

Fig. 8. Average free-surface position at $x/\delta = 25$ for a turbulent liquid sheet with standard flow conditioning at $\dot{m}_{cut}/\dot{m}_{fl} = 0.0\%$ (a); 1.0% (b); and 1.9% (c). The inner walls of the nozzle exit are indicated by the dashed outline; flow is out of the page. Note that the vertical (y) axis is shown at 5× magnification.

IV. B. Mass Collection Experiments

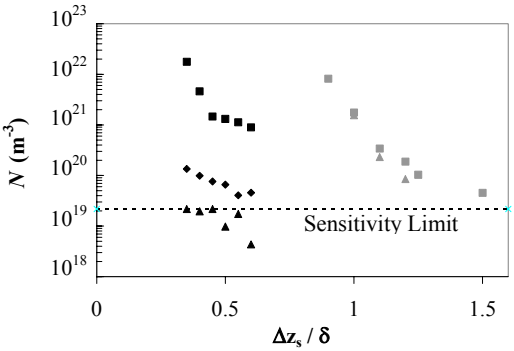

Fig. 9. Equivalent number density *vs.* $\Delta z_s/\delta$ for standard (black) and no screen (grey) configurations at $\dot{m}_{cut}/\dot{m}_{fl} = 0.0\%$ (■), 1.0% (◆), and 1.9% (▲).

Figure 9 shows equivalent number density as a function of cuvette standoff for standard (black) and no screen (grey symbols) flow conditioning configurations with BL cutting at $\dot{m}_{cut}/\dot{m}_{fl} = 0.0\%$ (■), 1.0% (◆), and 1.9% (▲) at $x/\delta = 25$. The density of drops due to turbulent breakup at the jet free surface increases as Δz_s decreases. Not surprisingly, there are more drops near the source of breakup, namely the jet surface. Note that any measurement below the sensitivity limit indicates a collected mass of zero within experimental error. Secondary effects such as aerodynamic shear, drop re-entrainment, and evaporation limit the spatial distances over which drops can be detected or collected. Approaching the jet, N should therefore increase from zero at a sufficiently large standoff value with a sharp increase as the free surface.

BL cutting reduces the hydrodynamic source term; a marked reduction in breakup is already observed for the standard configuration at a cut rate of 1.0% over all standoff distances. Moreover, breakup is completely suppressed at $\dot{m}_{cut}/\dot{m}_{fl} = 1.9\%$. For the no screen configuration, breakup is observed farther from the free surface. In addition, BL cutting appears to have less impact on the no screen cases, with smaller reductions in N compared with the standard configuration cases. The dominant impact of the fine screen seen here is consistent with the trends observed in the PLIF data; in all cases, the (absence of the) fine screen has a much more significant impact upon jet quality than BL cutting.

The breakup correlations were applied to a turbulent liquid sheet matching the experimental Weber number. Based upon these results, flow conditioning and a contracting nozzle already reduce the mass flux by 3–5 orders of magnitude. Since the experimental conditions in these studies are not identical to those used to establish the correlations, reductions in breakup with respect to the correlations should be considered qualitative. Nevertheless, this discrepancy again demonstrates the sensitivity of these types of flows to initial conditions.

V. CONCLUSIONS

Primary turbulent breakup of liquid sheets at $Re = 1.2\times10^5$ and $We = 1.9\times10^4$ can be suppressed with appropriate combinations of flow conditioning upstream of and boundary-layer cutting downstream of the nozzle. Breakup is completely eliminated (within experimental error) at $\dot{m}_{cut}/\dot{m}_{fl} = 1.9\%$, but the free-surface fluctuations are similar at a given downstream location for $\dot{m}_{cut}/\dot{m}_{fl} > 1.0\%$. The (presence or absence of a) fine screen in the flow conditioner is the dominant factor influencing free-surface smoothness, with the average standard deviation of the free-surface position without a

fine screen 1.5 times that with a fine screen. The inability of BL cutting to suppress this additional surface ripple may be due to a large central disturbance in the *z*-component of velocity fluctuations that extends into the center of the flow, beyond the range of the cutter blade.[9] BL cutting can be used on a "well-conditioned" liquid sheet to eliminate the hydrodynamic source term, but it does not appear to be capable of eliminating breakup without well-designed flow conditioning.

Primary turbulent breakup in prototypical flows at the much higher Weber number of 10^5 will be comparable based upon the correlations, since Eq. (1) and the definition of ε suggests that G is independent of flow rate. The average droplet size and surface breakup efficiency would decrease with increasing *We*, but the rate of droplet emission would increase. Thus the breakup at prototypical flow rates would consist of smaller droplets of greater number but of equal mass flux compared to the scaled experiment. However, scaling based on the correlations may be inappropriate given the previously stated discrepancies between these investigations and the correlations.

PLIF results suggest that BL cutting changes the cross-sectional geometry of the flow, introducing sharp protrusions near the edges of the sheet that extend to the nominal free surface. Cutting also decreases the width (*y*-extent) of the jet at all downstream locations, reducing the width by almost 0.6 cm at $x/\delta = 25$ for $\dot{m}_{\mathrm{cut}}/\dot{m}_{\mathrm{fl}} = 1.9\%$. Calculations of beam standoff distances will probably need to be adjusted for streamwise variations in the cross-sectional shape of a slab jet, which continuously evolves from the original rectangular cross-section.

Equivalent number densities from the breakup of a single turbulent liquid sheet indicate that the hydrodynamic source term may be a significant design issue for thick liquid protection. For the standard flow conditioner configuration, "cutting" 1.0% of the total flow rate from each side of the jet will already meet the proposed upper limit of $N = 6\times10^{21}$ m^{-3} [Ref. 8]. Removing more fluid does not appear to significantly improve surface smoothness, but can be used to further reduce the number density of drops in the reactor chamber as required by new driver or target designs.

ACKNOWLEDGMENTS

This work was sponsored by the Office of Fusion Energy Sciences, US DOE, under award DE-FG02-98ER54499. We thank D.L. Sadowski and T.P. Koehler for their help and support.

REFERENCES

[1] R.W. MOIR, "The High-Yield Lithium-Injection Fusion-Energy (HYLIFE)-II Inertial Fusion Energy (IFE) Power Plant Concept and Implications for IFE," *Phys. Plasmas* **2**, 2447 (1995).

[2] S.P. LIN and R.D. REITZ, "Drop and Spray Formation from a Liquid Jet," *Annu. Rev. Fluid Mech.*, **30**, 85-105 (1998).

[3] K.A. SALLAM, Z. DAI and G.M. FAETH, "Liquid Breakup at the Surface of Turbulent Round Liquid Jets in Still Gases," *Int. J. of Multiphas. Flow*, **28**, 427-449 (2002).

[4] P.K. WU, R.F. MIRANDA, and G.M. FAETH, "Effects of Initial Flow Conditions on Primary Breakup of Nonturbulent and Turbulent Round Liquid Jets," *Atomization Spray*, **5**, 175-196 (1995).

[5] T. KARASAWA, M. TANAKA, K. ABE, S. SIGA, and T. KURABAYASHI, "Effects of Nozzle Configuration on the Atomization of a Steady Spray," *Atomization Spray*, **2**, 411-426 (1992).

[6] S.G. DURBIN, M. YODA, S.I. ABDEL-KHALIK, D.L. SADOWSKI and T.P. KOEHLER, "Assessment and Control of Primary Turbulent Breakup of Thick Liquid Sheets in IFE Reactor Cavities—The 'Hydrodynamic Source Term'," *Fusion Sci. Technol.*, To Appear (2005).

[7] S.G. DURBIN, T.P. KOEHLER, J.J.R. REPERANT, M. YODA, S.I. ABDEL-KHALIK and D.L. SADOWSKI, "Surface Fluctuation Analysis for Turbulent Liquid Sheets," *Fusion Sci. Technol.*, **45**, 1 (2004).

[8] R. PETZOLDT, B. RICKMAN, D. GOODIN and L. BROWN, "Heavy Ion Fusion Target Materials Selection and Removal of Tungsten Carbide from Flibe," Presented at ARIES-IFE Quarterly Meeting, Atlanta, GA (2003).

[9] S.G. DURBIN, M. YODA, and S.I. ABDEL-KHALIK, "Flow Conditioning Design in Thick Liquid Protection," *Fusion Sci. Technol.*, To Appear (2005).

MS #007: Presented at 16th Technology of Fusion Energy Meeting (Madison, WI)
Accepted for publication *Fusion Science and Technology* (2005)

FLOW CONDITIONING DESIGN IN THICK LIQUID PROTECTION

S.G. Durbin†, M. Yoda, and S.I. Abdel-Khalik

G. Woodruff School of Mechanical Engineering
Georgia Institute of Technology
Atlanta, GA 30332-0405 USA
†(404) 385-1891 gte397r@mail.gatech.edu

The HYLIFE-II conceptual design proposed using arrays of high-speed oscillating and stationary slab jets, or turbulent liquid sheets, to protect the reactor chamber first walls from damaging neutrons, ions and X-rays. Flow conditioning can be used to reduce turbulent fluctuations in these liquid sheets and thereby reduce surface ripple, or free-surface fluctuations, and delay jet breakup. Several flow conditioning configurations are studied experimentally for vertical turbulent sheets of water issuing downwards from nozzles of thickness (small dimension) δ = 1 cm into ambient air for Reynolds numbers $Re = 5.0 \times 10^4$ and 1.2×10^5. In particular, the role of one or more fine screens in the flow conditioner was studied. As the flow conditioning element immediately upstream of the nozzle inlet, fine screens have been shown to have a major impact upon the sheet free-surface geometry. Planar laser-induced fluorescence was used to measure the free-surface geometry of the liquid sheet and its fluctuations in the near field at streamwise distances downstream of the nozzle exit $x \leq 25\delta$. Laser-Doppler velocimetry was used to quantify the impact of different conditioning configurations on the cross-stream velocity component and its fluctuations just upstream of the nozzle exit. The results indicate that minor differences in velocity and velocity fluctuations near the nozzle exit can lead to major variations in free-surface geometry, and that free-surface fluctuations are strongly affected by changes in flow conditioner design, even in the near-field region of the flow. A single-screen configuration was shown to produce the smoothest jets at both Reynolds numbers, with fluctuations of 3.3% at $Re = 1.2 \times 10^5$ and $x = 25\delta$.

I. INTRODUCTION

Thick liquid protection has been suggested as a solution for first wall protection and heat removal in inertial fusion energy (IFE) reactor chambers. The High-Yield Lithium-Injection Fusion Energy (HYLIFE-II) conceptual IFE power plant proposed using liquid sheets, or slab jets, of molten Flibe (Li_2BeF_4) for cooling and attenuation of damaging radiation and target debris.[1] The side walls of the chamber are shielded by a lattice of stationary jets that allows target injection and heavy-ion driver beam propagation, while protecting the reactor chamber first walls from the fusion event. Thick liquid protection can therefore help make fusion energy commercially attractive by reducing chamber size and extending chamber lifetime, thus considerably reducing the cost of electricity produced by fusion.[2]

Nozzle and flow conditioner designs that create smooth stationary jets are important for effective protection of the first walls and final focus magnets. Minimizing the surface ripple, or free-surface fluctuations, of liquid sheets will minimize driver beam clipping while maximizing protection. For effective thick liquid protection, the distance between the driver beam and the jet free surface should not exceed 0.5 cm, or about 0.07δ.[3]

Although previous work has addressed how nozzle geometry affects free-surface smoothness in such flows,[4,5] we are unaware of any work evaluating how different flow conditioner designs affect free-surface smoothness. In channel flows, placing a fine screen (FS) after a honeycomb (HC) section can greatly reduce turbulent fluctuations.[6] Subsequent work shows that adding both a coarse screen upstream of the HC and a second FS downstream of the HC-FS combination is even more effective in reducing such fluctuations.[7]

Experiments were performed for turbulent sheets of water issuing vertically downwards into ambient air at Reynolds numbers $Re = U_o \delta / \nu = 5\times10^4$ and 1.2×10^5, where U_o and δ are the average velocity and the short dimension of the sheet, respectively, at the nozzle exit and ν is the liquid kinematic viscosity. The flows proposed for HYLIFE-II have δ = 7 cm and $Re = 2.4\times10^5$. These results are therefore at about half the prototypical Re and a much smaller δ. The effects of three different flow conditioner configurations were evaluated in terms of velocity profiles just upstream of and free-surface smoothness up to 25δ downstream of the nozzle exit.

II. EXPERIMENTAL DESCRIPTION

II. A. Flow Loop

Water, pumped from the bottom receiving tanks, passed through the flow conditioning section and nozzle, forming the liquid sheet in the open test section in the recirculating facility.[8] A chiller was used to keep the water in the receiving tanks 5.5 m below the test section at 24°C. The coordinate system used here has an origin at the center of the nozzle exit, with x along the flow direction and y and z along the long and short dimensions of the nozzle, respectively.

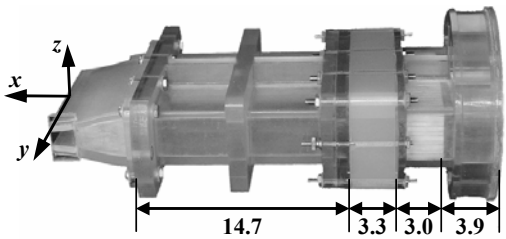

Fig. 1. Flow conditioner assembly (2-S configuration) with LDV nozzle. All dimensions in cm.

The flow conditioner (Fig. 1) in all cases consisted of a stainless steel (SS) perforated plate (50% open area ratio, 4.8 mm diameter staggered holes), PP, followed by a 2.5 cm section of polycarbonate (circular cells of diameter 0.32 cm), HC. The edge-to-edge x-distance between the PP and HC was 3.9 cm. The three different flow conditioner configurations used here were:

1) No screen (0-S): the flow conditioner described above with an edge-to-edge x-distance between the HC and the upstream end of the nozzle of 15.2 cm.
2) One screen (1-S): a SS FS (30 × 30 mesh size, 37.1% open area ratio, 0.33 mm wire diameter, 0.51 mm open cell width), FS-1, was placed 0.5 cm downstream of the downstream end of the HC. This configuration is the same as used in previous studies.[4,5,8]
3) Two screens (2-S): a second SS FS (40 × 40 mesh size, 36.0% open area ratio, 0.25 mm wire diameter, 0.38 mm open cell width), FS-2, was added to the 1-S configuration 3.3 cm downstream of FS-1 using an additional flange.

In the 0-S and 1-S configurations, the overall x-dimension of the flow conditioner was 21.6 cm; it was 24.9 cm for the 2-S configuration. The nozzle downstream of the flow conditioner followed a 5th order polynomial contraction along z with a contraction ratio of 3 and exit y- and z- dimensions of δ = 1 cm and W_o = 10 cm, respectively. The nozzle exit had a slight taper with a slope of 4°.[8] One of the two flat sides of the nozzle (fabricated from Vantico 7510 using stereolithography rapid prototyping) was milled away for -3.6 cm $\le x \le 0$ and replaced with a 0.56 cm thick flat plate of polycarbonate (Lexan) to provide optical access for LDV measurements.

II. B. Laser-Doppler Velocimetry (LDV)

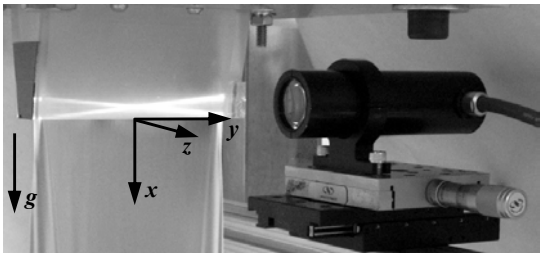

Fig. 2. Photo of LDV probe head and nozzle with optical window (shown obtaining u data).

Velocity and turbulence intensity profiles were measured directly at the nozzle exit using a single-component LDV system (VioSense MiniLDV-80) in backscatter mode with a working distance of 80 mm and a probe volume with FWHM dimensions of 100 × 1200 × 40 μm ($x \times y \times z$) (Fig. 2). Velocity profiles along z were measured at $x = -6$ mm through the polycarbonate window on the flat side of the nozzle. The water in the flow loop was seeded with TiO_2 particles (typical diameter ≈ 0.3 μm) at a volume fraction of about 3.4 ppm.

The Doppler bursts were converted to voltage signals by an avalanche photo-diode (APD), bandpass filtered by a Krohn-Hite 3940, digitized by a National Instruments 5112 onto a PC HD, and converted to velocity using a FFT. The resultant velocity samples were then used to calculate mean and rms fluctuations of the x and z velocity components. Profiles of the mean and rms fluctuations of the x-velocity component u and u', respectively, were obtained at $2.438 \le y/\delta \le 4.838$ with no frequency shift. The probe head was then rotated 90° about y and used to obtain the mean and rms fluctuations of the z-velocity component, or w and w', respectively, with a frequency shift of 1.3 MHz at $1.188 \le y/\delta \le 4.838$. The frequency shift was required to shift the velocity data ($|w| < 1$ m/s) above the pedestal frequency and to resolve directional ambiguities.[9]

Stray reflections of the laser beams at the polycarbonate-water interface made it impossible to obtain data for $y/\delta > 4.838$. Near the center of the flow at $y/\delta = 1.188$, the beam half-angle of the LDV probe of $\kappa = 7.4°$ also precluded obtaining w measurements near the side walls, restricting $|z/\delta| \le 0.17$. The average sampling rate was 20 Hz; 10^3 velocity samples were used to calculate mean and rms fluctuation values. In all cases,

each velocity dataset was acquired over at least $2\times10^4\,\tau$, where the convective time scale $\tau = \delta / U_o$.

III. RESULTS AND DISCUSSION

III. A. LDV Profiles

Profiles were acquired for the three different flow conditioning configurations at Reynolds numbers $Re = 5\times10^4$ and 1.2×10^5. The local nozzle thickness and contraction angle are b = 10.95 mm and 5.5°, respectively. The mean streamwise velocity profiles indicate the flow is uniform for all Reynolds and flow conditioning configurations. The mean transverse velocity profiles vary linearly with z with $|w/U_o| \le \tan(5.5°)(\delta/b)$. The mean velocity profiles for the 1-S configuration are shown in Figure 3. Although not shown here, similar u and w profiles were obtained for the 0-S and 2-S configurations.

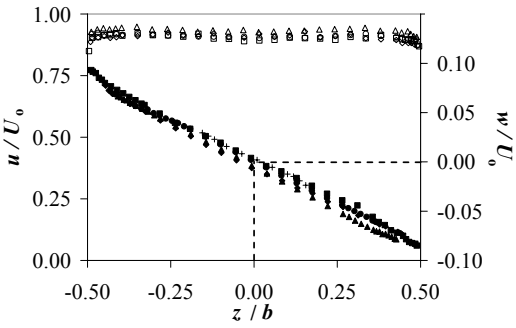

Fig. 3. Normalized profiles of u (open) and w (closed symbols) for 1-S configuration at $Re = 1.2\times10^5$ and y / δ = 4.838 (■), 4.438 (◆), 4.163 (▲), 3.688 (●), and 1.188 (+). Note: Profile at $y / \delta = 1.188$ for w only.

Figure 4 shows normalized profiles of u' and w' for the 1-S configuration at all y-locations. The fluctuations are relatively constant over the central 75% of the flow, or $|z/b| \le 0.375$, with a sharp increase in fluctuations near the nozzle walls due to the turbulent boundary layer. Overall, the streamwise fluctuations are about twice the transverse fluctuations. The 95% confidence level for the u' and w' data is about 0.1%.

Figure 5 compares the velocity fluctuations of the 0-S (◆), 1-S (▲), and 2-S (■) flow conditioning configurations at $Re = 1.2\times10^5$ and $y / \delta = 4.438$. The 2-S configuration exhibits considerably lower u', as compared to 0-S and 1-S. However, measurements of w' do not indicate that the 2-S configuration has lower transverse velocity fluctuations as compared with 1-S.

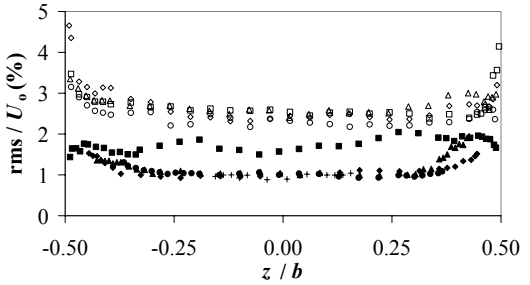

Fig. 4. Normalized profiles of u' (open) and w' (closed symbols) for the 1-S configuration at $Re = 1.2\times10^5$ and y / δ = 4.838 (■), 4.438 (◆), 4.163 (▲), 3.688 (●), and 1.188 (+). Note: Profile at $y / \delta = 1.188$ for w' only.

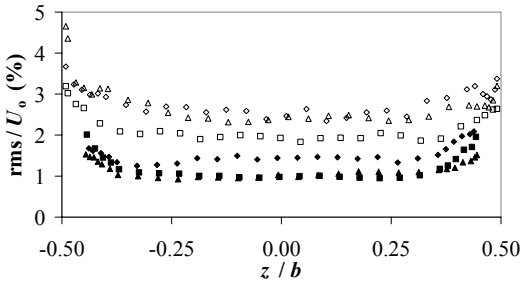

Fig. 5. Normalized profiles of u' (open) and w' (closed symbols) for the 0-S (◆), 1-S (▲), and 2-S (■) flow conditioning configurations at $Re = 1.2\times10^5$ and y / δ = 4.438.

TABLE I. Average Streamwise and Transverse Velocity Fluctuations for $Re = 1.2\times10^5$

	u' / U_o (%)			w' / U_o (%)		
y / δ	0-S	1-S	2-S	0-S	1-S	2-S
4.838	2.6	2.6	2.0	1.7	1.7	1.9
4.438	2.6	2.5	2.0	1.4	1.0	1.0
3.688	2.6	2.3	1.8	1.3	1.1	1.0
1.188	–	–	–	1.9	1.0	1.0
average	2.6	2.5	1.9	1.5	1.2	1.2

Table I summarizes the average velocity fluctuations for characteristic y-locations and all flow conditioning configurations at $Re = 1.2\times10^5$. These results are averaged over $|z/b| \le 0.375$, or the central 75% of the flow. The addition of the second screen reduced the streamwise fluctuations at all locations. The streamwise fluctuations are identical within experimental error for the 0-S and 1-S configurations. Results at $Re = 5\times10^4$ averaged over $|z/b| \le 0.375$ and all y-locations give u' / U_o = 3.1, 2.6, and 2.4% for the 0-S, 1-S, and 2-S configurations, respectively. Although these normalized values are

higher than those for $Re = 1.2\times10^5$, the absolute values of u' are lower.

The measured transverse fluctuations for the 1-S and 2-S configurations are identical within the 95% confidence interval at all locations, although the 0-S case shows marked increases in w' for $y / \delta < 2.438$. Measurements (not included in the table) give normalized values for the 0-S case ranging from 1.6–2.3% for y/δ = 1.638–0.338, respectively. Finally, results at $Re = 5\times10^4$ give spatially averaged values of w' / U_o of 1.8, 1.4, and 1.5% for the 0-S, 1-S, and 2-S configurations, respectively; the absolute values of the transverse fluctuations are again lower than those at $Re = 1.2\times10^5$.

III. B. Free Surface Fluctuations

Planar laser-induced fluorescence (PLIF) was used to obtain the free-surface geometry and calculate the standard deviation of the z-position of the free surface, or σ_z.[8] Technique details are given in Durbin *et. al.*[10] Figure 6 is a graph of σ_z/δ averaged over the central 75% of the flow ($|y/W_o| \le 0.375$) as a function of x/δ for the 1-S (▲) and 2-S (■) configurations at $Re = 5\times10^4$. The 2-S configuration displays higher free surface fluctuations at all downstream locations, even though 1-S and 2-S have nearly identical u' and w'.

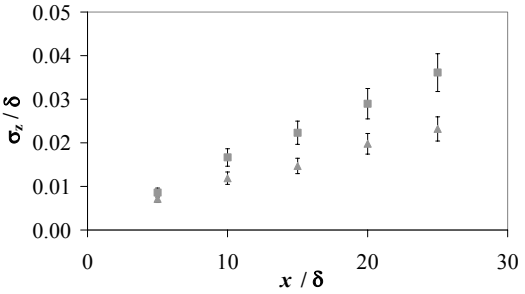

Fig. 6. Graph of σ_z / δ *vs.* x / δ for 1-S (▲) and 2-S (■) flow conditioning configurations at $Re = 5\times10^4$. The error bars denote 95% confidence intervals.

Figure 7 gives the normalized free surface fluctuation as a function of y / δ for 0-S (grey) and 1-S (black symbols). A significant central disturbance is evident in the 0-S case, which was also observed in the transverse velocity fluctuations. The 1-S (and, though not shown here, 2-S) configuration exhibits regions of relatively constant free surface fluctuation near the center of the jet.

Figure 8 compares σ_z/δ as a function of x/δ for the three flow conditioner configurations at $Re = 1.2\times10^5$. The 1-S and 2-S configurations produced jets with similar levels of σ_z. The 0-S configuration yielded significantly rougher jets due in large part to the central disturbance (*cf.* Fig. 7).

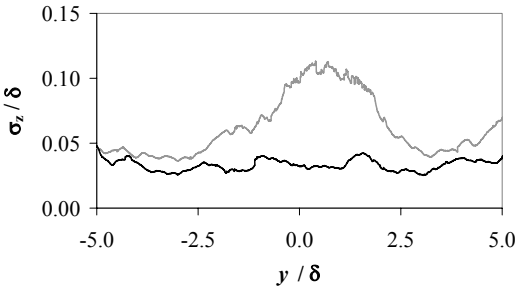

Fig. 7. Plot of σ_z / δ *vs.* y / δ for the 0-S (grey) and 1-S (black) flow conditioning configurations at $x / \delta = 25$ and $Re = 1.2\times10^5$.

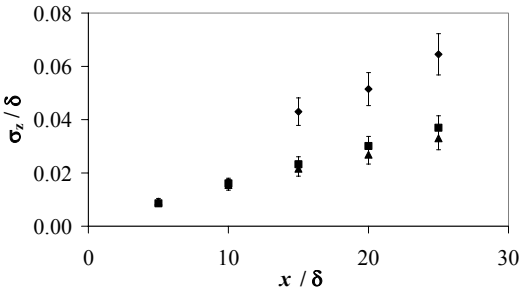

Fig. 8. Plot of σ_z / δ *vs.* x / δ for the 0-S (◆), 1-S (▲) and 2-S (■) flow conditioning configurations at $Re = 1.2\times10^5$. The error bars denote 95% confidence intervals.

III. C. Loss Coefficients

Table II. Loss Coefficient across the Flow Conditioner for $Re = 1.2\times10^5$

Configuration	ΔP (kPa)	U_{in} (m/s)	U_o (m/s)	K_L
0-S	69	2.35	10.72	1.25
1-S	103	2.36	10.75	1.84
2-S	121	2.38	10.84	2.11

The pumping power required to drive the flow scales with the losses across the entire system; here, the flow conditioner / nozzle assembly is a significant source of loss. The impact of adding screens to the flow conditioner was therefore experimentally quantified in terms of the loss coefficient across the flow conditioner / nozzle assembly $K_L = [2(\Delta P) + \rho U_{in}^2]/(\rho U_o^2)$, where ΔP is the pressure loss across the flow conditioner / nozzle, ρ is the fluid density, and U_{in} is the mean velocity at the inlet of the assembly. As expected, adding screens increases ΔP. Table II shows the pressure loss data and

the corresponding loss coefficients at $Re = 1.2\times10^5$ for the three flow conditioning configurations studied here.

IV. CONCLUSIONS

The objective of this study was to quantify the effects of different flow conditioner designs upstream of the nozzle on both velocity fluctuations near the nozzle exit and surface smoothness downstream of the exit. Three conditioner configurations, with zero, one or two screens (denoted by 0-S, 1-S and 2-S, respectively), were evaluated.

At $Re = 1.2\times10^5$, the 0-S configuration had significantly higher transverse velocity rms fluctuations w', and higher σ_z (due to a large central disturbance of the flow) than either the 1-S or 2-S configurations. The 0-S and 1-S configurations had similar levels of streamwise velocity fluctuations u', however. The 2-S configuration had lower u' than either the 0-S or 1-S configurations, as expected from previous studies of flow conditioner designs. But this decrease in streamwise velocity fluctuations was not reflected in surface ripple; the 2-S and 1-S configurations had essentially identical σ_z. Higher levels of streamwise turbulence may actually help stabilize the sheet by increasing the turbulent viscosity. At $Re = 5\times10^4$, similar trends were observed except that the 2-S configuration has higher σ_z than the 1-S configuration despite having similar u' and w'.

In terms of implications for thick liquid protection schemes, both the 1-S and 2-S configurations meet the surface ripple criteria for HYLIFE-II at *Re* up to about half the prototypical value, with $\sigma_z < 0.04\delta$ over the range of downstream distances studied. The 0-S configuration did not meet this criterion with $\sigma_z > 0.06\delta$. Given that the loss coefficient across the flow conditioner for the 2-S configuration is 69% and nearly 15% greater than that for the 0-S and 1-S configurations, respectively, a flow conditioner design with a single screen appears to be the best compromise between surface smoothness and pumping power.

In terms of the fluid dynamics of turbulent liquid sheets, this work has demonstrated that even quite small changes in velocity fluctuations can significantly impact free-surface smoothness, and that such effects can be quantified and correlated using, for example, LDV. The results at the higher *Re* are in agreement with previous studies that suggest that free-surface wave amplitudes are primarily determined by transverse (*vs.* streamwise) velocity fluctuations, and that higher levels of streamwise velocity fluctuations can actually have a stabilizing effect on free-surface smoothness.[11]

ACKNOWLEDGMENTS

This work was sponsored by the Office of Fusion Energy Sciences, US DOE, under award DE-FG02-98ER54499. We thank D.L. Sadowski and T.P. Koehler for their help and support.

REFERENCES

[1] R.W. MOIR, "The High-Yield Lithium-Injection Fusion-Energy (HYLIFE)-II Inertial Fusion Energy (IFE) Power Plant Concept and Implications for IFE," *Phys. Plasmas*, **2**, 2447 (1995).

[2] R.W. MOIR, ET AL, "HYLIFE-II: A Molten-Salt Inertial Fusion Energy Power Plant Design—Final Report," *Fusion Technol*., **25**, 5 (1994).

[3] J.F. LATKOWSKI and W.R. MEIER, "Heavy-Ion Fusion Final Focus Magnet Shielding Design", *Fusion Technol.*, **39**, 798 (2001).

[4] J.J.R. REPERANT, S.G. DURBIN, M. YODA, S.I. ABDEL-KHALIK and D.L. SADOWSKI, "Studies of turbulent liquid sheets for protecting IFE reactor chamber first walls," *Fusion Eng. Des.*, **63–64**, 627 (2002).

[5] S.G. DURBIN, M. YODA, S.I. ABDEL-KHALIK and D.L. SADOWSKI, "Turbulent Liquid Sheets for Protecting IFE Reactor Chamber First Walls," *Fusion Sci. Technol.*, **44**, 307 (2003).

[6] R.I. LOEHRKE and H.M. NAGIB, "Control of Free Stream Turbulence by Means of Honeycombs: A Balance Between Suppression and Generation," *J. Fluids Eng.*, **98**, 342 (1976).

[7] C. FARELL and S. YOUSSEF, "Experiments on Turbulence Management Using Screens and Honeycombs," *J. Fluids Eng.*, **118**, 26 (1996).

[8] S.G. DURBIN, T.P. KOEHLER, J. REPERANT, M. YODA, S.I. ABDEL-KHALIK and D.L. SADOWSKI, "Surface Fluctuation Analysis for Turbulent Liquid Sheets," *Fusion Sci. Technol.*, **45**, 1 (2004).

[9] F. DURST, A. MELLING and J. WHITELAW, *Principles and Practice of Laser-Doppler Anemometry* (2nd ed.), Academic Press, London (1981).

[10] S.G. DURBIN, M. YODA, and S.I. ABDEL-KHALIK, "Impact of Boundary-Layer Cutting and Flow Conditioning on Free-Surface Behavior in Turbulent Liquid Sheets," *Fusion Sci. Technol*., To Appear (2005).

[11] K. HEUKELBACH, "Untersuchung zum Einfluss der Düseninnenströmung auf die Stabilität von flächigen Flüssigkeitsstrahlen" [English translation: An Investigation of the Influence of the Flow Inside the Nozzle upon the Stability of Liquid Sheets], Ph.D. Thesis, Technische Universität Darmstadt.

REFERENCES

Abbott, R., Pemberton, S., Peterson, P.F., Sun, G.P, Wright, P., Holmes, R., Latkowski, J., Moir, R., and Springer, K., 2001, "Cylindrical liquid jet grids for beam-port protection of thick-liquid heavy-ion fusion," *Fusion Technol.*, **39**, 732-738.

Abdou, M.A., Ying, A., Morley, N., Gulec, K., Smolentsev, S., Kotschenreuther, M., Malang, S., Zinkle, S., Rognlien, T., Fogarty, P., Nelson, R., Nygren, R., McCarthy, K., Youssef, M.Z., Ghoniem, N., Sze, D., Wong, C., Sawan, M., Khater, H., Woolley, R., Mattas, R., Moir, R., Sharafat, S., Brooks, J., Hassanein, A., Petti, D., Tillack, M., Ulrickson, and M., Uchimoto, T., 2001, "On the exploration of innovative concepts for fusion chamber technology," *Fusion Eng. and Des.*, **54**, 181-247.

Aidun, C.K., 1997, "Hydrodynamics of streaks on the forming table," *TAPPI J.*, **80**, 155-162.

Anno, J.N., 1977, The mechanics of liquid jets, Lexington, Mass: Lexington Books.

Asare, H.R., Takahashi, R.K., and Hoffman, M.A., 1981, "Liquid sheet jet experiments: comparison with linear theory," *J. Fluids Eng.*, **103**, 591-604.

Aslanov, S., 1999, "Theory of drops formation along disintegration of a thin liquid jet," *J. Aerosol Sci*., **30**, 333-334.

Baird, M.H.I. and Davidson, J.F., 1962, "Annular jets-I (Fluid Dynamics)," *Chem. Eng. Sci*., **17**, 467-472.

Benedict, L.H. and Gould, R.D., 1996, "Towards better uncertainty estimates for turbulence statistics," *Exp. Fluids*, **22**, 129-136.

Bidone, G., 1829, "Experiences sur la forme et sur la direction des veines et des courants d'eau lances par diverse ouvertures," Imprimerie Royale, Turin, 1-136.

Blink, J.A., Hogan, W.J., Hovingh, J., Meier, W.R., and Pitts, J.H., 1985, "The high-yield lithium-injection fusion-energy (HYLIFE) reactor," UCRL-53559, Lawrence Livermore National Laboratory.

Bogy, D.B., 1979, "Drop formation in a circular liquid jet," *Annu. Rev. Fluid Mech*., **11**, 206-227.

Boussinesq, J., 1877, *Mem. Acad. Sci*., Paris, **23**, 639.

Bourque, R.F., Meier, W.R., and Monsler, M.J., 1992 "Overview of the OSIRIS IFE reactor conceptual design," *Fusion Technol*., **21**, 1465-1469.

Burke, R.J. and Cutting, J.C., 1974, "Direct conversion of neutron energy and other advantages of a large yield per pulse, inertial-confinement fusion reactor," *J. of the Electromechanical Soc.*, 1st Topical Meeting on the Technology of Controlled Nucl. Fusion, 53-62.

Cavanaugh, C.J. and Peterson, P.F., 1994, "Scale modeling of oscillating sheet jets for the HYLIFE-II inertial confinement fusion reactor," *Fusion Technol.*, **26**, 917-21.

Chandrasekhar, S., 1961, Hydrodynamic and hydromagnetic stability, Oxford: Clarendon Press.

Chen, T.F. and Davis, J.R., 1964, "Disintegration of a turbulent water jet," *A.S.C.E. Proc*., **90**, 175.

Chigier, N.A., 1991, "The physics of atomization," 5th International Conference on Liquid Atomization and Spray Systems (ICLASS – 91), Gaithersburg, MD.

Chub, D.L. and Calfo F.D., 1993, "A study of thin liquid sheet flows," NASA Technical Memorandum 106323.

Collins, J.C., 2000, "Velocity and free-surface measurements of free plane jets," Master's thesis, Georgia Institute of Technology.

Dahm, W.J.A., 1985, "Experiments on entrainment, mixing and chemical reactions in turbulent jets at large Schmidt number," Ph.D. thesis, California Institute of Technology.

Dai, A., Chou, W.H., and Faeth, G.M., 1998, "Drop formation due to turbulent primary breakup at the free surface of plane liquid wall jets," *Phys. Fluids*, **10**, 1147-1157.

Delene, J.G., 1994, "Advanced fission and fossil plant economics – implications for fusion," *Fusion Technol.*, **26**, 1105-1110.

Drain, L.E., 1980, The laser-Doppler technique, New York: Wiley.

Durbin, S.G., Yoda, M., Abdel-Khalik, S.I., and Sadowski, D.L., 2003, "Turbulent liquid sheets for protecting IFE reactor chamber first walls," *Fusion Sci. and Technol.*, **44**, 307-311.

Durbin, S.G., Koehler, T.P., Reperant, J.R.R., Yoda, M., Abdel-Khalik, S.I., Sadowski, D.L., 2004, "Surface fluctuation analysis for turbulent liquid sheets," *Fusion Sci. and Technol.*, **45**, 1-10.

Durbin S.G., Yoda, M., Abdel-Khalik, S.I., Sadowski, D.L., and Koehler, T.P., 2005, "Assessment and control of primary turbulent breakup of thick liquid sheets in IFE reactor cavities – the 'hydrodynamic source term'," *Fusion Sci. and Technol.*, **47**, 1-11.

Durst, F., Melling, A., Whitelaw, J.H., 1981, Principles and practice of laser-Doppler anemometry, New York: Academic Press.

Elwell, L.C., 2000, "Dynamics of stationary and obliquely oscillating free plane jets," Master's thesis, Georgia Institute of Technology.

Erikson, J.I., 1952, *J. Rat. Mech*., **1**, 521.

Esser, P.D. and Abdel-Khalik, S.I., 1980, "Dynamics of vertical annular liquid jets," *J. Fluids Eng*, **106**, 45-51.

Faeth, G.M., Hsiang, L.-P., and Wu, P.-K., 1995, "Structure and breakup of sprays," *Int. J. Multiphase Flow*, **21**, 99-127.

Farell, C. and Youssef, S., 1996, "Experiments on turbulence management using screens and honeycombs," *J. Fluids Eng.*, **118**, 26-32.

Glenn, L.A., 1981, "Transport processes in an inertial confinement fusion reactor," *Nucl. Eng. Des*., **64**, 375.

Goldstein, R.J., ed., 1996, Fluid mechanics measurements, 2nd ed., Washington, DC: Taylor and Francis.

Grant, R.P. and Middleman, S., 1966, "Newtonian jet stability," *AIChE J*., **12**, 669.

Grinstein, F.F., 2001, "Vortex dynamics and entrainment in rectangular free jets," *J. Fluid Mech*., **437**, 69-101.

Gutmark, E. J. and Grinstein, F. F., 1999, "Flow control with noncircular jets," *Annu. Rev. Fluid Mech.*, **31**, 239-272.

Hagerty, W.W. and Shea, J.F., 1955, "A study of the stability of plane fluid sheets," *J. Applied Mech.*, **22**, 509-514.

Hasan, M. Z., Mitsutake, Y., and Monde, M., 1998, "A multilayered annular liquid metal jet blanket concept for ICF reactors," *Proc. Symp. Fusion Eng*., **2**, 617-620.

Hayter, A.J., 1995, Probability and statistics for engineers and scientists, Boston, Mass: PWS Publishing.

Hassberger, J.A., 1983, "Stability of the FMET high speed free surface liquid jet flowing along a curved back wall," *Proc. 10th Symp. Fusion Engineering*, **2**, 1849-1853.

Hertzberg, J.R., and Ho, C.M., 1995, "Three-dimensional vortex dynamics in a rectangular sudden expansion," *J. Fluid Mech.*, **289**, 1-27.

Heukelbach, K., 2003, "Untersuchung zum einfluss der düseninnenströmung auf die stabilität von flächigen flüssigkeitsstrahlen," [English translation: "An investigation of the influence of the flow inside the nozzle upon the stability of liquid sheets], Ph.D. Thesis, Technische Universität Darmstadt.

Hoffman, M.A., Takahashi, R. K., and Monson, R.D., 1980, "Annular liquid jet experiments," *J. Fluids Eng*, **102**, 344-349.

Hovingh, J., 1977, "Stability of a flowing circular annular liquid curtain with a vertical axis subjected to surface tension forces," Internal Memorandum No. 598A-77-108, Lawrence Livermore National Laboratory.

House, P.A., 1999, "Beamline and first vessel wall shielding in HYLIFE-II," UCID-136107, Lawrence Livermore National Laboratory.

Howard, J.E., 1979, "On the stability of the flow of thin liquid-lithium flows," *Nucl. Sci. Eng*., **69**, 94-99.

Hoyt, J.W. and Taylor, J.J., 1977a, "Turbulence structure in a water jet discharging in air," *Phys. Fluids*, **20**, S253-257.

Hoyt, J.W. and Taylor, J.J., 1977b, "Waves on water jets," *J. Fluid Mech*., **83**, 119-127.

Itoh, K., Tsuji, Y., Nakamura, H., and Kukita, Y., 1999, "Initial free surface instabilities on high speed water jet simulating a liquid-metal target," *Fusion Technol*., **36**, 69-84.

Karasawa, T., Tanaka, M., Abe, K., Shiga, S., and Kurabayashi, T., 1992, "Effects of nozzle configuration on the atomization of a steady spray," *Atomization Sprays*, **2**, 411-426.

Kihm, K.D. and Chigier, N.A., 1990, "Experimental investigations of annular liquid curtains," *J. Fluids Eng.*, **112**, 61-66.

Koehler, T.P., 2004, "Quantification of initial conditions in turbulent liquid sheets using laser-Doppler velocimetry," Master's thesis, Georgia Institute of Technology.

Konkachbaev, A.I., Morley, N.B., Gulec, K., and Sketchley, T., 2000, "Stability and contraction of a rectangular liquid metal jet in a vacuum environment," *Fusion Eng. Des.*, **51-52**, 1109-1114.

Kotsovinos, N.E., 1976, "A note on the spreading rate and virtual origin of a plane turbulent jet," *J. Fluid Mech*., **77**, 305-311.

Krothapalli, A., Baganoff, D., and Karamcheti, K., 1981, "On the mixing of a rectangular jet," *J. Fluid Mech*., **107**, 201-220.

Lasheras, J.C. and Hopfinger, E.J., 2000, "Liquid jet instability and atomization in a coaxial gas stream," *Annu. Rev Fluid Mech.*, **32**, 275-308.

Latkowski, J.F. and Meier, W.R., 2001, "Heavy-ion fusion final focus magnet shielding designs", *Fusion Technol*., **39**, 798-803.

Lin, S.P., Lian, Z.W., and Creighton, B.J., 1990, "Absolute and convective instability of a liquid sheet," *J. Fluid Mech.*, **220**, 673-689.

Lin, S.P. and Reitz, R.D., 1998, "Drop and spray formation from a liquid jet," *Annu. Rev. Fluid Mech.*, **30**, 85-105.

Loehrke, R.I. and Nagib, H.M., 1976, "Control of free-stream turbulence by means of honeycombs: a balance between suppression and generation," *J. Fluids Eng.*, **98**, 342-353.

Maniscalco, J.A. and Meier, W.R., 1977, "Liquid lithium 'waterfall' inertial confinement fusion reactor concept," *Transactions of the American Nuclear Society*, **26**, 62-63.

Mansour, A. and Chigier, N., 1991, "Dynamic behavior of liquid sheets," *Phys. Fluids A*, **3**, 2971-2980.

Mazallon, J., Dai, Z., and Faeth, G.M., 1999, "Primary breakup of nonturbulent round liquid jets in gas crossflows," *Atomization Sprays*, **9**, 291-311.

McCarthy, M.J. and Molloy, N.A., 1974, "Review of stability of liquid jets and the influence of nozzle design," *Chem. Eng. J.*, **7**, 1.

Merzkirch, W., 1987, "Flow visualization," New York: Academic Press.

Miesse, C.C., 1955, "Correlation of experimental data on the disintegration of liquid jets," *Ind. Eng. Chem*., **47**, 1690.

Moir, R.W., Adamson, M.G., Bangerter, R.O., Bieri, R.L., Condit, R.H., Hartman, C.W., House, P.A., Langdon, A.B., Logan, B.G., Orth, C.D., Petzoldt, R.W., Pitts, J.H., Post, J.H., Sacks, R.F., Tobin, M.T., Williams, W.H., Dolan, T.J., Longhurst, G.R., Hoffman, M.A., Schrock, V.E., Peterson, P.F., Bai, R.Y., Chen, X.M., Liu, J., Sze, D.K., and Meier, W.R., 1991, "HYLIFE-II progress report," UCID-21816, Lawrence Livermore National Laboratory.

Moir, R.W., 1992, "HYLIFE-II inertial fusion energy power plant design," *Fusion Technol*., **21**, 1475-1486.

Moir, R.W., Bieri, R.L., Chen, X.M., Dolan, T.J., Hoffman, M.A., House P.A., Leber R.L., Lee, J.D., Lee, Y.T., Liu, J.C., Longhurst, G.R.,Meier, W.R., Peterson, R.F., Petzoldt, R.W., Schrock, V. E., Tobin, M.T., and Williams, W.H., 1994, "HYLIFE-II: a molten-salt inertial fusion energy power plant design- final report," *Fusion Technol.*, **25**, 5-25.

Moir, R.W., 1995, "The High-Yield Lithium-Injection Fusion-Energy (HYLIFE)-II inertial fusion energy (IFE) power plant concept and implications for IFE." *Phys. Plasmas*, **2**, 2447-2452.

Moir, R.W., 1997, "Liquid first walls for magnetic fusion energy configurations," *Nucl. Fusion*, **37**, 557.

Moir, R.W., 2001, "Chamber, target and final focus integrated design," *Nucl. Instrum. Meth. A*, **464**, 140-151.

Monsler, M., Maniscalco, J., Blink, J., Meier, W., and Walker, P., 1978, "Electric power from laser fusion: the HYLIFE concept*," Proc. 13th Intersociety Energy Conversion Engineering Conf.*, San Diego, California, August 20-25; see also UCRL-1259, Lawrence Livermore National Laboratory.

Morley, N.B., Ying, A.Y., Gaizer, A., Sketchley, T., Knonachbaev, A.I., and Abdou, M. A., 1998, "Experimental investigation of free liquid metal jets in vacuum: preliminary results for IFE chamber wall protection applications," *Fusion Technol.*, **34**, 1035-1040.

Nakamura, H., Itoh, H., Kukita, Y., Ida, M., Kato, Y., and Meakawa, H., 1997, "Water experiment of high-speed, free surface, plane jet along concave wall," *Proc. 8th Int. Topl. Mtg. Nuclear Reactor Thermal-Hydraulics*, **3**, 1268-1279.

Paul, D.D., 1978, "Dynamics of Newtonian annular jets," MS Thesis, University of Wisconsin-Madison, Nuclear Engineering Department.

Parsheh, M., Brown, M.L., and Aidun, C.K., 2005, "On the orientation of stiff fibres suspended in turbulent flow in a planar contraction," Accepted for publication *Journal of Fluid Mechanics*.

Ramos, J.I., 1998, "Annular liquid jets and other axisymmetric free-surface flows at high Reynolds numbers," *Appl. Math. Modelling*, **22**, 423-452.

Rangel, R.H. and Sirignano, W.A., 1991 "The linear and nonlinear shear instability of a fluid sheet," *Phys. Fluids A*, **3**, 2392-2400.

Lord Rayleigh (J.W. Strutt), 1894, "Theory of Sound," The Macmillan Company, Ltd., London, England, second edition; two volumes reprinted by Dover Publications, New York, N.Y., 1954, **2**, 376-381.

Reperant, J.J.R., 2002, "Studies of turbulent liquid sheets for protecting IFE reactor chamber first walls," Master's thesis, Georgia Institute of Technology.

Rochau, G.E., Morrow, C.W., and Pankuch, P.J., 2003, "A concept for containing inertial fusion energy pulses in a Z-pinch driven power plant," *Fus. Sci. Technol.*, **43**, 447-455.

Rosenthal, M.W., Haubenreich, P.N., and Briggs, R.B., 1972, "The development status of molten-salt breeder reactors," ORNL-4812, Oak Ridge National Laboratory.

Sallam, K.A., Dai, Z., and Faeth, G.M., 1999, "Drop formation at the surface of plane turbulent liquid jets in still gases," *Int. J. of Multiphase Flow*, **25**, 1161-1180.

Sallam, K.A., Dai, Z., and Faeth, G.M., 2002, "Liquid breakup at the surface of turbulent round liquid jets in still gases," *Int. J. of Multiphase Flow*, **28**, 427-449.

Schubauer, G.B., Spangenberg, W.G., and Klebanoff, P.S., 1950, "Aerodynamic characteristics of damping screens," NACA TN 2001.

Seifritz, W. and Naegele, H., 1975, "Uranium and thorium shells serving as tampers of D-T fuel pellets for electron-beam-induced fusion approach," *Trans. Am. Nucl. Soc*., **21**, 18.

Sfeir, A.A., 1976, "The velocity and temperature fields of rectangular jets," *Int. J. Heat Mass Transfer*, **19**, 1289-1297.

Sfeir, A.A., 1978, "Investigation of three dimensional turbulent rectangular jets," *AIAA Paper* no. 78-1185.

Sforza, P.M., Steiger, M.H., and Trentacoste, N., 1966, "Studies on three-dimensional viscous jets," *AIAA J.*, **4**, 800-806.

Söderberg, L.D. and Alfredsson, P.H., 1998, "Experimental and theoretical stability investigations of plane liquid jets," *Eur. J. Mech. B/Fluids*, **17**, 689-737.

Söderberg, L.D., 2003, "Absolute and convective instability of a relaxational plane liquid jet," *J. Fluid Mech.*, **493**, 89-119.

Squire, H.B., 1953, "Investigation of the instability of a moving liquid film," *Br. J. Appl. Phys.*, **4**, 167-169.

Sterling, A.M. and Sleicher, C.A, 1975, "The instability of capillary jets," *J. Fluid Mech*., **68**, 477-495.

Tan-atichat, J., Nagib, H.M., and Loehrke, R.I., 1982, "Interaction of free-stream turbulence with screens and grids: a balance between turbulence scales," *J. Fluid Mech.*, **114**, 501-528.

Taylor, G.I., 1959a, "The dynamics of thin sheets of fluid: I. Water bells," *Proceedings of the Royal Society A*, **253**, 289-295.

Taylor, G.I., 1959b, "The dynamics of thin sheets of fluid: II. Waves on fluid sheets," *Proceedings of the Royal Society A*, **253**, 296-312.
Wada, Y., 1950, *J. Phys. Soc.* Japan, **5**, 259-439.

Waganer, L. M., 1994, "Innovation leads the way to attractive inertial fusion energy reactors – Prometheus-L and Prometheus-H," *Fusion Eng. Des*., **23**, 251-297.

Wu, P.K. and Faeth, G.M., 1993, "Aerodynamic effects on primary and secondary spray breakup," *Atomization Sprays*, **3**, 265-289.

Wu, P.K. and Faeth, G.M., 1995, "Onset and end of drop formation along the surface of turbulent liquid jets in still gases," *Phys. Fluids A*, **7**, 2915-2917.

Wu, P.K., Miranda, R.F., and Faeth, G.M., 1995, "Effects of initial flow conditions on primary breakup of nonturbulent and turbulent round liquid jets," *Atomization Sprays*, **5**, 175-196.

Wu, P.K., Tseng, L.K., and Faeth, G.M., 1992, "Primary breakup in gas/liquid mixing layers for turbulent liquids," *Atomization Sprays*, **2**, 295-317.

Ying, A. and Abdou, M., 1998, "Scaling criteria for IFE liquid wall protection scheme simulation," *Fusion Eng. and Des.*, **42**, 555-561.

York, J.L., Stubbs, H.E., and Tek, M.R., 1953, "The mechanics of disintegration of liquid sheets," *J. Fluids Eng.*, 1279-1286.